UNIVERSITÀ DEGLI STUDI DI PARMA

Dottorato di ricerca in SCIENZE DELLA TERRA

Ciclo XXIX

Synthetic pyroxenes for technological applications

Coordinatore:
Chiar.mo Prof. Fulvio Celico

Tutor:
Chiar.mo Prof. Mario Tribaudino

Dottorando: Claudia Gori

“Credo di poter affermare che nella ricerca scientifica
né il grado di intelligenza né la capacità di eseguire
e portare a termine il compito intrapreso
siano fattori essenziali per la riuscita
e per la soddisfazione personale.
Nell'uno e nell'altro contano
maggiormente la totale dedizione e
il chiudere gli occhi davanti alle difficoltà:
in tal modo possiamo affrontare i problemi che altri,
più critici e più acuti, non affronterebbero.”

Rita Levi Montalcini

Alla mia famiglia e ad Andrea

Contents

2. PYROXENE

3. CERAMIC MATERIALS AND COLORANTS

4. SOME INFORMATION ABOUT COBALT AND ZINC

5. SYNTHESIS AND SAMPLE CHARACTERIZATION

Abstract

Pyroxenes are a group of important rock-forming inosilicate minerals of special interest to Earth and Planetary Sciences. They are major constituents in the lower crust and upper mantle, as well as of evolved and undifferentiated solid bodies of the Solar System. One of the most intriguing features of this family of silicates is the wide range of chemical substitutions that occur in a relatively simple structure. Extended chemical substitutions may be studied in synthetic pyroxenes to provide a simple model in order to interpret the structural modifications that occur as a function of temperature, pressure and composition, and to reconstruct the sequence of natural processes of cooling and crystallization of the igneous rocks. Such informations can be gathered by careful laboratory investigations by means of microprobe analysis, electron microscopy, X-ray diffraction and spectroscopic techniques. Synthetic pyroxenes with wide compositional ranges, that go beyond the compositions commonly found in those natural, are also studied in order to investigate the flexibility of the pyroxene structure, the occurrence of new phase transitions and the effect of cation substitutions on such phase transitions, as well as the effect of the electronic transitions on the structural changes for those pyroxenes containing transition metals in their octahedral sites. More recently the properties of synthetic pyroxenes containing transition metals were investigated in view of the discovery of a multiferroic behaviour, as well as of their properties as ceramic pigments, since transition metals are often chromophores, capable of imparting specific colors to the pigment.

This dissertation reports the results derived from the project aimed to explore some pyroxene structures used as a basis for the production of advanced materials with technological applications, such as, for example, production of ceramic pigments with colorimetric properties enhanced with respect to the commercial colorants, *i.e.* cobalt-olivine Co_2SiO_4 and cobalt-spinel $CoAl_2O_4$. Solid solutions of synthetic pyroxenes were obtained by doping their octahedrally coordinated sites with transition metal ions (*i.e.*

Co^{2+} and Zn^{2+}). Pyroxenes containing cobalt were synthesized at ambient pressure by using method of growth from melt and flow, while those containing zinc were obtained in high pressure conditions (5 GPa) by using a multi-anvil apparatus. The analytical techniques adopted to investigate the chemical, crystallographic and physical properties of the synthesized compounds are: single crystal and powder X-ray diffractions, visible, near infrared (VIS-NIR) and infrared (IR) spectroscopies, colorimetric analysis and technological tests.

The main results presented in this thesis, concern:

1) the synthesis of pyroxenes along the $CaZnSi_2O_6$-$Zn_2Si_2O_6$ series, in order to explain how a predominantly ionic bond becomes covalent affecting the crystallographic characteristics of the zinc pyroxene, and its geochemical behaviour in silicate melts. The crystal structure and chemical behaviour of pyroxenes belonging to the $CaZnSi_2O_6$-$Zn_2Si_2O_6$ series, was then compared with those belonging to $CaCoSi_2O_6$-$Co_2Si_2O_6$, diopside-enstatite, hedenbergite-ferrosilite series. Preliminary data of IR spectroscopy performed on $CaZnSi_2O_6$-$Zn_2Si_2O_6$ solid solution are also presented;

2) the synthesis of a new pigment based on the $CaCo_xMg_{1-x}Si_2O_6$ pyroxene structure, low in cobalt content, whose colorimetric behaviour is similar to that observed in conventional ceramic pigments higher in cobalt content (*i.e.* Co-olivine an Co-spinel);

3) the determination of the "averaged" crystal structure in crystals of $CaCo_xMg_{1-x}Si_2O_6$ pyroxene series;

4) the definition of the optical properties along the different directions in crystals of $CaCo_xMg_{1-x}Si_2O_6$ pyroxene series;

5) the discovery of an antiferromagnetic ordering at $T_{Néel=}$ 10 K in $CaMgSi_2O_6$-$CaCoSi_2O_6$ solid solution that occurs when the cobalt content in the octahedral sites of the pyroxene crystal structure is higher than 0.7 atoms per formula unit.

The final goal of this work is the characterization of $CaCo_xMg_{1-x}Si_2O_6$ pigment from the technological viewpoint by simulating the production process of ceramic tiles, in order to assess, in terms of color stability and strength, its performances under industrial conditions, and compare them with those exhibited by conventional ceramic pigments ($CoAl_2O_4$ or Co_2SiO_4).

Riassunto

I pirosseni sono un gruppo di importanti minerali che formano le rocce, di particolare interesse per le Scienze della Terra e planetarie. Essi sono i principali costituenti della crosta inferiore e mantello superiore, nonché di corpi solidi evoluti e indifferenziati del Sistema Solare. Una delle caratteristiche più interessanti di questa famiglia di silicati è la vasta gamma di sostituzioni chimiche che avvengono in una struttura relativamente semplice. Le estese sostituzioni chimiche possono essere studiate in pirosseni sintetici per fornire un modello semplice al fine di interpretare le modificazioni strutturali che avvengono in funzione di temperatura, pressione e composizione, e ricostruire la sequenza dei processi naturali, di raffreddamento e cristallizzazione, delle rocce ignee. Tali informazioni possono essere raccolte attraverso accurate indagini di laboratorio mediante analisi alla microsonda, microscopia elettronica, diffrazione di raggi X e tecniche spettroscopiche. Pirosseni sintetici con intervalli di composizione che vanno oltre le composizioni comunemente trovate in quelli naturali, sono anche oggetto di studi approfonditi volti ad indagare la flessibilità della struttura del pirosseno, l'insorgere di nuove transizioni di fase e l'effetto delle sostituzioni cationiche su tali transizioni di fase nonché l'effetto delle transizioni elettroniche sui cambiamenti strutturali per quei pirosseni che contengono metalli di transizione nei siti ottaedrici. Le proprietà dei pirosseni sintetici contenenti metalli di transizione, sono state più recentemente studiate in vista della scoperta di un comportamento multiferroico, nonché delle loro potenziali applicazioni come pigmenti ceramici, dal momento che i metalli di transizione sono spesso dei cromofori in grado di impartire colori specifici al pigmento.

Questa tesi riporta i risultati ottenuti dal progetto finalizzato ad esplorare alcune strutture di pirosseno da usare come base per la produzione di materiali avanzati con applicazioni tecnologiche, ad esempio, per la produzione di pigmenti ceramici con proprietà colorimetriche migliori rispetto ai coloranti disponibili in commercio, quali il silicato di cobalto (cobalto-olivina) e l'alluminato di cobalto (cobalto-spinello). Soluzioni solide di pirosseni sintetici sono state ottenute dopando i siti a coordinazione ottaedrica con ioni

dei metalli di transizione (Co^{2+} e Zn^{2+}). I pirosseni contenenti cobalto sono stati sintetizzati a pressione ambiente mediante metodo di crescita da fuso e da flusso, mentre quelli contenenti zinco sono stati ottenuti in condizioni di alta pressione (5 GPa) utilizzando un apparato multi-anvil. Le tecniche di analisi adottate per indagare le proprietà chimiche, cristallografiche e fisiche dei composti sintetizzati sono: diffrazione a raggi X su polveri e su cristallo singolo, spettroscopia del visibile, vicino infrarosso (VIS-NIR) e infrarosso (IR), analisi colorimetriche e prove tecnologiche.

I principali risultati presentati in questa tesi, riguardano:

1) la sintesi di pirosseni lungo serie $CaZnSi_2O_6$-$Zn_2Si_2O_6$, per spiegare come un legame prevalentemente ionico diventa covalente influenzando le caratteristiche cristallografiche del pirosseno di zinco nonché il suo comportamento geochimico in fusi silicatici. La struttura cristallina e il comportamento chimico di pirosseni appartenenti alla serie $CaZnSi_2O_6$-$Zn_2Si_2O_6$, è stato poi confrontato con pirosseni appartenenti alle serie $CaCoSi_2O_6$-$Co_2Si_2O_6$, diopside-enstatite ed hedenbergite-ferrosilite. Tra i risultati vengono presentati anche i dati preliminari di spettroscopia IR effettuata sulla soluzione solida $CaZnSi_2O_6$-$Zn_2Si_2O_6$;

2) la sintesi di un nuovo pigmento basato sulla struttura del pirosseno $CaCo_xMg_{1-x}Si_2O_6$ a basso contenuto di cobalto e il cui comportamento colorimetrico è simile a quello osservato nei pigmenti ceramici convenzionali a più alto contenuto di cobalto (Co-olivina e Co-spinello);

3) la determinazione del struttura cristallina "media" nei cristalli della serie di pirosseni $CaCo_xMg_{1-x}Si_2O_6$;

4) la definizione delle proprietà ottiche lungo le diverse direzioni nei cristalli della serie di pirosseni $CaCo_xMg_{1-x}Si_2O_6$;

5) la scoperta di un ordinamento antiferromagnetico, a una temperatura di Néel= 10 K nella soluzione solida $CaMgSi_2O_6$-$CaCoSi_2O_6$ quando il contenuto di cobalto nel sito ottaedrico della struttura del pirosseno è maggiore di 0,7 atomi per formula unitaria.

L'obiettivo finale di questo lavoro è la caratterizzazione del pigmento $CaCo_xMg_{1-x}Si_2O_6$ dal punto di vista tecnologico simulando il processo di produzione delle piastrelle ceramiche, al fine di valutare in termini di stabilità del colore e resistenza, le sue prestazioni in condizioni industriali, e confrontarle con quelle mostrate dai coloranti ceramici convenzionali come $CoAl_2O_4$ (spinello) o Co_2SiO_4 (olivina).

List of publications

Refereed Journal/Conference publications

Manuscript listed in chronological order

Gori, C., Tribaudino, M., Mantovani, L., Delmonte, D., Mezzadri, F., Gilioli, E. and Calestani, G. (2015) Ca-Zn solid solutions in C2/c pyroxenes: Synthesis, crystal structure, and implications for Zn geochemistry. *American Mineralogist*, 100 (10), 2209-2218.

Gori, C., Tribaudino, M., Mantovani, L., Gatta, G.D., Delmonte, D., Mezzadri, F., Gilioli, E., and Calestani, G. (2016) Synthesis and crystal structure of *C2/c* Ca(Co, Mg)Si_2O_6 pyroxenes: effect of the cationic substitution on the cell volume. *Mineralogical Magazine,* https://doi.org/10.1180/minmag.2016.080.160 (in press).

Abstracts

Gori, C., Tribaudino, M., Mantovani, L., Delmonte, D., Mezzadri, F., Gilioli, E. and Calestani, G. *Ca-Zn substitution in clinopyroxenes: anomalous solution behavior and implications for mantle petrology.* SGI (Italian Geological Society)-SIMP (Italian Society of Mineralogy and Petrology) Conference: The future of italian geosciences, the italian geosciences of the future, september 10-12, 2014, Milan, Italy. [oral contribution]

Gori, C., Tribaudino, M., Mantovani, L., Skogby, H., Hålenius U., Delmonte, D., Mezzadri, F., Gilioli, E. and Calestani, G. *Ceramic and magnetic properties of synthetic cobalt-doped diopside.* 2nd European Mineralogical Conference (EMC2016), september 11-15, 2016, Rimini, Italy. [oral contribution]

Gori, C., Tribaudino, M., Mantovani, L., Delmonte, D., Mezzadri, F., Gilioli, E. and Calestani, G. *Crystal structure refinement of synthetic Ca-Zn clinopyroxenes.* First European Crystallography School (ECS1), august 31 - september 6, 2014, Pavia, Italy. [poster]

Gori, C., Tribaudino, M., Mantovani, L., Skogby, H., Hålenius U., Delmonte, D., Mezzadri, F., Gilioli, E. and Calestani, G. *Synthesis and coloring performance of the Ca(CoMg)Si_2O_6 pyroxene ceramic pigment.* SIMP (Italian Society of Mineralogy and Petrology), Il Pianeta Dinamico: sviluppi e prospettive a 100 anni da Wegener , september, 2-4, 2015, Florence, Italy. [poster]

Gori C., Tribaudino M., Mantovani L., Skogby H., Hålenius U., Delmonte D., Mezzadri F., Gilioli E. and Calestani G. *Structural refinement, crystal chemistry and optical spectra of Co-doped synthetic diopside*. 8th European Conference on Mineralogy and Spectroscopy (ECMS2015), september, 9-11, 2015, Rome, Italy. [poster]

1. INTRODUCTION

Pyroxenes are among the major constituents of the lower Earth crust and the upper mantle, as well as of rocky planets and meteorites (Ringwood 1975; Anderson 1989; Deer *et al.*, 1992). Pyroxenes are a class of inosilicates whose general formula can be expressed as $M2M1T_2O_6$, where $M2$ is a distorted six-/eight-fold coordinated polyhedron, $M1$ is a more regular octahedron and T is a slightly distorted tetrahedron (Burnham *et al.*, 1967).

In natural pyroxenes, the *M2* site is occupied by larger cations, such as Ca, Na, Mg, Fe^{2+}, and Li, the *M1* site is occupied by Mg, Fe^{2+}, Fe^{3+}, Al, and Cr, whereas the *T* site is occupied by only Si and Al. These are the most common cations in the rock-forming pyroxenes; others do occur in trace amounts or as major constituents in synthetic pyroxenes (Cameron and Papike, 1981). In synthetic pyroxenes, the *M2* site can also be filled by Sr, Co, Ni, Mn and Zn; the *M1* site can be filled by Co, Ni, Cr, Mn, Ni, Zn, Sc, Ti, Cu, Ga and V; Ge can fully exchange with Si in the tetrahedral site (Ohashi *et al.*, 1990; Redhammer and Roth 2004; Redhammer *et al.*, 2012; Redhammer and Tippelt 2014; Tribaudino *et al.*, 2005a, b; Arlt and Angel 2000; Tribaudino *et al.*, 2002; Heuer *et al.*, 2005; Tribaudino *et al.*, 2009; Thompson *et al.*, 2005; Hugh-Jones *et al.*, 1994).

The crystal chemical behaviour of the pyroxene structure provides models on the structural changes related to the composition (*X*) and *P-T* conditions induced by cationic substitutions. Since the pyroxene structure is able to accommodate different transition elements in its *M1* and *M2* cation sites, pyroxenes may be synthesized obtaining extended solid solutions with compositional ranges that go beyond those observed in natural pyroxenes and whose properties are not yet explored. This extends the interest in pyroxenes from petrology (as rock-forming minerals) to material science. For example, $NaFeSi_2O_6$ was reported as a multiferroic phase (Jodlauk *et al.*, 2007; Redhammer *et al.*, 2008, 2009, 2013), diopside as a scaffold for prosthetic applications (Ghomi *et al.*, 2012; Karamiana *et al.*, 2014); enstatite chondrites as host for high luminescent nanoparticles (Zhang *et al.*, 1996), and cobalt-pyroxene as a pigment in ceramic materials (Mantovani *et al.*, 2015).

1.1. Background, challenges and objectives

One of the most interesting physical properties in pyroxenes is the capability to change their colour as a function of the substituent cation. Especially the ions of transition elements, which are called chromophores, are highly absorptive of selected wavelengths of light and possess strong pigmenting capabilities. As mentioned above, since the pyroxene structure is flexible and able to accommodate different transition elements, it allows to obtain a wide range of colours and shades.

This Ph.D. project was funded under the program named 'Advanced materials (in particular ceramics) for industrial applications'. Advanced materials are produced from synthetic raw materials typically constituted of pure or nearly pure chemical compounds. They are used in electronics, mechanics, in the production of energy and for pigment applications. This thesis is focused on the synthesis and the characterization of an advanced ceramic material obtained from the pyroxene structure.

We have focused on Zn and Co pyroxenes, whose structural and physical properties and their possible applications as advanced ceramics, were little discussed.

Our investigation on Co pyroxenes was focused on the synthesis of a colouring pigment which is resistant to high temperature and leaching and which could be considered as a potential candidate for the production of ceramic pigments. On Zn pyroxenes we aimed to obtain a phase with peculiar physical properties, owing to the covalent behaviour of Zn in monoclinic $Zn_2Si_2O_6$ pyroxenes.

A great part of this thesis will be devoted to cobalt-pyroxenes, where a full set of results, comprising synthesis, crystal chemistry, optical characterizations and technological testing, was obtained.

In particular, the thesis aims to synthesize a new pink cobalt-based ceramic pigment, with the purpose of reducing the cobalt amount used in the ceramic industry, to cope with economic and environmental issues related to the cobalt toxicity and production costs. Co^{2+} is generally associated with the blue colour, which is typical of its tetrahedral coordination, like in akermanite $Ca_2CoSi_2O_7$ (Co-akermanite) or in spinel $CoAl_2O_4$ (Co-spinel), but in Co-pyroxene, the six-fold coordinated Co^{2+} that populates the *M*1 and *M*2 sites, gives the pink colour (White *et al.*, 1971; Llusar *et al.*, 2001).

Cobalt-pyroxene ($CaCoSi_2O_6$) was recently tested as a pigment for ceramic applications (Mantovani *et al.*, 2015), but it revealed some unresolved issues. First, the temperature range for the synthesis is quite narrow, between 1000 and 1200 °C; at lower temperature oxidation to Co^{3+} and formation of stable $Ca_2CoSi_2O_7$ (Co-akermanite) occur. As mentioned above, in Co-akermanite, Co is present in tetrahedral coordination and acts as a blue (instead of pink) pigment; Co-akermanite has a high colouring efficiency and, even a low fraction in the run product, hides the pink hue of Co^{2+} in octahedral coordination. Co-akermanite disappears only after prolonged heating in a silica-oversaturated environment. Besides, in technological tests the $CaCoSi_2O_6$ pigment acts as a dye, dissolving into the glassy phase under the aggressive environmental conditions, typical of ceramics manufacturing (Mantovani *et al.*, 2015). In fact, Co^{2+} usually occurs in tetrahedral coordination in a silicate glass and the resulting colour is blue (Dondi and Eppler, 2014; Hunault *et al.*, 2016). Moreover, the amount of Co^{2+} for the synthesis of $CaCoSi_2O_6$ is lower than in the cobalt-based conventional ceramic pigments, such as $CoAl_2O_4$ or Co_2SiO_4 (Co-spinel and Co-olivine, respectively), but it is still high considering environmental and economic concerns. Our investigation aims to synthesize a pigment with the lowest possible cobalt content, still maintaining a similar colouring performance of the available and conventional ceramic pigments.

This dissertation reports mainly the results derived from the studies performed on solid solutions between diopside (ideally $CaMgSi_2O_6$, symbolized 'Di') and $CaCoSi_2O_6$ (Co-pyroxene). Diopside has a stability field extended up to higher temperature than $CaCoSi_2O_6$ (melting at 1391 °C at 0.0001 GPa), and metastable akermanite does not occur in Mg-pyroxenes. Therefore, we may expect a wider stability field for Ca-Mg-Co-pyroxenes. In addition, only few crystal chemical data are available for pyroxenes of the $CaMgSi_2O_6$-$CaCoSi_2O_6$ series.

The clinopyroxenes along the $CaMgSi_2O_6$-$CaCoSi_2O_6$ join will be investigated by a combined structural-spectroscopic and technological approach, according to the following steps:

1) a number of pyroxenes along the $CaMgSi_2O_6$-$CaCoSi_2O_6$ series will be synthesized, following two different procedures at room pressure, and trying to obtain crystals large

enough for the subsequent UV-VIS-NIR investigations on oriented crystals. The synthesized samples will be characterized by X-ray powder diffraction and electron microprobe analysis in WDS and EDS modes;

2) the structural changes induced by the cation substitution at the *M*1 site will be investigated by single-crystal X-ray diffraction, showing the effect on the structure (at the atomic level) and on the unit-cell volume. Only few structure refinements based on single-crystal X-ray data for $Ca(Co,Mg)Si_2O_6$ pyroxenes are available in literature (Tabira *et al.* 1993); however, in Tabira *et al.* (1993), the composition is non-stoichiometric: a significant fraction of Co^{2+} at the *M*2 site was observed;

3) optical spectra will be taken from the synthesized materials.

The Co^{2+} optical spectrum has been studied with various synthetic compounds (Wildner, 1996), but only a small number of publications have been devoted to optical spectroscopy study of Co^{2+} ion in silicate matrices (White *et al.*, 1971; Taran and Rossmann, 2001; Ardit *et al.*, 2012; Dondi *et al.*, 2014). In an octahedral coordination environment, the optical spectrum of Co^{2+} ion is expected to consist of three spin-allowed optical absorption bands arising from the $^4T_{1g} \rightarrow {}^4T_{2g}$, $^4T_{1g} \rightarrow {}^4A_{2g}$ and the $^4T_{1g} \rightarrow {}^4T_{1g}$ (^4P) electronic transitions (White *et al.*, 1971; Taran and Rossmann, 2001);

4) technological tests will be performed to verify the performance and the possible industrial application of the synthesized pigments in a ceramic environment;

5) the magnetic behaviour of the synthesized pyroxenes will be investigated by means of SQuID measurements, to clarify how magnetic interactions occur between the octahedral chains and how they are related to the cobalt content in the pyroxene structure.

A final and more limited part of this thesis, will be devoted to Zn pyroxenes, which were the subject of our investigation in the first Ph.D. year. Firstly, to study the cationic substitution mechanism at the *M1* and *M2* cation sites, pyroxenes belonging to the $CaZnSi_2O_6$-$Zn_2Si_2O_6$ series were synthesized and characterized. Experimental data are present in literature only for the two end-members (extreme terms of the solid solution), *i.e.* on $CaZnSi_2O_6$ (Huber *et al.*, 2012) and $Zn_2Si_2O_6$ (Syono *et al.*, 1971; Morimoto *et al.*, 1975), whereas data are lacking for the intermediate compositions, *i.e.* those involving the substitution mechanism of Zn with Ca in the *M2* site of Ca-Zn pyroxenes. The series will be investigated by using powder and single-crystal X-ray diffraction and IR spectroscopy.

1.2. Structure of the thesis

This thesis consist of 9 chapters, including this introduction and the concluding remarks:

Chapter 2 gives information about pyroxene structure, crystal chemistry and phase diagrams at room temperature and high pressure of the Ca-Fe, Ca-Mg, Ca-Co and Ca-Zn pyroxene series.

Chapter 3 is an introduction to ceramic materials and explains the difference between dyes and pigments.

Chapter 4 explores physical, chemical features and the history of cobalt and zinc elements and introduces the use of cobalt in pigments and ceramics.

Chapter 5 introduces the various synthesis methods used to generate pyroxenes along the $CaMgSi_2O_6$-$CaCoSi_2O_6$ series and the analytical techniques adopted to characterize the synthesized pyroxenes.

Chapter 6 presents the main scientific achievements of this PhD project, concerning synthesis, structure, UV-VIS-NIR spectral optical properties, colorimetry and technological tests performed on the $CaMgSi_2O_6$-$CaCoSi_2O_6$ series.

Chapter 7 presents the results of magnetic measurements performed on the $CaMgSi_2O_6$-$CaCoSi_2O_6$ series.

Chapter 8 presents results of studies performed on the $CaZnSi_2O_6$-$Zn_2Si_2O_6$ pyroxene solid solution (paper published, *American Mineralogist*, 2015, 100, 2209-2218).

Chapter 9 concludes the dissertation with final remarks.

Chapter 2

PYROXENE

2. PYROXENE

2.1. Structure

The structure of pyroxenes can be ideally described in terms of alternating tetrahedral and octahedral layers parallel to the (100) plane. Within the tetrahedral layer, each *T*-tetrahedron has four oxygen atoms at the vertices, two of them are shared with adjacent SiO_4 tetrahedra to form infinite chains parallel to the c-axis (Cameron and Papike, 1980). Two adjacent oxygens form the edge of the tetrahedron, at a distance of 2.6 Å and, as each tetrahedron of the chain is repeated twice in a unit cell along the c-axis, the periodicity is approximately 5.2 Å (Figure 2.1a).

The formula unit for the tetrahedral chain is $[Si_2O_6]^{4-}$.

Since each tetrahedral chain is independent and able to provide stable geometrical configurations with an extensive range of cations and over a wide range of temperature and pressure conditions, the pyroxene structure can show a higher flexibility than, for instance, phyllo- or tectosilicates.

The octahedral layer contains six- to eight-coordinated *M* cations whose positions are the *M1* and *M2* sites. The *M1* site is coordinated by six oxygen arranged in an octahedral configuration and lies between the apices of the opposite tetrahedra; the *M2* site is irregularly coordinated by six or eight oxygen and lies between the bases of the opposite tetrahedra (Figure 2.1b). The *M2* coordination depends on the size of the cation which occupies the site.

As mentioned above, the size and shape of the tetrahedral polyhedra remain constant over a wide range of temperatures and pressures, while the *M* polyhedra may expand and contract; therefore the silicate chain changes its length to accomodate these variations by a rotation of the individual tetrahedra (Cameron and Papike, 1981). In particular a contraction and expansion of the *M* octahedral, by changing site occupancy, pressure and/or temperature, reduces and increases the chain length.

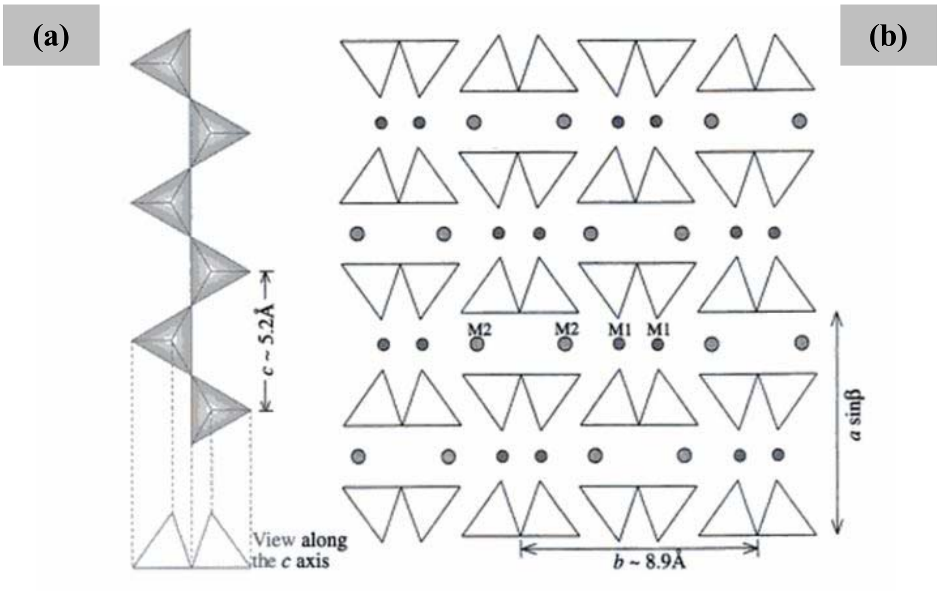

Figure 2.1. (**a**) A single pyroxene chain which extends along the c-axis with its periodicity. The chain repeats after every two SiO_4 tetrahedra, yielding an approximately 5.2 Å repeat distance. This defines the length of the unit cell in the c-axis direction, *i.e.* the *c* lattice parameter (Wentzcovitch *et al.*, 1995). (**b**) The arrangement of SiO_4 chains in the pyroxene structure viewd along the c-axis. The *M1* cations form chains of edge-sharing octahedra between the apices of the tetrahedra, while the *M2* polyhedra form chains between the bases of the tetrahedra. The b-axis repeat (8.9 Å) corresponds to the distance of two tetrahedral chains on the same layer pointing in the same direction; the a-axis is the distance of corresponding tetrahedra in a direction normal to the b-axis (for the images Putnis 1992).

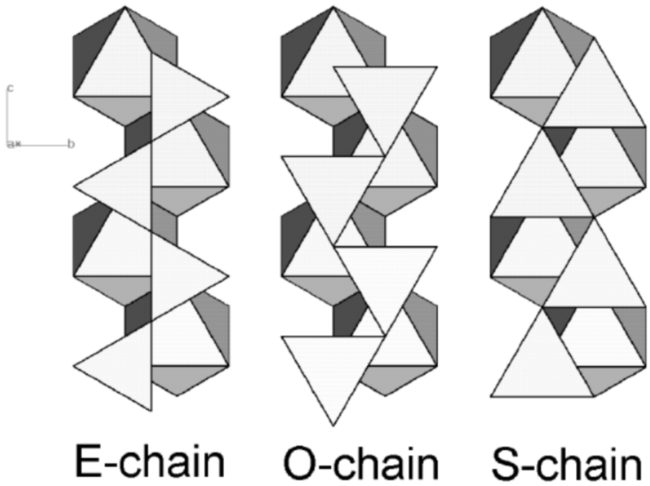

Figure 2.2. Representation of a fully extended tetrahedral chain for an ideal pyroxene structure (after Cameron and Papike, 1981); O-chain and S-chain are the two possible senses of tetrahedral rotation (Thompson and Downs, 2003). The rotated configurations are based on a close-packed arrangement of oxygen atoms with a tetrahedral to octahedral edge ratio of 1:1. Cubic close-packing of oxygen atoms produces a tetrahedral-octahedral configuration referred as an O rotation, whereas hexagonal close-packing produces a S-rotation (Cameron and Papike, 1980). The completely rotated O and S configurations represent the geometric extremes produced by rotating tetrahedra in the chains in opposite directions about imaginary lines passing through oxygen O1 and perpendicular to the (100) layer (Cameron and Papike, 1980).

In the ideal pyroxene structure the chains are straight, but in reality they are kinked by an angle (O3-O3-O3 angle or kinking angle) which varies from structure to structure and with changing temperature and pressure (Wentzcovitch *et al.*, 1995). The O3-O3-O3 angle describes the geometrical arrangement of the tetrahedral chains and the orientation of the tetrahedral chains relative to the octahedral chains (Thompson 1970; Papike *et al.*, 1973; Tribaudino *et al.*, 2002).

Thompson (1970) called the structures with straight chains and the O3-O3-O3 angle of 180°, ‘extended structures’ (Figure 2.2; termed E-chain, after Papike *et al.*, 1973) and he showed that, a rotation of the tetrahedra in a model E-chain in either direction by 30° about an axis passing through the apical O1 anion perpendicular to the (100) plane, brings the anion into a cubic close-packed arrangement (Thompson and Downs, 2003). Taking as reference the kinking angle of diopside ($CaMgSi_2O_6$), a tetrahedral chain with an O3-O3-O3 angle greater than 180°, has been referred to as S-rotated (Figure 2.2), while if the angle is less than 180°, the traditional notation is O-rotated (Figure 2.2; Thompson and Downs, 2004). Although each tetrahedron in a fully rotated chain is only rotated 30° from the extended chain position, the O3-O3-O3 angle is formed by the sum of the rotation of two tetrahedra, so a fully O-rotated chain has an angle of 120° and a fully S-rotated chain, of 240° (Thompson and Downs, 2003, 2004).

Depending on the configuration and arrangement of the silica chains and the octahedral layers, pyroxene may exhibit two different structural symmetry, *i.e.* monoclinic ($C2/c$) and orthorhombic ($Pbca$).

In $C2/c$ space groups the *M1* and *M2* sites occur in special positions on the two-fold axis of rotation, parallel to the b-axis, whereas in $Pbca$ and $P2_1/c$ structures, the *M* sites occupy general positions. The *T* site is at the center of the tetrahedron, and oxygen atoms occupy general positions in all space groups. In $C2/c$ structures (Figure 2.3) the symmetrically equivalent chains are related to 2-fold axis of rotation. In $P2_1/c$ structures [Figure 2.4(a-b)] the tetrahedral chains are non-symmetrically equivalent (A and B chains), so that the symmetry is reduced (the diad axis through the *M1* and *M2* sites becomes a screw 2_1 axis).

The A and B chains are kinked in opposite sense. The stacking of the layers is the same in $P2_1/c$ and in $C2/c$ pyroxenes and along a-axis all layers are stacked in the same way.

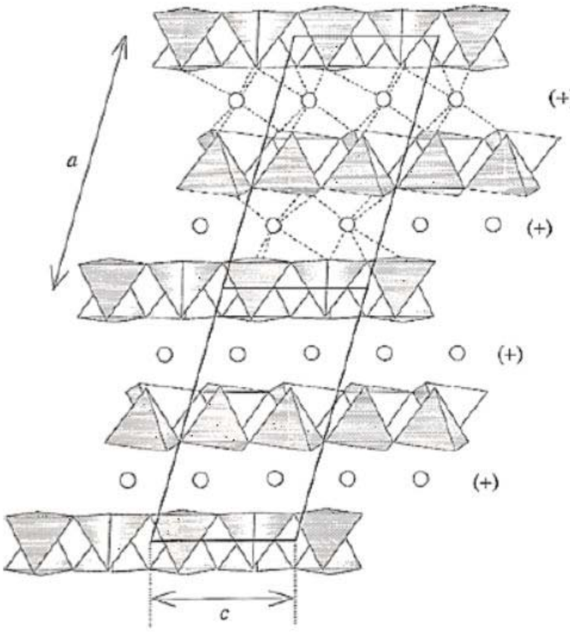

Figure 2.3. A clinopyroxene structure $C2/c$ viewed along the the b-axis. The chain layers are staggered along the c-axis; the *M* octahedra are oriented in the same direction (labelled +; Putnis 1992).

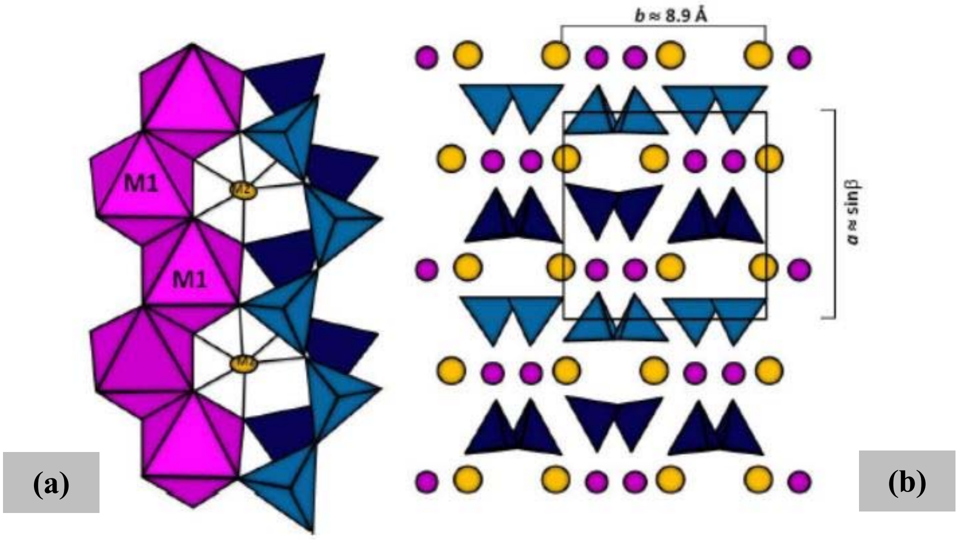

Figure 2.4. (**a**) A $P2_1/c$ pyroxene viewed along the a-axis. Light blue and deep blue tetrahedral chains represent the A and B chains, respectively; (**b**) a $P2_1/c$ pyroxene structure viewed along the c-axis (Putnis 1992).

In *Pbca* pyroxenes (Figure 2.5) subsequent layers are stacked in opposite directions and new glide planes normal to the a- and c-axes are formed. Therefore, in orthopyroxene the unit-cell is about twice the unit-cell of the monoclinic one ($a_{\text{opx}}= 2a\text{sen}\beta_{\text{cpx}}$; $b_{opx}= b_{cpx}$; $c_{opx}= c_{cpx}$; Figure 2.6), but *b* and *c* parameters remain the same and the silicate chains are non-equivalent.

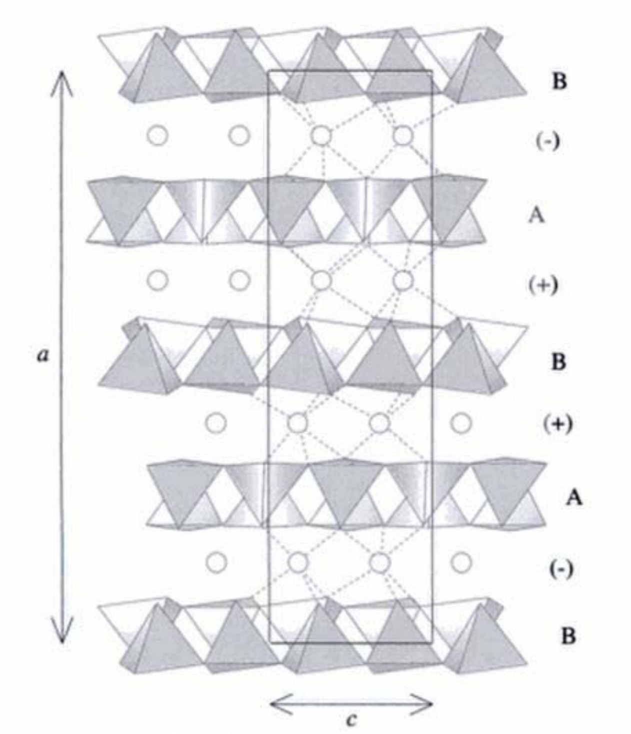

Figure 2.5. A orthopyroxene structure viewed along the b-axis. A and B are the non-equivalent chains. There are two possible orientations for the *M* octahedra (labelled + and -).

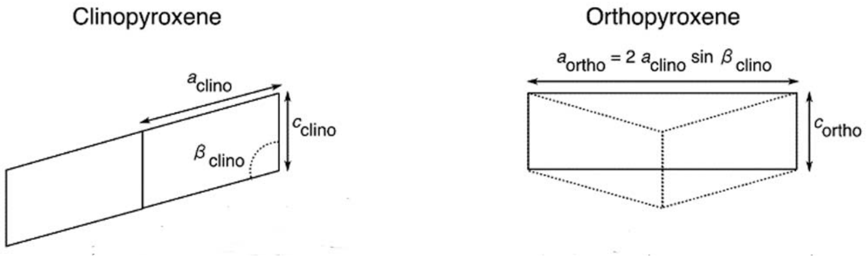

Figure 2.6. The relationship between the monoclinic and orthorhombic unit cells. The *a* lattice parameter of the orthorhombic unit cell is approximately twice the d-spacing of the 100 planes of the monoclinic structure (Putnis, 1992).

A way of looking at the different pyroxene structure types (*C*2/*c, P*2$_1$/*c* and *Pbca*) is to describe them in terms of the different stacking sequences of the octahedral layers and/or of symmetrically distinct tetrahedral chains in adjacent layers (Cameron and Papike, 1981). This is a helpful way to understand the relationship between the structures and the mechanism by which one structure transforms to another. The *b* and *c* lattice parameters are similar in all structures, while the *a* lattice parameter depends on the chain arrangement. The chains are arranged in layers parallel to (100) and these layers are stacked relative to one another in different ways in *C*2/*c, P*2$_1$/*c* and *Pbca* structure types. A pair of opposing chains and the *M1* sites between the apices forms an 'I-shaped beam' which lies parallel to [001] (Prewitt, 1980; Figure 2.7). Each tetrahedral-octahedral-tetrahedral 'I-beam' unit is designed + or – , depending on the orientation of the octahedra between the chain apices. Within a single octahedral layer each octahedron has a pair of triangular faces [lie parallel to (100)], the apices of the upper and lower face of each pair are pointed in an opposite sense but all faces, on one side on an octahderal layer, point in the same direction. In the positive octahedral strip, the apices of the upper triangular faces of each octahedron point in a +c direction, while, in a negative strip, they point in a –c direction, depending on the relative positions of the chains along their length.

The site-labelling scheme proposed by Burnham *et al.* (1967) is used in this thesis. In *C*2/*c* pyroxenes, there are two types of *M* sites, labelled *M*1 and *M*2 and the *T* (Si) tetrahedron site. In the *C*2/*c* structure, each of the four symmetrically equivalent chains of tetrahedra, is assigned to a letter (A, B, C and D), and each tetrahedron of the chain is referred with a number (1 or 2). The oxygen atoms in each tetrahedron are labelled as O1, O2 and O3, followed by the letter of the chain they belong to, and by 1 or 2, depending on the tetrahedron to which they are bonded. The O3 is a bridging oxygen atom shared between the SiO_4 tetrahedra, the O1 and O2 are the non-bridging oxygen atoms. Using Burnham's labelling scheme, and according to the site symmetry, in diopside $CaMgSi_2O_6$ Ca has four pairs of symmetrically equivalent *M*2-O distances with O1A1,B1, O2C2,D2, O3C1,D1, and O3C2,D2; Mg and Co are bonded to six oxygen atoms and form three pairs of symmetrically equivalent *M*1–O distances with O1A1,B1, O1A2,B2 and O2C1,D1.

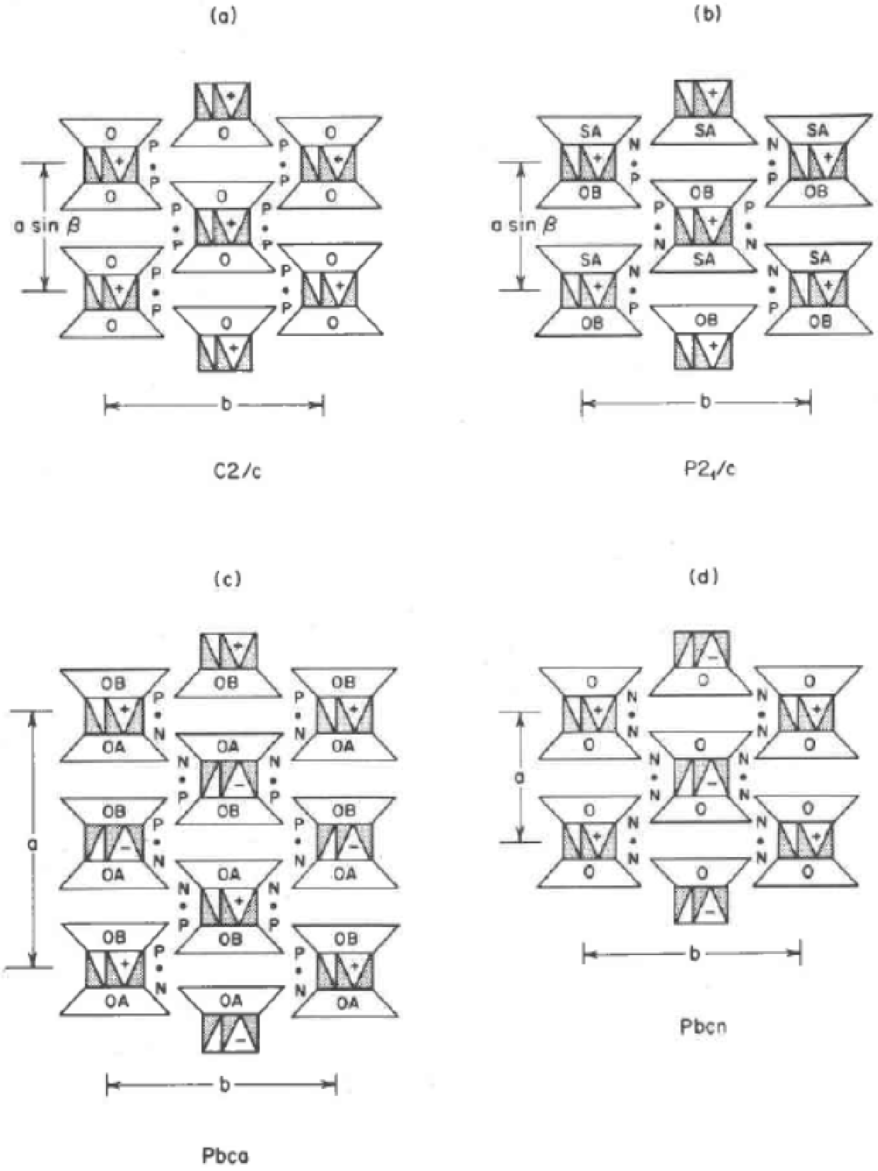

Figure 2.7. I-beam diagrams of the four pyroxenes structure types (*Pbca*, *Pbcn*, *C2/c*, $P2_1/c$). The symbol within the I-beam units provide information on the symmetry and orientation of individual coordination polyhedra: S and O are referred to the rotation of the tetrahedral chain; *M1* octahedra are labeled + or – and are referred to their skew or orientation between the tetrahedral chain apices; A and B of the tetrahedral layers refer to two symmetrically-distinct chains (chains that are kinked by different amounts and/or chains whose tetrahedra are distorted differently; Cameron and Papike, 1981).

2.2. The Ca-Mg-Fe pyroxene quadrilateral and phase diagrams

A major goal of this thesis is the synthesis of the pyroxene phases with technological interest. An acquaintance with phase diagrams to choose the best synthesis conditions and to predict and interpret the experimental results is therefore a preliminary request. However, most literature experimental data on pyroxenes were done on Ca-Mg-Fe-Al-Si pyroxenes, which represent, most closely, the composition of natural pyroxenes from basaltic, gabbroic and peridotitic rocks. Data on pyroxenes with different compositions, are few and scanty.

Here we will start our discussion on the simplified systems representing natural pyroxene compositions; first of all, the so called pyroxene quadrilateral of the $Mg_2Si_2O_6$ (Enstatite-**En**)- $Fe^{2+}_2Si_2O_6$ (Ferrosilite-**Fs**)- $CaMgSi_2O_6$ (Diopside-**Di**)- $CaFe^{2+}Si_2O_6$ (Hedenbergite **Hd**) system (Figure 2.8). Then we will continue with the discussion on Co (paragraph 2.3) and Zn (paragraph 2.4) pyroxenes.

The pyroxene quadrilateral is a part of the triangular phase diagram with vertices $Ca_2Si_2O_6$ (Wo), $Mg_2Si_2O_6$ (En) and $Fe^{2+}_2Si_2O_6$ (Fs) (Morimoto *et al.*, 1988). Although wollastonite ($Ca_2Si_2O_6$) has a structure based on chains of SiO_4 tetrahedra, the chains have a three-tetrahedra repeat, rather than a two-tetrahedra repeat (see Figure 2.1, paragraph 2.1) and belongs to a class of structures called *pyroxenoids*.

In the Di-Hd-En-Fs system complete substitution exists between diopside and hedenbergite (Ca-rich pyroxenes) and between enstatite and ferrosilite (Ca-poor pyroxenes), since ferrous iron and magnesium, have identical charge and similar ionic sizes (*i.e.* $^{VI}Fe^{2+}$ 0.78 Å and $^{VI}Mg^{2+}$ 0.72 Å, Shannon 1976; Cameron and Papike, 1981; Downs 2003). By this respect, we expect complete solid solutions also when Co^{2+} and Zn^{2+} exchange for Mg^{2+} or Fe^{2+}. The ionic radii of Zn^{2+} and Co^{2+}, respectively 0.74 and 0.745 Å, are actually very similar to that of Mg^{2+}.

The diopside-hedenbergite solid solution has a structure close to the ideal pyroxene topology with monoclinic space group *C*2/*c* (Figure 2.3, paragraph 2.1). Compositions near the enstatite-ferrosilite join are orthorhombic (Figure 2.5, paragraph 2.1) if contain less than about 5% Wo and monoclinic (pigeonite) if Wo value is between 5 and 20 %.

At high-temperature (above about 1000 °C) enstatite has the *Pbcn* space group with almost straight silicate chains, which are equivalent to one another. This form of orthorhombic pyroxene is termed protoenstatite. As it is shown in Figure 2.9, below 1000 °C, protoenstatite transforms to orthoenstatite (*Pbca*) and to clinoenstatite below 600 °C (*C*2/*c*; Pacalo and Gasparik, 1990).

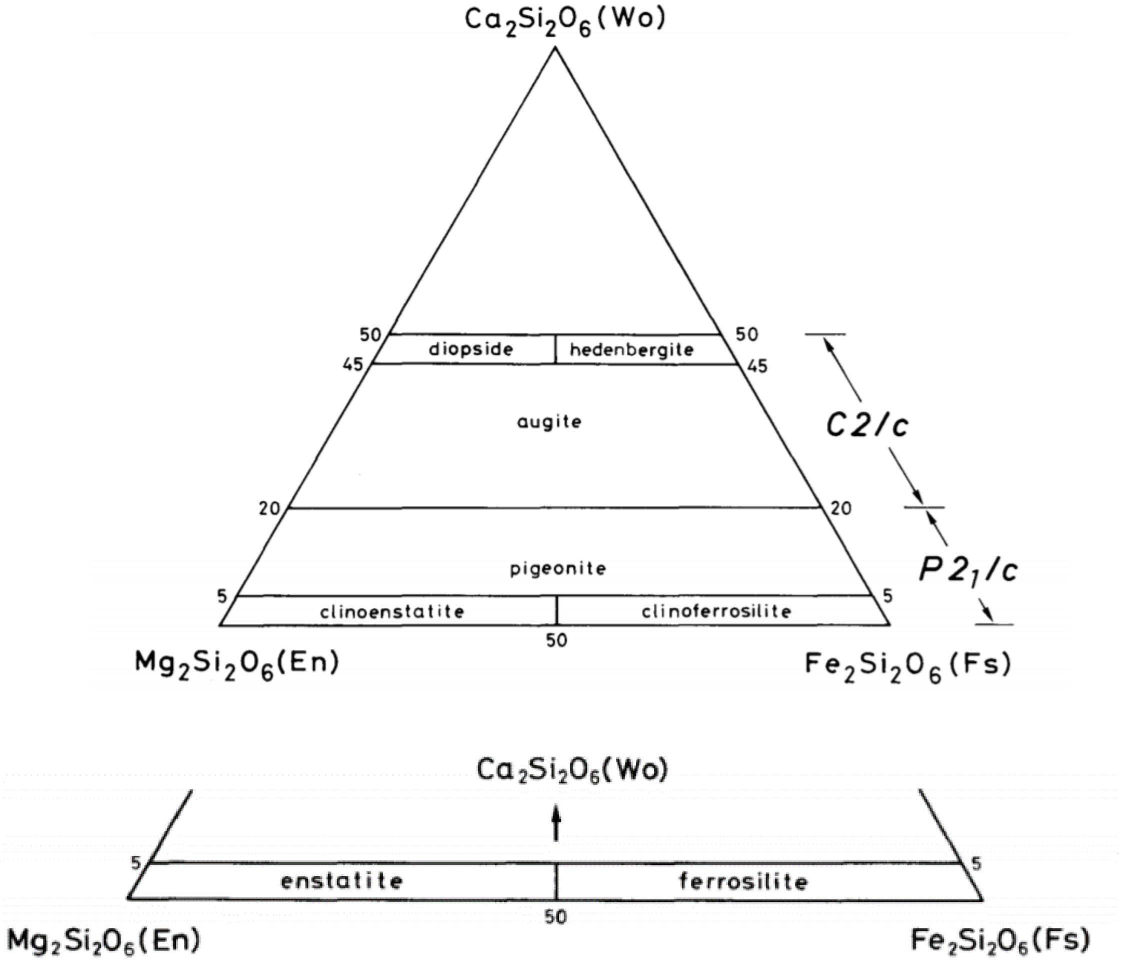

Figure 2.8. Above: Composition ranges of the Ca-Mg-Fe clinopyroxenes with accepetd names. Below: Composition ranges of orthopyroxene with accepted names (Morimoto, 1988). Note that there is complete Mg-Fe substitution and small amounts of Ca substitution into the orthopyroxene solid solution series. Mg-rich varieties of orthopyroxene are called enstatite, whereas Fe-rich varieties are called ferrosilite. $Ca_2Si_2O_6$ is the chemical formula for wollastonite, but wollastonite does not have a pyroxene structure. Solid immiscibility is present between the diopside-hedenbergite series and the orthopyroxene (enstatite-ferrosilite) series.

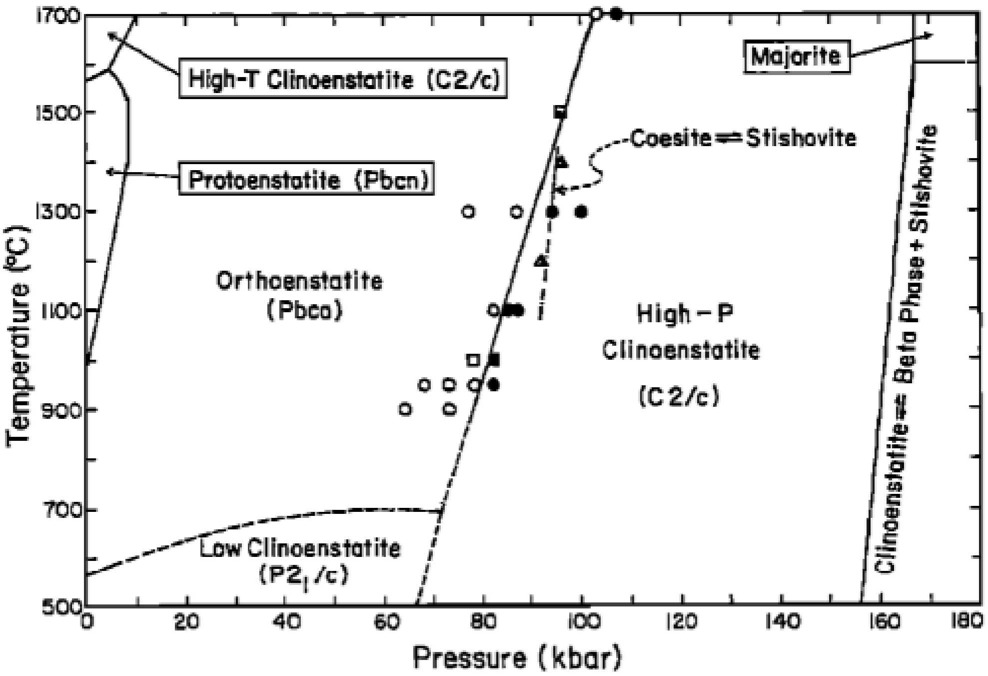

Figure 2.9. Temperature-pressure phase diagram for the $MgSiO_3$ system (Pacalo and Gasparik, 1990).

Ferrosilite is not stable at low pressure and breaks down to a mixture of fayalite and quartz (Figure 2.10; Lindlsey and Munoz, 1969). The orthoferrosilite structure (*Pbca*) is stable at pressures above 10 kbar and temperatures above 400-600 °C. Likewise, the breakdown of the pyroxene phase in an olivine + silica assemblage and the stabilization at higher pressure, occur in pyroxenes where Zn and Co exchange for Fe, albeit at different pressure conditions.

Experiments on the $MgSiO_3$ system (Pacalo and Gasparik, 1990; Kanzaki, 1991; Angel *et al.*, 1992a) have confirmed that orthoenstatite and ferrosilite transform at high temperature and pressure in a clinopyroxene phase with *C*2/*c* symmetry. As discussed in the previous paragraph, high temperature and high pressure *C*2/*c* pyroxenes have a different structure, but both revert, during fast cooling or decompression, to the $P2_1/c$ phase, which is the form we observe at room conditions. Orthoenstatite of composition $MgSiO_3$ transforms to this high-pressure clinoenstatite structure at the pressures and temperatures corresponding to a depth of 200-300 km within the Earth's upper mantle (Figure 2.11; Hugh-Jones *et al.*, 1994).

By analogy with $MgSiO_3$, ferrosilite transforms to a *C*2/*c* phase at high pressures and reverts to *P*2_1/*c* clinoferrosilite upon pressure release (Hugh-Jones and Angel 1994; Akimoto *et al.*, 1965); the phase diagram of $FeSiO_3$ is then very similar to that of $MgSiO_3$ (Angel *et al.*, 1992a; Angel and Hugh-Jones, 1994). The transformation from the orthorhombic to monoclinic structure at high pressure was observed also in $Co_2Si_2O_6$ (Akimoto *et al.*, 1965, Mantovani *et al.*, 2014); the high pressure and high temperature transformations from *P*2_1/*c* to *C2/c* are also expected, but yet to be confirmed. In Zn pyroxenes the changes are more complex and will be discussed in Chapter 8.

At ambient temperature, pyroxenes containing less than 15% Ca in the Ca(Mg,Fe)SiO_3-(Mg,Fe)SiO_3 solid solution range are stable as a low-symmetry *P*2_1/*c* structure (Ohashi *et al.*, 1975); as the temperature is increased, a high-T (high-symmetry) *C*2/*c* structure is stabilized (Smyth and Burnham 1972; Sueno *et al.*, 1984; Tribaudino *et al.*, 2002).

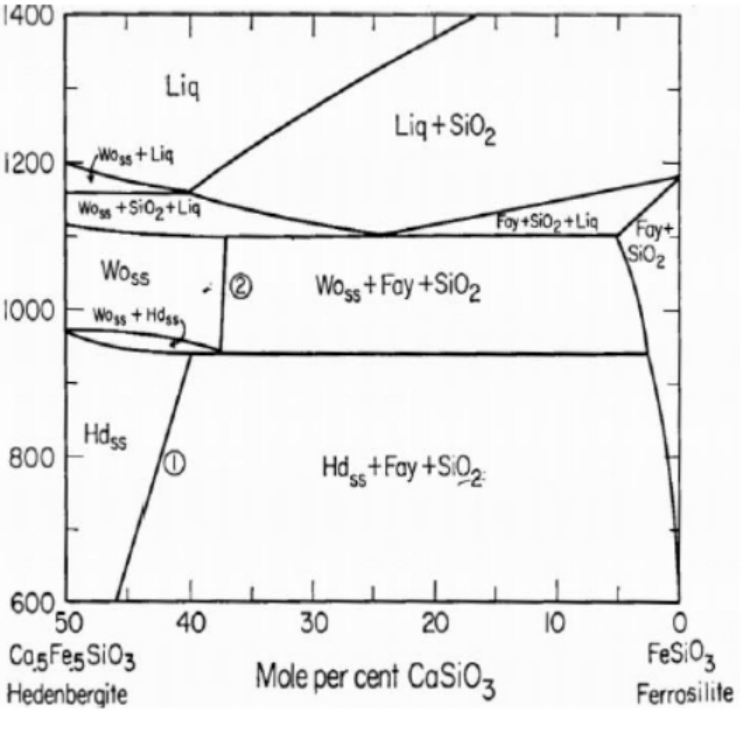

Figure 2.10. Subsolidus phase relations in the enstatite-ferrosilite join at low pressure. Hd= hedenbergite; Wo= wollastonite; Fay= fayalite; Liq= liquidus; ss= solid solution (Lindsley and Munoz, 1969).

Mantle clinopyroxenes are solid solutions of the two end-member of the join Di-En (Gasparik, 1989), but the solid solutions are most extended on the Ca-rich side of this join. The compositional range of the mantle clinopyroxenes varies with pressure and temperature (Gasparik, 1990). In both Ca-Mg and Ca-Fe pyroxenes there is an asymmetric miscibility gap between Ca-rich and Ca-poor compositions with higher solubility in the Ca-richer side, which widens with increasing pressure (Gasparik and Lindsley, 1980; Lindlsley and Munoz, 1969).

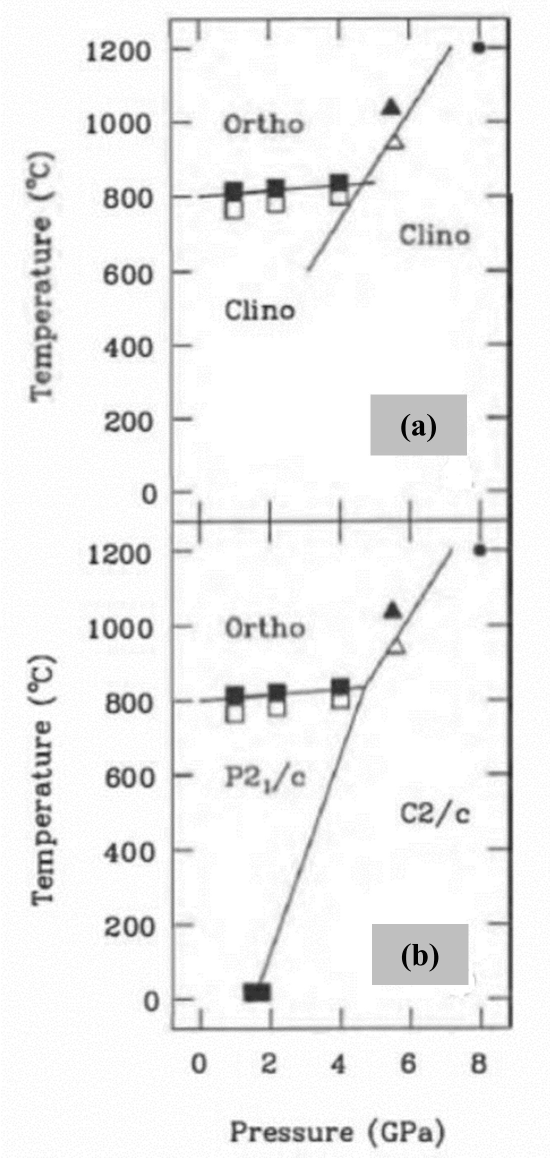

Figure 2.11. (**a**) Phase diagram of $MgSiO_3$ (ignoring the low-pressure breakdown to fayalite + quartz and the existence of a structurally distinct *C*2/*c* phase stable at high temperatures), deduced from experiments quenched from high pressures and temperatures (Hugh-Jones *et al.*, 1994).
(**b**) Phase diagram of $FeSiO_3$. We have the same topology as that of $MgSiO_3$, with a stability field for a *C*2/*c* ferrosllite phase at high pressures. By analogy with $MgSiO_3$, this phase is expected to revert to $P2_1/c$ clinoferrosilite upon pressure release (Hugh-Jones *et al.*, 1994).

The phase diagram of the Di-En join was first described by Boyd and Schairer (1964). As it is shown in Figure 2.12a, at high dry pressure the melting temperature increases and a wide solid solution in the subsolidus (in a narrow field between solidus and miscibility gap), can be obtained (Lindsley 1980). In Hd-Fs pyroxenes the phase diagram (Figure 2.12b) is similar to that of Ca-Mg ones but with larger miscibility in the Ca-richer pyroxene side and lower melting temperature (Lindsley and Munoz, 1969).

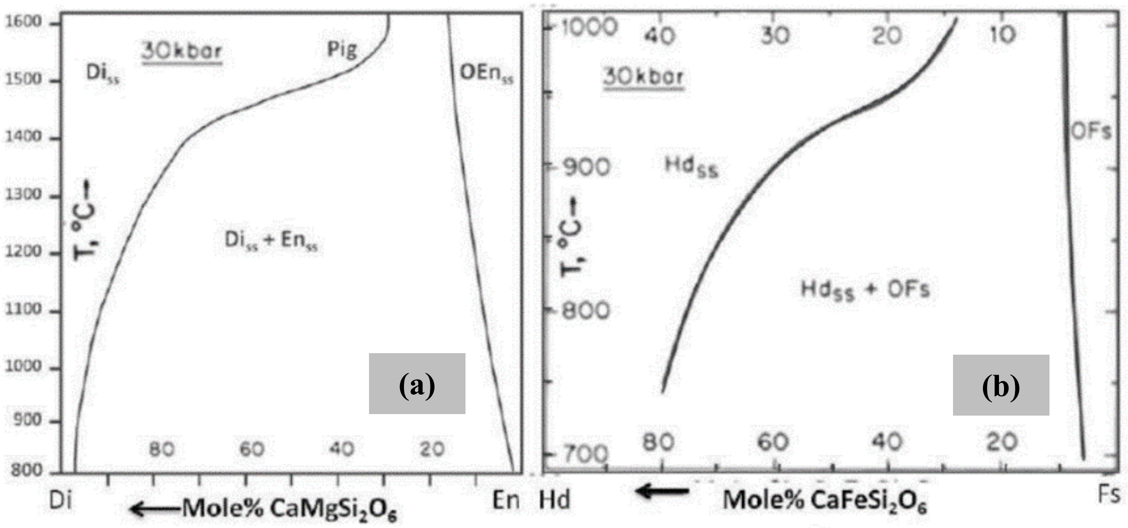

Figure 2.12. (**a**) Phase diagram of diopside-enstatite series (Lindsley, 1980) at 3 GPa; (**b**) phase diagram of hedenbergite-ferrosilite series (Lindsley and Munoz 1969) at 3 GPa.

2.3. Cobalt-pyroxene phase diagrams

Preliminary data and studies on Ca-Co pyroxenes were done by Navrotsky and Coons (1976) which have synthesized some crystals of monoclinic $CaCoSi_2O_6$ at a temperature of T= 1150 °C, finding the melting point at about 1400 °C. Durand *et al.* (1996) synthesized the end-member Ca-Co pyroxenes, using the sol-gel method and annealing at T= 1100 °C, to study its magnetic properties, while White *et al.* (1971) and Burns (1993) have studied the visible absorption spectrum of this phase. Further syntheses were conducted via ceramic routes in the range of temperature 1000-1250 °C by Masse *et al.* (1999), that reported coexistence of pyroxene and other phases, like Co-akermanite and quartz without determining whether they are metastable or not. Both Masse *et al.* (1999) and Navrotsky and Coons (1976) have found incongruent melting for the composition $CaCoSi_2O_6$ between 1175 and 1250 °C.

In all these studies, the synthesis was performed empirically, with no aim to detail the phase stability with other phases. A first study on the stability of the orthorhombic and monoclinic $Co_2Si_2O_6$ was done by Akimoto *et al.* (1965), showing that Co-orthopyroxene could be synthesized at 2 GPa and 800 °C, while the formation of monoclinic $Co_2Si_2O_6$ occurs above 7 GPa. At room pressure only the end-member $CaCoSi_2O_6$ can be synthesized, as shown by Mukhopadhyay and Jacob (1996), in a study on the phases in the CoO-CaO-SiO_2 system. In their study Mukhopadhyay and Jacob (1996) found some solid solutions close to $CaCoSi_2O_6$. However, the first study to investigate intermediate cobalt pyroxenes in the $CaCoSi_2O_6$-$CoCoSi_2O_6$ series was done by Mantovani *et al.* (2013), who demonstrated that, in the isothermal binary section along the $CaCoSi_2O_6$-Co_2Si2O_6 compositions, pyroxenes have a limited solution on the Ca-rich side and are destabilized into a 3-phase assemblage consisting of quartz + Co-clinopyroxene + Co-olivine. Phase equilibria in Ca-Co pyroxene are similar to those in the Ca-Fe pyroxene, because only at high pressure (P > 3 GPa) the pyroxene phases through the join are stabilized, whereas at lower pressure olivine +quartz are stable.

In a subsequent paper Mantovani *et al.* (2014) have synthesized the Ca-Co pyroxene series at P= 3 GPa and T between 1100 and 1350 °C and have studied the effect of the subtitution of Ca with Co on the phase transition and on the extension of the miscibility gap. The phase diagram of the Ca-Co pyroxenes, is similar to that of Ca-Fe and Ca-Mg ones, with a wide asymmetric miscibility gap and higher solubility in the Ca-rich side of the gap (Mantovani *et al.*, 2014). The pyroxene solubility decreases on the Ca-rich side with temperature, and it is lower when the cation, which exchanges for Ca in the *M2* site, is smaller [Mantovani *et al.*, 2014; Figures 2.13(a-b)]. As it is shown in Figure 2.13b, a single clinopyroxene phase with Ca content of about 0.5 a.p.f.u. at P= 3GPa is stable at 1500 °C for Ca-Mg, 1280 °C for Ca-Co and 900 °C for Ca-Fe pyroxenes. At 1350 °C the Ca-Co pyroxene solubility is almost complete, but for a narrow miscibility gap between clino- and orthopyroxenes (between $Ca_{0.1}Co_{1.9}$ and $Ca_{0.2}Co_{1.8}$).

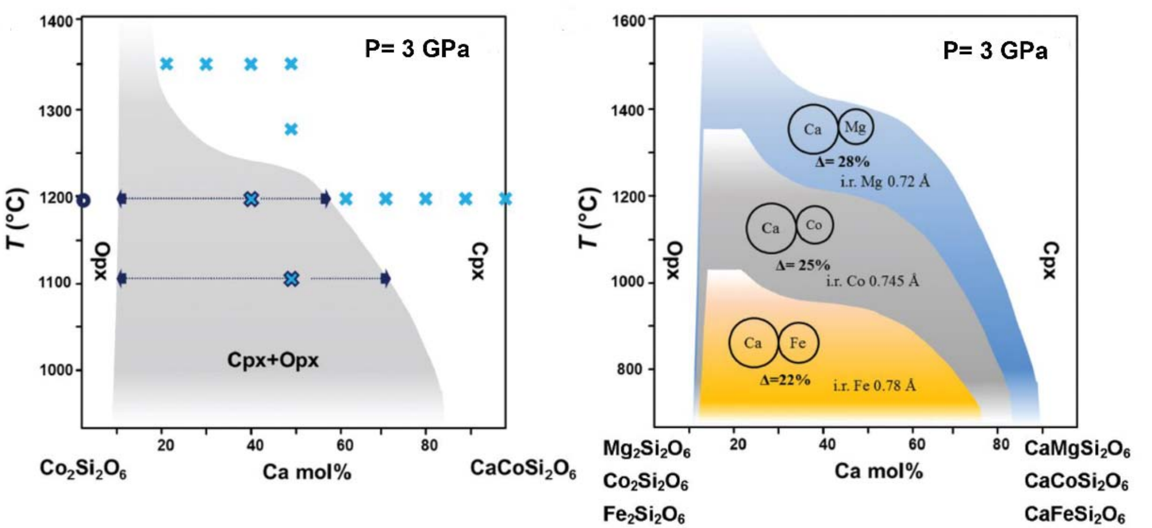

(a) **(b)**

Figure 2.13. (**a**) Sketch of a phase diagram of the join $CaCoSi_2O_6$-$Co_2Si_2O_6$ at P= 3 Gpa. Light blue crosses represent the monoclinic single phase; deep blue circles represent the orthorhombic phase. Crosses into the miscibility gap represent the coexistence of ortho- and clinopyroxene (Mantovani *et al.*, 2014). (**b**) comparison between phase diagrams of Ca-Mg (Gasparik and Lindlsey, 1980); Ca-Fe (Lindsley and Munoz, 1969) and Ca-Co pyroxenes (Mantovani *et al.*, 2014). *Notes*: The shape of the miscibility gap has been determined with reference to literature data for the Ca-Fe and Ca-Mg pyroxenes and it was loosely constrained by the synthesis conditions (Mantovani *et al.*, 2014).

In Ca-Co pyroxenes with decreasing Ca in the *M2* site, a transition from *C*2/*c* to *P*2_1/*c* symmetry occurs, as in Ca-Mg and Ca-Fe pyroxenes. The transition however occurs at different amounts of Ca, *i.e.* 0.6, 0.4 and 0.3 Ca atoms per formula unit in Ca-Mg, Ca-Co and Ca-Fe pyroxenes, respectively. In fact, both the solubility and the composition at which the *C*2/*c* to *P*2_1/*c* phase transition occurs in the different series, change with increasing difference in the cation radius (Mantovani *et al.*, 2013, 2014, Ohashi *et al.*, 1975; Newton e*t al.*, 1979; Tribaudino 2000; Tribaudino *et al.*, 2005).

The above similarities between $CaMgSi_2O_6$-$Mg_2Si_2O_6$, $CaCoSi_2O_6$-$Co_2Si_2O_6$ and $CaFeSi_2O_6$-$Fe_2Si_2O_6$ pyroxenes are not found in $CaZnSi_2O_6$-$Zn_2Si_2O_6$ pyroxenes (Huber *et al.*, 2012; Gori *et al.*, 2015), as it will be discussed in Chapter 8.

2.4. Zinc-pyroxene phase diagrams

Zinc is a relatively common element in the Earth's crust, being present by 75 ppm. However, as zinc shows a marked preference for chalcophile behaviour, it most occurs in sulphides, like sphalerite (ZnS), while in silicates it occurs as a trace element, being a major phase only in rare silicate phases like willemite (Zn_2SiO_4), hardystonite ($Ca_2ZnSi_2O_7$) or hemimorphite [$Zn_4Si_2O_7(OH)_2 \bullet (H_2O)$]. In very few occurences it is also found as a major component in pyroxene.

Clinopyroxene showing high-zinc concentrations was collected in the Franklin area of New Jersey, U.S.A, Essene and Peacor (1987); this phase has been named *petedunnite*, for Dr. Pete J. Dunn of the Department of Mineral Sciences of the Smithsonian Institution, Washington D.C. The chemical composition of natural petedunnite is that of a solid solution between the pure $CaZnSi_2O_6$ end-member and the johansennite ($CaMnSi_2O_6$). The name and mineral status have been approved by the IMA Commission on New Minerals and Mineral Names. Natural petedunnite may have formed by exchange of original diopside-hedenbergite-johannsenite solid solutions with the Zn-rich fluids (Essene and Peacor, 1987). In petedunnite the $CaZnSi_2O_6$ end-member is most present, and Zn is the dominant *M1* cation, but the pure $CaZnSi_2O_6$ phase was not found in nature. Hereafter we will refer the end-member $CaZnSi_2O_6$ as petedunnite.

Synthetic petedunnite was obtained by Essene and Peacor (1987) in the system CaO-ZnO-SiO_2 at 900 °C and high-pressure (2 GPa) and the duration of the experiment was about 6 days. In Nestola *et al.* (2010) petedunnite was newly synthesized, but at higher pressure (6 and 8 GPa). The high pressure synthesis was needed as $CaZnSi_2O_6$ is not stable at room conditions. Segnit (1954) and Fehr and Huber (2001) performed synthesis experiments in the system CaO-ZnO-SiO_2 at pressure conditions below the stability boundary of petedunnite. Segnit (1954) determined the solid phases relations in equilibrium with the liquid phase and observed the phase assemblege willemite + hardystonite + quartz (Zn_2SiO_4+$Ca_2ZnSi_2O_7$+SiO_2) at 1164 °C/1 atm.

The phase relations of petedunnite were determined experimentally at *P-T* conditions up to 25 GPa and 1100 °C. Single-phase petedunnite is formed at high pressures (P= 1.9-2.0 GPa) and 900-1000 °C. The stability field of willemite + hardystonite + quartz is restricted toward lower temperatures by zinc-feldspar ($CaZnSi_3O_8$). At the high temperatures and pressures of 1100 °C and 2.5 GPa, petedunnite decomposes under dry conditions to a melt-bearing assemblage (petedunnite + quartz + liquid; Huber *et al.*, 2012, Figure 2.14). At T < 650 °C zinc-feldspar is decomposed in petedunnite + quartz, and petedunnite in hardystonite + willemite + zinc-feldspar (Huber *et al.*, 2012).

In a series of related papers, the phase relations of petedunnite in the system CaO-ZnO-SiO_2 (Figure 2.15), the thermodynamic properties of petedunnite and the miscibility of petedunnite with hedenbergite-johannsenite-diopside solid solutions, were discussed, as well as the importance of zinc as a petrographic indicator in skarn deposits (Heuer *et al.*, 2005, 2002a, 2002b; Huber *et al.*, 2004; Huber and Fehr, 2003).

Petedunnite is not the only Zn-pyroxene. Two polymorphs of $ZnSiO_3$ have been synthesized under high pressures and temperatures (Figure 2.16) by Syono *et al.*, (1971) and have the monoclinic (*C*2/*c*) and orthorhombic (*Pbca*) pyroxene structures. According to Syono *et al.*, (1971), the clinopyroxene $ZnSiO_3$ is stable above 30 kbar and 850 °C, while the orthorhombic phase is metastable at all conditions. Olesh *et al.* (1982) and Doroshev *et al.* (1983) studied the subsolidus phase relations along the join ZnO-SiO_2 and determined, with experimental analyses, the stability field of zinc-clinopyroxene up to 10 GPa, while Morimoto *et al.* (1975) and Arlt and Angel (2000), investigated its structure. Arlt and Angel (2000) studied the different structural modifications that occur in $ZnSiO_3$ with pressure (*C*2/*c* and *P*2_1/*c*).

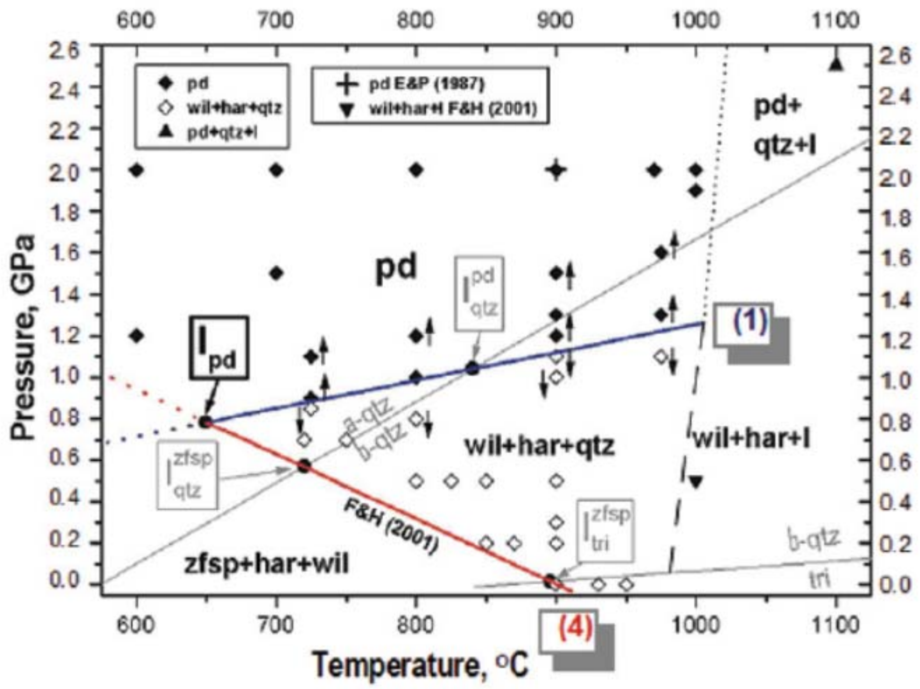

Figure 2.14. Pressure *vs*. temperature plot of data on $CaZnSi_2O_6$ composition obtained for reaction 1 (in blue): 4 pd= wil+ 2 har+ 3 qtz. Symbols: open diamonds, wil+har+qtz; filled diamonds, pd; upward triangle, pd+qtz+liquid; downward triangle, wil+har+liquid. Data for the high-low quartz transition are taken from Mirwald and Massonne (1980). The location of reaction 4 (in red): 4 zfsp= wil+ 2 har+ 7 qtz, is given by Fehr and Huber (2001). Error bars are within symbol size (Huber *et al*., 2012).

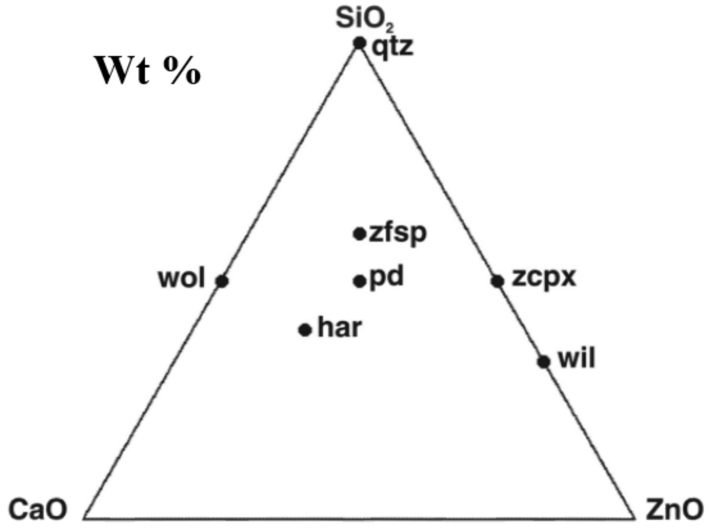

Figure 2.15. Projection of ternary and binary phases in the system CaO-ZnO-SiO_2 (mol%). wol= wollastonite; wil= willemite; zcpx= zinc-clinopyroxene; har= hardystonite; pd= petedunnite; zfsp= zinc-feldspar.

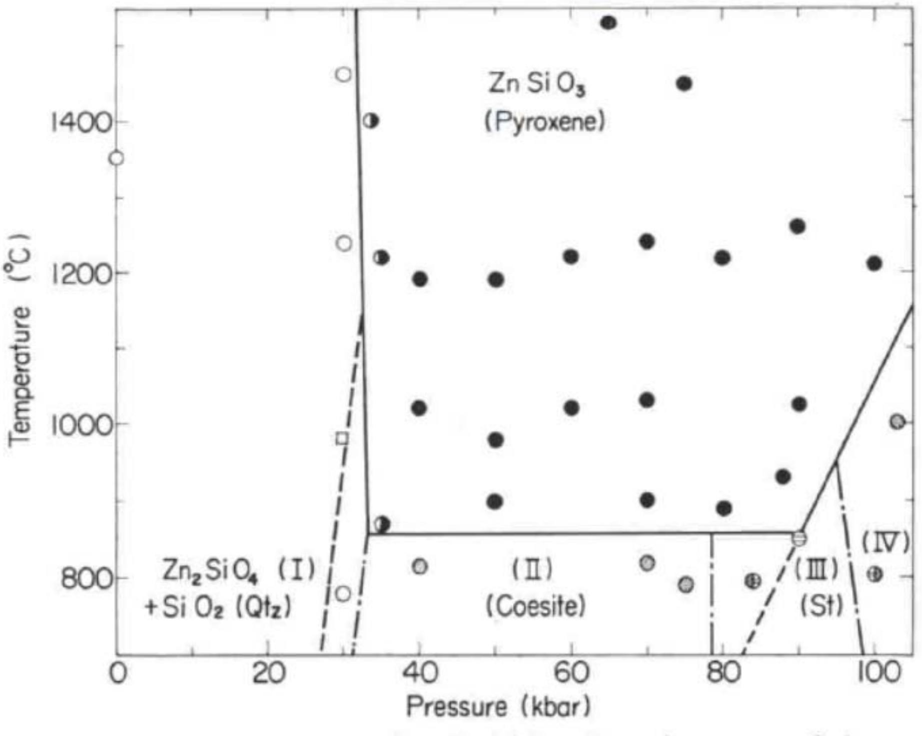

Figure 2.16. Phase diargam for $ZnSiO_3$ (Syono *et al.*, 1971).

In Zn pyroxenes we have two major points of interest. One is the peculiar behaviour of Zn^{2+} in the distorted coordination of the *M2* site, as found in the $ZnSiO_3$ phases. The Zn^{2+}, which bond with oxygen according to a ionic behaviour in the *M1* site, shows a peculiar fourfold coordination in the *M2* site, like it is found in willemite (Zn_2SiO_4). The preference of Zn for the four-coordinated sites is stronger than that of other divalent cations with similar ionic radius, and it is probably due to the covalent character of Zn^{2+} ions which form sp^3-type hybrid bonding in the crystal (Morimoto *et al.*, 1975). In the case of $ZnSiO_3$ polymorphs the tendency of Zn atoms to maintain tetrahedral coordination is stronger in monoclinic $ZnSiO_3$ than in the orthorhombic $ZnSiO_3$. A further difference is that the unit-cell twin relation observed between the orthorhombic and monoclinic polymorphs is not applicable to $ZnSiO_3$ because monoclinic $ZnSiO_3$ has a *C*2/*c* structure, with a lattice centering that is not present in the orthorhombic *Pbca* (Morimoto *et al.*, 1975). In fact, the clinopyroxene $ZnSiO_3$ has the *β* angle exceptionally large if compared to conventional *C*2/*c* pyroxenes with divalent cations, and comparable with that of $LiAlSi_2O_6$ spodumene (Morimoto *et al.*, 1975).

Secondly, the structural analysis at high pressure of the $ZnSiO_3$ (Arlt and Angel, 2000), revealed that the *C*2/*c* structure of $ZnSiO_3$ transforms to a $P2_1/c$ and then to a *C*2/*c* structure at higher pressure. The interpretation is that the *C*2/*c* structure is a high temperature structure, like it is observed in pigeonites during the heating, and the compression has the same effect as decreasing pressure on the structure. This leads to several questions to be answered: 1) at which Zn content we have a switch to the covalent behaviour? 2) is there a relation between the covalent behaviour of Zn and the stability of a *C*2/*c* phase, instead of a $P2_1/c$ phase at room conditions? Pyroxenes with the *M2* site occupied by cations of similar ionic radius, like Co^{2+} or Mg^{2+} have a $P2_1/c$ room temperature structure 3) how does this affect the partitioning of Zn as a trace element? 4) does this peculiar crystal chemical behaviour of Zn-pyroxenes have some effect on the physical properties of Zn-pyroxenes?

We can answer by studying the system between $CaZnSi_2O_6$ and Zn_2Si_2O, where the Zn^{2+} enters the *M2* site, to verify how the Zn entrance modifies the bonding behaviour in the *M2* site. In this thesis our efforts were basically involved in synthesis and crystal chemical studies along the system $CaZnSi_2O_6$-$Zn_2Si_2O_6$. The results are summarized in Gori *et al.* (2015) which is a part of this thesis (Chapter 8). Further studies on the physical properties are underway, showing interesting results on the dielectric properties and the hardness of the monoclinic $ZnSiO_3$ phase; their publication will be the subject of separate investigation.

Chapter 3

CERAMIC MATERIALS AND COLORANTS

3. CERAMIC MATERIALS AND COLORANTS

3.1. Ceramic materials

Ceramics in a wider sense are a group of non-metallic inorganic solids, primarily held by ionic and covalent bonding.

The first used ceramic materials were potteries and their use dates from the time of ancient civilisations. The word ceramic is in fact derived from a Greek word ‘κεραμος’ (kéramos) meaning ‘potter’ or ‘pottery’, which was clay mould with water, and solidified by burning. This is apparent in the proto-indo european suffix ‘ker’, meaning ‘to burn’. Hence, kéramos infers ‘burned substance’ or ‘burned earth’.

Today, we can define two broad types of ceramics, traditional and advanced.

Traditional ceramics are those derived from naturally occurring raw materials and include clay-based products such as tableware and sanitary ware as well as structural clay wares (bricks and pipes). In this category there are also cements, glasses and refractories (Segal, 1991).

Advanced ceramics are developed from chemical synthetic routes or from naturally occurring materials that have been highly refined. Advanced materials are referred to as structural components, if their use depends on their mechanical behaviour, while they are referred to as electroceramics if the application relies on their electrical and magnetic properties (Segal, 1991). Advanced ceramics are usually produced by powder compaction followed by firing at high temperature. Microstructures and grain size within the ceramic solid depend on the sintering process and the heat treatment.

Colour is an important characteristic of many ceramic products such as dinnerware, tile, porcelain enamel, sanitary ware, and some glasses and structural clay products.

The availability of colouring agents has played, and continues to play, a key role in the cultural and artistic development of our society. In prehistoric times, the only mineral colouring agents known were the so-called earth pigments, mostly iron and manganese oxides and hydroxides (*i.e.* sienna, umber and ocher), clay minerals (*e.g.* green earth and white clay) and chalk. These mineral pigments provided a limited palette of colours that ranged from light yellow to brown and black, depending on the relative proportion of the mineral constituents. In antiquity, the colour palette was expanded to include a variety of yellow, red, green and blue, in connection with the development of mining techniques and ore processing, which increased the availability of coloured rocks and minerals, and of natural and synthetic colours. Yet, only in the nineteenth century, synthetic pigments, which could be classified as advanced materials (for the time) were first synthesized, *e.g.* the synthesis of ultramarine by Gmelin (1828; The Quarterly journal of science, literature and art, Volume 25).

Ceramic material can be coloured in three general ways (Dondi and Eppler 2014):

- by transition metal ions that are coloured. This method is used by organometallic dyes (soluble salts) though adequate tinting strength and purity of colour are difficult to be obtained by this way;
- by inducing precipitation of a suitable crystalline phase during processing;
- by dispersing within a ceramic material a coloured crystalline phase that is insoluble in the matrix. This crystalline phase, commonly called a pigment, imparts its colour to the matrix.

The various ceramic colorants can be classified according to their crystal structure, melting point, density, refractive index, chemical composition, colour bestowed and behaviour during firing. Many crystal structures used as ceramic colorants are solid solutions and different formulation are used to vary the colour obtained. Colour variations within a given structural class are very important: since pigments within a given class have excellent chemical and physical compatibility, is possible to mix them to obtain intermediate shades, *e.g.* in the spinel class (Dondi and Eppler, 2014).

3.2. Ceramic colorants: pigments and dyes

The Colour Pigments Manufacturers Association (CPMA) defines pigments as '*coloured, black, white or fluorescent particulate organic or inorganic solids which usually are insoluble in, and essentially physically and chemically unaffected by, the vehicle or substrate in which they are incorporated. Pigments alter appearance by selective absorption and/or by scattering of light. Pigments are usually dispersed in vehicles or* *substrates for application, as for instance in the manufacture or inks, paints, plastics or other polymeric materials. Pigments retain a crystal or particulate structure throughout the coloration process*'.

Pigments must fulfill several requirements to be used in ceramic materials: they must be resistant to the high temperature (most of pigment structures have a melting point over 1500 °C), they must withstand the corrosive environment of molten glaze, the rates of pigment dissolution or reaction in contact with the liquid phase of ceramic body or molten glaze at high temperature must be low, the crystals should remain sufficiently intact during the firing process, the particle size required for uniform dispersion of the pigment in the ceramic matrix, has to be fine (1–10 µm; Dondi and Eppler, 2014; Kirk-Othmer 1998b). Most of the materials used in ceramics as pigments are oxides and silicates because of their greater stability in oxygen-containing ceramic systems (Dondi and Eppler, 2014). Ceramic pigments consist mostly of refractory crystals containing colour centers (Forés *et al.*, 2000) frequently produced by the ions of such transition metals as Co, Cr, Fe, Mn, Ni, and V.

The Ecological and Toxicological Association of Dyes and Organic Pigment Manufacturers (ETAD) defines dyes as '*coloured or fluorescent organic substances only, which impart colour to a substrate by selective absorption of light. They are soluble and/or go through an application process which, at least temporarily, destroys any crystal structure by absorption, solution, and mechanical retention, or by ionic or covalent chemical bonds*'. Dyes provide brighter colour than conventional pigments, but they are less light stable and less permanent (Rothon 2012). Their properties are almost exclusively defined by their chemical structure and electronic properties of the chromophore molecules. Dyes are soluble in water and/or an organic solvent, while pigments are insoluble in both types of liquid media. Dyes are of two types, *i.e.* synthetic and natural. Synthetic dyes are most based on petroleum compounds, whereas natural dyes are obtained from plant, animal, and mineral matters (Singh and Bharati 2014).

Ceramic pigments (and dyes) behave as light filters by absorbing some wavelengths in the visible spectrum. Their colour (and brightness) stems from the complementary wavelengths of visible light that are reflected/scattered through a subtractive colour mixing. The light absorption is caused by electronic transitions of different origin (Dondi and Eppler, 2014) that produce absorption bands in the optical spectra that differ in intensity and width (affecting the colour purity). The colours achievable with ceramic pigments and dyes may be represented in the a^*-b^* plane of the CIE L^* a^* b^* colour space (McLaren, 1976; for the CIE Lab colour space see Chapter 5, paragraph 5.2.6).

Chapter 4

SOME INFORMATION ABOUT COBALT AND ZINC

4. SOME INFORMATION ABOUT COBALT AND ZINC

4.1. Cobalt metal: properties and applications

4.1.1. Physical and chemical features

Cobalt is a transition metal (atomic number 27) belonging to the VIII group of the periodic table.

Cobalt metal (Figure 4.1) is shiny, grey, brittle with a close packed hexagonal (CPH) crystal structure at room temperature, but which changes at 421 °C to a face-centered cubic form (FCC). Cobalt has a high melting point (1493 °C) and retains its strength to a high temperature; it is ferromagnetic (nickel and iron are as well) and retains this property to 1100 °C, a higher temperature (Curie-Point) than any other material.

Cobalt has the electronic configuration $3d^7 4s^2$ and shows valencies of (II) and (III). Cobalt (II, III) oxide is a chemical mixed-valence compound containing both Co (II) and Co (III) oxidation states, with the formula Co_3O_4. It can be formulated as $Co^{II}Co^{III}{}_2O_4$ or $CoO \cdot Co_2O_3$. Cobalt(II) oxide, CoO, converts to Co_3O_4 if heated to around 600-700 °C in air ($2Co_3O_4 \leftrightarrow 6CoO + O_2$). Above 900 °C, CoO is stable. The Co (II) and Co (III) ions have the electronic configurations $3d^7$ and $3d^6$, respectively, thus loosing the $4s^2$ electrons. Cobalt reacts with most inorganic or organic acids to form simple Co(II) salts, such as CoS_2, $Co(NO_3)_2$ or $CoCl_2$ and it can also form other sulfides, carbonates, halides and a vast range of organic and inorganic compounds; many of these compounds find commercial use.

Figure 4.1. Pure metallic cobalt (image from www.periodictable.com).

4.1.2. Cobalt toxicity

Cobalt is a naturally occurring element in the Earth's crust. Cobalt displays siderophile properties. It forms several rather rare minerals, including smaltite $(Co,Ni)As_{(2-2.5)}$, cobaltite (Co,Fe)AsS and linnaeite $(Co,Ni)_3S_4$ and is present as an accessory element in olivine, pyroxene, amphibole, mica, garnet and sphalerite. It may also be associated with the iron sulphides pyrite, arsenopyrite and pyrrhotite and in oxides, such as magnetite (Ure and Berrow 1982). In early magmatic processes Co^{2+} substitutes for Fe^{2+} and Mg^{2+}, which are similar in charge and ionic radius, so Co is generally enriched in mafic relative to felsic igneous rocks (Wedepohl 1978) and, together with Cr and Ni, is indicative of mafic rocks. In continental crust cobalt has an average bulk abundance of 29 $mg \cdot Kg^{-1}$ (McLennan and Taylor 1999).

Minerals contain very little Co (< 20 ppm) and in sedimentary rocks it tends to vary with the Fe and Mn content and its concentration is related to the abundance of mafic minerals; it is concentrated in fine or very-fine grained rocks and mudrocks. Cobalt is most mobile under acidic and reducing environmental conditions. Co(II) may bind to humic and fulvic acids and inorganic colloids (Qian *et al.*, 1998).

Cobalt is an essential component of vitamin B_{12} and very small amounts are needed for many animals and humans to stay healthy. In manufactory it is used in alloys, batteries, chemistry/crystal sets, drill bits and machine tools, dyes and pigments (Cobalt Blue), magnets, some metal-on-metal hip implants (Figure 4.2), tires.

Figure 4.2. Metal-on-metal hip replecement devices may be cause seriuos health problems, including cobalt poisoning (image from www.yourlawyer.com).

In the medical field, cobalt-60 is used in radiotherapy and for sterilizing medical equipment.

Regardless of these perceived advantages, cobalt is not without its problems. Cobalt can accumulate to toxic levels in the liver, kidney, pancreas, and heart, as well as in the skeleton and in skeletal muscle. Exposure to cobalt can thus occur through inhalation, oral or dermal (skin) routes (Figure 4.3). Industrial plants may leak cobalt and other toxic metals into the environment. Once cobalt particles enter the atmosphere, they settle to the ground and enter the food and water supply; most of the population is thus exposed to cobalt through food, water, and air. Cobalt makes its way through the environment from factory sludges and cannot be destroyed. Also, it's been reported that hip replacements containing cobalt have caused problems due to nano particles of cobalt breaking away and contaminating the body.

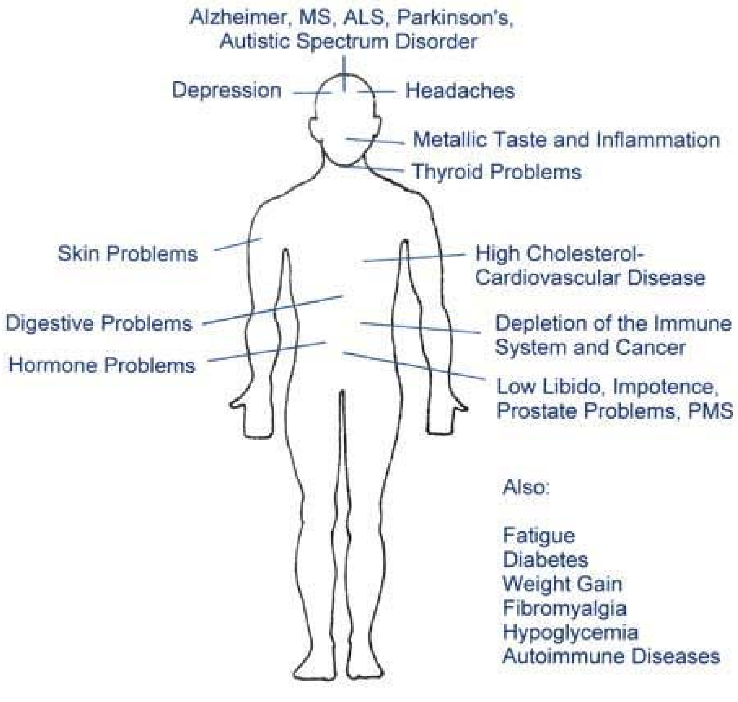

Figure 4.3. Cobalt heavy metal may be accumulate in toxic amounts, in the body (image from remodelingyourhealth.com).

Another worrisome cobalt poisoning occurs from industrial settings where large amounts of drilling, polishing, or other processes release fine particles containing cobalt into the air. Breathing this substance for long periods, can cause problems that are similar to asthma or pulmonary fibrosis. Cobalt poisoning that occurs from constant contact with your skin will likely cause irritation and rashes that go away slowly. Absorbing a large amount of cobalt over longer periods of time can lead to serious health problems, such as: cardiomyopathy, deafness, thyroid problems (Figure 4.3).

4.1.3. History of cobalt

The word is accepted as derived from the Greek via medieval German. Records of the name only go back to 1335 when it was applied to gnomes living in the mines in the Schneeberg Mountains in Germany. Another origin of the word cobalt is dated back to the sixteenth century German term ‘kobold’, meaning goblin, or evil spirit. Kobold was used to describe cobalt ores that, while being smelted for their silver content, gave off poisonous arsenic trioxide. The earliest application of cobalt was in compounds used for blue dyes for pottery, glass and glazes. Egyptian and Babylonian pottery dyes with cobalt compounds can be dated back to 1450 B.C. (Figure 4.4). Chinese pottery from Tang (600-900 AD) and Ming dynasties (1350-1650 AD) also contained blue colours made from cobalt-containing minerals.

Figure 4.4. Egyptian cobalt blue pottery (image from it.pinterest.com).

The metal itself has been isolated in 1735 by the Swedish scientist Georg Brandt and its metallic use stems from the American automotive entrepreneur Elwood Haynes' studies and patents in the early 1900s. He developed a new corrosion resistant alloy, which he referred to as stellite. Patented in 1907, stellite alloys contain high cobalt and chromium contents and are completely non-magnetic. The Co-Cr alloys and superalloys caused a great leap in cobalt use; they are still in use as well as the are the Al-Ni-Co magnets (Alnico) invented in the 1930s.

Cobalt sources have changed over its history and, in the last decade, sources have diversified with increasing amounts coming from nickel ores and recycling of scrap and cobalt-containing intermediates. The industrial importance of cobalt resulted in the London Metal Exchange (LME) introducing cobalt futures contracts in 2010.

4.1.4. The use of cobalt in pigments and ceramics

Cobalt is a fascinating chromophore and cobalt compounds have been used since historical times as a dye in porcelain, glass, pottery, tiles. The ability of cobalt-containing minerals to impart colour has been important for thousand years going back to the Egyptians and Persians. Cobalt-based ceramic pigments include cobalt in many formulations and are widely used for coloured glazes in the ceramic industry. The pigments are prepared by mixing the ingredients as simple oxides or mixed oxide and silicates and then calcining and grinding back to a fine powder Dondi and Eppler 2014).

Thanks to its unique combination of solubility, stability, colouring effect, cobalt has no real substitute as a pigment for application in ceramics. There is a wide range of various historical cobalt pigments (Table 4.1, Figure 4.5); some of them are more important in the history of paintings, like the cobalt and cerulean blue which were most used by the French Impressionists, while others are more often used for decorating ceramic objects or producing ceramic glaze (Jonyanaité *et al.*, 2009).

For example, cobalt yellow (aureolin, K_3 [$Co(NO_2)_6$]) appeared in trade as a pigment in 1860 and it was used together with the Indian yellow. Because of the remarkable effect this pigment is perfectly suitable for various painting techniques: aquarelle, tempera and oil. Also, it is used in glass, porcelain painting, and enamel. The most important violet cobalt pigments are different phosphates and have been known since the end of the eighteenth century: cobalt violet brilliant light ($CoNH_4PO_4 \cdot H_2O$) and cobalt violet dark [$Co_3(PO_4)_2$]. Cobalt cerulean blue ($CoO \cdot nSnO_2$) was discovered in 1789 and it was used in enamel art and porcelain painting. Cobalt blue dark and cobalt blue light ($CoO \cdot Al_2O_3$) pigments were already used in ancient Egypt for decorating pottery. Cobalt blue greenish ($Cr_2O_3 \cdot CoO \cdot Al_2O_3$) was produced in the middle of the nineteenth century and it was used for decorating porcelain (the colour of pigment varies from bluish green to greenish blue depending on the molar ratio of aluminium and chromium). Cobalt green bluish ($CoO \cdot ZnO$) which is resistant to light and suitable for all painting techniques, was synthesized in 1778 and became more widely used later, in the nineteenth century glaze (Jonyanaité *et al.*, 2009). The blue pigment ultramarine which was derived from the painstaking refinement of lapislazuli rock could be substituted by smalt blue that was obtained by grinding cobalt-doped glass to an ultrafine powder. The only way to obtain a cobalt-based blue pigment, at least until the introduction in 1802 of Thénard's cobalt blue (synthetic cobalt aluminum oxide, with the spinel structure; Pigment Compendium: A Dictionary of Historical Pigments) was through the use of Co-doped silicate glass ($CoO \cdot nSiO_2$), which allowed Co^{2+} ions to be stabilized by partly filling tetrahedral sites (Colomban 2013; Delamare 2013).

TABLE 4.1. Cobalt-based historical pigments (Jonyanaité *et al.*, 2009).

Cobalt-based historical pigments	
yellow	$K_3 [Co(NO_2)_6]$
violet brilliant light	$(CoNH_4PO_4 \cdot H_2O)$
violet dark	$(Co_3 (PO_4)_2)$
cerulean blue	$(CoO \cdot nSnO_2)$
blue	$(CoO \cdot Al_2O_3)$
blue greenish	$(Cr_2O_3 \cdot CoO \cdot Al_2O_3)$
green bluish	$(CoO \cdot ZnO)$
blue smalt	$(CoO \cdot nSiO_2)$

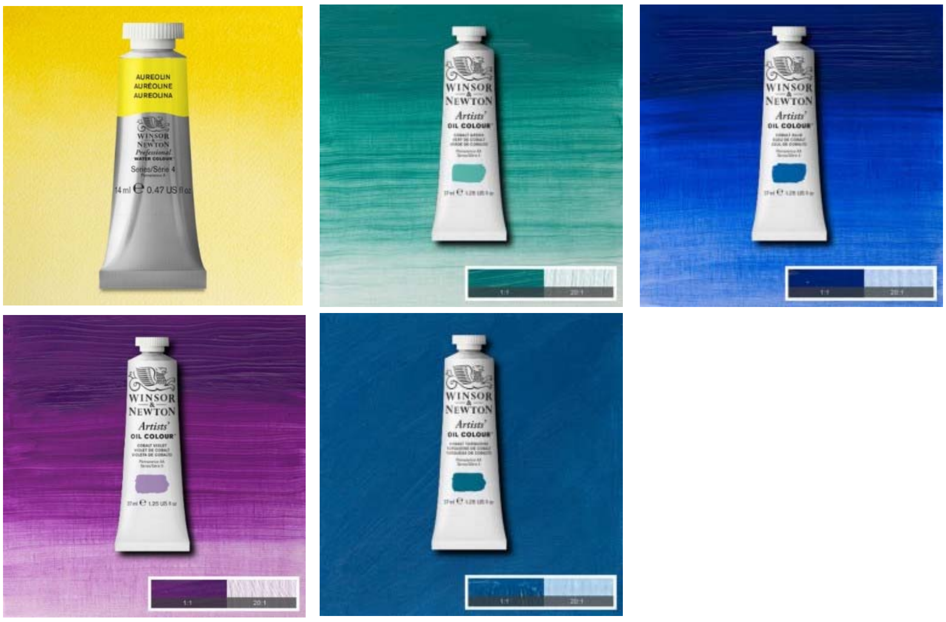

Figure 4.5. Cobalt pigments (images from www.bellearti.it and www.cheapjoes.com).

4.2. Zinc metal: properties and applications

4.2.1. Physical and chemical features

Zinc is a metal (atomic number 30) belonging to the IIb group of the periodic table. Zinc is a bluish, white, lustrous metal (Figure 4.6). It is hard and brittle at ambient temperatures but becomes duttile and malleable under heating at temperature between 110 and 150 °C. Zinc has the electronic configuration $3d^{10}4s^2$ and one main oxidation state (II). The Zn (II) ion has the electronic configurations $3d^{10}$ thus loosing the $4s^2$ electrons. Metal Zn has an hexagonal crystal stucture.

Figure 4.6. Pure metallic zinc (image from www.periodictable.com).

4.2.2. Zinc toxicity

We have already mentioned something about zinc in Chapter 2, paragraph 2.4: its geochemical behaviour, its occurrence in several minerals, especially in pyroxene and silicates.

Zinc becomes enriched in mafic relative to felsic rocks while its distribution in sedimentary rocks, is controlled by the abundance of ferromagnesian silicates, magnetite and clay minerals. Zinc has also a great affinity for organic matter and high value occur in oil shale (Wedepohl 1978).

Zinc mobility in the environment is greatest under oxidizing, acidic conditions and more restricted under reducing conditions. Anthropogenic sources of zinc are significant, arising mainly from industrial activities (mining, coal and waste combustion, steel processing). Since the zinc production and the industrial applications are still rising, pollution may cause the zinc amounts in drinking water and soils to reach levels that can cause health problems.

Zinc is an essential trace element for humans, animals and higher plants. About 11 mg per day are suggested for adult; it is a key component of enzymes and is in the protein hormone insuline. Deficiency of zinc may cause growth retardation, dermatitis and slow wound healing, defective immune system. Zinc-shortage can even cause birth defects. Zinc toxicity is not so much a problem as deficiency, although excess zinc can cause health problems such as stomach cramps, skin irritations, vomiting, nausea, pancreas damage and arteriosclerosis (Plum *et al.*, 2010). Fish can accumulate zinc causing biomagnification along the food chain and plants often take up more zinc than their systems can handle (Figure 4.7).

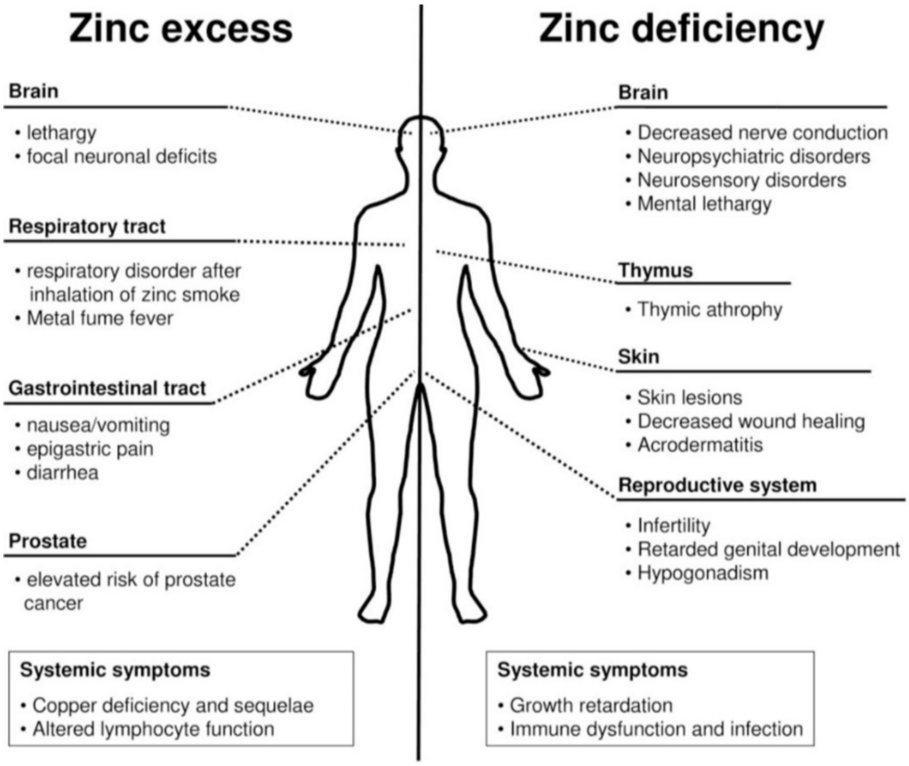

Figure 4.7. Impact of zinc on human health (Plum *et al.*, 2010).

4.2.3. History of zinc

Centuries before zinc was recognized as a distinct element, zinc ores were used for making brass (a mixture of copper and zinc). A brass dating from 3000 BC has been found in Babylonia and Assyria. An alloy containing 87% zinc was found in prehistoric ruins in Transylvania. The smelting of zinc ores with copper was apparently discovered in Cyprus and was used later by the Romans. Metallic zinc was produced in the thirteenth century in India by reducing calamine (zinc carbonate, $ZnCO_3$) with organic substances such as wool. It was Marco Polo (1254-1324) from Venice who reported the production of zinc oxide in Persia. At this time the Persians used a solution of zinc vitriol ($ZnSO_4 \cdot 7H_2O$) to treat eye inflammations.

Zinc sulphate ($ZnSO_4$) is used in medicine as an adstringent and antiseptic even today. By 1374 zinc had been recognized by the Hindus as a new metal, the eighth known in that day and age, and zinc production and trading was already underway on a limited scale. Zinc refining in China was carried out on a large scale by the 1500s. The metal was rediscovered later in Europe by the German chemist Andreas Marggraf in 1746 (Partington, 1961), and indeed he was the first to recognize it as a new metal. The element was probably named by the alchemist Paracelsus after the German word *Zinke* (tooth), but the name ‘zinc’ only came into general use in the seventeenth century following rediscovery of the material.

4.2.4. The use of zinc

The main use of zinc is as an anticorrosion coating but it is also used as a constituent of brass; it is used for the negative plates in some electric batteries and for roofing and gutters in building construction. Zinc was the primary metal used in making American pennies. As the oxide (ZnO) is used in the manufacture of paints, rubber products, cosmetics and pharmaceuticals (Figure 4.8), floor coverings, plastics, printing inks, soap, textiles, electrical equipment; as the sulphide (ZnS) is used in making luminous paints, fluorescent lights and X-ray screens. Zinc oxide is also known as a white pigment, together with the zinc silicate (willemite, Zn_2SiO_4; Forés *et al.*, 2000). Zinc metal is included in most single tablet, it is believed to possess anti-oxidant properties which protect against premature aging of the skin and muscles of the body.

Figure 4.8. Zinc oxide extensively used as a pigment in plastic, pharmaceuticals and cosmetics (image from www.glochem.com).

Chapter 5

SYNTHESIS AND SAMPLE CHARACTERIZATION

5. SYNTHESIS AND SAMPLE CHARACTERIZATION

5.1. Synthesis procedures

Two different synthesis procedures were adopted to obtain different compositions of $Ca(Co_xMg_{1-x})Si_2O_6$ pyroxenes: 1) crystals growth from melt and 2) growth from flux which acts as a solvent. By following an industrial-like process to conventional manufacture of ceramic pigments, both procedures were carried out at room pressure.

5.1.1. Melt-grown method

In the melt-growth method, samples with $x=$ 0.2, 0.4, 0.5, 0.6, 0.8 Co atoms per formula unit (a.p.f.u.) were synthesized from oxide mixtures of each desired stoichiometric composition (Gori *et al.*, 2016, in press). The samples obtained will be hereafter referred to as 'Di-Co20', 'Di-Co40', 'Di-Co50', 'Di-Co60' and 'Di-Co80', respectively. The syntheses were performed at *IMEM*-CNR (*Institute of Materials for Electronics and Magnetism*) in Parma, Italy. The oxide powders (CaO, MgO, Co_3O_4 and SiO_2) were ground in an agate mortar, pressed into pellets, placed into platinum crucibles and heated in a muffle furnace (Figure 5.1) at 1500 °C for two hours, and then quenched to obtain amorphous products. Afterwards, the synthesis products were annealed at 1250 °C, until the crystallization was completed.

We obtained single crystals sized up to 500 μm (Figure 5.3), homogenous, free of impurities and pink in colour, but with slightly different shades.

The syntheses were also attempted by solid-state reaction, but even after prolonged treatment (*e.g.* 30 days at 1150 °C), we did not manage to obtain single phase pyroxene: together with micro-crystals of pyroxene (5-10 μm long), also metastable akermanite and cristobalite phases were obtained. The synthesis conditions are reported in Table 5.1.

5.1.2. Flux-grown method

The synthesis performed by the flux-growth method, were done at steps of $x=$ 0.25 Co a.p.f.u., using stoichiometric quantities of mixed reagent-grade precursors at the laboratories of the Department of Geosciences, Swedish Museum of Natural History, in Stockholm, Sweden. The samples obtained are hereafter referred to as ‘Di-Co25’, ‘Di-Co50’, ‘Di-Co75’ and ‘Co100’. Several tests were made, changing the pyroxene/flux ratio (see Table 5.2). The oxide mixtures (MgO, Co_3O_4, CaO and SiO_2) of each desidered composition were mixed with Ba-borate [samples are then referred to as ‘flux(A)-grown samples’] or Na-tetraborate [then referred to as ‘flux(B)-grown samples’] acting as flux compounds, and were homogenized under acetone in an agate mortar. Approximately 2 g of these mixtures were placed in platinum crucibles, covered by lids, and placed in a muffle furnace shown in Figure 5.2. The temperature was first increased to 1200 °C and then kept constant for 24 h to allow for complete dissolution of the oxides and homogenization. Subsequently, the temperature was decreased to 800 °C, with a linear cooling path and the samples were allowed to slowly cool to obtain large crystals.

All flux-growth products consisted of pyroxene and borate crystals were dispersed in residual glass. Borate crystals and glass were thus dissolved in a diluted HCl solution and then in 1 molar solution of sodium hydroxide. Single-crystals were elongated along the c-axis with dimensions up to 1 mm; flux(A)-grown crystals were pink in colour (Figure 5.4), while those flux(B)-grown were brownish (Figure 5.5). The synthesis conditions are reported in Table 5.2.

TABLE 5.1. Synthesis conditions for melt-grown pyroxene series.

Synthesis steps		**$Co_{0.2}Mg_{0.8}$**	**$Co_{0.4}Mg_{0.6}$**	**$Co_{0.5}Mg_{0.5}$**	**$Co_{0.6}Mg_{0.4}$**	**$Co_{0.8}Mg_{0.2}$**
1st step: heating	T (°C)	1500	1500	1500	1500	1500
	t (h)	2	2	2	2	2
2nd step: quenching	T (°C)	room	room	room	room	room
3rd step: subsequent annealing cycle	T (°C)	1250	1250	1250	1250	1250
	t (h)	1	1	1	1	1

TABLE 5.2. Synthesis conditions for flux(A)- and (B)-grown pyroxene series.

Sample name	**T range (°C)**	**Flux type**	**Cpx:flux**	**Atmosphere**
Flux(A)				
$Co_{0.25}Mg_{0.75}$	1200-800	BaB_2O_4	02:01.1	air
$Co_{0.50}Mg_{0.50}$	1200-800	BaB_2O_4	02:01	air
$Co_{0.75}Mg_{0.25}$	1200-800	BaB_2O_4	02:00.9	air
$Co_{1.0}$	1200-800	BaB_2O_4	02:00.7	air
Flux(B)				
$Co_{0.25}Mg_{0.75}$	1200-800	$Na_2B_4O_7$	2.:1	air
$Co_{0.50}Mg_{0.50}$	1200-800	$Na_2B_4O_7$	2.:1	air
$Co_{0.75}Mg_{0.25}$	1200-800	$Na_2B_4O_7$	2.:1	air
$Co_{1.0}$	1200-800	$Na_2B_4O_7$	2.:1	air

Figure 5.1. Muffle furnace installed at *IMEM*-CNR (Parma, Italy) used for synthesis performed with the melt-grown method.

Figure 5.2. Muffle furnace installed at the Department of Geosciences, Swedish Museum of Natural History (Stockholm, Sweden) used for synthesis performed with the flux-grown method.

Nominal composition	Name
$CaCo_{0.20}Mg_{0.80}Si_2O_6$	**Di-Co20**
$CaCo_{0.40}Mg_{0.60}Si_2O_6$	**Di-Co40**
$CaCo_{0.50}Mg_{0.50}Si_2O_6$	**Di-Co50**
$CaCo_{0.60}Mg_{0.40}Si_2O_6$	**Di-Co60**
$CaCo_{0.80}Mg_{0.20}Si_2O_6$	**Di-Co80**

(a)

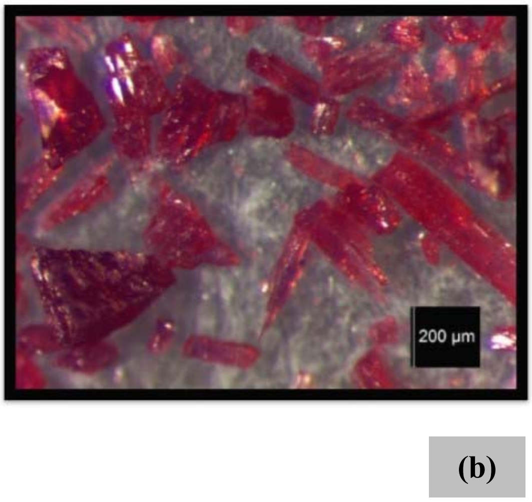

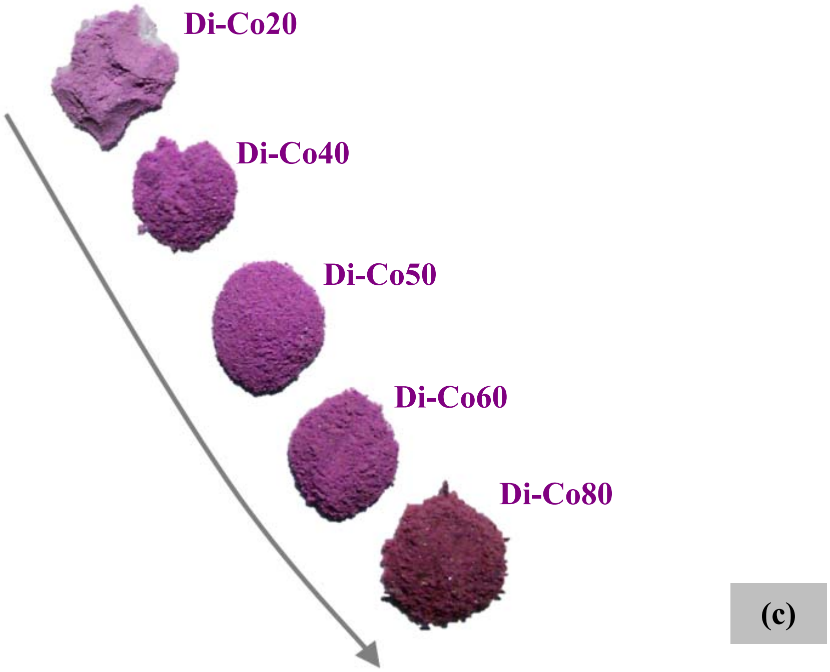

Figure 5.3. Synthesis products obtained by quenching from melts: (**a**) the nominal composition of each synthesized sample; (**b**) size of the crystals in any sample synthesized; (**c**) synthesis products consist of polycristalline powders, pink in colour with slightly different shades.

Nominal composition	Name
$CaCo_{0.25}Mg_{0.75}Si_2O_6$	**Di-Co25**
$CaCo_{0.50}Mg_{0.50}Si_2O_6$	**Di-Co50**
$CaCo_{0.75}Mg_{0.25}Si_2O_6$	**Di-Co75**
$CaCoSi_2O_6$	**Co100**

(a)

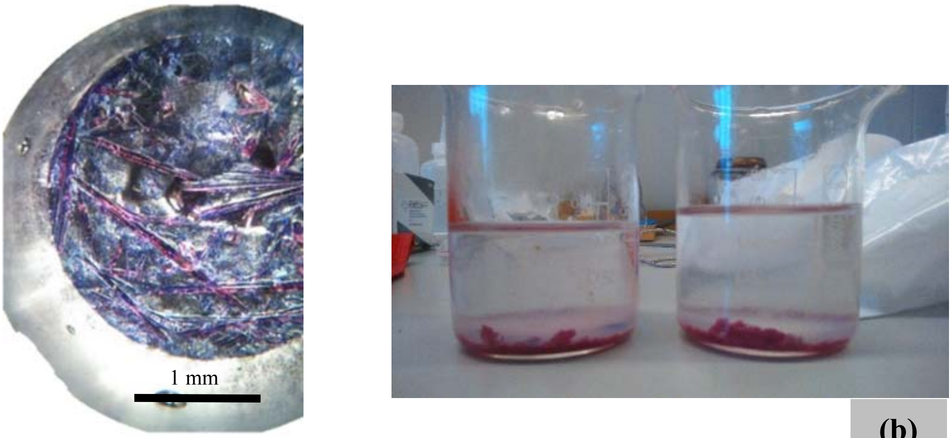

(b)

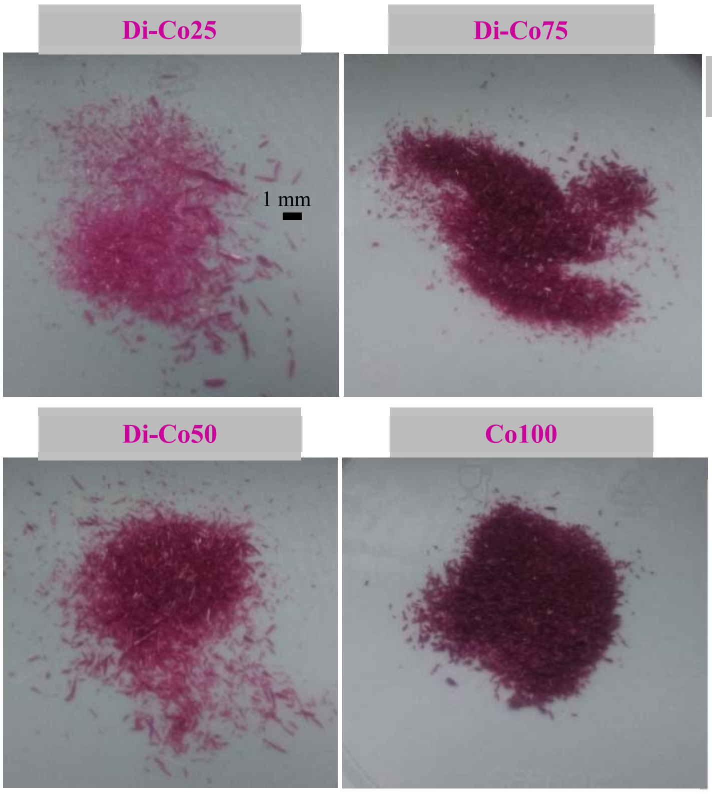

Di-Co25 **Di-Co75** **(c)**

Di-Co50 **Co100**

Figure 5.4. Synthesis products obtained by flux: (**a**) the nominal composition of each synthesized sample; (**b**) flux(A)-grown synthesis products together with borate crystals and glass on the left, and the dissolution of glass and borate crystals on the right; (**c**) pyroxene crystals obtained after dissolution, pink in colour with slightly different shades.

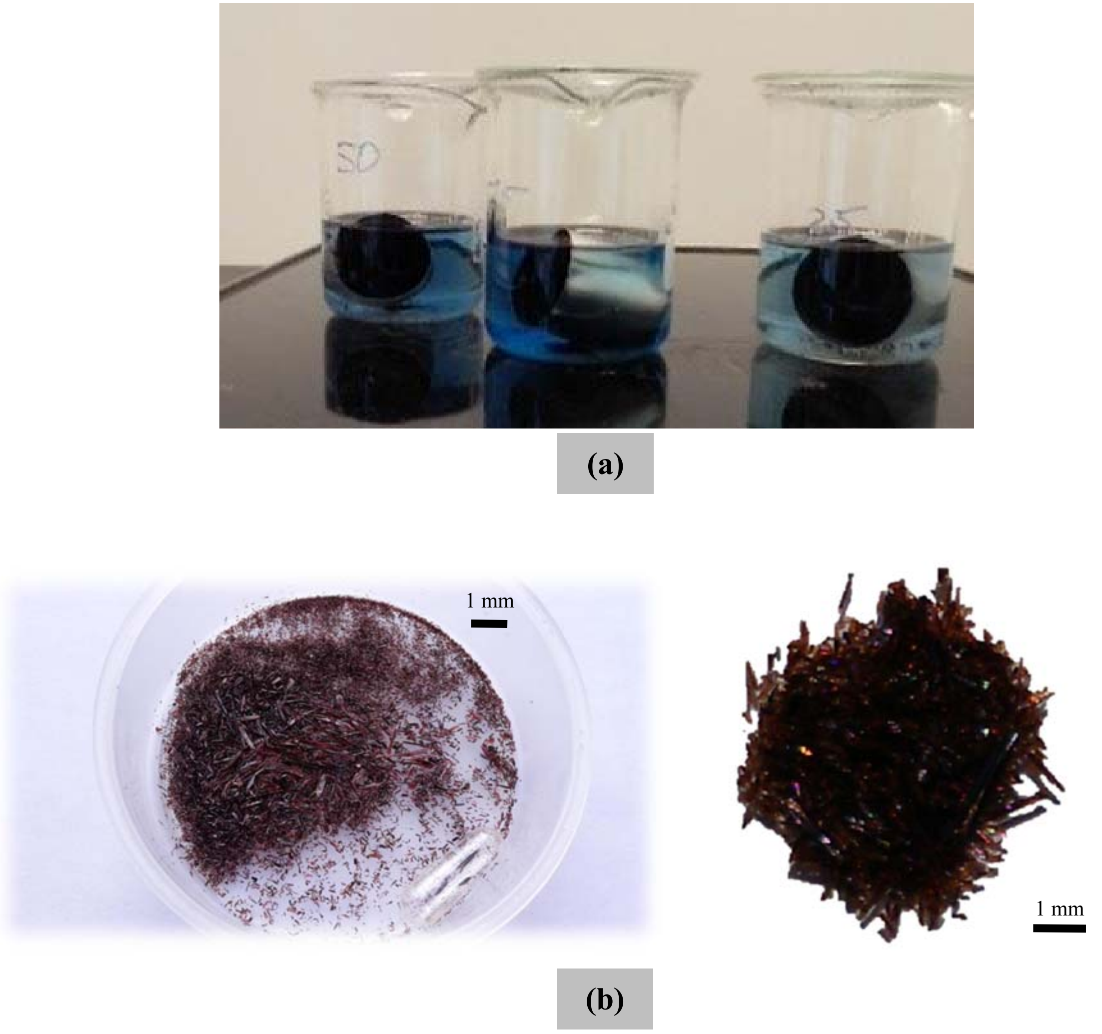

Figure 5.5. Synthesis products obtained by flux: (**a**) the dissolution of glass and borate crystals (**b**) flux(B)-pyroxene crystals obtained after dissolution (size and colour). *Notes*: differences in colour with composition are negligible. The nominal composition is the same of the flux(A)-samples.

5.2. Analytical methods

5.2.1. Electron microscope analysis (SEM-EDS)

The melt- and flux-grown samples were observed and chemically analyzed by using the scanning electron microscopy (SEM) in EDS mode (Gori *et al.*, in press).

A few crystals of each synthesis product were embedded in epoxy, polished and then analyzed with a Jeol 6400 SEM, equipped with an Oxford-INCA EDS, operated at 20 kV, installed at the Department of Physics and Earth Sciences, University of Parma, Italy.

SEM-EDS analyses have shown that melt-grown samples, are small in size and not well shaped, while crystals of either flux(A)- and flux(B)-series are large in size and very well shaped. The chemical composition data for each sample were obtained from the average of 10-15 point analyses. Electron back-scattered images were also collected, those for flux(A)- and flux(B)-grown samples are represented in Figures 5.6 and 5.7.

In melt-grown samples SEM-EDS analyses have confirmed the expected stoichiometry, without showing extra phases.

In flux(A and B)-grown samples the crystals, after preliminary examination at EDS, have shown a deviation from the nominal composition, which is expected for the presence of glass coexisting with pyroxene in the products and thus it has been necessary to analyze these latter samples also in the WDS mode, to obtain a more precise compositional determination.

5.2.2. Electron microprobe analysis (EMPA-WDS)

The crystals obtained with the flux-growth method, were also chemically analyzed by using an electron microprobe in WDS mode.

The analyses were performed by using a JEOL SuperProbe JXA-8200, operated at 15 kV, installed at the Department of Earth Sciences, University of Milan, Italy. The probe operated with a current of 5nA. The size of the electron beam is of about 1 micron.

The chemical composition data are the average of 10 spot analyses per analyzed crystal and the analytical error is within 3%. The standards used are: synthetic grossular (Si, Ca), olivine (Mg), omphacite (Na), sanbornite (Ba) and metallic cobalt.

FLUX(A)-GROWN

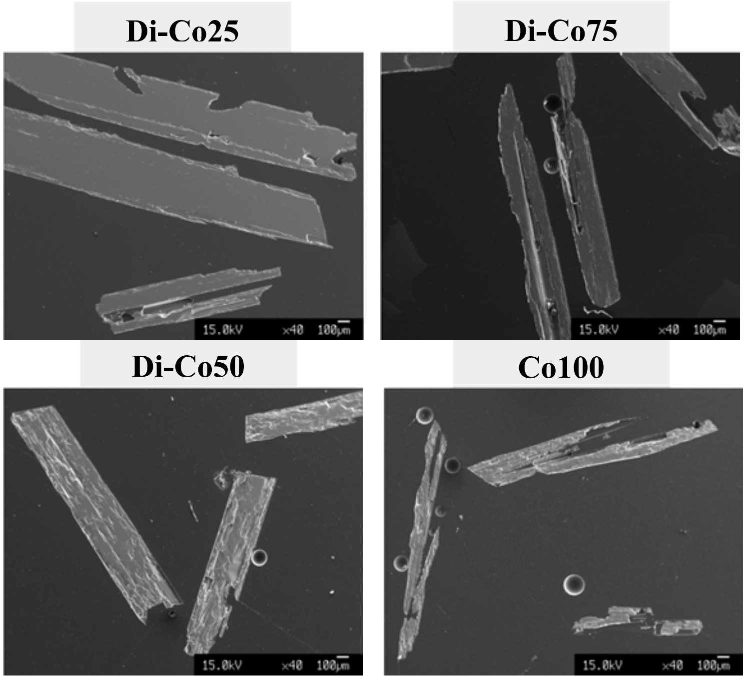

Di-Co25 Di-Co75 Di-Co50 Co100

Figure 5.6. Backscattered images of flux(A)-grown samples, showing the homogeneity, shape and size of crystals for each composition.

FLUX(B)-GROWN

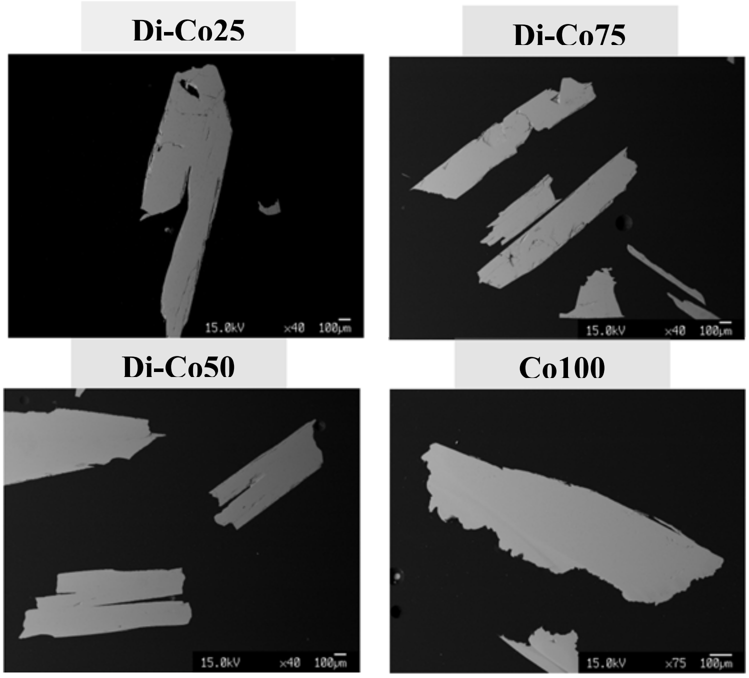

Di-Co25 Di-Co75 Di-Co50 Co100

Figure 5.7. Backscattered images of flux(B)-grown samples, showing the homogeneity, shape and size of crystals for each composition.

5.2.3. X-ray powder diffraction (XRPD)

Powder X-ray diffraction was performed only on melt-grown samples by using a Bruker D2 PHASER diffractometer equipped with a solid-state thermo electron detector, operating with CuK$_{\alpha1}$ radiation (λ= 1.5406 Å) and installed at the Department of Physics and Earth Sciences, University of Parma, Italy.

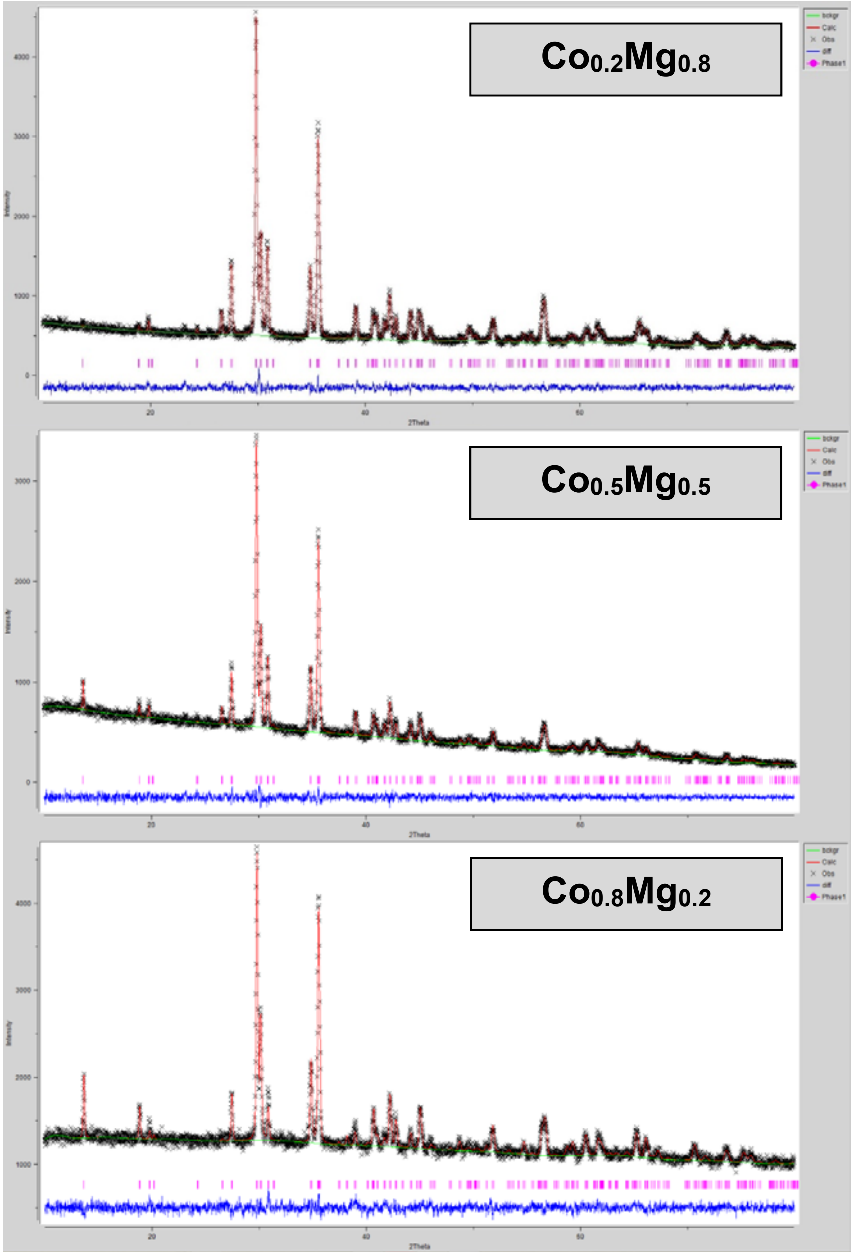

Figure 5.8. Rietveld refinement of the X-ray diffraction powder pattern, obtained by using GSAS-EXPGUI software package (Larson and Von Dreele 1994; Toby 2001). Phase 1 (in pink) is the clinopyroxene and it is the only phase which was found in any sample after the syntheses.

Rietveld analyses were performed to determine the unit cell parameters and the phase ratio, using the GSAS-EXPGUI software package (Larson and Von Dreele 1994; Toby 2001). Starting atomic parameters for the Ca-(Co,Mg) pyroxenes were taken from Tabira *et al*, 1993. Rietveld analyses of powder patterns indicate that clinopyroxene is the only crystalline phase present (phase 1 in Figure 5.8). Rietveld refinement results are reported in Table 5.3.

TABLE 5.3. Cell parameters and goodness of fit from Rietveld refinement of the X-ray diffraction powder pattern.

Sample	**$Co_{0.2}Mg_{0.8}$**	**$Co_{0.4}Mg_{0.6}$**	**$Co_{0.5}Mg_{0.5}$**	**$Co_{0.6}Mg_{0.4}$**	**$Co_{0.8}Mg_{0.2}$**
a (Å)	9.7526(3)	9.7655(6)	9.7651(5)	9.7727(5)	9.7811(5)
b (Å)	8.9607(4)	8.9682(6)	8.9770(6)	8.9800(5)	8.9764(5)
c (Å)	5.2440(2)	5.2428(3)	5.2399(3)	5.2408(2)	5.2397(2)
β (°)	105.878(3)	105.786(4)	105.782(5)	105.738(4)	105.640(5)
V (Å^3)	440.790(15)	441.845(48)	442.033(21)	442.694(19)	443.013(19)
Diffractometer	Bruker D2	Bruker D2	Bruker D2	Bruker D2	Bruker D2
Scan range (°)	7-80° 2θ	7-80° 2θ	7-80° 2θ	7-80° 2θ	7-80° 2θ7
Chi-square	1.27	1.09	1.14	1.17	1.25
wR_p	0.048	0.047	0.049	0.04	0.031
R_p	0.038	0.037	0.039	0.032	0.025

5.2.4. Single-crystal X-ray diffraction

Single crystals suitable for size and optically free of defect (under polarized light microscopy) were selected for the X-ray diffraction experiments. Intensity data were collected on a Bruker AXS Smart diffractometer, equipped with an APEX II CCD operating with Mo*K*α radiation and installed at the Department of Chemistry, University of Parma, Italy. Data for the full reflection spheres up to 2θ= 64° were collected, corrected for absorption effect using a multi-scan method (*SADABS*; Sheldrick, 1996). Corrections for Lorentz-polarization effects were also applied. The reflection conditions showed no violation of the extinction rules for the *C*2/*c* symmetry, as expected for members of this series on the basis of the symmetry of the end-members (Bruno *et al.*, 1982; Ghose *et al.*, 1987).

The *SHELX-97* program (Sheldrick, 1997), implemented in the *WinGX* suite (Farrugia, 1999), was used for the anisotropic structure refinements. The refinements of the synthetic pyroxenes converged with agreement factors between 2.2 and 3.4%. The expected site occupancies, retrieved from stoichiometry and confirmed by SEM-EDS and EMP-WDS results, required the *M*2 site to be occupied by Ca, *M*1 by Co and Mg in different proportions, and the tetrahedral site by Si. The refined site occupancies for melt-grown samples did not deviate significantly from the expected stoichiometry, while flux-grown have shown differences. Details pertaining to the data collection protocols and to the unit-cell parameters, structure refinements, relative fractional atomic coordinates in unit-cell, atomic site occupancies, atomic thermal displacement parameters, bond lengths and polyhedral volumes, for each flux(A)-grown sample, are reported in Chapter 6, paragraph 6.2 as Tables 6.3, 6.4 and 6.5. Regarding melt-grown samples, data collection and the results of single-crystal X-ray structure refinements are outlined in Gori *et al.*, 2016 (in press) and reported in Chapter 6, paragraph 6.2 as Tables 6.6, 6.7 and 6.8. The site-labelling scheme proposed by Burnham *et al.* (1967) is used (Chapter 2, paragraph 2.1).

5.2.5. Optical Absorption and Near Infrared Spectroscopies (UV-VIS-NIR)

As the diffraction methods gives information on the ‘averaged’ crystal structure (*i.e.* long-range), the use of spectroscopic methods is necessary to study the local distances between the central metal ion and its surrounding oxygen-based polyhedron (short-range structure).

In the synthetic samples studied, the light absorption is caused by electronic transitions, which are governed by crystal field theory (CFT). The crystal field theory (CFT) describes the origin and consequences of interactions of the surroundings arranged around the central transition metal ion. These interactions are electrostatic fields originating from the anions (termed ‘ligands’), treated as point negative charges situated on a lattice about the transition metal ion. Transition metals are specific in having incompletely filled 3*d* atomic orbitals, and different energy levels within *3d* orbitals in crystals.

Different ligands have different effects on the energies of the *d* orbitals of the central ion. Interaction with light causes electrons to be excited between the split 3*d* orbital energy levels, leading to absorption bands in the visible and near infrared regions of the electromagnetic spectrum and causing colour in chemical compounds and minerals containing cations of the first series transition elements (Burns 1993). Some ligands have strong electrical fields which cause a large energy gap when the *d* orbitals split into two groups. Others have much weaker fields producing much smaller gaps. The greater the splitting, the more energy is needed to promote an electron from the lower group of orbitals to the higher ones.

In terms of the colour of the light absorbed, greater energy corresponds to shorter wavelengths. The changes induced on the central metal ion depend on the type, positions and symmetry of the surrounding ligands which defines the geometry of the coordination site. In particular, if the ligand changes, the metal ion will change cooordination and the resulting colour as well.

Co^{2+}, which belongs to the first row transition metals and has the d^7 electronic configuration (Chapter 4, paragraph 4.1.1) is therefore potentially a cation able to show crystal filed absorption and impart colour. In 'Di'-Co-pyroxene series, $^{VI}Co^{2+}$ ion replaces the smaller one $^{VI}Mg^{2+}$ at the octahedral *M1* site, giving synthetic compounds pink in colour. The bands observed in OAS and NIR spectra will therefore depend on the energies and the number of the split components of Co^{2+} ion of the *M1* $Co^{2+}O_6$ octahedron.

Only few data on optical studies of Co^{2+} ion in the pyroxene structure are available in literature (White *et al.*, 1971, Taran and Rossmann, 2001). Since in the pyroxene structure Co^{2+} enters the octahedral site (*M1*), in accordance with the d^7 electronic energy level diagram, the optical spectrum of Co^{2+} ion is expected to consist of three *d-d* spin-allowed optical absorption bands (Figure 5.9) arising from the $^4T_{1g} \rightarrow {}^4A_{2g}$, $^4T_{1g} \rightarrow {}^4T_{1g}$ (^4P) and $^4T_{1g} \rightarrow {}^4T_{2g}$ electronic transitions, which originate by Co^{2+} in an octahedral ligand field (Llusar *et al.*, 2001, Taran and Rossmann, 2001; White *et al.*, 1971). In the pyroxene structure, six ligands surround cobalt with a single pair on each axis. This raises the energies of $d_{x^2-y^2}$, d_{z^2} relative to those of d_{xy} d_{xz} d_{yz} (Figure 5.10).

Optical absorption and near infrared spectroscopies were performed on the synthesized samples by using spectrometers installed at the Department of Geosciences, Swedish Museum of Natural History (Stockholm, Sweden), to define the optical properties along the different directions in pyroxene crystals. Sample preparation consisted first of crystallographic orientation on (100) and (010) by optical methods; since the melt-grown crystals were small in size, the oriented sections were prepared only for the flux(A and B)-grown crystals. All samples were then embedded in plastic resin and polished on parallel surfaces.

Polarized, room-temperature spectra in the near infrared region (2000-15000 cm^{-1}, 5000-666 nm) were recorded using a Bruker Vertex 70 spectrometer equipped with a NIR source, a CaF_2 beam-splitter, and an InSb detector. A total of at least 200 scans with a resolution of 4 cm^{-1} were acquired using a KRS-5 wiregrid-polarized.

Polarized, room-temperature optical absorption spectra were recorded in the spectral range 30000-10000 cm^{-1} (333-1000 nm, UV-VIS spectral region) on double-sided polished single crystals at a spectral resolution of 1 nm using an AVASPEC-ULS2048X16 spectrometer attached via a 400 μm UV fiber cable to a Zeiss Axiotron UV-microscope. A 75 W Xenon arc lamp was used as a light source and Zeiss Ultrafluar 10× lenses served as objective and condenser. A UV-quality Glan-Thompson prism with a working range from 40000 to 3704 cm^{-1} (250 to 2700 nm) was used as polarizer. The wavelength scale of the spectrometer was calibrated against Ho_2O_3-doped and Pr_2O_3/Nd_2O_3-doped standards (Hellma glass filters 666F1 and 666F7).

The flux-grown spectra were measured along the three optical indicatrix directions (E//X, *i.e.* α ; E//Y, *i.e.* β; E// Z, *i.e.* γ), while those melt-grown were measured along two perpendicular directions (named 'p_1' and 'p_2'). The thickness of the underlying plastic resin was estimated from the intensity of its C-H stretching bands. The absorption component from the plastic resin was subtracted from all the absorption spectra (UV-VIS-NIR) and then all spectra were normalized to the thickness of each analyzed single-crystal. The recorded spectra were fitted using the OriginLab software assuming Gaussian peak shapes. Absorbance bands were deconvoluted in order to obtain frequency (peak centroid).

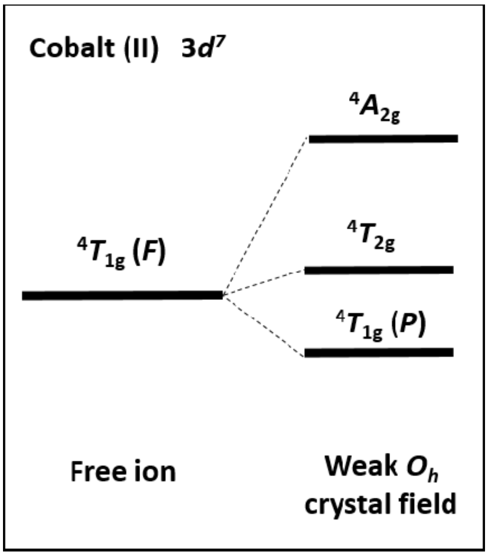

Figure 5.9. Electron Configuration for Octahedral d^7 Co^{2+} Transition-Metal ion.

The position of the peaks after deconvolution was analyzed taking advantage of the Tanabe-Sugano diagrams (Tanabe and Sugano, 1954; Figure 5.11), which predict the electromagnetic absorption of cobalt complexes where cobalt ion is in octahedral coordination. The analyses derived from the diagrams were then compared to experimental spectroscopic data.

Taking into account spectroscopic data, a calculation of the crystal field splitting energy (*Dq*), generated by ligands attached to a cobalt metal center, was done. Also the *Racah B* parameter, which reflects the degree of covalency of the *M*-O bond, was calculated. The calculations for both *Dq* and *Racah B* parameter were made by fitting the mean energy of spin-allowed *d-d* for d^7 Co^{2+} ion in six-fold coordination (Burns 1993), and by applying the simplified Tanabe-Sugano equations: $Dq = (n_2 - n_1)/10$; $B = (n_2 + n_3 - 3n_1)/15$ (Underhill *et al.*, 1966), where n_1 is the band at ~ 7000 cm^{-1}, n_2 the band at ~ 14000 cm^{-1} and n_3 at ~ 19000 cm^{-1} and assuming that n_1 is the $T_{1g} \rightarrow T_{2g}$, n_2 the $T_{1g} \rightarrow A_{2g}$ and n_3 the $T_{1g} \rightarrow T_{1g}$ components.

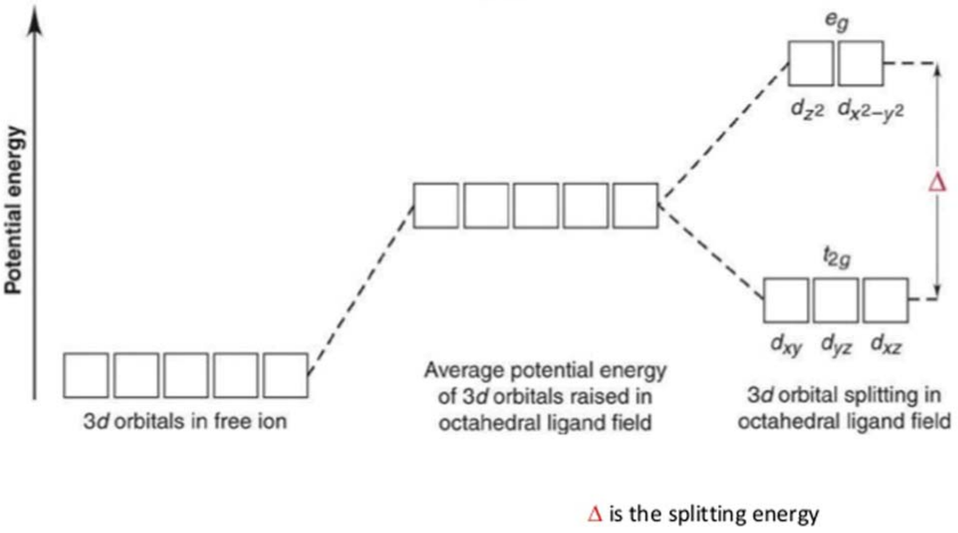

Figure 5.10. The splitting of *d*-orbital energies by an octahedral field of ligands.

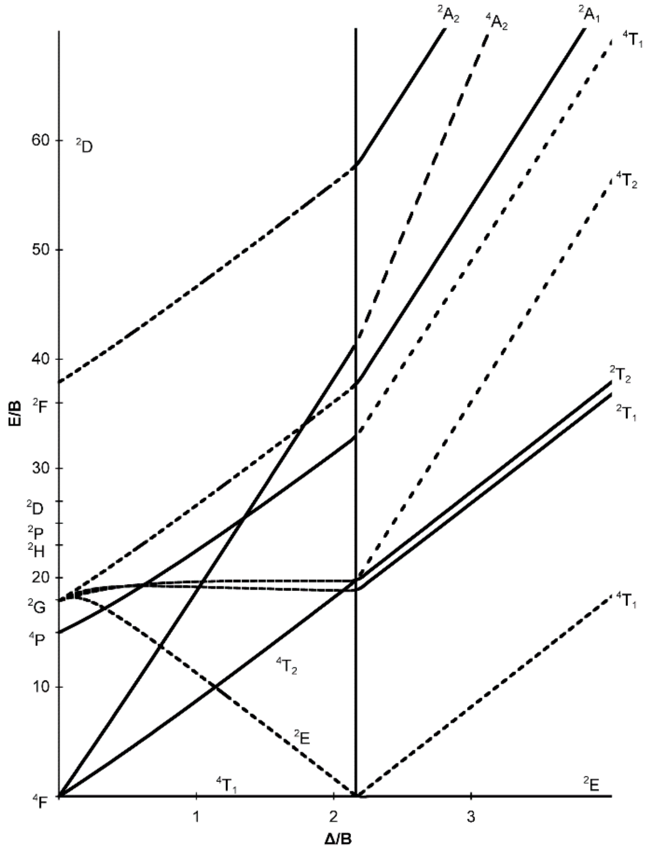

Figure 5.11. Tanabe-Sugano diagram: the x-axis is in terms of the crystal field splitting parameter, *Dq*, or Δ_{oct}, scaled by the *Racah B Parameter*. The y-axis is in terms of energy of a electronic transition, E, scaled by *B*. Each line represents the energy of an electronic state while varying the strength of octahedral ligand field. And while only a few electronic states are spin allowed the spin forbidden electron transitions are included since spin forbidden transitions can appear in spectrum. Each term is created from the splitting of term symbols from spherical to octahedral symmetry. Diagrams for d^7 metal ions have a discontinuity in energies as the ligand field is varied. The discontinuity, shown with the vertical line, represents complexes changing from high-spin to low-spin complexes. At the line, the spin pairing energy is equal to the crystal field splitting energy. To the left of the line metal complexes are high-spin as the spin pairing energy is greater than that of the ligand field splitting. To the right of the line metal complexes are low-spin as the spin pairing energy is less than that of the ligand field splitting energy (Tanabe and Sugano, 1954).

5.2.6. Colour analysis (CIE-*L*a*b**)

The determination of colour can be carried out by visual (human) inspection or by using a colour measuring instrument. Although human inspection is quite robust even in the presence of changes in illumination, the determination of colour is in this case, subjective and extremely variable from observer to observer (Leon *et al.*, 2006).

For these reasons, colour must be determined through the use of colour measuring instrumentation. At present, colour spaces and numerical values are used to create, represent and visualize colours in two and three dimensional space (Trussel *et al.*, 2005). The colour has been measured usually in *L*a*b** units using either a colorimeter or specific data acquisition and image processing systems (Leon et *al.*, 2006).

*L*a*b** is an international standard for colour measurements, adopted by the Commission Internationale d'Eclairage (CIE) in 1976 (McLaren, 1976; Figure 5.12). Colour opposition correlates with discoveries in the mid-1960s that between the optical nerve and the brain, retinal colour stimuli are translated into distinctions between light and dark, red and green, and blue and yellow. CIELAB indicates these values with three axes: *L**, *a**, and *b**. The luminescence or lightness component (*L**) increases from the bottom to the top of the three-dimensional model (darkest black at *L**= 0, brightest white at *L**= 100); parameters *a** and *b** are the chromatic components. In particular, *a** represents the red/green field (green= -*a**; red= +*a**) and *b** the yellow/blue field (blue= - *b**; yellow= +*b**).

Colorimetric analyses were carried out both on the synthesized crystals (pigments) and on the glazes and frits containing them, obtained from technological tests, to assess the changes in colour and to relate the colour components with the different phases and compositions.

The colour was measured by diffuse reflectance spectroscopy in the extended visible range (360-780 nm) using a Hunterlab MSXP4000 Miniscan spectrophotometer with integrated sphere (di/8°) installed at the Department of Physics and Earth Sciences, University of Parma, Italy. Colour is expressed according to the CIE three-dimensional Lab colour space.

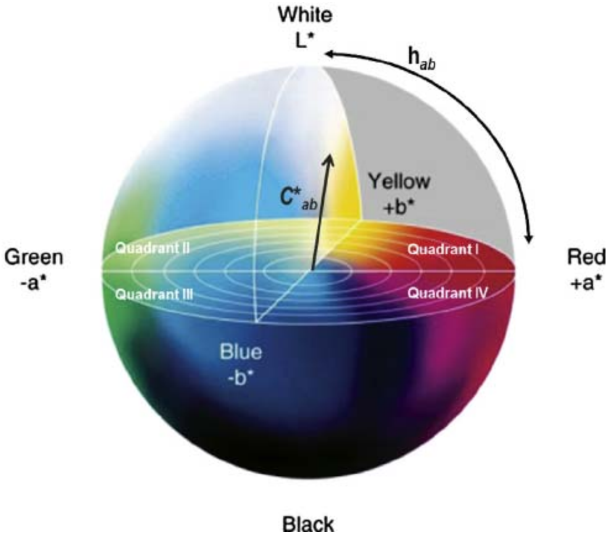

Figure 5.12. The CIE-$L^*a^*b^*$ colour space. The central vertical axis represents lightness (signified as L^*) whose values run from 0 (black) to 100 (white). The colour axes are based on the fact that a colour can't be both red and green, or both blue and yellow, because these colours oppose each other. On each axis the values run from positive to negative.

5.2.7. Technological tests to ceramic pigments

The technological behaviour of all the synthesized pigments [melt and flux(A)-grown] belonging to the 'Di-Co' series was assessed by adding the pigment to different ceramic glazes (S1, S3 and S5) and frits (F4) for different types of wall and floor tiles, whose chemical and physical properties are reported in Table 5.4. The glaze S1 represents a typical coating for porcelain stoneware tiles, the S3 and S5 are representative glazes for porous wall tiles, while the frit F4 is designed for low temperature, third fire applications. This was performed at the *Institute of Science and Technology for Ceramics* (*ISTEC*-CNR), Faenza, Italy.

A ceramic glaze is a coating with both vitreous and crystalline phases, which has been fused to a ceramic body through firing. It is composed by glasses (so-called frits) and minerals (feldspars, wollastonite, calcite, dolomite, etc) which are used to modulate the melting temperature and the glass-to-crystals ratio. Glazes are generally colourless, but need to be decorated in a huge array of colours, resulting from minerals and inorganic compounds (pigments and dyes; Dondi and Eppler, 2014). Glazes range from being completely transparent to being completely opaque. Most opaque or partially opaque glazes derive their effect due to either tiny particles or trapped air bubbles held in suspension within the glaze.

Frits are the main components of classic ceramic glazes, though present-day formulations are made up to a large extent by minerals (in order to get higher maturing temperatures). A frit is prepared to convert some ingredients that are water soluble (alkali carbonates and nitrates, boric anhydride) into an insoluble, granulated glass, whose major constituents are silica, alkaline and alkaline-earth oxides. A frit is achieved by melting raw materials in a basin furnace from which the liquid phase is spilled into cold water: quenching causes the glass formation and fragmentation by the heat shock; the fragments are then ground to obtain a fine powder.

In the technological testing carried out by us, both single crystals and powders of all the synthesized pigments [melt and flux(A)-grown], except the Di-Co50 belonging to the melt-grown series, were added to the glazes and then pressed to obtain button-shaped pellets (Figure 5.13). Only a portion of the grounded powder was used in order to obtain a concentration of about 5% by weight of pigment into the glazes. Pulverized pigments were added in two different glazes (S1, S3), each annealed at its firing temperature (T_1). Single crystals sized up to 400-500 μm were added in two different glazes (S3, S5) and heated at 1100 °C, following two different kinetic paths, *i.e.* at 1100 °C for 1 minute and 10 minutes. Flux(A)-grown pigments (5% by weight) were tested, in powder form, into the F4-frit and heated at about 700 °C. All glazes and frits containing our pigments, were first observed under optical microscope, then colour parameters were recorded and later were analyzed by SEM-EDS.

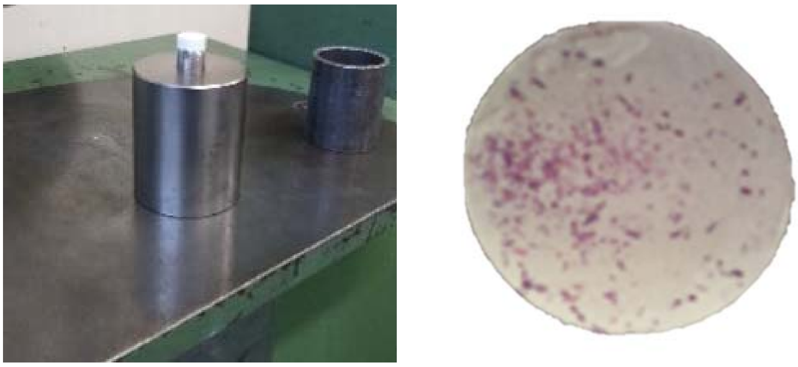

Figure 5.13. On the left: tablet press used to obtain button-shaped pellets (on the right), by applying appropriate pressures on the glazes containing pigments.

TABLE 5.4. Ceramic frit and glazes used for pigment testing: chemical composition, physical properties and firing behaviour.

		Frits	Glazes		
Component/Property	Unit	F4	S1	S3	S5
SiO_2	%wt.	49.3	53.5	49.7	48.0
ZrO_2		0.2	<0.1	8.1	2.0
B_2O_3		19.8	<0.1	2.4	2.0
Al_2O_3		3.3	25.2	19.7	16.0
MgO		0.3	3.4	0.2	1.0
CaO		2.5	8.9	12.6	11.0
ZnO		6.0	<0.1	<0.1	5.0
BaO		9.2	<0.1	3.2	7.0
PbO		0.8	<0.1	<0.1	<0.5
Li_2O		2.0	<0.1	<0.1	<0.5
Na_2O		5.1	5.6	2.2	2.0
K_2O		1.1	3.0	1.3	3.0
Maturing temperature (softening) T_1	°C	720	1210	1100	1100
Temperature of half sphere T_2		820	1275	1195	1175
Temperature of melting T_3		855	1305	1230	1230
Viscosity at T_1	kPa s	2.99	4.65	5.24	4.57
Surface tension at T_1	mN m^{-1}	292	378	383	371
Refractive index	1	1.549	1.526	1.561	1.558
Coeff. thermal expansion $\alpha_{20\text{-}400\ °C}$	MK^{-1}	6.07	6.83	4.97	6.44
Theoretical density	g cm^{-3}	2.617	2.680	2.824	2.948

Chapter 6

RESULTS AND DISCUSSION

6. RESULTS AND DISCUSSION

This chapter, which is organized in four paragraphs, reports the findings of the studies performed on the 'Di-Co' ($CaMgSi_2O_6$-$CaCoSi_2O_6$) pyroxene solid solution, their elaboration and subsequent interpretation.

As previously mentioned, different methodologies of investigation were used for collecting data. The title of each paragraph corresponds to the methodology of investigation.

Paragraph 6.1. *Chemistry*: chemical analyses, in order to determine the chemical composition and to confirm the expected stoichiometry of each sample; they were complemented by the results from UV-VIS-NIR spectroscopy and single crystal partitioning.

Paragraph 6.2. *Crystal structure refinement*: single-crystal X-ray diffraction to explain the cation substitution mechanism and the effect on the pyroxene structure.

Paragraph 6.3. *UV-VIS-NIR absorption spectra*: optical absorption and near infrared absorption spectroscopies to investigate the causes of colour that resides in the electronic transitions generated in transition metal ions (crystal field theory), and obtain more information on the local structure of the $CaMg_xCo_{1-x}Si_2O_6$ pyroxene series.

Paragraph 6.4. *Colorimetric and technological behaviour*: colorimetric analsysis to calculate the chromatic characteristics of the pigments and technological tests to pigments to evaluate their conformity, stability and colour rendering.

6.1. Chemistry

As reported in Chapter 5, paragraphs 5.2.1 and 5.2.2, melt-grown samples were analyzed only by EDS, whereas for flux-grown (A and B) samples also WDS analysis was performed. The analyses obtained in melt-grown samples did not show a significant deviation from the expected stoichiometry; this was confirmed by the site occupancies refined from single crystal X-ray diffraction (paragraph 6.2). Instead, a significant deviation from the nominal stoichiometry was found in flux-grown samples (A and B);

the results of chemical WDS analyses performed on flux-grown samples (A and B) are reported in Tables 6.1 and 6.2.

In flux-grown crystals (A and B) Na and Ba are also present, likely coming from reaction with the flux compounds. Flux-grown crystals (A and B) are free of impurities and uniform in composition but a slight deviation from the expected stoichiometry is observed, except for Co100, together with a Ca deficiency.

Site occupancies and crystal chemical formulae were obtained taking into account also the results of crystal structure refinement (paragraph 6.2) and UV-VIS-NIR spectroscopy (paragraph 6.3). At first, we found, in all samples, that the tetrahedral sites are filled with stoichiometric Si (Si= 2.00 a.p.f.u.). No Co or Mg was present in the site, as revealed by both the refinement of site occupancies, and by the constant value of the <*T*-O> bond distances, to a value of 1.630 Å, found in pyroxene tetrahedra filled by Si^{4+} only (Hugh Jones *et al.*, 1994). A further evidence came by the lack of Co^{2+} peaks in tetrahedral coordination in the UV-VIS-NIR spectra.

In flux(A)-samples, Mg^{2+} and Co^{2+} are allocated to fill the *M1* position and Ca is confined to the *M2* position together with the almost negligible amount of Ba and Na (see Table 6.1). In all samples the measured Ca does not fill completely the *M2* site (see Table 6.1); it may be related to some Co^{2+} and Mg^{2+} in the *M2* site, or to a slight non-stoichiometry of the cation in the *M2* site. We tested different models of cation occupancies for the *M2* site, *i.e.* with the missing *M2* site either filled by Co, Mg or vacant, but the missing *M2* site is too small to be constrained by single crystal refinements. Moreover, the absence of peaks in the UV-VIS-NIR spectra (paragraph 6.3) that indicate Co in the *M2* site, indicates that, if some Co or Mg enters the *M2* site it is in negligible amount. Structure refinements will be discussed in more details in paragraph 6.2.

In flux(B)-grown samples Mg^{2+} and Co^{2+} are allocated to fill the *M1* position (Mg + Co= 1.00 a.p.f.u.). These samples have a Ca-deficiency higher than flux (A) (see Table 6.2) Here, the refinement with Co in the *M2* site, to account for the missing Ca, slightly improved the agreement factor. The presence of Co^{2+}, although in little amount at the *M2* site, is confirmed by the UV-VIS-NIR spectra (paragraph 6.3). In flux(B)-grown samples the brownish colour of the crystals which is different from the colour expected in the Co-bearing phase (Dondi *et al.*, 2014; Mantovani *et al.*, 2014), is probably due to small amounts of Co^{3+}. This was confirmed by UV-VIS-NIR spectroscopy (paragraph 6.3). Taking into account all these results, the flux(A)-grown samples will be referred to as 'Di-Co16', 'Di-Co40', 'Di-Co64' and 'Co100' (Table 6.1), while those(B) will be referred to as 'Di-Co21', 'Di-Co40', 'Di-Co74' and 'Co100' (Table 6.2).

TABLE 6.1. Chemical analysis results for the flux(A)-grown samples.

Flux(A)-grown	Di-Co16	Di-Co40	Di-Co64	Co100
Oxide (wt.%)	*El. mass%*	*El. mass%*	*El. mass%*	*El. mass%*
Na^{+}	0.01	0.02	0.01	0.01
Ba^{2+}	0.05	0.06	0.02	0.03
Co^{2+}	5.45	13.32	20.34	29.68
Ca^{2+}	24.49	23.92	23.18	22.04
Mg^{2+}	15.93	10.99	6.28	0.21
Si^{4+}	54.49	52.32	50.8	48.61
Total:	**100.42**	**100.62**	**100.61**	**100.58**
Cation (a.p.f.u.)	*Norm. El%*	*Norm. El%*	*Norm. El%*	*Norm. El%*
Na^{+}	0	0	0	0
Ba^{2+}	0	0	0	0
Co^{2+}	0.16	0.40	0.64	0.99
Ca^{2+}	0.96	0.98	0.98	0.98
Mg^{2+}	0.87	0.62	0.37	0.01
Si^{4+}	2.00	1.99	2.00	2.01
Sum	**4.00**	**4.01**	**4.00**	**3.99**

TABLE 6.2. Chemical analysis results for the flux(B)-grown samples.

Flux(B)-grown	Di-Co21	Di-Co40	Di-Co74	Co100
Oxide (wt.%)	*El. mass%*	*El. mass%*	*El. mass%*	*El. mass%*
Na^{+}	0.17	0.16	0.14	0.11
Co^{2+}	7.12	13.12	22.96	30.84
Ca^{2+}	23.77	22.99	21.82	21.01
Mg^{2+}	14.87	11.22	5.25	0.15
Si^{4+}	53.42	52.81	50.21	48.45
Total:	**99.35**	**100.29**	**100.39**	**100.56**
Cation (a.p.f.u.)	*Norm. El%*	*Norm. El%*	*Norm. El%*	*Norm. El%*
Na^{+}	0.01	0.01	0.01	0.01
Co^{2+}	0.21	0.40	0.74	1.03
Ca^{2+}	0.95	0.94	0.93	0.94
Mg^{2+}	0.83	0.64	0.31	0.01
Si^{4+}	2.00	2.01	2.01	2.01
Sum	**4.01**	**4.00**	**4.00**	**3.99**

6.2. Crystal structure refinement

In this section the results of crystal structural refinements on the $CaCoSi_2O_6$-$CaMgSi_2O_6$ melt- and flux(A)-grown pyroxenes will be discussed. Part of the reported results, namely from melt-grown samples, have been published in Gori *et al.* (2016, in press). Here the results on melt-grown samples will be complemented with those from flux(A)-grown samples.

Single crystal data show that all samples [melt and flux(A)] belong to the monoclinic crystal system *C*2/*c*. The crystal structure of a *C*2/*c* pyroxene projected down the a-axis [onto (100)], is represented in Figure 6.1.

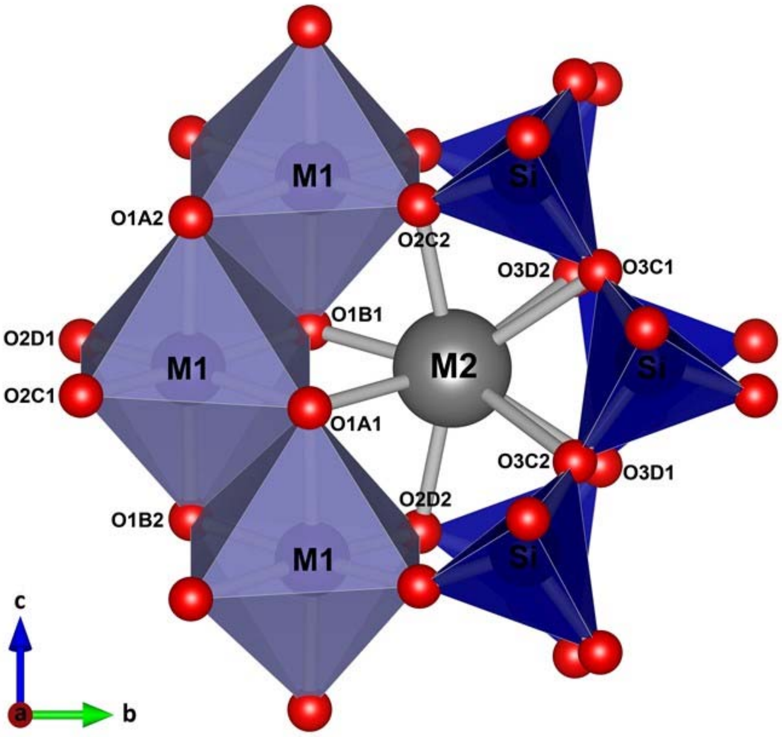

Figure 6.1. The crystal structure of the *C*2/*c* clinopyroxenes viewed along the a-axis. The SiO_4 tetrahedra and the $(Mg,Co)O_6$ octahedra are shown as closed polyhedra. The atoms are labeled after Burnham *et al.* (1967). The crystal structure is visualized by using the VESTA software package (Momma and Izumi, 2008).

6.2.1. Melt- and flux(A)-grown samples

In the melt- and flux(A)-grown series, the expected site occupancies, retrieved from stoichiometry and obtained by SEM-EDS and EMPA analysis together with the signle-crystal data, were considered to refine the structural parameters.

In details at first, the *M2* site was modelled using the Ca and Co scattering factors, while using the Co and Mg scattering factors for the *M1* site. The occupancies of the *M1* and *M2* site were refined with free variables*, i.e.* imposing occupancies but considering the SEM-EDS and EMP data. The *T* site was modeled with Si scattering factor.

Constraints were applied also to atom coordinates and displacement parameters to provide a way of restraining the sum of the occupancies of a multi-component disorder to be unity and of restraining the occupancies to fit the charge balance and chemical analysis of any crystal with the *M2* and *M1* sites occupied by a mixture of cations. The atoms occupying the same site [(Ca,Co) for the *M2* site and (Co,Mg) for the *M1* site) were constrained to have the same positional and displacement parameters.

T site was refined with a fixed occupancy of 1 because refinement with unconstrained occupancies showed no significant deviations from this value. Secondly, the *M2* site and *T* site were modelled using the Ca and Si scattering factors, respectively, and both with a fixed occupancy of 1. Co and Mg were constrained into the *M1* site with the fixed occupancies, which were obtained by chemical analyses. The cation distribution at the octahedral and tetrahedral sites was obtained taking into account the structural refinements with the *M2* site completely filled by calcium, with cobalt and magnesium solely ordered at the *M1* site (see paragraph 6.1). As previously mentioned (Chapter 5, paragraph 5.2.4), the structural parameters are listed in Tables 6.3, 6.4 and 6.5 for the flux(A)-grown samples, and in Tables 6.6, 6.7 and 6.8 for the melt-grown samples.

TABLE 6.3. Details pertaining to the unit-cell parameters and structure refinements for flux(A)-grown pyroxenes of the Ca(Co$_x$Mg$_{1-x}$)S$_2$O$_6$ (‘Di-Co’) series.

	Diopside	Di-Co16	Di-Co40	Di-Co64	CaCoSi$_2$O$_6$
Space group	*C*2/*c*	*C*2/*c*	*C*2/*c*	*C*2/*c*	*C*2/*c*
Z	4	4	4	4	4
a (Å)	9.750(1)	9.754(1)	9.774(2)	9.788(2)	9.801(1)
b (Å)	8.926(1)	8.926(1)	8.944(1)	8.945(2)	8.959(1)
c (Å)	5.251(1)	5.257(1)	5.251(1)	5.256(1)	5.250(1)
β (°)	105.90(1)	105.81(2)	105.66(2)	105.50(3)	105.42(1)
V (Å^3)	439.5(1)	440.39(1)	441.99(1)	443.46(1)	444.45(1)
Diffractometer	Philips PW1100	Bruker AXS Smart	Bruker AXS Smart	Bruker AXS Smart	Bruker AXS Smart
Radiation	MoKα	MoKα	MoKα	MoKα	MoKα
F > 4σ	649	731	748	719	722
Number of parameters	–	47	47	47	47
R_{int} (%)	–	1.87	2.34	2.64	3.08
2θmax (°)	–	64.14	64.60	63.66	63.39
$R_{4\sigma}$ (F)%	2.0	2.12	2.45	2.52	2.90
wR_2 (%)		6.18	7.04	6.89	7.33
GooF	–	0.723	1.177	0.830	0.904

Notes: Data for diopside (CaMgSi$_2$O$_6$) and CaCoSi$_2$O$_6$ from Bruno *et al.* (1982) and this thesis, respectively. Standard deviation in brackets.

TABLE 6.4. Fractional atomic coordinates and equivalent displacement parameters (Å^2) of flux(A)-grown pyroxenes of the Ca(Co$_x$Mg$_{1-x}$)S$_2$O$_6$ (‘Di-Co’) series.

Site		Diopside	Di-Co16	Di-Co40	Di-Co64	CaCoSi$_2$O$_6$
M2	*y/b*	0.3011(1)	0.30089(5)	0.30032(6)	0.30001(6)	0.29930(7)
	Ueq	0.0068(1)	0.0071(1)	0.0080(1)	0.0075(1)	0.0070(1)
M1	*y/b*	0.9082(1)	0.90810(7)	0.90793(6)	0.90784(5)	0.90763(4)
	Ueq	0.0040(1)	0.0040(1)	0.0022(1)	0.0026(1)	0.0045(1)
T	*x/a*	0.2866(1)	0.28655(4)	0.28680(6)	0.28696(6)	0.28725(6)
	y/b	0.0933(1)	0.09322(5)	0.09299(6)	0.09283(5)	0.09264(6)
	z/c	0.2302(1)	0.23001(8)	0.2302(1)	0.2303(1)	0.2306(1)
	Ueq	0.0039(1)	0.0034(1)	0.0045(1)	0.0040(1)	0.0035(1)
O1	*x/a*	0.1159(1)	0.1159(1)	0.1166(1)	0.1169(1)	0.1174(2)
	y/b	0.0877(1)	0.0876(1)	0.0879(1)	0.0880(1)	0.0882(2)
	z/c	0.1423(2)	0.1431(2)	0.1445(3)	0.1460(3)	0.1470(3)
	Ueq	0.0056(1)	0.0049(2)	0.0062(3)	0.0057(3)	0.0057(3)
O2	*x/a*	0.3615(1)	0.3615(1)	0.3613(2)	0.3612(1)	0.36105(2)
	y/b	0.2496(2)	0.2496(1)	0.2494(2)	0.2492(2)	0.2489(2)
	z/c	0.3196(3)	0.3197(2)	0.3203(3)	0.3207(3)	0.3215(3)
	Ueq	0.0077(2)	0.0068(2)	0.0080(3)	0.0077(3)	0.0072(3)
O3	*x/a*	0.3507(1)	0.3508(1)	0.3508(1)	0.35078(1)	0.35069(1)
	y/b	0.0179(1)	0.0181(1)	0.0183(2)	0.0187(2)	0.0193(2)
	z/c	0.9957(3)	0.9951(2)	0.9946(3)	0.9943(3)	0.9937(3)
	Ueq	0.0070(2)	0.0057(2)	0.0069(3)	0.0064(3)	0.0058(3)

Notes: special positions: $x = 0$ and $y = 0.25$ for the *M2* and *M1*, respectively. Atomic labelling scheme after Burnham *et al.* (1967). Data for diopside (CaMgSi$_2$O$_6$) and CaCoSi$_2$O$_6$ from Bruno *et al.* (1982) and this thesis, respectively. Standard deviation in brackets.

TABLE 6.5. Bond lengths (Å), polyhedral volumes (Å^3) and angles of flux(A)-grown pyroxenes of the $Ca(Co_xMg_{1-x})S_2O_6$ ('Di-Co') series.

	Diopside	Di-Co16	Di-Co40	Di-Co64	$CaCoSi_2O_6$
M2(Ca)-O1A1, B1[a] × 2	2.361(1)	2.359(1)	2.357(1)	2.353(1)	2.350(2)
M2(Ca) -O2C2, D2× 2	2.337(1)	2.341(1)	2.340(1)	2.343(1)	2.339(2)
M2(Ca)-O3C1, D1× 2	2.566(1)	2.571(1)	2.582(2)	2.592(1)	2.606(2)
M2(Ca)-O3C2, D2× 2	2.724(1)	2.722(1)	2.724(1)	2.723(1)	2.723(2)
<*M2*(Ca)-O>	2.497	2.498	2.501	2.503	2.505
$V_{M2(Ca)}$ (Å^3) 8-coord.	25.73	25.76	25.82	25.89	25.94
M2 along b-axis†	3.680	3.681	3.686	3.685	3.689
M1(Co,Mg)-O1A2, B2× 2	2.060(1)	2.056(1)	2.062(1)	2.066(1)	2.072(2)
M1(Co,Mg)-O1A1, B1× 2	2.125(1)	2.123(1)	2.129(1)	2.130(1)	2.137(2)
M1(Co,Mg)-O2C1, D1× 2	2.057(1)	2.068(1)	2.078(1)	2.090(1)	2.096(2)
< *M1*(Co,Mg)-O>	2.081	2.082	2.090	2.095	2.102
$V_{M1(Co,Mg)}$ (Å^3) 6-coord.	11.92	11.95	12.09	12.19	12.29
OAV‡ (M1)	17.01	17.02	16.10	15.65	15.14
M1 along b-axis†	1.445	1.446	1.444	1.442	1.440
T(Si)-O1	1.601(1)	1.602(1)	1.603(2)	1.605(2)	1.605(2)
T(Si)-O2	1.585(1)	1.587(1)	1.590(2)	1.589(1)	1.589(2)
T(Si)-O3A1	1.667(1)	1.670(1)	1.669(1)	1.668(1)	1.666(1)
T(Si)-O3A2	1.686(1)	1.687(1)	1.685(1)	1.687(1)	1.686(2)
< *T*(Si)-O>	1.635	1.637	1.637	1.637	1.637
$V_{T(Si)}$ (Å^3) 4-coord.	2.223	2.230	2.231	2.234	2.233
TAV‡	27.40	27.48	26.64	25.92	24.59
O3A1-*T*(Si)-O3A2	104.12(1)	104.2(1)	104.1(1)	104.2(1)	104.3(1)
T(Si)-O3-*T*(Si)	135.9 (1)	135.9(1)	135.8(1)	135.8(1)	135.8(1)
O3-O3-O3	166.1(1)	165.9(1)	165.8(1)	165.5(1)	165.0(1)
O3A1-O3A2	2.645(1)	2.648	2.646	2.649	2.648
T along b-axis†	2.230	2.235	2.241	2.243	2.250

Notes: [a]Label scheme after Burnham *et al.* (1967).

†*M2*(Ca) contribution: (0.5-y/bO1)b; *M1*(Co,Mg) contribution: (y/bO2-y/bO1)b; *T*(Si) contribution: (0.5-y/bO2)b.

Data for diopside ($CaMgSi_2O_6$) and $CaCoSi_2O_6$ from Bruno *et al.* (1982) and this thesis, respectively.

‡The tetrahedral- and octahedral-angle variance (TAV and OAV, respectively) represent an alternative measure of polyhedron distortion and were calculated using the equations developed by Robinson *et al.* (1971). Standard deviation in brackets.

TABLE 6.6. Details pertaining to the unit-cell parameters and structure refinements for melt-grown pyroxenes of the $Ca(Co_xMg_{1-x})Si_2O_6$ (‘Di-Co’) series.

	Diopside	Di-Co20	Di-Co40	Di-Co50	Di-Co60	$CaCoSi_2O_6$
Space group	*C*2/*c*	*C*2/*c*	*C*2/*c*	*C*2/*c*	*C*2/*c*	*C*2/*c*
Z	4	4	4	4	4	4
a (Å)	9.750(1)	9.769(2)	9.775(1)	9.774(2)	9.780(1)	9.802(1)
b (Å)	8.926(1)	8.926(2)	8.941(1)	8.937(2)	8.945(1)	8.962(1)
c (Å)	5.251(1)	5.253(1)	5.256(1)	5.249(1)	5.249(1)	5.249(1)
β (°)	105.90(1)	105.83(3)	105.82(1)	105.76(1)	105.64(1)	105.40(1)
V (Å^3)	439.5(1)	440.7(2)	441.9(1)	441.3(2)	442.2(1)	444.5(1)
Diffractometer	Philips PW1100	Bruker AXS Smart	Bruker AXS Smart	Bruker AXS Smart	Bruker AXS Smart	Sintex P1
Radiation	MoKα	MoKα	MoKα	MoKα	MoKα	MoKα
F > 4σ	649	698	701	662	696	–
Number of parameters	–	49	49	49	49	–
R_{int} (%)	–	1.7	2.4	–	1.9	–
2θmax (°)	–	62.78	63.28	62.79	63.35	65.00
$R_{4\sigma}$ (F)%	2.0	2.2	2.8	3.4*	2.3	2.5
wR_2 (%)	–	6.0	8.6	9.3*	6.2	–
GooF	–	0.927	0.946	1.025	1.095	–

Notes: Data for $CaCoSi_2O_6$ (obtained by Rietveld refinement) and diopside ($CaMgSi_2O_6$) from Mantovani *et al.* (2014) and Bruno *et al.* (1982), respectively. *after correction for twinning; every reflection is treated as a unique one.

TABLE 6.7. Fractional atomic coordinates and equivalent displacement parameters (Å^2) of melt-grown pyroxenes of the $Ca(Co_xMg_{1-x})Si_2O_6$ (‘Di-Co’) series.

Site		Diopside	Di-Co20	Di-Co40	Di-Co50	Di-Co60	$CaCoSi_2O_6$
M2	*y/b*	0.3011(1)	0.30039(6)	0.2998(7)	0.29940(9)	0.29954(5)	0.29907(5)
	Ueq	0.0068(1)	0.0099(1)	0.0093(2)	0.0091(2)	0.0097(1)	0.0091(3)
M1	*y/b*	0.9082(1)	0.90799(7)	0.90787(7)	0.90781(9)	0.90775(4)	0.90750(3)
	Ueq	0.0040(1)	0.0068(1)	0.0084(2)	0.0085(2)	0.0060(1)	0.0058(3)
T	*x/a*	0.2866(1)	0.28674(5)	0.28692(6)	0.28719(8)	0.28699(5)	0.2872785)
	y/b	0.0933(1)	0.09313(5)	0.09305(6)	0.09297(8)	0.09289(5)	0.09262(5)
	z/c	0.2302(1)	0.2305(1)	0.2308(1)	0.2312(1)	0.2308(1)	0.23080(9)
	Ueq	0.0039(1)	0.0055(1)	0.0050(2)	0.0047(2)	0.0057(1)	0.0052(4)
O1	*x/a*	0.1159(1)	0.1161(1)	0.1166(2)	0.1168(2)	0.1170(2)	0.1176(1)
	y/b	0.0877(1)	0.0878(1)	0.0880(2)	0.0881(2)	0.0880(2)	0.0881(1)
	z/c	0.1423(2)	0.1433(3)	0.1441(3)	0.1448(4)	0.1456(2)	0.1473(2)
	Ueq	0.0056(1)	0.0070(2)	0.0069(3)	0.0063(4)	0.0076(2)	0.0073(2)
O2	*x/a*	0.3615(1)	0.3617(1)	0.3615(2)	0.3617(2)	0.3614(1)	0.3613(1)
	y/b	0.2496(2)	0.2495(2)	0.2494(2)	0.2491(2)	0.2492(1)	0.2487(1)
	z/c	0.3196(3)	0.3207(3)	0.3212(3)	0.3217(4)	0.3215(2)	0.3222(2)
	Ueq	0.0077(2)	0.0093(2)	0.0089(3)	0.0092(4)	0.0097(2)	0.0094(2)
O3	*x/a*	0.3507(1)	0.3506(1)	0.3508(1)	0.3509(2)	0.3509(1)	0.3508(1)
	y/b	0.0179(1)	0.0182(2)	0.0186(2)	0.0187(2)	0.0187(1)	0.0192(1)
	z/c	0.9957(3)	0.9953(3)	0.9951(3)	0.9952(4)	0.9947(4)	0.9939(2)
	Ueq	0.0070(2)	0.0079(2)	0.0073(3)	0.0070(4)	0.0080(4)	0.0077(2)

Notes: special positions: $x = 0$ and $y = 0.25$ for the *M2* and *M1*, respectively. Atomic labelling scheme after Burnham *et al.* (1967). Data for $CaCoSi_2O_6$ and diopside ($CaMgSi_2O_6$) from Ghose *et al.* (1987) and Bruno *et al.* (1982), respectively. Standard deviation in brackets.

TABLE 6.8. Bond lengths (Å), polyhedral volumes (Å^3) and angles of of melt-grown pyroxenes of the $Ca(Co_xMg_{1-x})Si_2O_6$ ('Di-Co') series.

	Diopside	Di-Co20	Di-Co40	Di-Co50	Di-Co60	$CaCoSi_2O_6$
M2(Ca)-O1A1, B1[a] × 2	2.361(1)	2.356(1)	2.354(2)	2.348(2)	2.351(1)	2.349 (1)
M2(Ca) -O2C2, D2× 2	2.337(1)	2.334(2)	2.333(2)	2.327(2)	2.333(1)	2.332(1)
M2(Ca)-O3C1, D1× 2	2.566(1)	2.576(1)	2.585(2)	2.587(2)	2.590(1)	2.603(1)
M2(Ca)-O3C2, D2× 2	2.724(1)	2.727(1)	2.729(1)	2.728(2)	2.726(1)	2.724(1)
<*M2*(Ca)-O>	2.497	2.498	2.500	2.498	2.500	2.502
$V_{M2(Ca)}$ (Å^3) 8-coord.	25.73	25.75	25.80	25.73	25.79	25.85
M2 along b-axis†	3.680	3.679	3.683	3.681	3.685	3.686
M1(Co,Mg)-O1A2, B2× 2	2.060(1)	2.068(1)	2.074(2)	2.077(2)	2.084(1)	2.095(1)
M1(Co,Mg)-O1A1, B1× 2	2.125(1)	2.127(1)	2.133(2)	2.133(2)	2.132(1)	2.136(1)
M1(Co,Mg)-O2C1, D1× 2	2.057(1)	2.059(1)	2.063(2)	2.063(2)	2.065(1)	2.071(1)
< *M1*(Co,Mg)-O>	2.081	2.085	2.090	2.091	2.093	2.101
$V_{M1(Co,Mg)}$ (Å^3) 6-coord.	11.92	11.99	12.09	12.10	12.15	12.28
OAV‡ (M1)	17.01	16.45	16.02	15.68	15.49	14.6
M1 along b-axis†	1.445	1.443	1.443	1.439	1.442	1.437
T(Si)-O1	1.601(1)	1.604(1)	1.602(2)	1.603(2)	1.602(1)	1.604(1)
T(Si)-O2	1.585(1)	1.587(1)	1.588(2)	1.586(2)	1.589(1)	1.588(1)
T(Si)-O3A1	1.667(1)	1.668(1)	1.670(1)	1.668(2)	1.669(1)	1.666(1)
T(Si)-O3A2	1.686(1)	1.685(1)	1.686(2)	1.684(2)	1.685(1)	1.684(1)
< *T*(Si)-O>	1.635	1.636	1.637	1.635	1.636	1.636
$V_{T(Si)}$ (Å^3) 4-coord.	2.223	2.229	2.233	2.226	2.229	2.230
TAV‡	27.4	27.31	26.08	26.02	26.23	25.3
O3A1-*T*(Si)-O3A2	104.12(1)	104.23(5)	104.21(6)	104.24(8)	104.17(5)	104.3(1)
T(Si)-O3-*T*(Si)	135.9 (1)	136.0(1)	135.8(1)	135.9(1)	135.7(1)	135.7(1)
O3-O3-O3	166.1(1)	165.9(1)	165.6(1)	165.5(2)	165.5(1)	165.07(1)
O3A1-O3A2	2.645(1)	2.6466(6)	2.6488(5)	2.6456(8)	2.6459(4)	2.644(1)
T along b-axis†	2.235	2.236	2.241	2.242	2.243	2.252

Notes: [a]Label scheme after Burnham *et al.* (1967).

†*M2*(Ca) contribution: (0.5-y/bO1)b; *M1*(Co,Mg) contribution: (y/bO2-y/bO1)b; *T*(Si) contribution: (0.5-y/bO2)b.

Data for diopside ($CaMgSi_2O_6$) and $CaCoSi_2O_6$ from Bruno *et al.* (1982) and Ghose *et al.* (1987), respectively.

‡The tetrahedral- and octahedral-angle variance (TAV and OAV, respectively) represent an alternative measure of polyhedron distortion and were calculated using the equations developed by Robinson *et al.* (1971). Standard deviation in brackets.

In the $CaMgSi_2O_6$-$CaCoSi_2O_6$ pyroxene series, the only substitution occurs at the *M*1 site, where Co can replace Mg and results in a slight increase in the average *M*1-O bond distance (up to 0.021 Å, Figure 6.3b), in response to the different ionic radii of the two cations (*i.e.* $^{VI}Co^{2+}$ 0.745 Å and ^{VI}Mg 0.72 Å; Shannon and Prewitt, 1970).

Structural changes induced by the cation substitution on the melt- and flux(A)-grown samples can be summarized as the following:

- the unit-cell volume (Figure 6.2a) varies (increases) linearly along the series and with increasing average ionic radius of the *M1* site. This behaviour is in accordance with those of (*C*2/*c*) Ca$M1^{2+}Si_2O_6$ pyroxenes (Figures 6.2b);
- the longer *M*1-O1A1B1 and the shorter *M*1-O2C1D1 bond lengths increase less than the *M*1-O1A2B2 ones (Figure 6.3a);
- a slight increase in the average *M1*-O bond distance is observed (Figure 6.3b);
- the O-*M1*-O (*i.e.* OAV) angle decreases along the series because the geometry of the *M1* polyhedron tends to be regularized (Figure 6.3c);
- the substitution of Co for Mg at the *M*1 site affects also the geometry of the *M*2 polyhedron: as a consequence of a shift in the *M2* cation along the diad axis, the *M*2-O3C1D1 shows a small increase, *M*2-O3C2D2 is almost constant along the series and the *M2*-O2C2,D2 and *M2*-O1A1B1 bond distances decrease with increasing cobalt content (Figure 6.3d). On the whole, the *M*2-O bond distances and the *M*2 polyhedral volumes increase in response to Co for Mg substitution at the *M*1 site, even though the Ca occupancy at the *M*2 site remains unchanged;
- individual Si-O bond distances and Si-O-Si (intra-chain tetrahedral) angle are not affected by the cation substitution at the *M1* site but the tetrahedral angular distortion decreases along the series (*i.e.* with increasing cobalt content at the *M1* site; Figure 6.4); the chain extension angle (O3-O3-O3) show almost negligible variations, from 166.1° to 165.0° between diopside ($CaMgSi_2O_6$) and Co-pyroxene ($CaCoSi_2O_6$).

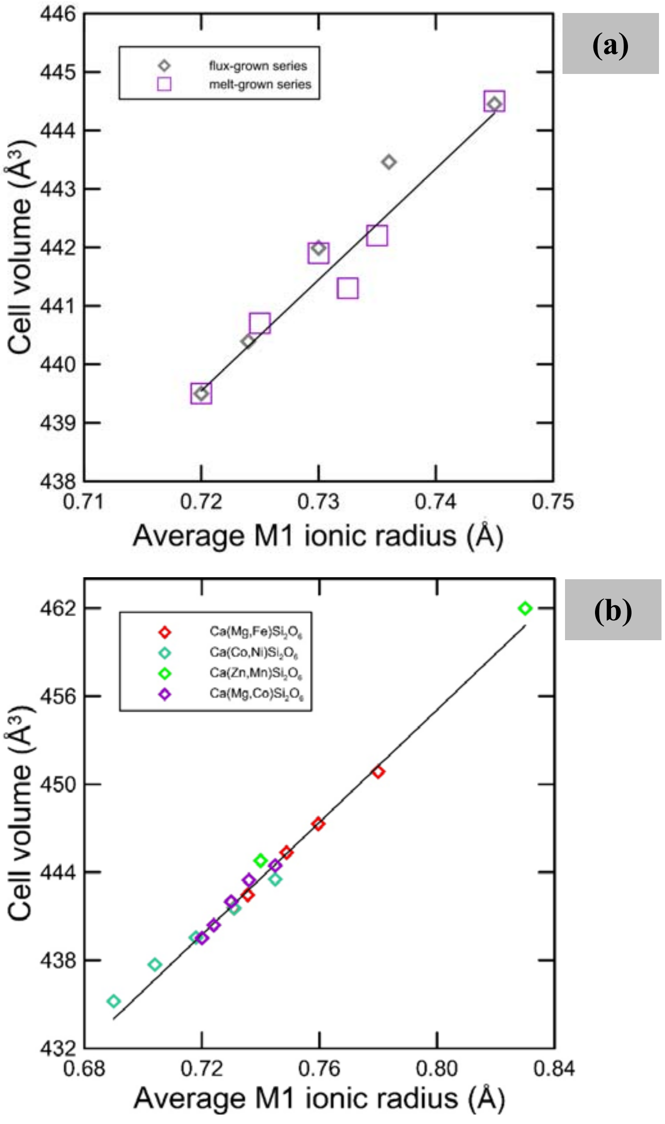

Figura 6.2. (**a**) Cell volume *vs.* average *M*1 ionic radius for 'Di-Co' melt- and flux(A)-pyroxene series. Flux(A)-grown pyroxene series is represented by open grey diamonds while melt-grown pyroxene series (Gori *et al.*, 2016 in press) by open purple squares. [Data of $CaCoSi_2O_6$ from Mantovani *et al*. (2014)]. (**b**) Cell volume *vs.* average *M*1 ionic radius for flux- and melt-grown $Ca(Mg,Co)Si_2O_6$ series compared to $Ca(Mg,Fe)Si_2O_6$, $Ca(Zn,Mn)Si_2O_6$ and $Ca(Co,Ni)Si_2O_6$ pyroxenes. [Data of $CaCoSi_2O_6$ from Ghose *et al.* (1987) and from this thesis; of $CaMgSi_2O_6$ from Bruno *et al.* (1982); of 'Di-Co' series from this thesis; $Ca(Mg,Fe)Si_2O_6$ from Raudsepp *et al.* (1990); $Ca(Co,Ni)Si_2O_6$ from Durand *et al.* (1996); $CaCoSi_2O_6$ and $CaNiSi_2O_6$ from Ghose *et al.* (1987) and Nestola *et al.* (2005) respectively; of $Ca(Zn,Mn)Si_2O_6$ from Nestola *et al.* (2010)].

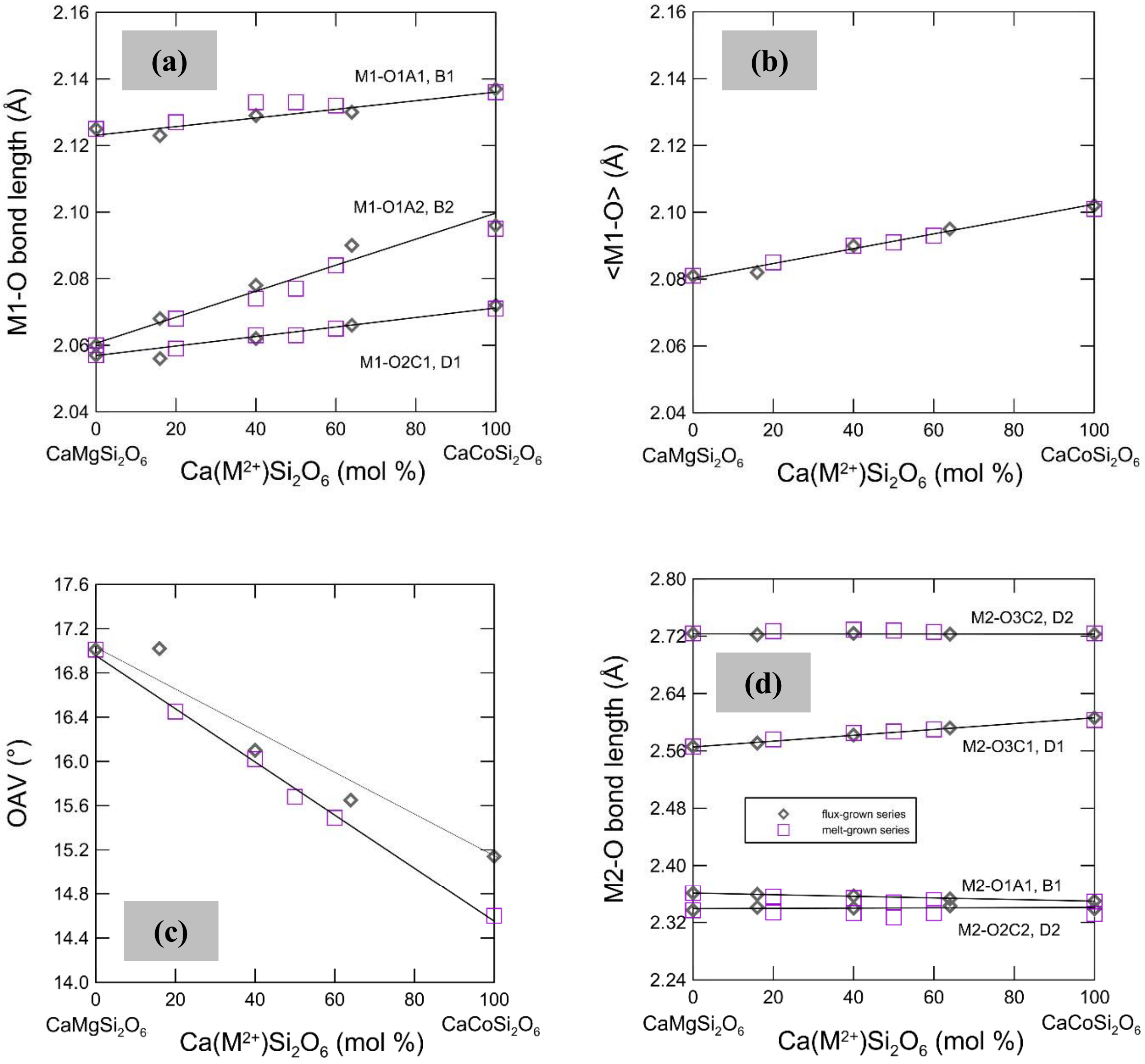

Figure 6.3. (**a**) *M*1-O bond-length variation with composition (Co content) at the *M*1 site in 'Di-Co' melt- and flux(A)-pyroxene series; (**b**) Average *M*1-O bond lengths *vs*. composition (Co content) at the *M*1 site; (**c**) OAV angle variation with composition (Co content) at the *M*1 site. (**d**) *M*2-O bond lengths *vs*. composition (Co content) at the *M*1 site. [Symbols as in Figure 6.2a. Data of $CaCoSi_2O_6$ from Ghose *et al.* (1987) and from this thesis; $CaMgSi_2O_6$ from Bruno *et al.* (1982); melt- $Ca(Mg,Co)Si_2O_6$ pyroxenes from Gori *et al.* (2016, in press) and of flux(A)- $Ca(Mg,Co)Si_2O_6$ pyroxenes from this thesis].

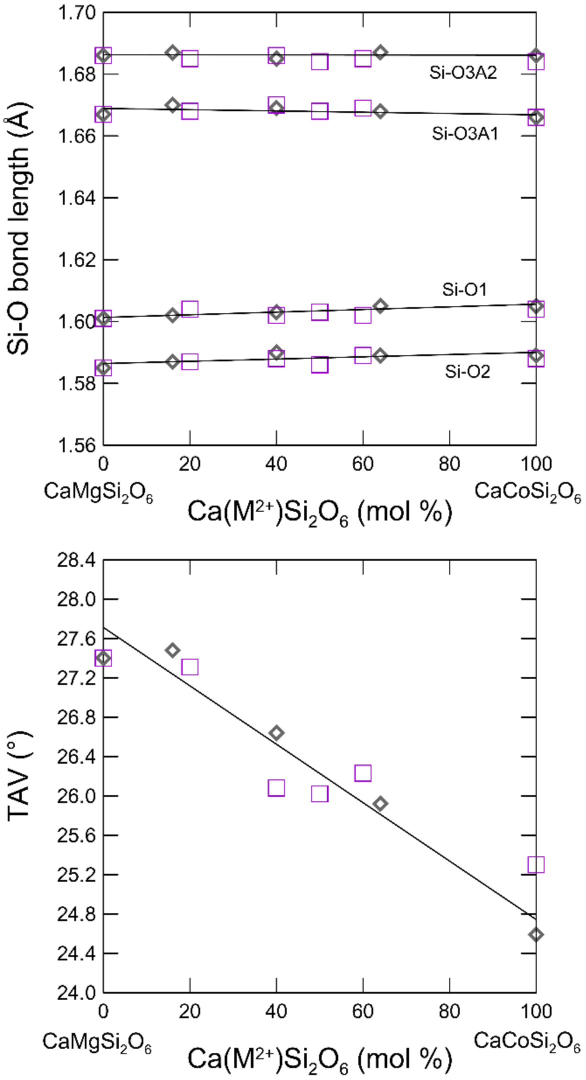

Figure 6.4. Above: Si-O bond lengths *vs.* composition (Mg content) at the *M*1 site in 'Di-Co' melt- and flux(A)-pyroxene series; below: TAV with composition in 'Di-Co' melt- and flux(A)-pyroxene series. [Symbols as in Figure 6.2a. References as in Figure 6.3].

The variations in the unit-cell parameters along the diopside-Co-pyroxene series are shown in Figure 6.5 (a-e). With increasing Co at the *M1* site, the length of the unit-cell edges along *a* and *b* parameters increase, the *c* parameter does not change significantly and the monoclinic *β* angle decreases. The axial expansion pattern in response to the Co-Mg substitution is *a* > *b* > *c*. The minor deformation of the tetrahedron gives rise to negligible changes in the length of the c-axis, as commonly observed in response to compositional, thermal and compressive strains in pyroxenes (Cameron *et al.*, 1973; Nestola *et al.*, 2007; Tribaudino and Mantovani, 2014).

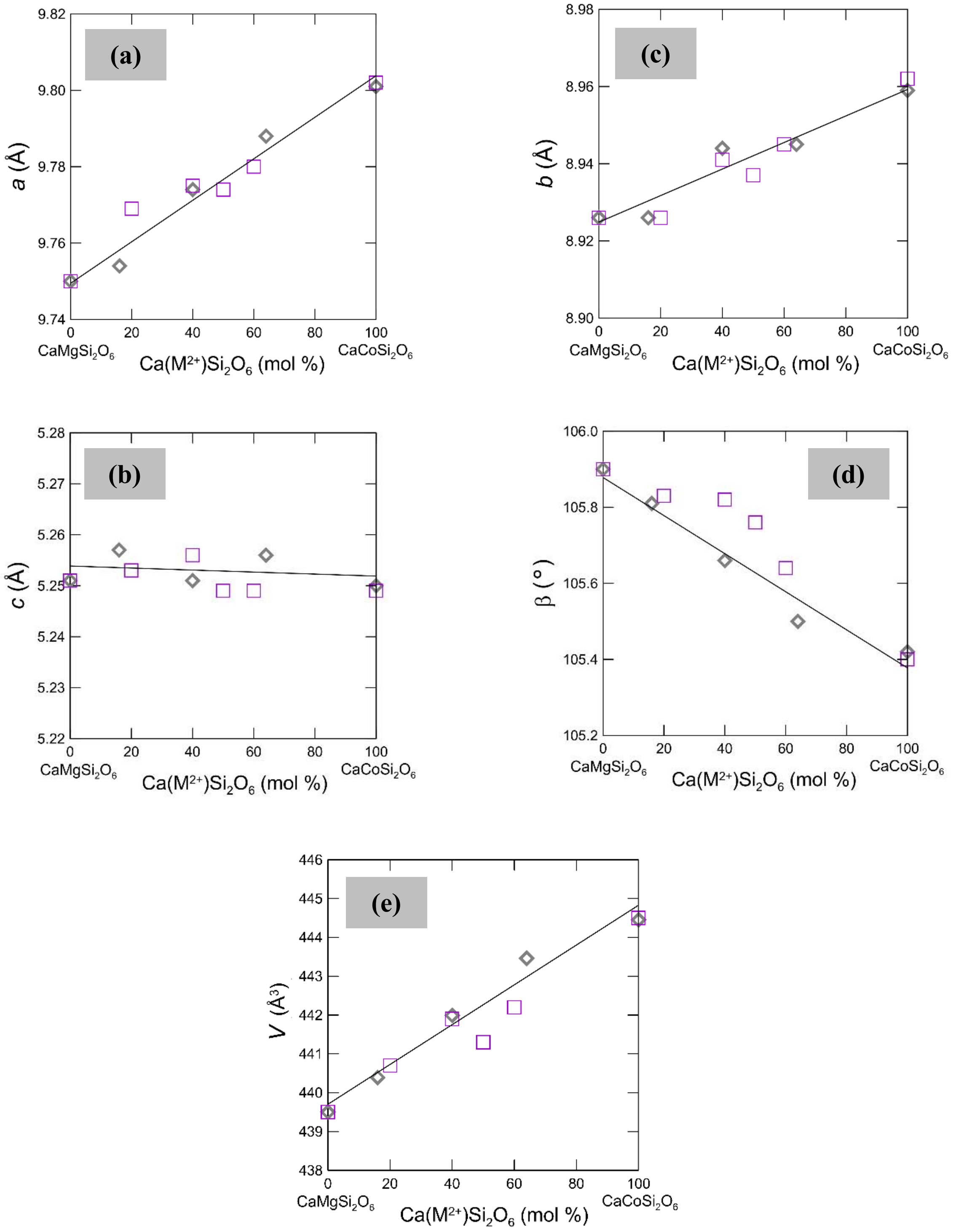

Figure 6.5. (**a-e**) Unit-cell parameters *vs.* Mg content at the *M*1 site in ‘Di-Co’ melt- and flux(A)-pyroxene series. [Symbols as in Figure 6.2a. Data of $CaCoSi_2O_6$, obtained by Rietveld refinement, are taken from Mantovani *et al.* (2014); of ‘Di-Co’ melt-series from Gori *et al.* (2016, in press) and of ‘Di-Co’ flux(A) series from this thesis].

The magnitude and the orientation of the Eulerian unit-strain ellipsoid between diopside and Co-pyroxene were calculated giving further insight into the unit-cell deformation.

For the calculations was used the Eulerian strain formalism with the unit components of the strain tensor derived according to a standard set of Cartesian axes (e_1, e_2 and e_3) oriented with respect to the crystallographic a-, b- and c-axes (Tribaudino and Mantovani, 2014; Ohashi 1972; Ohashi and Burnham, 1973). The strain tensor is geometrically represented by a strain deformation ellipsoid (Tribaudino and Mantovani, 2014). The three axes of the ellipsoid are related to the thermal expansion coefficients (ε_1, ε_2 and ε_3; Carpenter *et al.*, 1998) and are the diagonal components of the strain tensor (Ohashi and Burnham, 1973). The strain ellipsoid is constrained, in a monoclinic structure, by symmetry, to have two axes lying on the (010) plane and the third coincident with the b-axis. The relevant variables are the size of the axes and the orientation onto the (010) plane with respect to the crystallographic a- and c-axes.

The strain for the cation substitution of a smaller cation (Mg) by a larger one (Co) was calculated comparing the unit cell parameters of diopside with those of $CaCoSi_2O_6$ and $CaFeSi_2O_6$, and using the *Win_Strain* software (kindly provided by R.J. Angel, University of Padova to the website: http://www.rossangel.com), a modified version of the *Strain* program by Ohashi (1972). The unit-strain ellipsoid, with the components reported in Table 6.9, has the same orientation previously observed in the hedenbergite-diopside series (Nestola *et al.*, 2007), *i.e.* the major deformation (along ε_1) occurs on (010), describing an angle of about 36° to [100], and it is governed by the expansions of the *M2*-O3 bond distances observed here.

TABLE 6.9. Magnitude and orientation of the strain ellipsoid in different clinopyroxenes.

	Principal unit-strain components (x 10^{-3} mol^{-1})			Unit-strain ellipsoid orientation (°)								
	ε_1	ε_2	ε_3	$\varepsilon_1 \angle \mathbf{a}$	$\varepsilon_1 \angle \mathbf{b}$	$\varepsilon_1 \angle \mathbf{c}$	$\varepsilon_2 \angle \mathbf{a}$	$\varepsilon_2 \angle \mathbf{b}$	$\varepsilon_2 \angle \mathbf{c}$	$\varepsilon_3 \angle \mathbf{a}$	$\varepsilon_3 \angle \mathbf{b}$	$\varepsilon_3 \angle \mathbf{c}$
Di-Hd	18.0(2)	10.8(2)	-3.4(2)	38(1)	90	67(1)	90	0	90	128(1)	90	23(1)
Di-CaCo	9.1(2)	4.0(2)	-1.7(2)	36(1)	90	70(1)	90	0	90	126(1)	90	20(1)
CaCo-Hd	8.9(2)	6.8(2)	-1.8(2)	40(1)	90	65(1)	90	0	90	130(1)	90	25(1)

Notes: hedenbergite (Hd) data; Nestola *et al.* (2007); diopside (Di) data: Bruno *et al.* (1982); $CaCoSi_2O_6$ (CaCo): Mantovani *et al.* (2014).

6.2.2. Discussion

One of the most important experimental findings of this study is that the unit-cell volume of the $^{M2}Ca^{M1}(Co,Mg)^{T}Si_2O_6$ pyroxenes varies linearly along both series. In general, cell volume and *M1* polyhedral volume of (*C*2/*c*) Ca*M1*$^{2+}$$Si_2O_6$ pyroxenes increase with the (average) ionic radius of the *M1* cation (Figures 6.2a and 6.6). Also, the *M2* polyhedral volume increases with the expansion of the *M1* polyhedral volume (Figure 6.6); this is due to the 'steric effect', which adds to the contribution of ionic radii and Pauling bond strengths (Ghose *et al.*, 1987).

In order to cope with the different *M1* ionic radii and with the *M2* steric effect, the unit-cell volumes and the *M1* and *M2* polyhedral volumes of Ca-Fe and Ca-Co pyroxenes, were normalized to those of diopside. In Figure 6.7, the *M2* and *M1* polyhedral volumes in melt-grown $(Ca,Mg)MgSi_2O_6$, $(Ca,Fe)FeSi_2O_6$ and $(Ca,Co)CoSi_2O_6$ pyroxenes are plotted *vs.* the ionic radius of the *M2* cation. The diagram shows that the volume of the *M2* polyhedron is related to the *M2* cation radius, whereas the volume of the *M1* polyhedron does not change in response of the *M2* cation radius.

The contributions of the *M2* and *M1* polyhedra to the unit-cell volumes are shown in Figure 6.8(a-b). As the unit-cell contains four *M1* and four M*2* polyhedra, the *M2* and *M1* volumes were multiplied by 4, in order to give the overall contribution of the polyhedra to the changes in cell volume (Gori *et al.*, 2016 in press).

In samples where the substitution occurs only at the *M1* site, the *M1* polyhedral volume accounts for ≤ 30% of the volume expansion, whereas the *M2* eight-fold polyhedron accounts for about 10%, due to the steric effect (Figure 6.8a). Also, the sum of the *M1* and *M2* polyhedral expansions do not account for the entire cell volume change. Therefore, an expansion in the extra-polyhedral voids must also be considered (Gori *et al.*, 2016 in press). On the contrary, in pyroxene series with the cation substitution at the *M2* site, the *M2* polyhedral volume accounts, almost completely, for the unit-cell expansion, albeit with some difference between Ca-Fe, Ca-Co and Ca-Mg pyroxenes (Figure 6.8b).

The substitution of a given cation with one with larger ionic radius, has a very different effect on the unit-cell volume, whether it occurs at the *M2* site or at the *M1* site. The different effect of the *M2* and *M1* cation substitution was assessed comparing the *C*2/*c* structures of the $CaMgSi_2O_6$-$CaCoSi_2O_6$ and the $CaCoSi_2O_6$-$CoCoSi_2O_6$ series. In the $CaMgSi_2O_6$-$CaCoSi_2O_6$ series, the space group is always *C*2/*c*; in $CaCoSi_2O_6$-$CoCoSi_2O_6$ series the space group is *C*2/*c* between $CaCoSi_2O_6$ and $Ca_{0.4}Co_{0.6}CoSi_2O_6$, but it transform to $P2_1/c$ at higher Co-content (Mantovani *et al.*, 2014).

The average *M1* ionic radius and the unit-cell volume of $CaMgSi_2O_6$ and $CaCoSi_2O_6$ differ respectively by 0.025 Å and 5 Å^3, whereas the *M2* ionic radius and the cell volume of $CaCoSi_2O_6$ and $Ca_{0.4}Co_{0.6}CoSi_2O_6$, differ by 0.132 Å and 6.4 Å^3 (Mantovani *et al.*, 2014). This experimental finding shows how the same substituent cation can have a completely different effect if the substitution occurs at the *M1* site rather than at the *M2* site (Gori *et al.*, 2016 in press). The different response of the crystal structure to the *M1* and *M2* substitutions, gives also a clue to interpret the different effect on the unit-cell volume. The larger *M2* polyhedron allows the cation site to displace along the 2-fold axis; thus, a smaller cation finds its local coordination in a subsite, *i.e.* the *M2*' site (different from that of Ca), as previously observed by Rossi *et al.* (1987) and Gori *et al.* (2015). The substitution gives rise to a cation shift towards the O1 and O2 oxygen atoms, and thus away from the O3 oxygen atom. In addition, a slight deformation of the polyhedron shape occurs. The cation substitution at the *M2* site has, overall, only a small effect on its polyhedral volume. On the contrary, the *M1* polyhedron is more rigid as cations are closely bonded: a substitution with longer ionic-radius cation affects strongly the *M1*-O bond distances and the polyhedral volume, and the expansion somehow affects the whole structure (Gori *et al.*, 2016 in press).

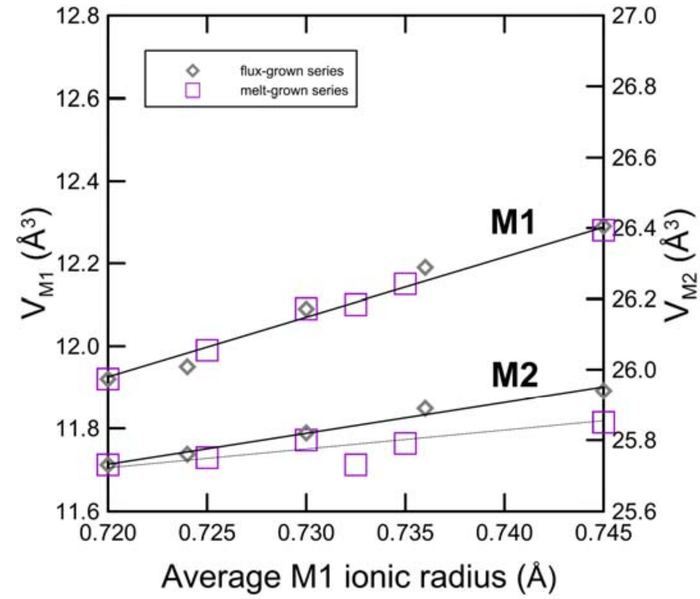

Figure 6.6. *M*1 and *M*2 polyhedral-volumes (*M*2 in eight-fold coordination) as a function of average ionic radius of the cation at *M*1, with the *M*2 site fully occupied by Ca in Ca(Mg,Co)Si_2O_6 melt-grown and flux-grown series. [Symbols as in Figure 6.2a; References as in Fig. 6.3]. The volume of polyhedra was calculated by using the *VESTA* software package (Momma and Izumi, 2008).

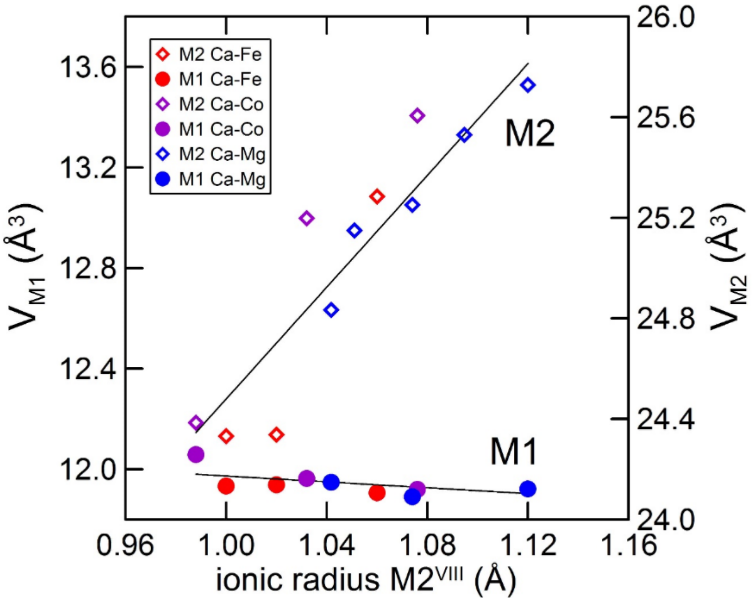

Figure 6.7. *M*1 and *M*2 polyhedral-volumes (*M*2 in eight-fold coordination) as a function of average ionic radius of the cation at *M*2 (in eight-fold coordination) in Ca-Co, Ca-Fe and Ca-Mg pyroxenes, with the *M*1 site filled respectively by Co, Fe and Mg, and with Ca-Co, Ca-Fe, Ca-Mg substitution at the *M*2 site. The volumes of the end-members were normalized to the value of diopside: *i.e.* the unit-cell, *M*1 and *M*2 volumes were corrected by subtracting the difference between those in diopside and hedenbergite for (Ca,Fe)FeSi_2O_6, and in diopside and CaCoSi_2O_6 for (Ca,Co)CoSi_2O_6 pyroxenes. [Data of 'Di-Co' melt-series from Gori *et al.* (2016, in press); (Ca,Co)CoSi_2O_6 from Mantovani *et al.* (2014) and Ghose *et al.* (1987); (Ca,Mg)MgSi_2O_6 from Tribaudino *et al.* (2005) and Bruno *et al.* (1982); (Ca,Fe)FeSi_2O_6 from Ohashi *et al.* (1975) and Nestola *et al.* (2007)]. The volume of polyhedra was calculated by using the *VESTA* software package (Momma and Izumi, 2008).

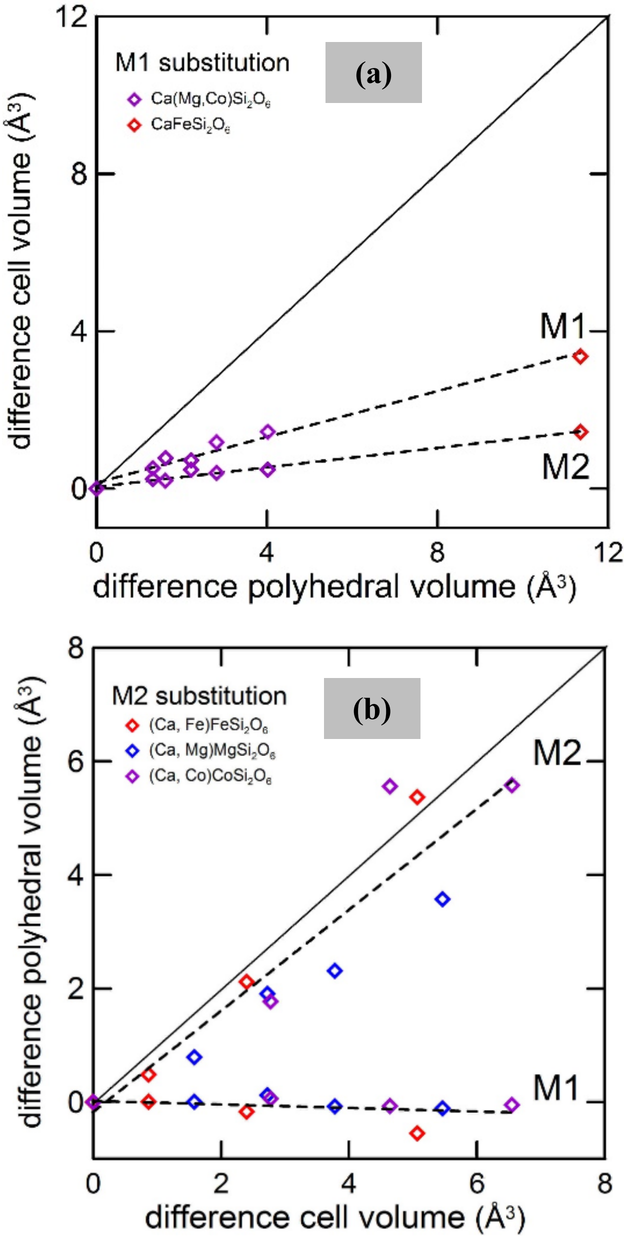

Figure 6.8. (**a**) Polyhedral-volume difference *vs*. cell-volume difference in Ca(Mg,Co)Si_2O_6 and $CaFeSi_2O_6$ pyroxenes with cation substitution at the *M1* site. (**b**) Polyhedral-volume difference *vs*. cell-volume difference with cation substitution at the *M2* site in (Ca,Co)$CoSi_2O_6$, (Ca,Mg)$MgSi_2O_6$, and (Ca,Fe)$FeSi_2O_6$ pyroxenes. [Data of melt-Ca(Mg,Co)Si_2O_6 pyroxenes from Gori *et al.* (2016, in press); $CaFeSi_2O_6$ from Nestola *et al.* (2007); (Ca,Co)$CoSi_2O_6$ from Mantovani *et al.* (2014) and Ghose *et al*. (1987); (Ca,Mg)$MgSi_2O_6$ from Tribaudino *et al*. (2005) and Bruno *et al.* (1982); (Ca,Fe)$FeSi_2O_6$ from Ohashi *et al.* (1975)].

6.3. UV-VIS-NIR absorption spectra

The UV-VIS-NIR investigations were performed on both crystals growth from melt and from flux. Regarding flux-samples, we have named as flux(A), those growth with Ba-borate flux, and flux(B) those grown with Na-tetraborate (Chapter 5, paragraph 5.1.2).

The ‘index ellipsoid’ that shows the polarized directions along which absorption spectra were measured in the monoclinic Co-doped diopside flux-grown crystals, is represented in Figure 6.9. In the analyzed spectral range (28000-4000 cm^{-1}, 357-2500 nm, *i.e.* UV-VIS-NIR spectral region), optical absorption spectra of flux(B)-grown are different than those produced by flux(A)- and melt-grown pyroxenes. The melt- and flux(A) spectra are instead very similar in the entire spectral range.

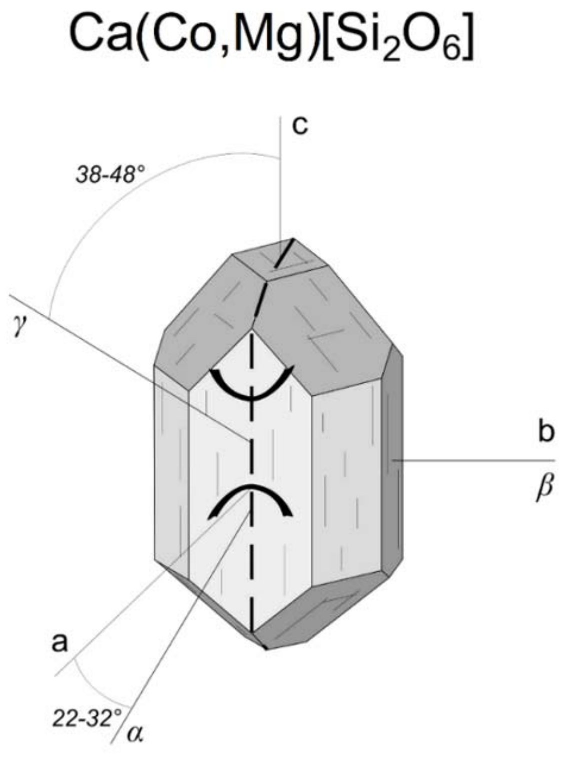

Figure 6.9. Schematic representation of an ellipsoid that depicts the orientation of refractive indices in a monoclinic diopside crystal. The representation may be also applied to the Co-diopside [Ca(Co,Mg)Si_2O_6], object of this study. Image from opticalmineralogy.blogspot.it/p/clinopyroxenes-diopside-augite.html.

6.3.1. Melt- and flux(A)-grown samples: band assignments and their interpretation

Both melt- and flux(A)-grown samples were treated and interpreted together, because of their analogies in the recorded UV-VIS-NIR spectra, which are shown in Figures 6.10(a-c) and 6.11(a-b). In the visible spectral region, all polarized, room temperature spectra are dominated by the three sets of absorption bands which are assumed to originate from the electronic transitions of Co^{2+} in an octahedral ligand field (Llusar *et al.*, 2001, Taran and Rossmann, 2001). In particular the recorded optical absorption spectra show one region of absorption at ca. 19000 cm^{-1} (~ 526 nm) caused by the spin-allowed electronic *d-d* transitions $^4T_{1g}$ $(F)\rightarrow{}^4\mathrm{T}_{1g}$ (P) in octahedrally coordinated Co^{2+}, according to literature data (White *et al.*, 1971; Burns 1993; Llusar *et al.*, 2001, Taran and Rossmann, 2001; Dondi *et al.*, 2014). Each of the observed band region is split in two absorption peaks due to first order spin orbit coupling effects. Additional absorption bands are observed at ca. 14000 cm^{-1} (~ 714 nm), but occur only in γ polarized [for flux(A)-grown samples] spectra and only in one of the two perpendicular directions in which were collected spectra for melt-samples (p_2); this band is assigned to the $^4T_{1g}$ $(F)\rightarrow{}^4A_{2g}$ (F) electronic transition, its intensity is weak and probably it corresponds to a spin-allowed electronic transition of Co^{2+} (Taran and Rossmann, 2001; Ballhausen and Weiner, 1963). In the near infrared region, according to White *et al.* (1971) and Taran and Rossman (2001), the lowest $^4T_{1g}$ $(F)\rightarrow{}^4T_{2g}$ (F) level is associated with the band at ca. 7000 cm^{-1} (~ 1430 nm), which is split in two absorption peaks, and with the bands at 5300 cm^{-1} (~ 1923, weak), which is split in two absorption peaks only in β polarized spectra.

Baseline subtraction was performed from the measured absorption spectrum before the peak fitting. The profiles, after peak fitting in the UV-VIS-NIR absorption spectra of representative polarized single crystals from melt- and flux(A)-grown samples, are plotted in Figure 6.12(a-b).

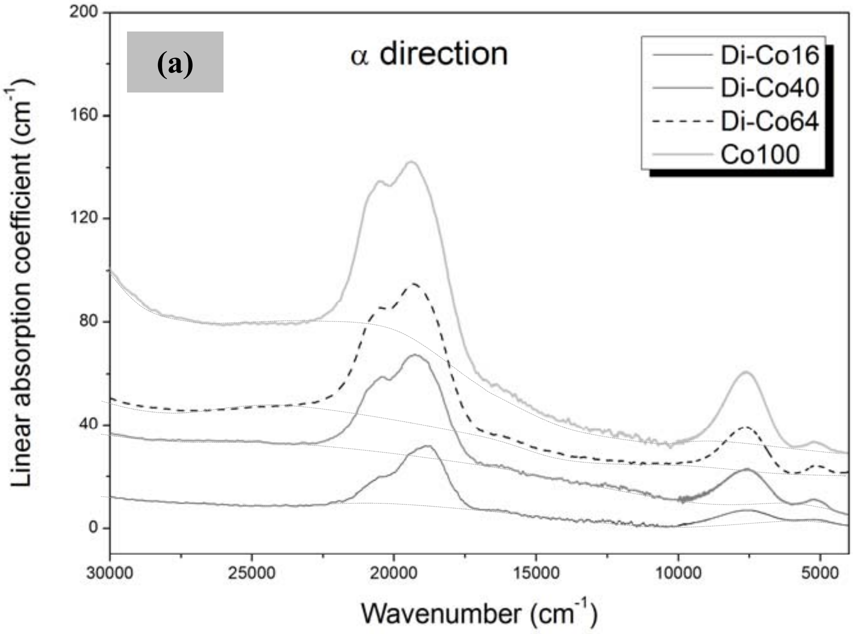

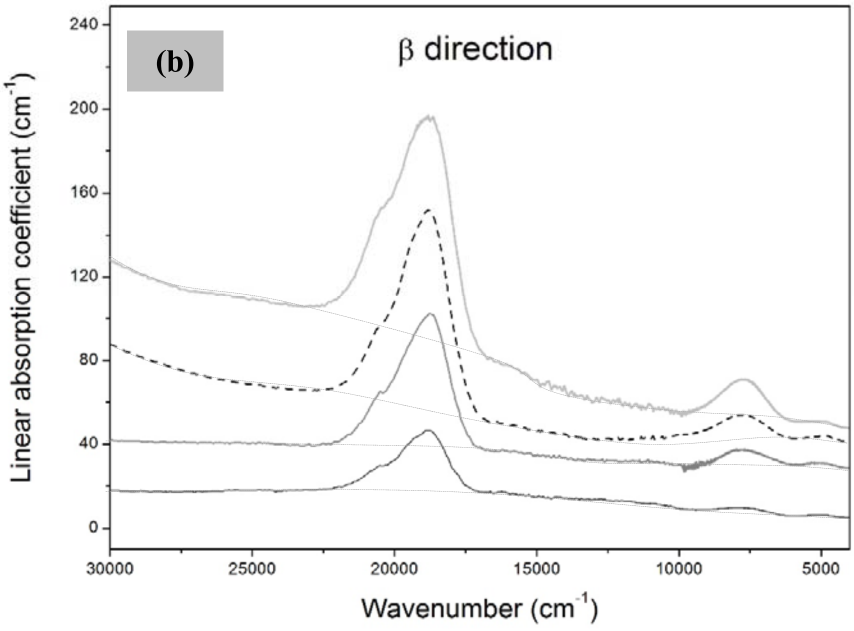

Figure 6.10. Polarized optical absorption spectra of flux(A)-grown samples, from Di-Co16 (bottom) to Co100 (top) in the 30000-4000 cm^{-1} (333-2500 nm) spectral range, along the three optical indicatrix directions (**a**) α, (**b**) β and (**c**, in the next page) γ. These spectra are represented only up to 4000 cm^{-1}, because of the lack of absorption bands at lower frequencies (4000-2000 cm^{-1}, 2500-5000 nm). The thin dotted lines represent the polynomial curve fitting used to obtain the baseline subtraction from each spectrum.

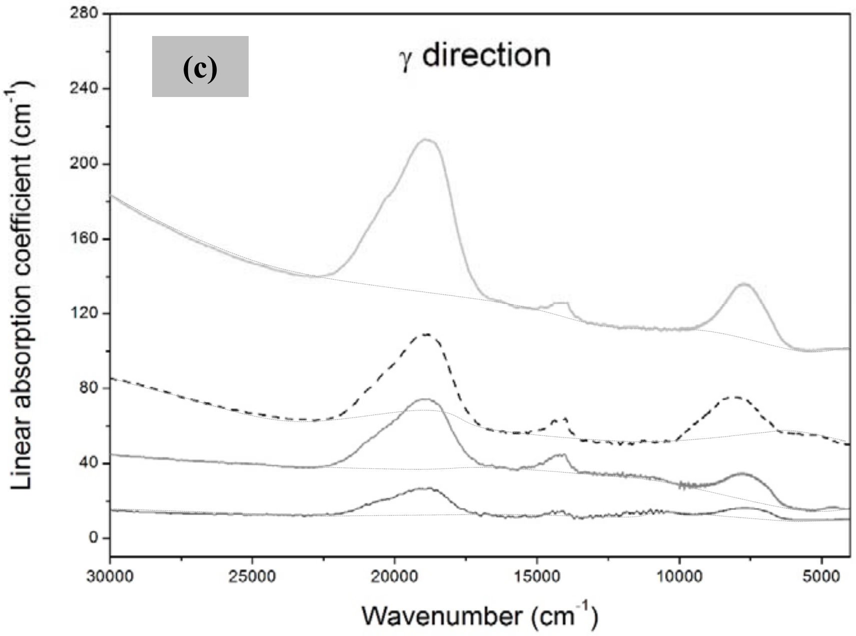

Figure 6.10. (**c**) Polarized optical absorption spectra of flux(A)-grown samples, from Di-Co16 (bottom) to Co100 (top) in the 30000-4000 cm^{-1} (333-2500 nm) spectral range, along γ direction. These spectra are represented only up to 4000 cm^{-1}, because of the lack of absorption bands at lower frequencies (4000-2000 cm^{-1}, 2500-5000 nm). The thin dotted lines represent the polynomial curve fitting used to obtain the baseline subtraction from each spectrum.

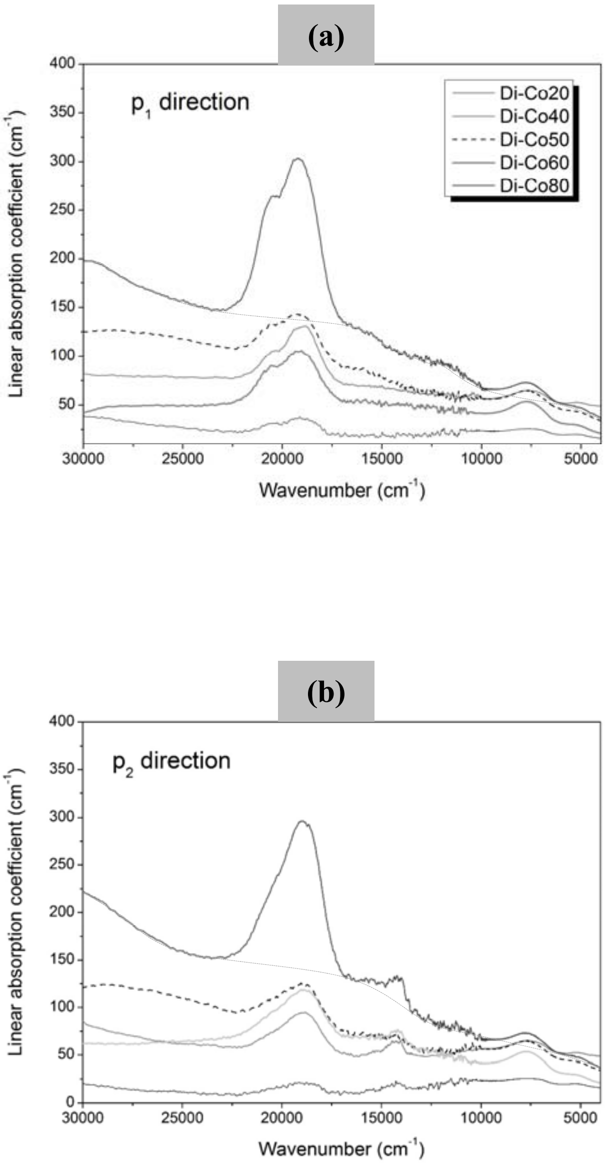

Figure 6.11. Polarized optical absorption spectra of melt-grown samples from Di-Co20 (bottom) to Di-Co80 (top) in the 30000-4000 cm^{-1} (333-2500 nm) spectral range, along the two perpendicular directions (**a**) p$_1$ and (**b**) p$_2$. These spectra are represented only up to 4000 cm^{-1}, because of the lack of absorption bands at lower frequencies (4000-2000 cm^{-1}, 2500-5000 nm). The thin dotted lines for Di-Co80 spectrum represent the polynomial curve fitting used to obtain the baseline subtraction from each spectrum of all melt-samples.

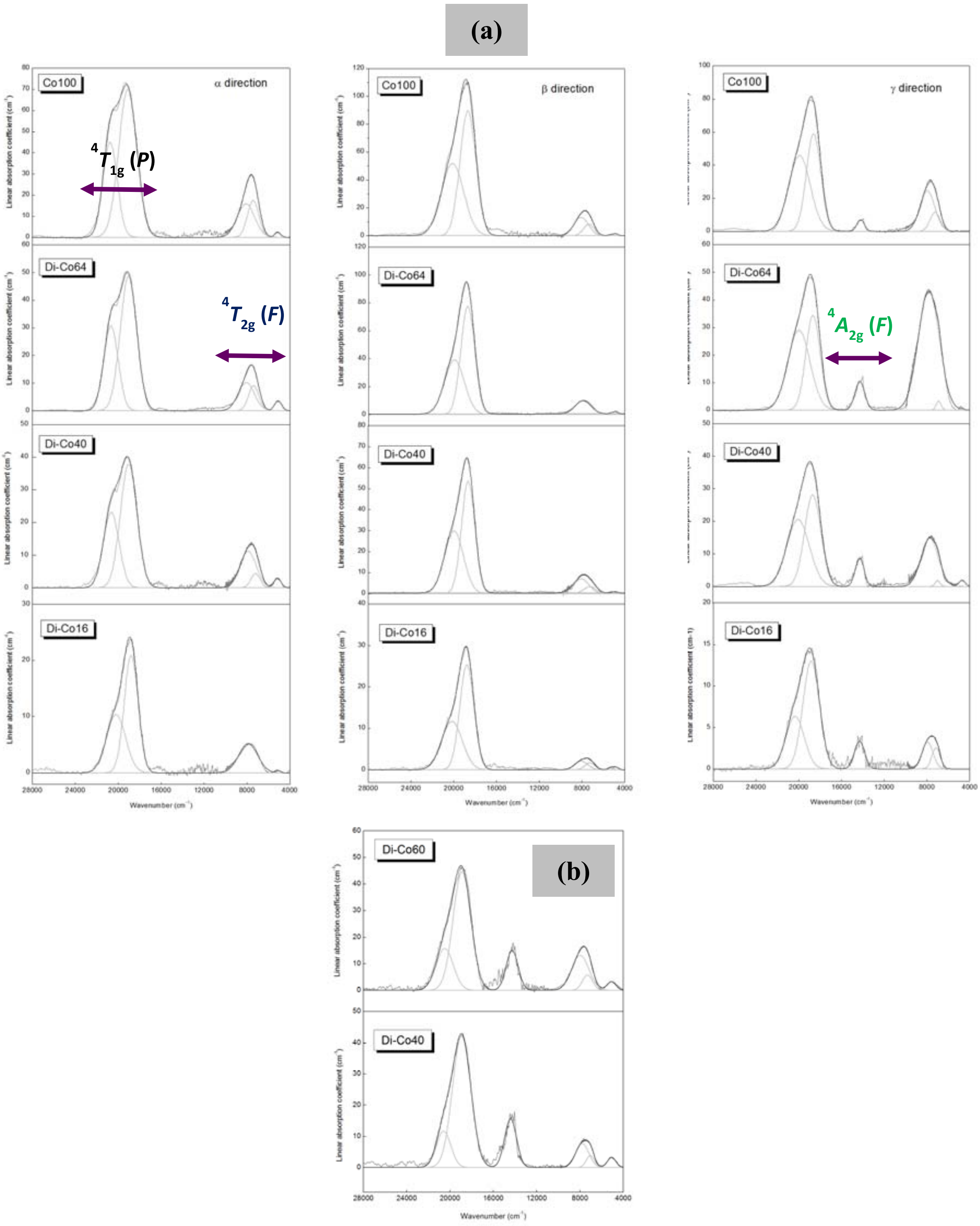

Figure 6.12. (**a**) Deconvolution of the α, β and γ polarized OAS and NIR spectra for flux(A)-grown samples in the 28000-4000 cm^{-1} (357-2500 nm) spectral range, after baseline subtraction; (**b**) deconvolution of the OAS and NIR spectra measured along p_2 direction for two of the melt-grown samples (Di-Co40 and Di-Co60) for the 28000-4000 cm^{-1} (357-2500 nm) spectral range. These spectra are represented between 28000-4000 cm^{-1} and not in the spectral range really measured (*i.e.* 30000-2000 cm^{-1}, 333-5000 nm) because of the lack of absorption bands at lower frequencies. (4000-2000 cm^{-1}, 2500-5000 nm) and at frequencies higher than 28000 cm^{-1} (357 nm).

It is evident from the fitted spectra, that the frequencies of the observed main bands caused by electronic transitions in octahedrally coordinated Co^{2+}, display only slight variations with increasing cobalt concentration, while the relative band intensities strongly increase with increasing cobalt content at the *M1* site [Figures 6.13(a-b) and 6.14(a-b)].

The position of the most intense bands [$^4T_{1g}$ (*P*)**]**, which correspond to the spin allowed *d-d* transition in Co^{2+} in an octahedral ligand field, is located within the green-yellow region of the visible spectrum (Figures 6.13a and 6.14a). Synthetic crystals [melt and flux(A)] thus appears in the complementary pink colour. In Table 6.10A-E (6.10A-D for flux(A)-grown and 6.10E for melt-grown), the weighted mean frequency for each of the two split absorption bands in the visible spectrum is reported, for convenience, as 18800 and 20300 cm^{-1} (532 and 493 nm), since is almost constant within the entire solid solution range. In the same table are also summarized linear absorption coefficients, band widths and integrated absorption coefficients for each recorded and fitted absorption band within the visible spectrum, associated to each sample. The peak positions of the absorption bands are summarized in Tables 6.11A and 6.11B.

TABLE 6.10(**A-D**). Frequencies, linear absorption coefficients, band widths and integrated absorption coefficients (along the three indicatrix directions) for recorded and fitted absorption bands within the visible spectrum. Data are referred to the flux(A)-grown series. *Notes:* Estimated relative uncertainties for linear absorption coefficients, band widths and integrated absorption coefficients values are 1%.

A Di-Co16	Frequencies (cm^{-1})	Linear absorption coefficient (cm^{-1})	Band widths (cm^{-1})	Integrated absorption coefficient (cm^{-2})	Band widths ratio
along α	18800	29	1450	31682	0.72
	20300	14	2019	21994	
along β	18800	36	1503	41060	0.74
	20300	16	2037	24384	
along γ	18800	17	1653	21454	0.96
	20300	8	1728	10934	

TABLE 6.10(**A-D**). Frequencies, linear absorption coefficients, band widths and integrated absorption coefficients (along the three indicatrix directions) for recorded and fitted absorption bands within the visible spectrum. Data are referred to the flux(A)-grown series. *Notes:* Estimated relative uncertainties for linear absorption coefficients, band widths and integrated absorption coefficients values are 1%.

B Di-Co40	Frequencies (cm^{-1})	Linear absorption coefficient (cm^{-1})	Band widths (cm^{-1})	Integrated absorption coefficient (cm^{-2})	Band widths ratio
along α	18800	52	1752	68954	1.10
	20300	31	1595	37811	
along β	18800	72	1435	77371	0.67
	20300	42	2154	68680	
along γ	18800	39	1608	46748	0.71
	20300	28	2250	47805	

C Di-Co64	Frequencies (cm^{-1})	Linear absorption coefficient (cm^{-1})	Band widths (cm^{-1})	Integrated absorption coefficient (cm^{-2})	Band widths ratio
along α	18800	68	1788	91607	1.11
	20300	44	1605	53216	
along β	18800	88	1531	124972	0.68
	20300	57	2265	97011	
along γ	18800	49	1589	58713	0.67
	20300	39	2372	70193	

D Co100	Frequencies (cm^{-1})	Linear absorption coefficient (cm^{-1})	Band widths (cm^{-1})	Integrated absorption coefficient (cm^{-2})	Band widths ratio
along α	18800	97	1954	143019	1.26
	20300	64	1548	74173	
along β	18800	98	1525	112378	0.71
	20300	76	2146	122773	
along γ	18800	83	1609	100382	0.65
	20300	69	2468	128753	

TABLE 6.10**E**. Frequencies, band widths and integrated absorption coefficients (average value along p_1 and p_2 directions) for recorded and fitted absorption bands within the visible spectrum. Data are referred to the melt-grown series. *Notes:* Estimated relative uncertainties for linear absorption coefficients, band widths and integrated absorption coefficients values are 2%.

E	Frequencies (cm^{-1})	Band widths (cm^{-1})	Integrated absorption coefficient (cm^{-2})	Band widths ratio
Di-Co20	18800	1745	37344	1.77
	20300	987	11319	
Di-Co40	18800	1359	94802	1.06
	20300	1285	33204	
Di-Co50	18800	1285	70366	0.88
	20300	1454	52742	
Di-Co60	18800	1243	67222	0.72
	20300	1738	73474	
Di-Co80	18800	1678	231034	1.21
	20300	2027	195381	

(a)

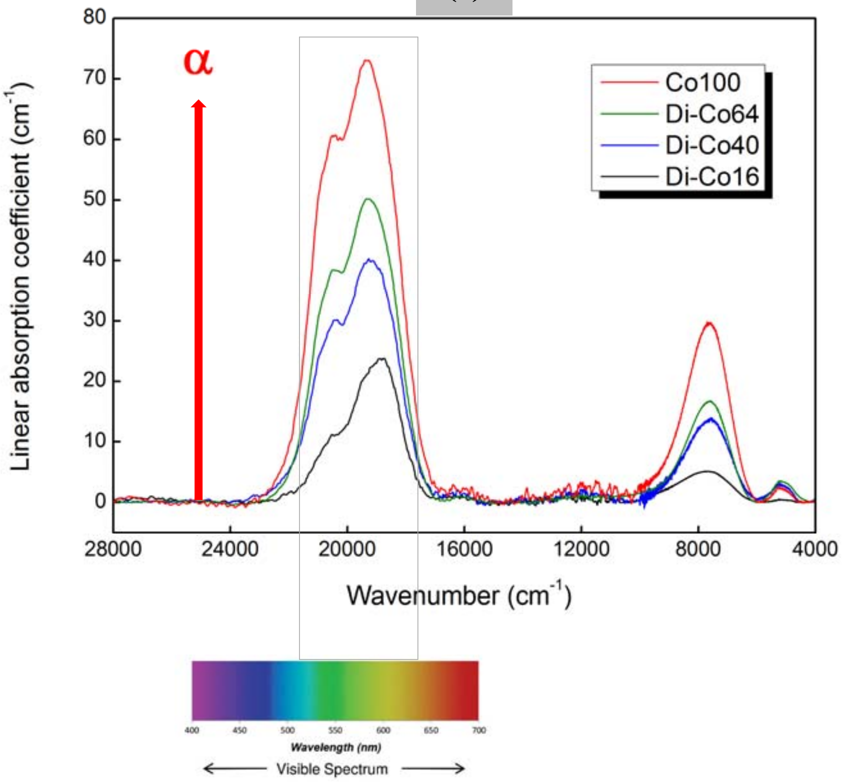

Figure 6.13. (**a**) The position of the most intense bands [$^4T_{1g}$ (P)] located within the green-yellow region of the visible spectrum for the flux(A)-grown series, in the spectrum measured along α, β and γ directions (β and γ in the next page). The band intensity increases along the flux(A)-grown series, from Di-Co16(bottom) to Co100 (top), as it is represented by the red arrow.

(a)

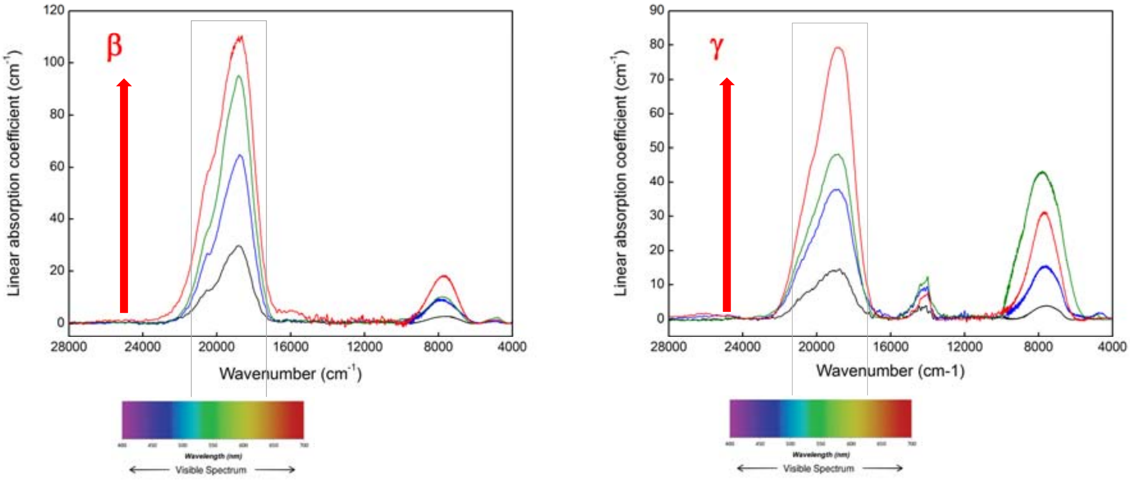

Figure 6.13. (**a**) The position of the most intense bands [$^4T_{1g}$ (P)] located within the green-yellow region of the visible spectrum for the flux(A)-grown series. The band intensity increases along the flux(A)-grown series, from Di-Co16(bottom) to Co100 (top), as it is represented by the red arrow.

(b)

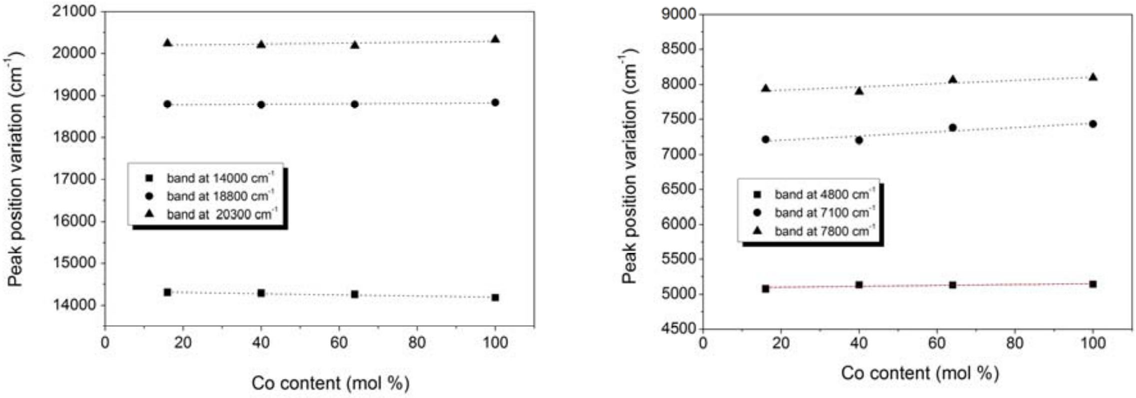

Figure 6.13. (**b**) Variations in frequency (cm^{-1}) with changing cobalt concentration in the 28000-4000 cm^{-1} (357-2500 nm) spectral range, for the flux(A)-grown samples. The absorption bands in the 4800-5300 cm^{-1} spectral range are represented with the label 'band at 4800 cm^{-1}' and the peak position values of the two bands, are averaged in the calculation.

(a)

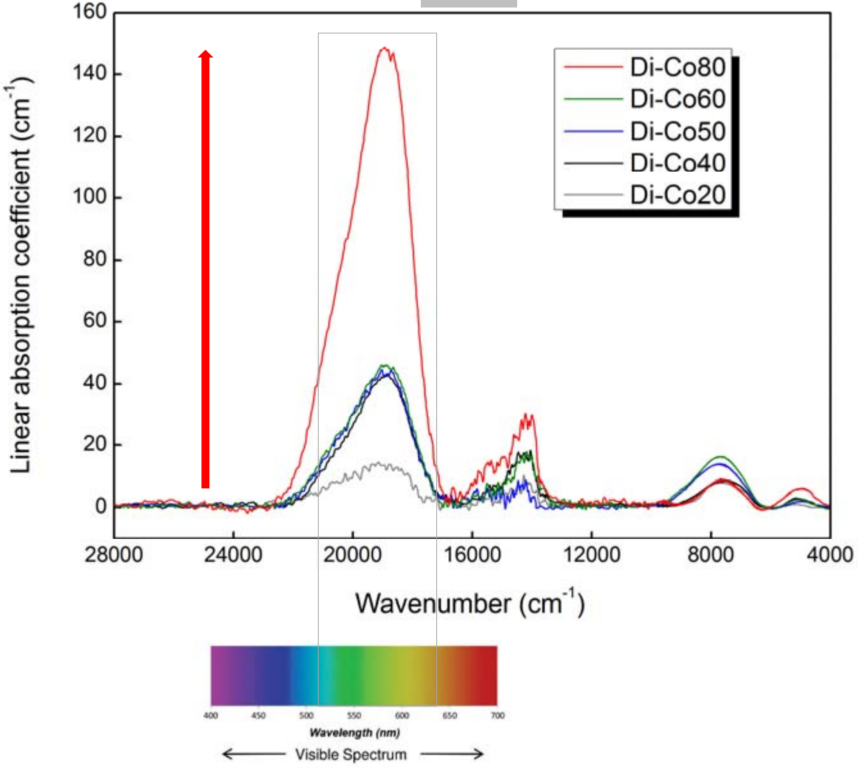

Figure 6.14. (**a**) The position of the most intense bands [$^4T_{1g}$ (P)] located within the green-yellow region of the visible spectrum for the melt-grown samples. The band intensity increases along the melt-grown series, from Di-Co20 (bottom) to Di-Co80 (top), as it is represented by the red arrow.

(b)

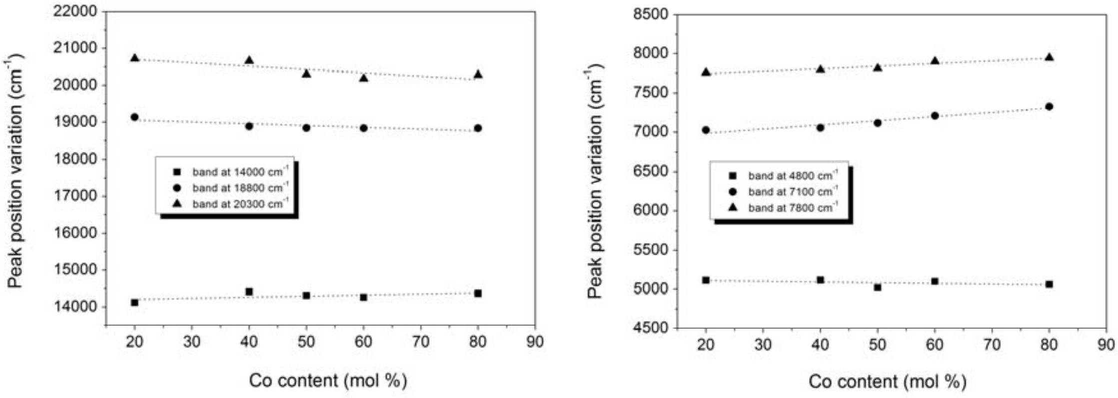

Figure 6.14. (**b**) Variations in frequency (cm^{-1}) with changing cobalt concentration in the 28000-4000 cm^{-1} (357-2500 nm) spectral range, for the melt-grown samples. The absorption bands in the 4800-5300 cm^{-1} spectral range are represented with the label 'band at 4800 cm^{-1}' and the peak position values of the two bands, are averaged in the calculation.

Considering the mean value along the three optical directions of the band width ratio for each flux(A)-sample, it is evident that it remains almost constant along the series, while for melt-grown series it shows irregular variations. The mean value along the three optical directions of the integrated absorption coefficient associated to the bands at 18800 and 20300 cm^{-1}, regularly increases with increasing cobalt content, in flux(A)-grown pyroxenes, less regularly in melt-grown ones (Tables 6.10A-D and 6.10E).

The linear absorption coefficient was calculated after that all spectra were normalized to the thickness of each analyzed single-crystal and considering the integrated absorption coefficient and the band width measured in each optical directions (α, β and γ) and not their mean value. Nevertheless the subtraction of the baseline from the spectrum and the peak fitting procedure contribute to the uncertainty of calculation of the linear absorption coefficients. In Figure 6.15(a-c) the linear absorption coefficient within the visible spectrum, is shown as a function of cobalt content in the pyroxene structure and along the three directions for the flux(A)-grown samples: the trend is linear and regular as expected, and Co100 sample exhibits the higher linear absorption coefficient value. As it is shown in Figure 6.15b, the higher linear absorption coefficients for each sample were measured along the β direction. The increase of the linear absorption coefficent within the visible spectrum, together with the greater differences in brightness (Chapter 6.4, paragraph 6.4.1) with increasing cobalt content along the series, explain the intensified hues of the flux(A)-crystals within the solid solution.

TABLE 6.11**A**. Band frequencies (average value along p_1 and p_2 directions) in cm^{-1} and assignments for cobalt-melt-grown pyroxene series.

$CaCo_xMg_{1-x}Si_2O_6$					Assignment
x= 0.20	x= 0.40	x= 0.50	x= 0.60	x= 0.80	
5110(2)	5120(10)	5020(2)	5100(3)	5060(4)	$T_{1g} \rightarrow T_{2g}$ (F)
7020(3)	7050(3)	7120(4)	7200(7)	7320(12)	
7750(12)	7790(8)	7800(9)	7900(21)	7940(60)	
14100(37)	1441(6)	14310(56)	14260(11)	14360(15)	$T_{1g} \rightarrow A_{2g}$ (F)
19140(28)	18890(20)	18840(29)	18830(23)	18830(25)	$T_{1g} \rightarrow T_{1g}$ (P)
20722(54)	20661(50)	20300(123)	20180(84)	20280(96)	

Standard deviation in brackets.

TABLE 6.11**B**. Band frequencies (average value along along α, β and γ directions) in cm^{-1} and assignments for cobalt-flux(A)-grown pyroxene series.

$CaCo_xMg_{1-x}Si_2O_6$					Assignment
x= 0.16	x= 0.40	x= 0.64	x= 1		
4950(10)	4890(16)	4890(6)	4980(4)	β	$T_{1g} \rightarrow T_{2g}$ (F)
5340(22)	5424(20)	5310(10)	5310(10)	β > α > γ	
7210(10)	7070(24)	7200(6)	7300(14)	γ > α > β	
7980(18)	7830(19)	7970(19)	8030(30)	α > γ > β	
14310(10)	14290(5)	14260(6)	14190(7)	γ	$T_{1g} \rightarrow A_{2g}$ (F)
18800(20)	18790(10)	18800(10)	18790(9)	β > α > γ	$T_{1g} \rightarrow T_{1g}$ (P)
20240(54)	20200(35)	20200(37)	20290(25)	β > α > γ	

Notes: frequencies data for Co100 fitted bands along α and γ directions are taken from one crystal, while those along β, from another crystal of the same composition. Standard deviation in brackets.

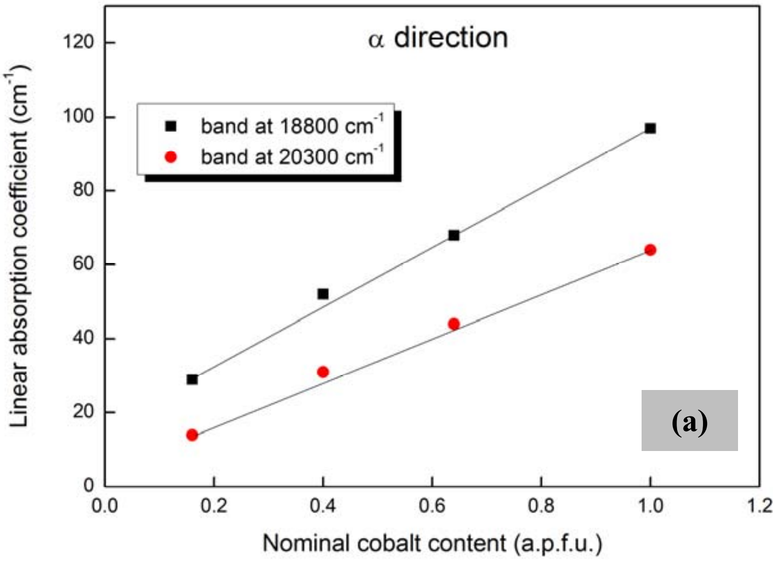

Figure 6.15. Linear absorption coefficient along (**a**) α, (**b**) β and (**c**) γ (β and γ in the next page) for the recorded and fitted absorption band at 18800 and 20300 cm^{-1} frequencies, as a function of the cobalt concentration in the flux(A)-grown pyroxene series.

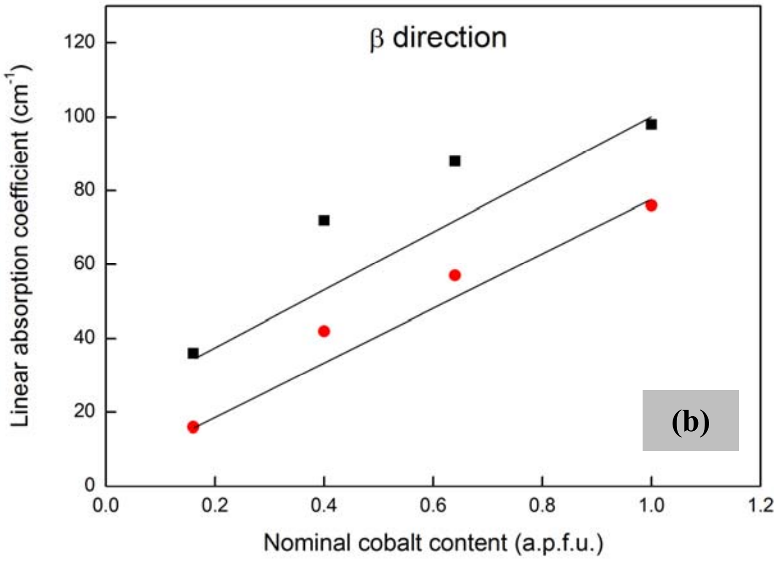

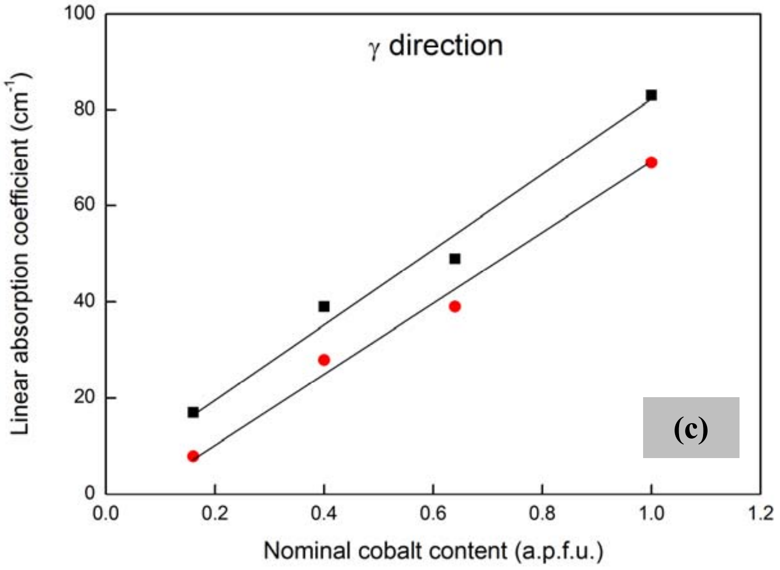

Figure 6.15. Linear absorption coefficient along (**b**) β and (**c**) γ for the recorded and fitted absorption band at 18800 and 20300 cm^{-1} frequencies, as a function of the cobalt concentration in the flux(A)-grown pyroxene series.

6.3.2. Flux(B)-grown samples: band assignments and their interpretation

Polarized, room-temperature optical absorption spectra recorded and analyzed for the flux(B)-grown samples are shown in Figure 6.16(a-b). All UV-VIS spectra are dominated by two bands that occur in the range 18800-20200 cm^{-1} (532-493 nm) and are assigned to the split spin-allowed *d-d* transition $^4T_{1g}$ $(F)\rightarrow{}^4T_{1g}$ (P) of Co^{2+} in an octahedral ligand field, according to literature data (White *et al.*, 1971; Burns 1993; Llusar *et al.*, 2001, Taran and Rossmann, 2001; Dondi *et al.*, 2014). The two strong bands at ~14000 cm^{-1} (714 nm), which are seen only in γ polarization, and the weak band at about 16800 cm^{-1} (595 nm; absent in Di-Co74 and Co100 samples), are usually assigned as the $^4T_{1g}$ $(F)\rightarrow{}^4A_{2g}$ (F) transition of Co^{2+} (Percival and Salje, 1989; Wildner and Langer, 1994). The latter is singly generated and display no splitting, while the splitting at 14000 cm^{-1} is assumed to be an effect of the Co^{2+} at the *M2* site, as it was not observed in flux(A)- and melt-grown spectra where absorption bands are caused solely by Co^{2+} in the *M1* site. The presence of Co^{2+} in the *M2* site was confirmed by chemical analysis (paragraph 6.1).

At higher wavenumber we have a background much higher than in flux(A)- and melt-samples, and a broad band occurs in the range 23500-25000 cm^{-1} (425-400 nm). This band and the higher background are interpreted as originated from cobalt ions other than $^{VI}Co^{2+}$. The peak position and band shape correspond to that of the low energy spin-allowed transition $^1A_{1g}\rightarrow{}^1T_{1g}$ of $^{VI}Co^{3+}$ ion (Taran and Rossmann, 2001). The O-Co^{3+} LMCT (ligand-to-metal charge-transfer) intensifies the UV-absorption edge in spectra of the flux(B)-grown samples and this is one cause of the colour change inducing a brownish tone that swamps the pink colour caused by transitions in *M1*Co^{2+}.

Polarized, room-temperature spectra in the near infrared (NIR) region, are dominated by the four (three in α polarization) bands at about 4800-5300 and 7100-8000 cm^{-1} (2080-1920 nm and 4080-1250 nm, respectively) that are assigned to the transition $^4T_{1g}$ (F) $\rightarrow{}^4T_{2g}$ (F) in Co^{2+} in the *M1* site (White *et al.*, 1971). The Gaussian curve fitting of the polarized UV-VIS-NIR absorption spectra of two representative pyroxene crystals with composition Di-Co40 and Co100, respectively, are plotted in Figure 6.17. The peak positions of the absorption bands as determined from peak-fitting are summarized in Table 6.12.

TABLE 6.12. Band frequencies (average value along along α, β and γ directions) in cm^{-1} and assignments for cobalt-flux(B)-grown pyroxene series. Since the band at 16800 cm^{-1} (595 nm) is absent in Di-Co74 and Co100 samples, is not reported in the Table. The first three transitions are related to *M1*Co^{2+} while the last one, at ca. 23500 cm^{-1}, is the Co^{3+} related band.

$CaCo_xMg_{1-x}Si_2O_6$				Assignment
$x = 0.21$	$x = 0.40$	$x = 0.74$	$x = 1$	
4860(4)	4850(4)	4890(7)	4840(6)	$T_{1g} \rightarrow T_{2g}$ (F)
5300(6)	5130(5)	5260(9)	5210(10)	
7070(4)	7070(4)	7150(5)	7200(7)	
7860(16)	7860(11)	7900(19)	7960(37)	
14160(13)	14170(8)	14020(75)	14120(5)	$T_{1g} \rightarrow A_{2g}$ (F)
14520(55)	14480(23)	14250(4)	14460(13)	
18840(34)	18860(11)	18740(17)	18750(11)	$T_{1g} \rightarrow T_{1g}$ (P)
20000(112)	20140(82)	19910(43)	20150(37)	
23630(17)	23780(10)	24010(20)	24280(18)	${}^1A_{1g} \rightarrow {}^1T_{1g}$

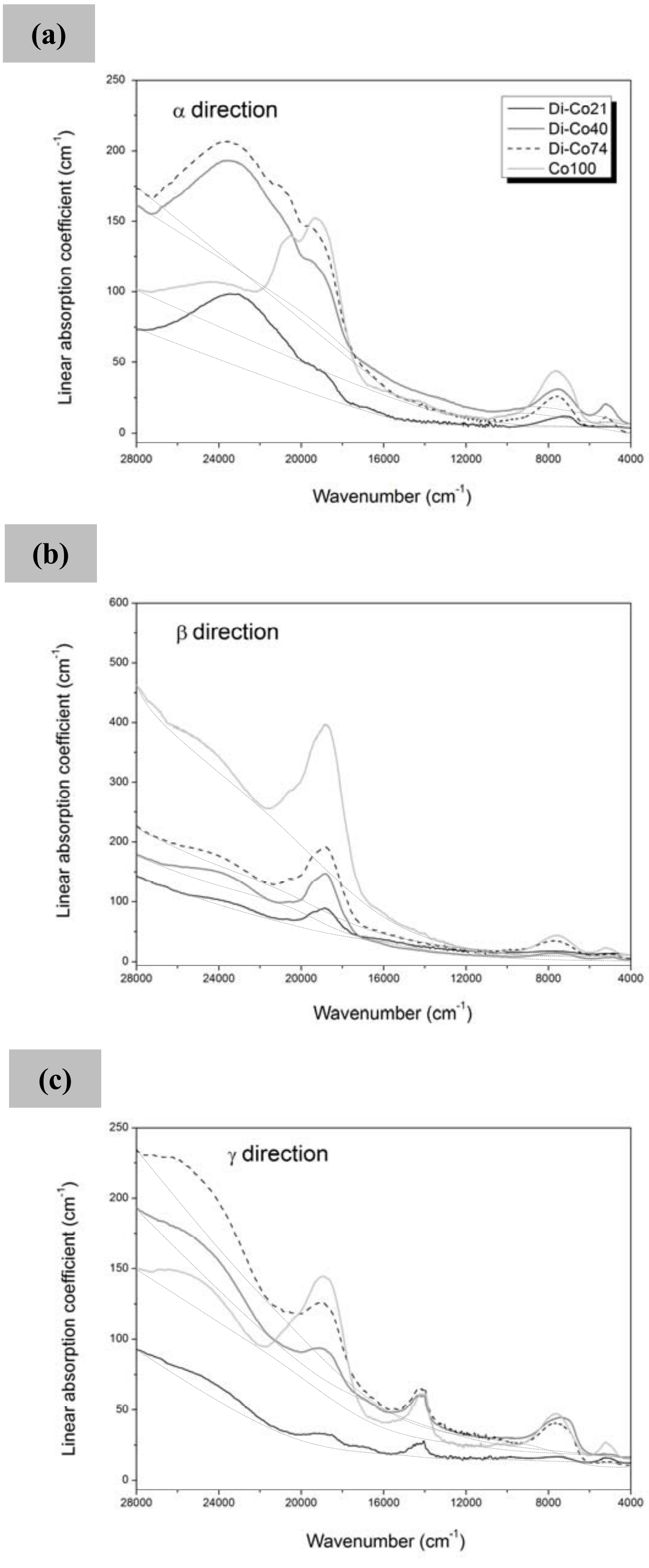

Figure 6.16. Polarized optical absorption spectra of flux(B)-grown samples, from Di-Co21 (bottom) to Co100 (top), in the 28000-4000 cm^{-1} (357-2500 nm) spectral range, along the three optical indicatrix directions (**a**) α, (**b**) β and (**c**) γ. The thin dotted lines represent the polynomial curve fitting used to obtain the baseline subtraction from each spectrum. These spectra are represented between 28000-4000 cm^{-1} and not in the spectral range really measured (*i.e.* 30000-2000 cm^{-1}, 333-5000 nm) because of the lack of absorption bands at lower frequencies. (4000-2000 cm^{-1}, 2500-5000 nm) and at frequencies higher than 28000 cm^{-1} (357 nm).

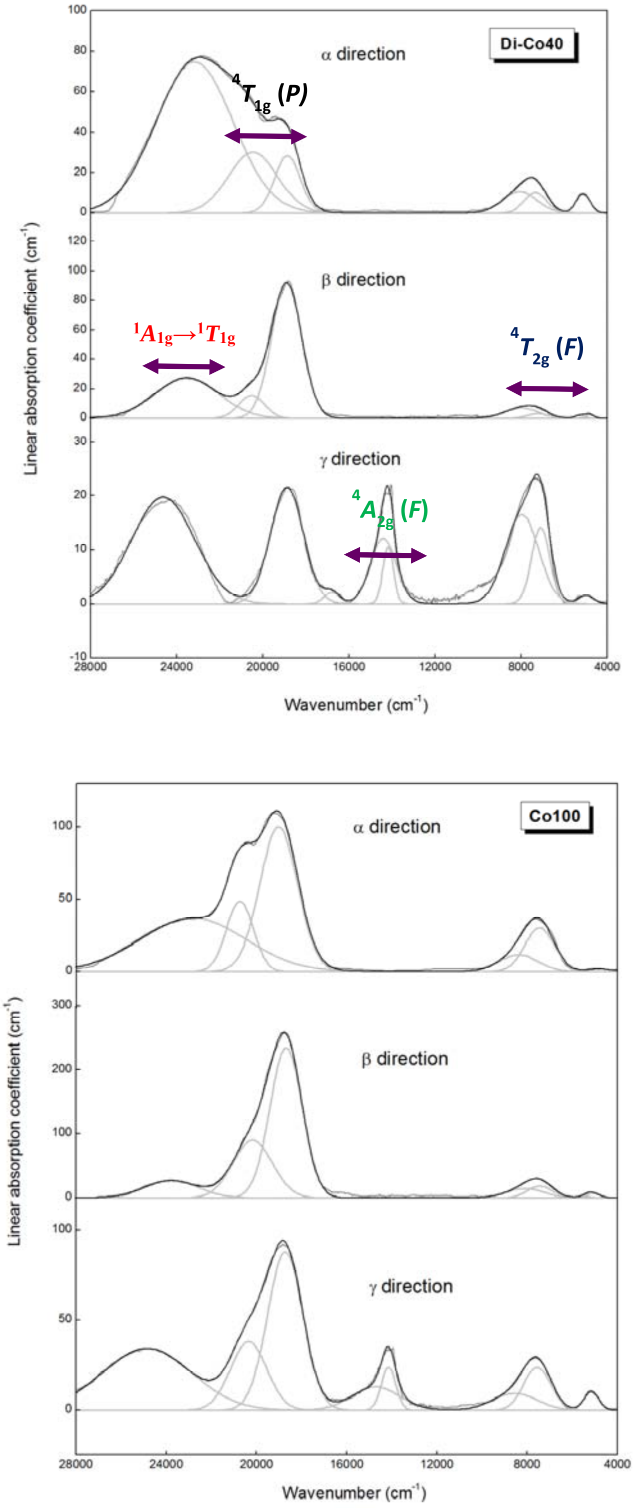

Figure 6.17. Deconvolution of the α, β and γ polarized OAS and NIR spectra for two of the flux(B)-grown samples in the 28000-4000 cm^{-1} (357-2500 nm) spectral range (above Di-Co40, below Co100), after baseline subtraction. These spectra are represented between 28000-4000 cm^{-1} and not in the spectral range really measured (*i.e.* 30000-2000 cm^{-1}, 333-5000 nm) because of the lack of absorption bands at lower frequencies. (4000-2000 cm^{-1}, 2500-5000 nm) and at frequencies higher than 28000 cm^{-1} (357 nm).

6.3.3. Crystal field strength and *Racah B* parameters

The peak assignments and the best fits of the energies of the spin-allowed *d-d* transitions for the octahedral coordinated Co^{2+} ion, led to the determination of both the crystal field strength *Dq* and inter-electronic repulsion *Racah B* parameters (Tables 6.13A and 6.13B). They were calculated by means of the Tanabe-Sugano diagram for d^7 electronic configurations, following the procedure outlined in paragraph 5.2.5.

Uncertainties in the calculation of *Dq*-values for Co^{2+} at *M1* are probably relatively large as the parameter is based on the difference in energy between two relatively broad absorption bands (*i.e.* at 7000 and 14000 cm^{-1}) and the energies of these bands are based on deconvolution that has resulted in variable widths for the two respective bands. Uncertainties in the calculated *Racah B*-parameter is probably even higher considering that it is based on calculations involving energies of three different fitted bands (*i.e.* at 7000, 14000 and 19000 cm^{-1}). However, we compared our results with those reported in White *et al.* (1971). In Figure 6.18, the peak positions for the cobalt-pyroxene ($CaCoSi_2O_6$) taken from White *et al.* (1971) and for a crystal with the same composition ($CaCoSi_2O_6$), belonging to the flux(A)-grown series, are plotted in a Tanabe-Sugano diagram. There is a slight difference in the peak positions in the two studies, which both fit rather well within the positions predicted by the diagram. To note, the two peaks at lower frequencies are shown separately in the diagram, but were averaged in the calculation of the *Racah* and *Dq* parameters, while the two peaks at higher frequencies were merged to an average position in the diagram. The difference between our sample and White *et al.* (1971) is mostly in the positions the $^4T_{1g}$ (F)$\rightarrow$$^4A_{2g}$ (F) electronic transition, that is at ca. 15000 cm^{-1} in White *et al.* (1971) and at 14000 cm^{-1} in this work. The calculated *Racah B* parameters for $CaCoSi_2O_6$ (Co100) are however very close to those reported in White *et al.* (1971).

By plotting the *Racah* and *Dq* parameters as a function of the Co content at the *M1* site, it is notable that, in either 'Di-Co' melt and flux-grown series, a similar trend is found (Figure 6.19). In both series the parameters increase their value, *i.e.* increase the repulsion energy with surrounding oxygens, with decreasing Co content, up to Di-Co40. Instead the two samples with the lowest Co content [Di-Co20 and Di-Co16 for the melt and flux(A)-grown series, respectively], deviate from the value expected from the linear trend observed in pyroxenes with higher Co content. The melt-grown pyroxenes shows higher *Racah B* and *Dq* values than the flux(A)-pyroxene series; it is not clear whether this is significant. Despite uncertainties in the calculations of *Dq* and *B*, we give higher reliability to the flux(A)-pyroxene series, where crystals were oriented and, therefore, measured in different orientations with the uncertainty in determining the exact peak positions, smaller than in the melt-grown series (see Tables 6.11A and 6.11B), where the calculated variation in *Dq* can not be regarded as significant (*i.e.* the variation is smaller than the expected error).

TABLE 6.13A. Crystal field parameters for Co^{2+} melt-grown pyroxene series (average value along the two perpendicular directions, p_1 and p_2). The average *M1*-O bond lengths are obtained after crystal structural refinement.

Compound	*Dq* (cm^{-1})	*B* (cm^{-1})	<*M1*-O> (Å)
$CaCo_{0.20}Mg_{0.80}Si_2O_6$	787	1020	2.085
$CaCo_{0.40}Mg_{0.60}Si_2O_6$	814	1025	2.090
$CaCo_{0.50}Mg_{0.50}Si_2O_6$	808	1011	2.091
$CaCo_{0.60}Mg_{0.40}Si_2O_6$	794	986	2.093
$CaCo_{0.80}Mg_{0.20}Si_2O_6$	802	992	-

Notes: X-ray single-crystal analysis have not been performed on Di-Co80 sample because it is constituted by not well-formed single crystals.

TABLE 6.13B Crystal field parameters for Co^{2+} flux(A)-grown pyroxene series (average value along α, β and γ directions). The average *M1*-O bond lengths are obtained after crystal structural refinement.

Compound	*Dq* (cm^{-1})	*B* (cm^{-1})	<*M1*-O> (Å)
$CaCo_{0.16}Mg_{0.84}Si_2O_6$	794	981	2.082
$CaCo_{0.40}Mg_{0.60}Si_2O_6$	798	991	2.090
$CaCo_{0.64}Mg_{0.36}Si_2O_6$	792	981	2.095
$CaCo_1Si_2O_6$	778	969	2.102

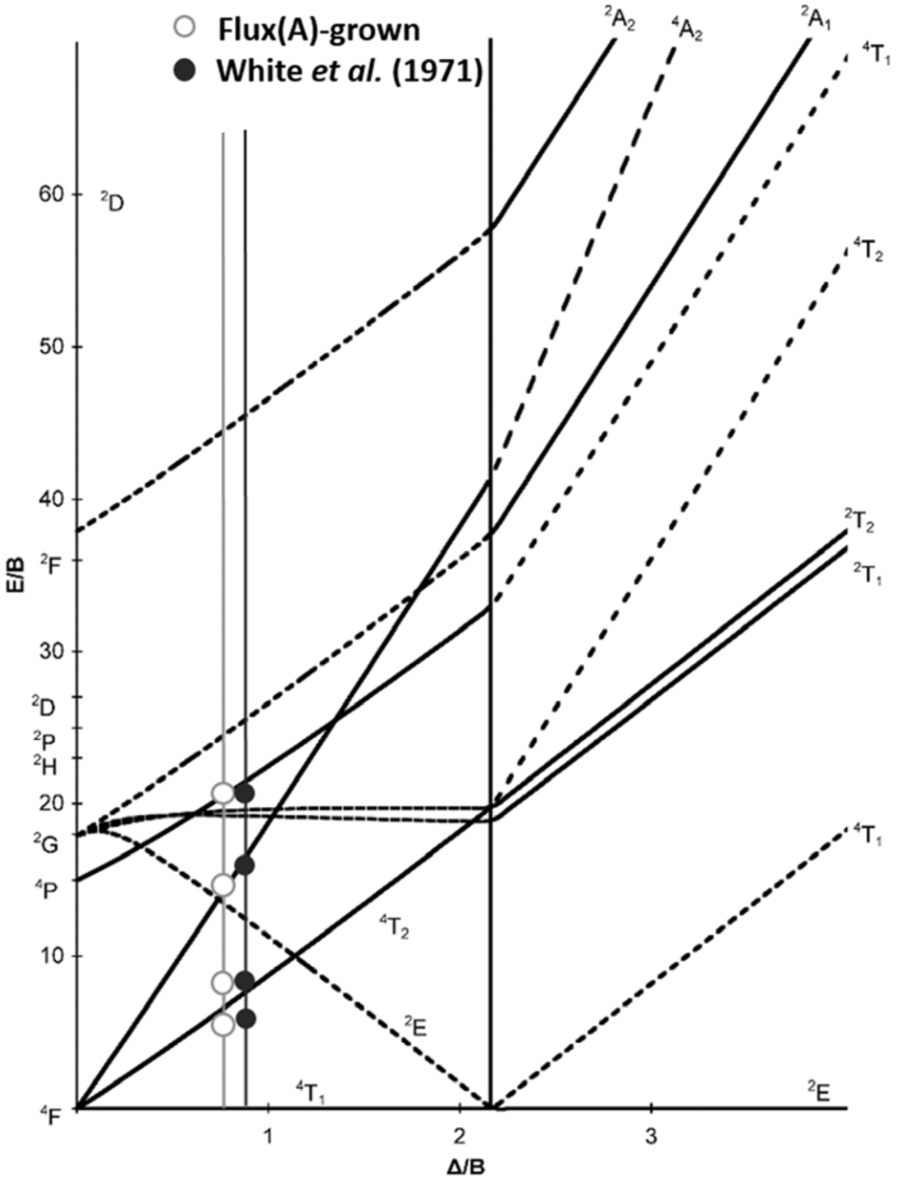

Figure 6.18. Energy level diagram for Co^{2+} in an octahedral field. *Dq* and *Racah B* parameters used in calculation are: *Dq*= 877 cm^{-1} and *B*= 971 cm^{-1} for the sample studied by White *et al.* (1971) and *Dq*= 778 cm^{-1} and *B*= 969 cm^{-1} for the sample studied in this thesis. Band frequencies for spin-allowed related to the literature data are shown by filled circles, while those of flux(A)-grown sample, by open circles. The x-axis is in terms of the crystal field splitting parameter, *Dq*, or Δ_{oct}, scaled by the *Racah B* Parameter. The y-axis is in terms of energy of a electronic transition, E, scaled by *B* (Chapter 5, paragraph 5.2.5.).

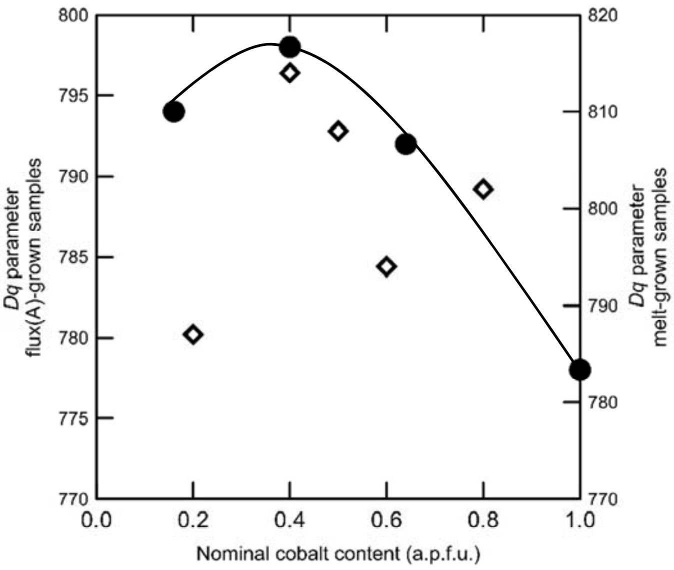

Figure 6.19. *Dq* as a function of nominal cobalt content at the *M1* site. Melt-grown pyroxenes are represented by open diamonds, while flux-grown ones by filled black circles.

The crystal field splitting energy (*Dq*) is related to the shift of the main optical bands of a transition metal ion in polyhedra, and therefore to the length of a metal-oxygen bond, which varies along the solid solution (Langer 2001, Langer *et al.*, 2004, Taran *et al.*, 2004; Hålenius *et al.*, 2010). The relation between *Dq* and bond distance has been used to achieve the local metal-oxygen distances (<Co-O> local) in the 'Di-Co' series (Ardit et *al.*, 2012).

As a rule, the crystal field parameters increase when the bond distances with oxygen atoms decrease. This is expected also in our Co pyroxenes, which show a decrease in the average bond distance, measured by single crystal X-ray diffraction, for the substitution of Co with the smaller Mg in the *M1* site. The crystal field parameters measure a decrease in bond distances related only to the local Co configurations, whereas the X-ray diffraction measure the bond lengths coming from an average of the local bond distances for Mg and for Co. The average X-ray diffraction structure may come from an average of local configurations, where each of the substituting cations has a specific environment, or from a ‘true’ structure, where the oxygen positions are the same independently from the cation occupying the *M1* polyhedron.

The local bond distances were calculated in the flux(A)-pyroxenes and compared with the average bond lengths (<*M1*-O>). Following the procedure discussed in Ardit *et al.* (2012), the <Co-O> local distances along the series were calculated by means of the crystal field parameter *Dq* (Table 6.14). For the flux(A)-grown samples they are quite similar to the average <*M1*-O> distances obtained from XRD data, in samples with nominal Co content of 0.40 and 0.64 a.p.f.u. (Figure 6.20). On the contrary the sample with lower Co content (0.16 a.p.f.u.) shows a significantly higher <Co-O> local distance than the average *M1*-O distance. It is not clear whether this difference is significant: the sample with lower Co content shows a spectrum with lower intensity and peak/background ratio (Figure 6.10); moreover, as it is shown in Table 6.11B, the error in determining the exact peak positions, obtained after the baseline subtraction and the peak fitting, is higher than in the other samples in the flux(A)-grown series. Although yet to be confirmed, the suggestion is that, at least in the samples with the higher cobalt content in flux(A)-grown series, the differences between local and average structure seem to be small.

For the melt-grown samples is not possible to give information about the local structure because of large uncertainty in the band deconvolution analysis of the absorption spectra (see Table 6.11A), as we have already mentioned.

TABLE 6.14. Local metal-oxygen bond lengths along the ‘Di-Co’ (flux-grown) pyroxene series.

Flux-grown	**<Co-O> local**	**<*M1*-O>**
0.16	2.093	2.082
0.40	2.091	2.090
0 .64	2.094	2.095
1.00	2.102	2.102

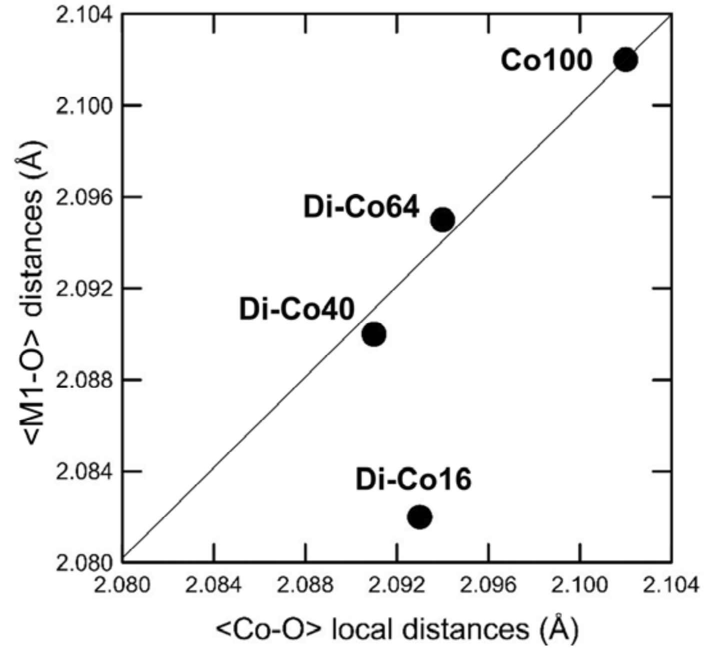

Figure 6.20. <Co-O> local distances *vs.* the observed <*M1*-O> distances.

6.4. Colorimetric and technological behaviour

6.4.1. Melt and flux(A)-grown samples: colour analysis

Colorimetric analyses were performed on the pigments obtained after syntheses: on powders for the melt-grown, and on single crystals for the flux(A) ones. The colour coordinates are shown in Tables 6.15A and 6.15B, together with the images of the 'as-synthesized' pigments. In all cases, regardless the amount of cobalt employed for the syntheses, the pyroxene pigments have shown a more or less intense pink colour.

As mentioned in the previous paragraph (6.3), the pink colour is due to the absorption within the green-yellow region of the visible spectra.

The best compromise between cobalt concentration and optical response was searched by comparing colorimetric parameters (CIE *a** and *b**) of 'Di-Co as-synthesized' pigment with those of cobalt pyroxene (Co-pyroxene) and of the industrial pigments, like cobalt silicate (Co-olivine; Llusar *et al.*, 2001) and cobalt aluminate (Co-spinel; Llusar *et al.*, 2001). To remind, Co-spinel exhibits a blue colour, due to the cobalt ion in tetrahedral coordination (Figure 6.21).

In the case of melt-grown Co-based pigment with $x\sim$ 0.20 Co a.p.f.u., the colour coodinates are similar to those exhibited by the Co-pyroxene pigment ($x=$ 1.00 Co a.p.f.u.), synthesized by Mantovani *et al.*, 2015. The Co content in $CaCo_{0.20}Mg_{0.8}Si_2O_6$ is lower (5 wt%) compared with 23% in $CaCoSi_2O_6$ (Co-px). To remind, in Co-olivine and Co-spinel the cobalt content in the structure, is 55 and 33 wt %, respectively. As the cobalt content increases, *b** and *a** shift to more positive values in both melt and flux-grown series. The colour coordinate CIE *L**, which defines the brightness, increases with decreasing cobalt content along both melt and flux-grown series (Figure 6.22). Melt-samples 'as-synthesized' pigments with 10-12 wt% of cobalt give a brightness CIE *L** ~62) similar to that of Co-pyroxene and Co-spinel (64 and 61 respectively). Pigments synthesized from flux, have shown always a lower brightness than the other Co-based pigments. This is apparent, comparing $CaCoSi_2O_6$ ($x=$ 1.0 a.p.f.u.) synthesized by flux, with Co-pyroxene, synthesized (Figure 6.22) by means of solid state method (Mantovani *et al.*, 2015).

According to the X-ray diffraction analysis the $CaCo_xMg_{1-x}Si_2O_6$ pyroxene is present as a single cobalt-bearing phase in both samples obtained by melt and flux. Moreover, careful observation at the optical microscope did not reveal overlooked flakes of glass. The differences in the *a** and *b** components are instead due to the different background and absorption peak intensities for the melt- and flux(A)-grown samples, whereas the absorption and positions of the peaks in the visible range, *i.e.* those at 20300 and 18800 cm^{-1} (493 and 532 nm, respectively), are quite similar in the two series (Chapter 6, paragraph 6.3). Therefore the different colorimetric response (CIE *L* a* b**) between the two series can be possibly explained considering the crystal-size: finely-ground powder for melt-samples, single crystals sized up to 1 mm for the flux ones.

TABLE 6.15. Colorimetric data (colour coordinates) of (**A**) melt-grown and (**B**) flux(A)-grown samples 'as-synthesized pigments'. Colour coordinates for $CaCoSi_2O_6$, Co_2SiO_4 and $CoAl_2O_4$ are taken from Mantovani *et al.*, 2015.

A As-synthesized sample		Di-Co20	Di-Co40	Di-Co60	Di-Co80	$CaCoSi_2O_6$	Co_2SiO_4	$CoAl_2O_4$
		🟪	🟪	🟪	🟪	🟪	🟪	🟦
	*L**	71.4	62.5	61.5	54.7	64.0	57.0	61.0
	*a**	22.4	29.5	27.9	23.2	26.0	19.0	9.0
	*b**	-14.7	-19.7	-16.8	-6.4	-9.0	-20.0	-30.2

B As-synthesized sample		Di-Co16	Di-Co40	Di-Co64	Co100
		🟪	🟪	🟪	🟪
	*L**	48.6	43.6	36.6	35.3
	*a**	33.4	31.4	27.6	24.0
	*b**	-5.6	-3.3	-2.7	-3.0

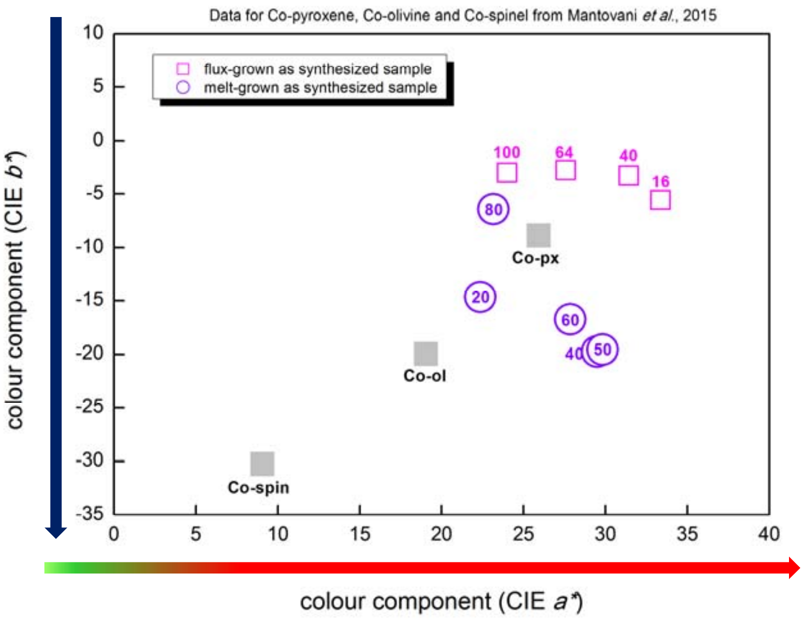

Figure 6.21. Colour components (CIE *a** *vs*. CIE *b**) for pyroxenes of the $Ca(Co_xMg_{1-x})Si_2O_6$ melt-(purple open circles) and flux(A)-grown (magenta open squares) series, 'as synthesized' pigments. For comparision the colour component for pure Co-pyroxene, Co-olivine and Co-spinel (Co-reference pigments, grey filled squares) are reported. [Data of Co-pyroxene, Co-olivine and Co-spinel from Mantovani *et al.*, 2015]. *Notes*: the numbers close to the symbols are to be intended as Di-Co20, Di-Co16,…etc. Colour coordinates *a** and *b** as reported in Tables 6.15A and 6.15B.

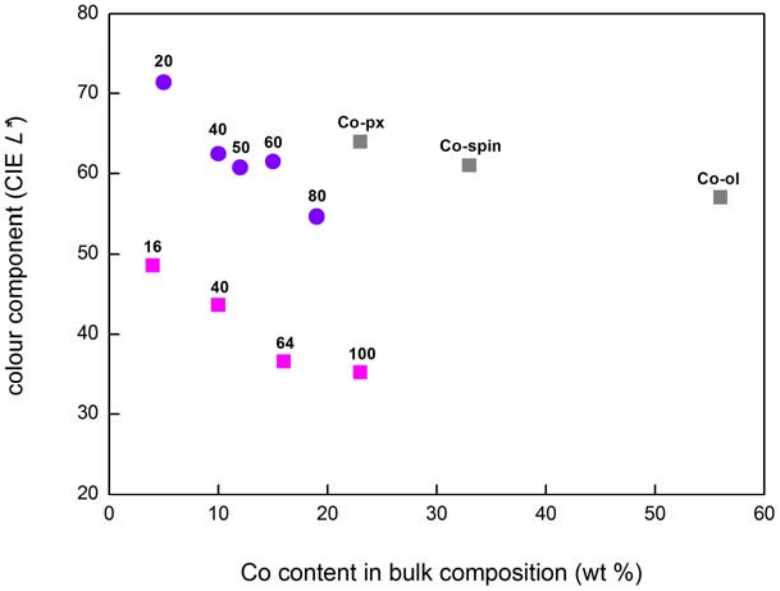

Figure 6.22. Colour component (CIE *L**) for pyroxenes of the $Ca(Co_xMg_{1-x})Si_2O_6$ melt-(purple filled circles) and flux(A)-grown (magenta filled squares) series, 'as synthesized' pigments. For comparision the colour component for pure Co-pyroxene, Co-olivine and Co-spinel (Co-reference pigments, grey filled squares) are reported. [References as in Figure 6.21]. *Notes*: the numbers close to the symbols are to be intended as Di-Co20, Di-Co16,…etc. Colour coordinate *L** as reported in Tables 6.15A and 6.15B.

6.4.2. Technological tests: colour analysis

Further colorimetric analyses were performed on the S1, S3 and F4 tests containing Co-based pigments (in powder form) after annealing at different temperatures (Chapter 5, paragraph 5.2.7). The colour coordinates are shown in Tables 6.16A and 6.16B, together with the images of the Co-pigment-bearing glazes and frits.

In Figure 6.23, colorimetric parameters (CIE *a** and *b**) of Co melt-grown samples ‘as-synthesized’ pigments and of glazes containing Co-based pigments are plotted together with those of Co-pyroxene, Co-olivine and Co-spinel pigments and of the glazes obtained using the Co-bearing phases as pigments.

TABLE 6.16. (**A**) Colorimetric data (colour coordinates) of the glazes obtained with melt-grown powdered pyroxenes of the reported composition after heating at 1200 °C for S1 and at 1100 °C for S3, together with those of the reference pigments that are Co-olivine, Co-spinel and Co-pyroxene. **(B**) Colorimetric data (colour coordinates) of the frits obtained using flux(A)-pigments (frit F4).

A		Di-Co20	Di-Co40	Di-Co60	Di-Co80	$CaCoSi_2O_6$	Co_2SiO_4	$CoAl_2O_4$
Glazes								
S1	*L**	47.2	41.1	37.8	31.5	32.8	27.9	39.4
	*a**	8.2	10.6	11.7	9.5	7.8	10.7	9.5
	*b**	-24.9	-27.8	-28.9	-22.5	-21.4	-22.6	-29.8
							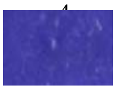	
S3	*L**	71.0	66.5	60.6	52.1	53.6	46.6	62.2
	*a**	3.9	4.7	5.6	6.6	5.0	8.8	3.9
	*b**	-19.2	-22.0	-24.6	-26.7	-23.7	-30.6	-25.3

B		Di-Co16	Di-Co40	Di-Co64	Co100
Frits					
F4	*L**	75.2	66.6	65.8	61.8
	*a**	10.1	13.7	16.6	17.3
	*b**	-9.7	-17.4	-17.6	-20.1

In the case of Co-spinel, the colour coordinates are similar for the pigment powder and the glazes (Figure 6.23; Mantovani *et al.*, 2015). This can be explained because, either if the pigment does not react with the glaze, or if it reacts releasing Co in the glass, we have that Co is in tetrahedral coordination, both in spinel and in the glassy matrix (Mantovani *et al.*, 2015; Dondi *et al.*, 2013).

In contrast, for Co-olivine, Co-pyroxene and melt-grown Co-pyroxenes, CIE *a** and *b** values in glazes are very different from the pigment powders: they become close, but not equal, to those of glazes coloured by spinel. It can be explained by the diffusion of cobalt into the glassy matrix of the glazes after the ceramic treatments (Salem *et al.*, 2011; Ozel *et al.*, 2010; Dondi and Eppler, 2014).

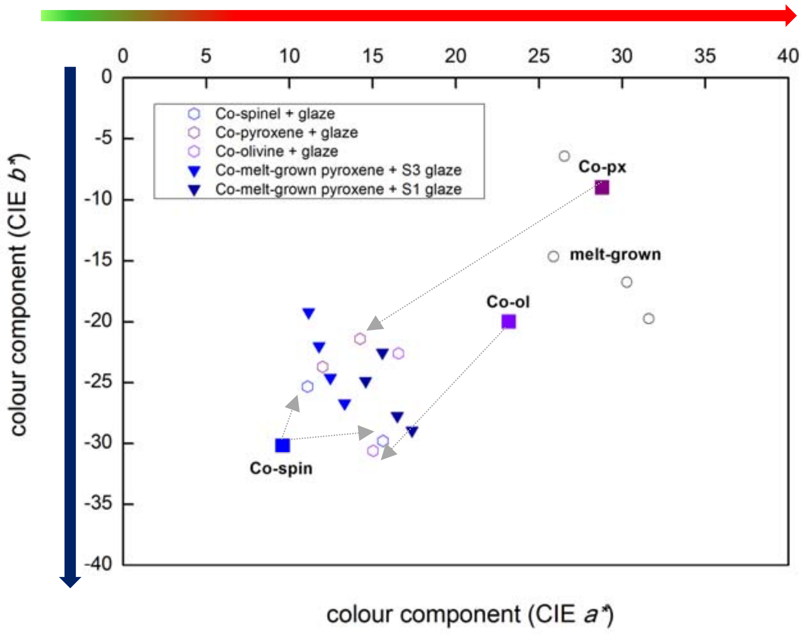

Figure 6.23. Colour plot of S1 and S3 glazes containing the Co-based reference pigments (Co-pyroxene, Co-olivine and Co-spinel) and our Co-based pigments. The sqaure symbols represent the colour coordinates of Co-px, Co-ol and Co-spin 'as-synthesized pigments', while the open black circles the Co-melt-grown samples 'as- synthesized pigments'. [References as in Figure 6.21]. Experimental conditions as reported in Chapter 5, paragraph 5.2.7. Colour coordinates as reported in Table 6.16A.

In Figures 6.24 and 6.25 the colorimetric parameters (CIE *L*a* b**) of the S1 and S3 glazes containing Co melt-grown pigments, of the F4 frits containing Co flux(A)-grown pigments, and of the S1 and S3 glazes containing the Co-based reference pigments, are shown. Even if a low fraction of cobalt goes into the glass in tetrahedral coordination, this is however sufficient to impart the blue colour, due to the much higher colouring power of Co in tetrahedral than in octahedral coordination (Dondi and Eppler, 2014). Therefore, in all tests, the S1 and S3 glazes containing our pigments, have shown a deep blue colour, like the Co-spinel based reference pigments (Llusar *et al.*, 2001). A blue coloration is obtained also for a cobalt concentration $x = 0.20$ a.p.f.u. ($b^* \sim -20$ for S1 and $b^* \sim -15$ for S3). Colorimetric analyses revealed that there is a strong correlation between the amount of cobalt in the glaze and the obtained hue: as Co increases, the b^* shifts to more negative values. This can be explained assuming that, after ceramic treatments, regardless of firing temperature and time, a chemical attack by the molten glaze occurs (Ozel and Turan, 2003; Mestre *et al.*, 2013; Dondi *et al.*, 2013), leading to the gradual leaching of Co^{2+} ion from the pyroxene crystal. This imparts a blue coloration due to the Co^{2+} in tetrahedral coordination into the glassy matrix (Salem *et al.*, 2011; Ozel *et al.*, 2010; Nelson and White, 1986; Hunault *et al.*, 2016; Keppler and Bagdassarov, 1999).

To verify and confirm the hypothesis of a chemical attack by the molten glaze, SEM–EDS analyses were performed on few chips of the S1, S3 and S5 glazes, embedded in epoxy and polished. The analytical results are discussed in the following paragraph.

Regarding colorimetric analyses performed on the F4 frits, as the amount of cobalt in the frit increases, CIE a^* value shift toward positive values, while b^* parameter is similar to that observed in S1 and S3 glazes containing Co-melt grown pigments. The only exception is in the frit containing Co-based pigment with $x \sim 0.16$ Co a.p.f.u., where b^* shifts toward values less negative than the other pigments and it can be associated with a lighter blue hue, closest to the violet.

The colour coordinate CIE L^*, increases with decreasing cobalt content in the Co-pyroxene pigments (Figure 6.25) tested both in the glazes and frits (S1, S3 and F4), and reaches the highest values for the S3 and F4 tests with $x \leq 0.2$ Co a.p.f.u. These values are much higher than those for Co-based reference pigments.

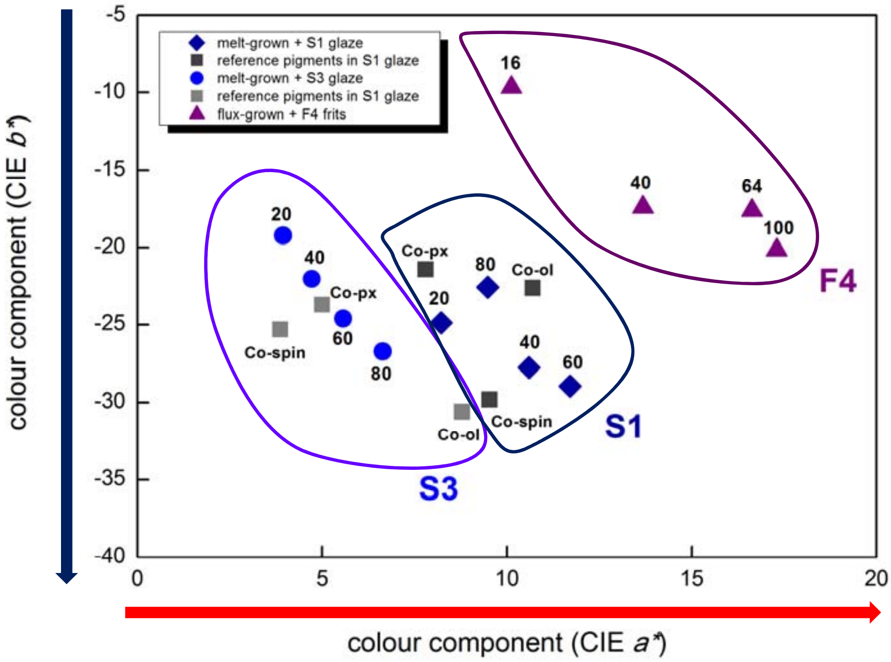

Figure 6.24. Colour plot (CIE *a** *vs*. CIE *b**) for S1 (dark-blue filled diamonds), S3 (blue filled circles) glazes containing the Co melt-grown pigments and F4 (purple filled triangles) frits containing the Co flux(A)-grown pigments. The data of S1 and S3 containing the Co-reference pigments (Co-pyroxene, Co-olivine and Co-spinel) are represented by grey and dark-grey filled squares, respectively. [References for Cobalt-based reference pigments as in Figure 6.21. Experimental conditions as reported in Chapter 5, paragraph 5.2.7. Colour coordinates *a** and *b** as reported in Tables 6.16A and 6.16B.

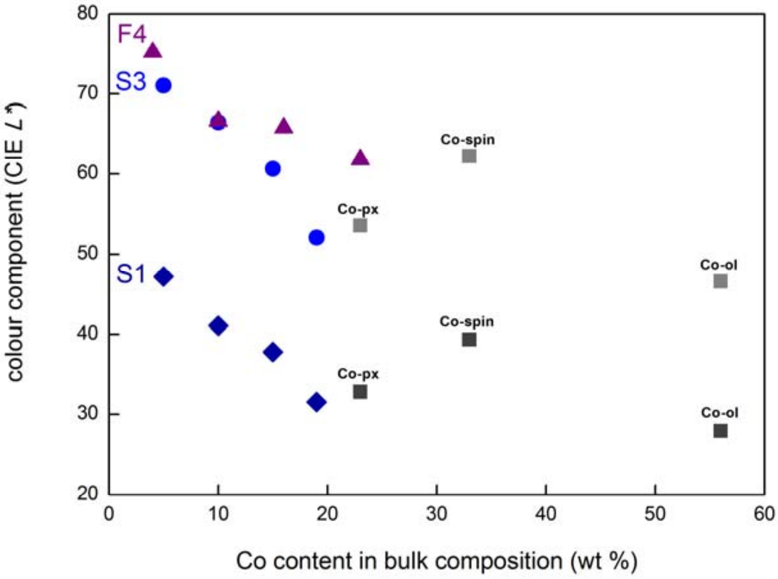

Figure 6.25. Colour component (CIE *L**) for S1 (dark-blue filled diamonds), S3 (blue filled circles) glazes and F4 (purple filled triangles) frits. For comparison data of S1 and S3 containing the Co-reference pigments (Co-pyroxene, Co-olivine and Co-spinel) are represented [References as in Figure 6.21; symbols as in Figure 6.24]. Experimental conditions as reported in Chapter 5, paragraph 5.2.7. Colour coordinate *L** as reported in Tables 6.16A and 6.16B.

6.4.3. Technological tests: SEM-EDS analysis

Technological tests were performed to assess the colour rendering and stability of the pigments based on the $CaCo_xMg_{1-x}Si_2O_6$ pyroxene structure, after annealing.

As mentioned in paragraph 5.2.7, several tests have been done, by using different industrial glaze compositions, and varying temperature ranges and times of firing:

1) a first series of test was carried out by using pigment crystals not previously pulverized dispersed in the S3 and S5 glassy matrices, and annealed at T= 1100 °C for 1 and 10 minutes (Figure 6.26a);
2) a second series was performed by using pulverized crystals dispersed in the S1 and S3 glassy matrices and annealed at T= 1200 °C and 1100 °C respectively (Figure 6.26b).
3) a last series of test was done by using pulverized crystals added to the F4 frit and annealed at 700 °C, as reported in Figure 6.27.

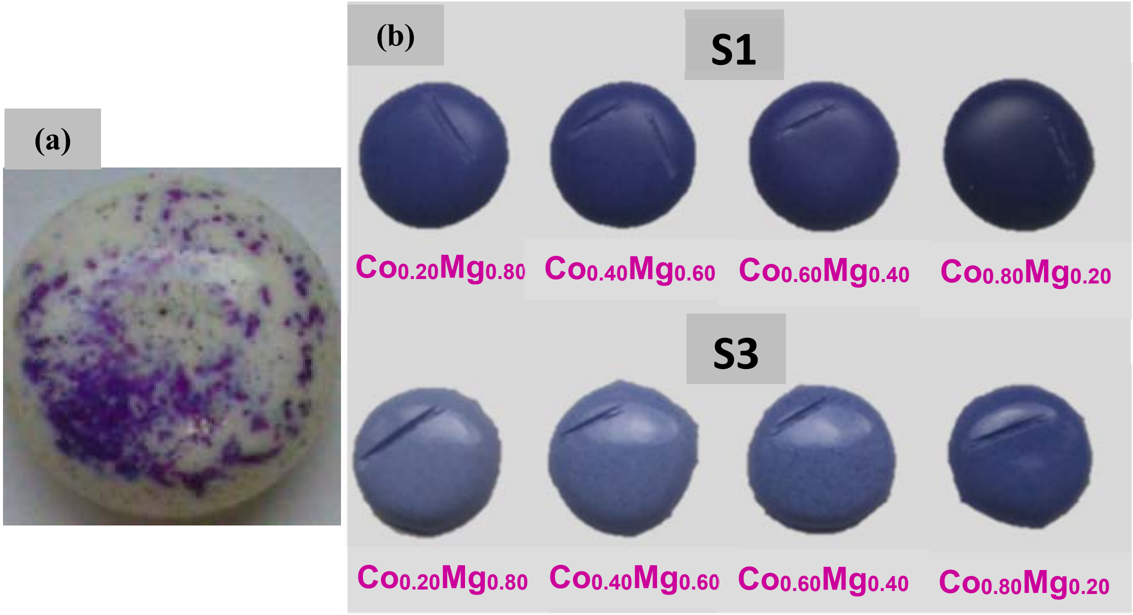

Figure 6.26. (**a**) an example of the S5 glaze containing single crystals of melt-grown Co-based pigments, after firing; (**b**) S1 (above) and S3 (below) glazes containing pulverized melt-grown Co-based pigments, after the heat treatments.

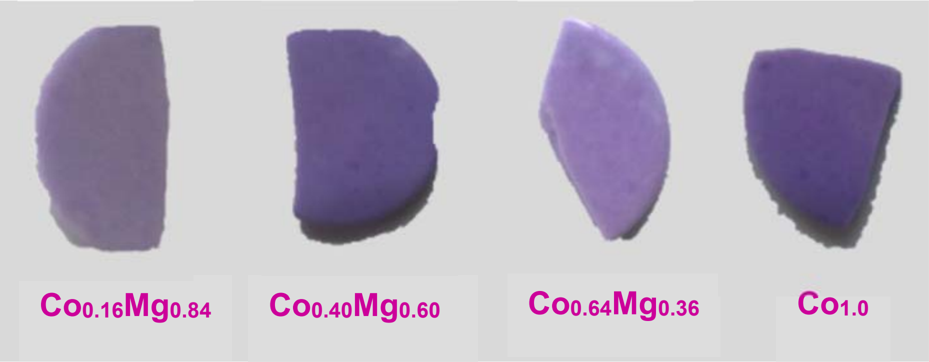

Figure 6.27. F4 frits containing pulverized flux(A)-grown Co-based pigments, after the heat treatments.

After the tests on the non-powdered pigments a white glaze with dispersed pink crystals, surrounded by a bluish rim were invariably found, indicating that the pigment was not homogeneous and uniformly dispersed within the glaze (Figure 6.26a). Both frits and glazes (second and third test runs) gave homogeneous samples, blue or dark blue for the glazes, pinkish or pink-blue for the frits (Figures 6.26b and 6.27).

SEM-EDS analyses were then performed on the first two tests, but not on the frits. S3 and S5 containing pigment crystals, and S1 and S3 containing pigment powders, were analyzed to confirm the hypotheses of the chemical attack and the pigment dissolution in the liquid phase at high temperatures (Ozel and Turan, 2003; Mestre *et al.*, 2013; Dondi *et al.*, 2013).

In the S3 and S5 analyses on non-powdered crystals, after heat treatments, the crystal size of the pigment decreases from 400-500 μm to 100-200 μm (Figures 6.28 and 6.29). Comparing the two runs at 1 minute (Figure 6.28) and 10 minutes (Figure 6.29), *i.e.* test 1, the grain size and the phase abundance of Co-pyroxene is the same. Even in the shorter runs (1 minute) the dissolution of the smallest Co-doped crystals occurs (Figure 6.28): the diffusion of cobalt into the glaze is evident and confirmed by the Figures 6.28b and 6.29c which show a concentration profile of Co across crystal and glass, after the heat treatments. A nearly stoichiometric $CaCo_{0.6}Mg_{0.4}Si_2O_6$ is formed and the cobalt amount into the glassy matrix is between 1 and 1.5 %, in both runs (1 min. and 10 mins.). The chemical attack by the molten glaze is revealed also by the reaction rims and rounded corners formed between the largest crystals and glazes in which the crystals are dispersed.

As expected, the cobalt content is high in the pyroxene crystal and drops in few microns to lower, but significant, values in the matrix. At the interface a compositional zoning is hardly visible, and the observed intermediate compositional values at the interface may be an average of glass and Co-pyroxenes phases, due to the analytical space resolution of about 2 µm. This indicates a sharp compositional interface and a fast rate of dissolution and reaction of the crystals in contact with the glassy phase of the molten glaze.

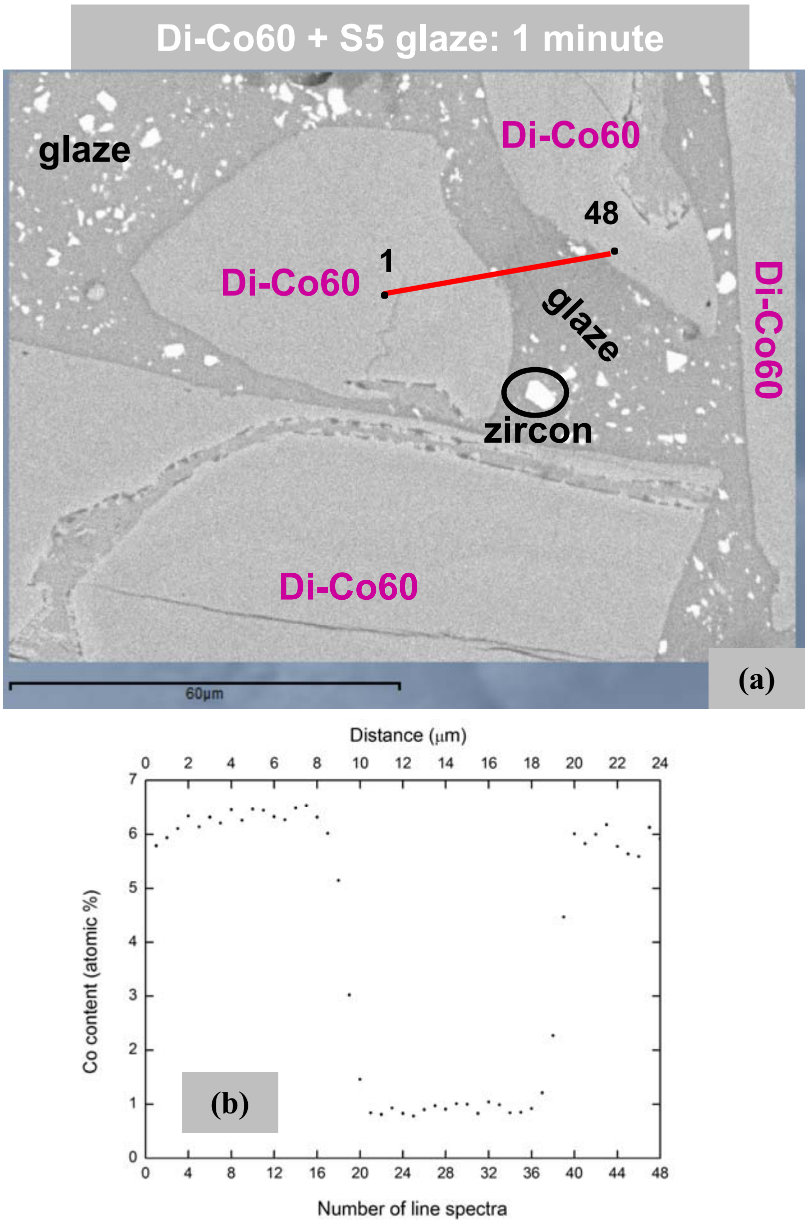

Figure 6.28. (**a**) SEM-EDS back-scattered image of the S5 glaze containing Co-based pigment crystals (melt-grown) of composition Di-Co60 and annealed at 1100 °C for 1 minute, *i.e.* belonging to the first series of tests (**b**) profile of the Co content across crystals and glazes (in red in Figure 6.28a), 48 analyses.

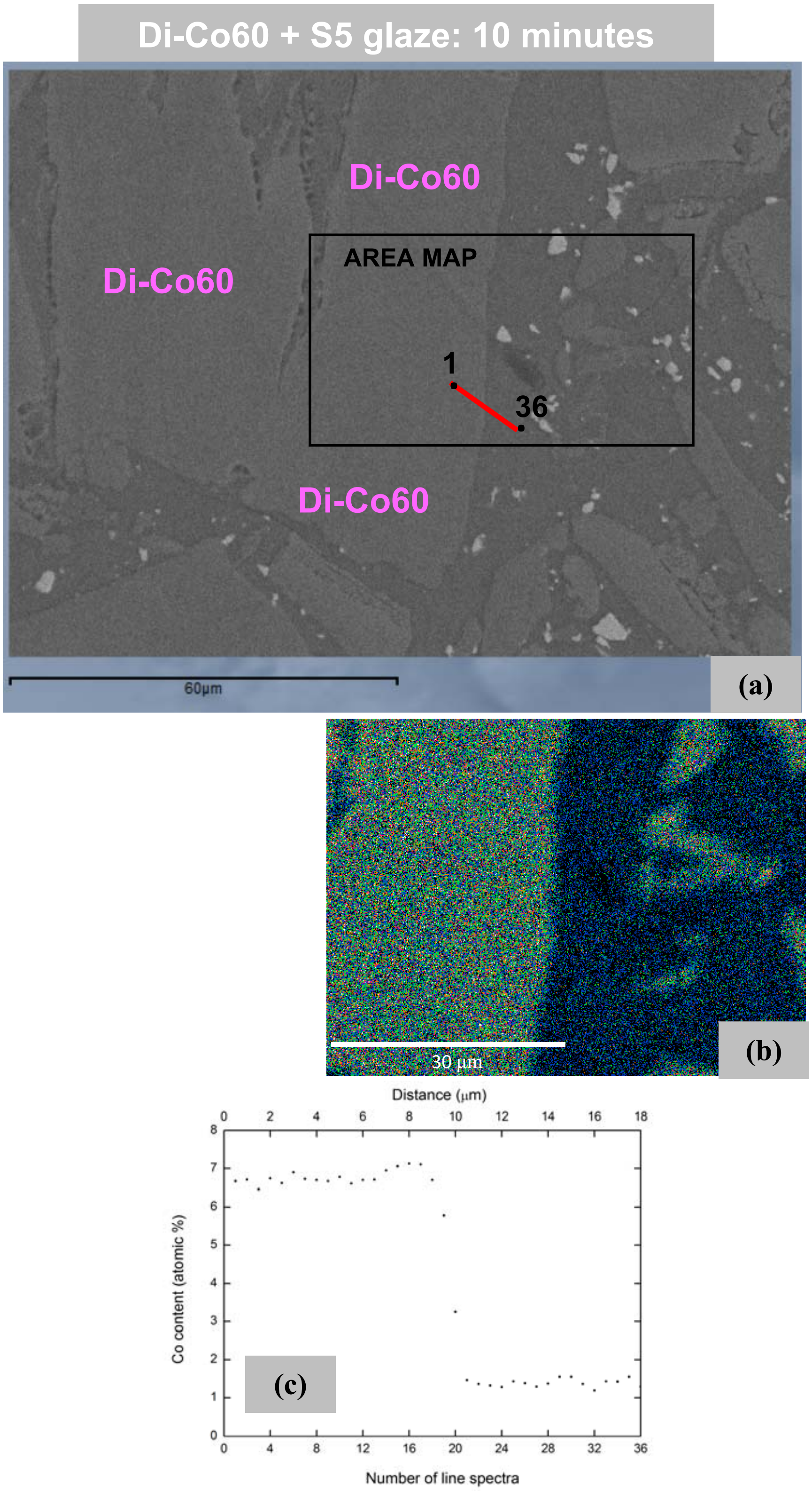

Figure 6.29. (**a**) SEM-EDS back-scattered image of the S5 glaze containing Co-based pigment crystals (melt-grown) of composition Di-Co60 and annealed at 1100 °C for 10 minutes; (**b**) SEM image with EDS mapping for cobalt; (**c**) cobalt content (atomic %) along the profile in red in Figure 6.29a (36 analyses) .

In Figure 6.30(a-b), the SEM images of the S1 and S3 glazes (test 2) containing the melt-grown Co-doped pigments are reported. Comparing the S1 and S3 glazes, which were heated at different temperatures (1200 °C and 1100 °C, respectively), the pyroxene is always present after any annealing. SEM-EDS analyses have shown that the chemical attack by the molten glaze occurred in both glazes, though the crystals in the S1, seem to be ‘quenched’ and embedded by the glassy matrix (Figure 6.30a).

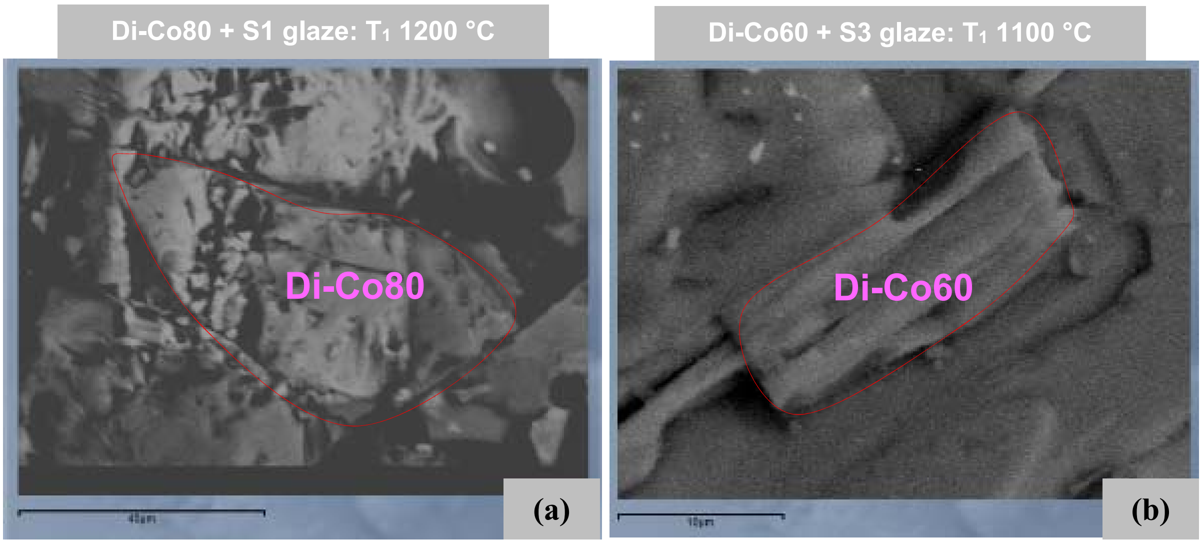

Figure 6.30. SEM-EDS back-scattered images of the S1 and S3 run products, which show the effect of the firing treatments on the crystal integrity of the Co-based pigment synthesized from melt. In (**a**) S1glaze containing Di-Co80, and annealed at T_1 1200 °C; in (**b**) S3 glaze containing Di-Co60 and annealed at T_1 1100 °C.

Although the effects of the heat treatments on the crystal integrity and appearance are different, the cobalt diffusion into the glassy matrix similarly occurs in both glazes, despite the different firing temperature. Quantitative analyses (Figure 6.31) have shown that cobalt amount in the glass is between 0 and 1 %. This suggests that the blue colour, darker in S1 glazes with respect to the S3, is not related to a higher content of Co in the glass, but possibly to a stronger reaction between the crystal and the glassy phase of the molten glaze.

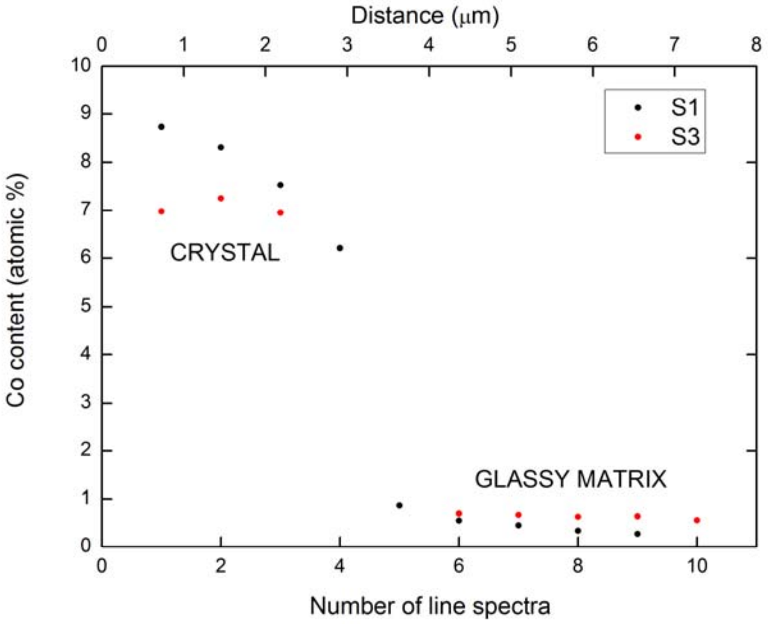

Figure 6.31. Cobalt diffusion into the glassy matrix (atomic %) after the firing at 1200 °C (S1) and 1100 °C (S3) of glazes containing powdered melt-grown samples of composition Di-Co80 and Di-Co60, respectively. S1 and S3 tests are represented with black filled and red filled circles, respectively.

6.4.4. Possible applications

The Co-based pigments synthesized along the $CaCoSi_2O_6$-$CaMgSi_2O_6$ series act as a dye, thus dissolving in part or completely in the liquid phase regardless of times and temperatures of firing, leading to the pyroxene breakdown with gradual leaching of Co^{2+} ions into the glassy matrix. A palette of blue ceramic dyes with different colour intensities can be obtained based on the cobalt-doped diopside lattice, with different cobalt contents. We have find then that our Di-Co20 melt-grown sample could be proposed as a blue pigment to minimize the Co content, while maintaining the colouring performance of the more widely used Co-spinel or Co-olivine pigments. Containing a lower amount of cobalt than conventional ceramic colorants, our pigment could significantly reduce the Co consumption, improving manufacturing cost and sustainability; a possible drawback is the relatively high temperature of synthesis, at $T \geq 1200$ °C. This advancement is particularly important today as, with the advent of the digital decoration by inkjet printing, cobalt is used practically in every ceramic tile, whatever its colour, because decoration files are arranged in quadrichromy, where both Cyan and Black are cobalt-bearing pigments and dyes. As a pink pigment also the Di-Co20 could be used, *e.g.* in painting, maintaining the pigment in a non-aggressive environment.

Chapter 7

MAGNETIC PROPERTIES OF $CaCo_xMg_{1-x}Si_2O_6$

7. MAGNETIC PROPERTIES OF $CaCo_xMg_{1-x}Si_2O_6$

Co, being a transition metal with unpaired electrons in the *d*-shell, has a magnetic moment. In each of the Co^{2+} ions in high spin state, there are three unpaired electrons, which promote a magnetic contribution to the magnetic moment of the mineral or compound. However, as generally in silicates, in pyroxenes the magnetic moments of Co and other transition metal atoms are randomly oriented at room temperature, so that the structure is paramagnetic at room conditions. At lower temperature ordering of the magnetic moments occurs. Ferro or antiferromagnetic behaviour arise whether the orientation of the spin vectors, is the same or opposite, respectively.

Complete magnetic structures in pyroxenes are only known for few end-members (Jodlauk *et al.*, 2007; Sawaoka *et al.*, 1968). A study by Durand *et al.* (1996) on $CaCoSi_2O_6$ pyroxene showed that, below the Néel temperature, the spin orientation of all the Co atoms in a given ribbon of the *M1* polyhedra, is the same but opposite to that of the adjacent *M1* ribbons. The resulting structure is therefore antiferromagnetic.

Despite the end-members were widely studied, in literature only few studies deal with the magnetic behaviour in pyroxene solid solutions (Wiedenman *et al.*, 1986; Eeckhout *et al.*, 2001).

In this chapter, we report the results of our investigations on the magnetic properties of the $CaCo_xMg_{1-x}Si_2O_6$ pyroxenes. In particular, it will be discussed how the different Co content*, i.e.* the different amount of the magnetic ion in the pyroxene crystal lattice along the series, affects the magnetic behaviour.

Magnetic measurements were performed by means of a Quantum Design MPMSXL-5 a Superconducting QUantum Interference Device (SQuID) magnetometer installed at the Department of Physics and Earth Sciences, University of Parma. The active part of this instrument is the so-called SQuID sensor, based on the superconductive Josephson effect. A general scheme of a SQuID sensor is represented in Figure 7.1.

Despite common susceptometers, SQuID is able to detect and quantify very low sample magnetization signals by means of precise measurements of variation in the magnetic flux through a highly sensitive sensor. SQuID magnetometer is able to perform different types of magnetic characterizations but, for the purpose of this thesis, only the results of magnetization measurements as a function of temperature with or without an applied magnetic field M(T) will be reported. They have been done on powdered samples from melt-synthesis of different compositions and on an oriented single crystal of $CaCoSi_2O_6$ belonging to the flux(A)-series. Small amounts of each analyzed sample were put inside the SQuID by means of probe constituted by a quartz dielectric straw, upon which the specimen is located, hold by wrapping it with a proper Teflon tape.

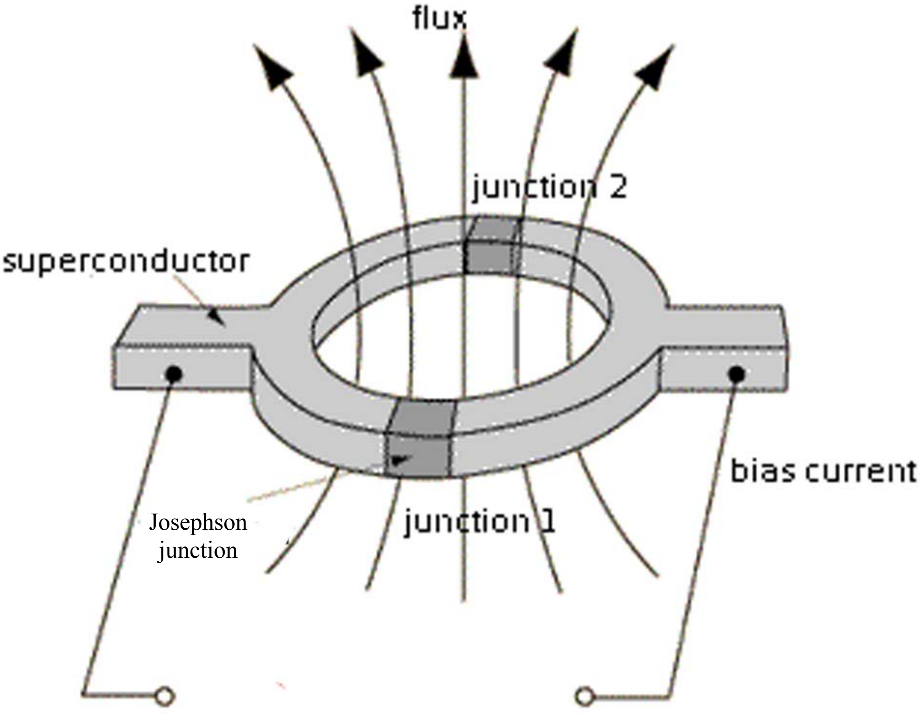

Figure 7.1. General scheme of SQuID sensor (image from inspirehep.net/record/865175).

Magnetization measurements in M(T) were carried out in the following ways:

1) ZFC (Zero Field-Cooling) measurement: the system is cooled from RT (Room Temperature, 300 K) to 5 K without applied magnetic field, then a low magnetic

field (100 or 1000 Oe) is switched on and data are collected during the thermal heating (5-300 K);

2) FC (Field-Cooled) measurement: the measure directly is started at the end of the ZFC measurement, the data are collected during cooling (300-5 K) in the same magnetic field.

Magnetic ZFC/FC measurements performed on the melt-series show that the temperature dependence of the magnetic susceptibility qualitatively follows a [1]Curie-Weiss law between 150 and 300 K (Figure 7.2). The samples synthesized from melt display a paramagnetic behaviour in the whole thermal range except for the sample with x= 0.8 Co a.p.f.u. (Di-Co80): indeed, as the temperature decreases below $T_{Néel}$ 8 K, it shows the typical cusp expected for a sample with global antiferromagnetic interactions (Figure 7.3).

The observed magnetic order in Di-Co80 is likely related to the presence of sufficiently high concentration of Co^{2+} ion at the *M1* site. Therefore, below the critical value of cobalt concentration, *i.e.* $x < 0.75$ Co a.p.f.u., the antiferromagnetic coupling disappears and, consequently, the system becomes paramagnetic.

---

[1] The Curie-Weiss law is a relation between magnetic susceptibilities and the absolute temperature, which is followed by ferromagnets, antiferromagnets, and some paramagnets. The Curie-Weiss law is usually written as:

$$\chi = C/(T+ \Theta)$$

where χ is the susceptibility, C is a constant for each material, T is the absolute temperature, and Θ is called the Curie temperature. A plot of $1/\chi$ *vs*. temperature is known as a Curie-Weiss plot. Ideally, it should be linear if the Curie-Weiss law is obeyed. From such a plot we can then extract the C constant from the inverse of the slope and the Θ from the y-intercept. The clue to antiferromagnetism is the behaviour of susceptibility above a critical temperature, called the Néel temperature (T_N). Above T_N, the susceptibility obeys the Curie-Weiss law for paramagnets but with a negative intercept indicating negative exchange interactions (Figure). It is not always precisely followed, and it breaks down in the region very close to the transition temperature. Often the susceptibility will behave according to a Curie-Weiss law in different temperature ranges with different values of C and Θ. (Image from www.irm.umn.edu)

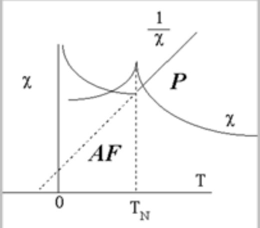

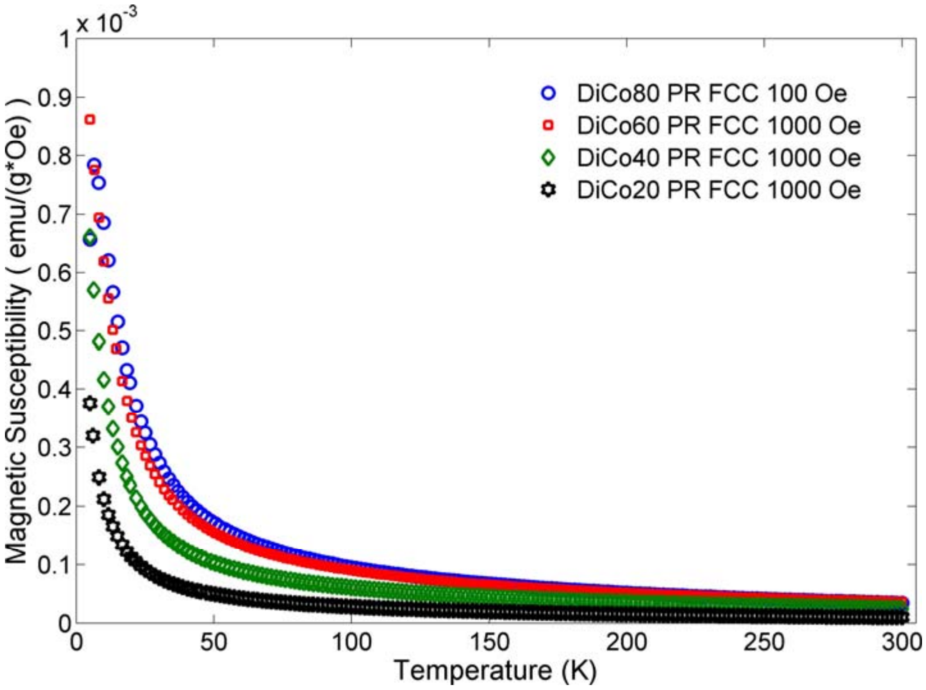

Figure 7.2. The temperature dependence of the χ_m magnetic susceptibility (emu/g · Oe) recorded at 100 Oe (for Di-Co80) and 1000 Oe for the other melt-grown samples.

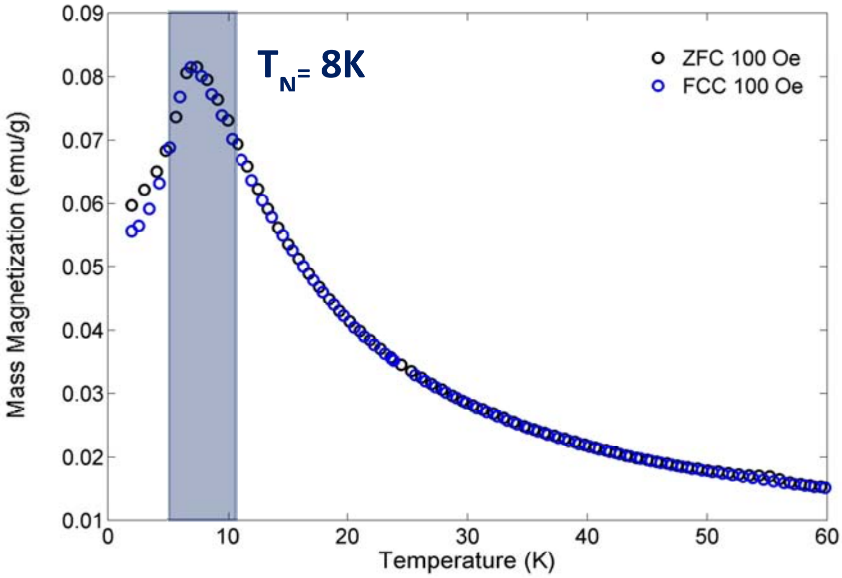

Figure 7.3. The temperature dependence of the σ mass magnetization (emu/g) for Di-Co80 melt-sample shows the arise of a long-range antiferromagnetic order (highligthed in blue).

Magnetic ZFC/FC measurements performed on the oriented $CaCoSi_2O_6$ (Co100) single crystal, were done to determine the principal magnetic properties as a function of the main crystallographic orientations (a, b and c-axes; Figure 7.4). ZFC curves were thus collected with a magnetic field applied (1000 Oe) parallel to the a- (a-ZFC), b- (b-ZFC) and c- (c-ZFC) axes (Figure 7.5).

Similarly to melt-grown Di-Co80 sample, Co100 shows that, at lower temperatures, the magnetic susceptibility qualitatively follows the global trend of an antiferromagnetic (AFM) material, in each orientation with a maximum on the curve at $T_{\text{Néel}}$ 10 K (Figure 7.5). Above $T_{\text{Néel}}$, in the paramagnetic domain, the magnetic susceptibility follows a Curie-Weiss law.

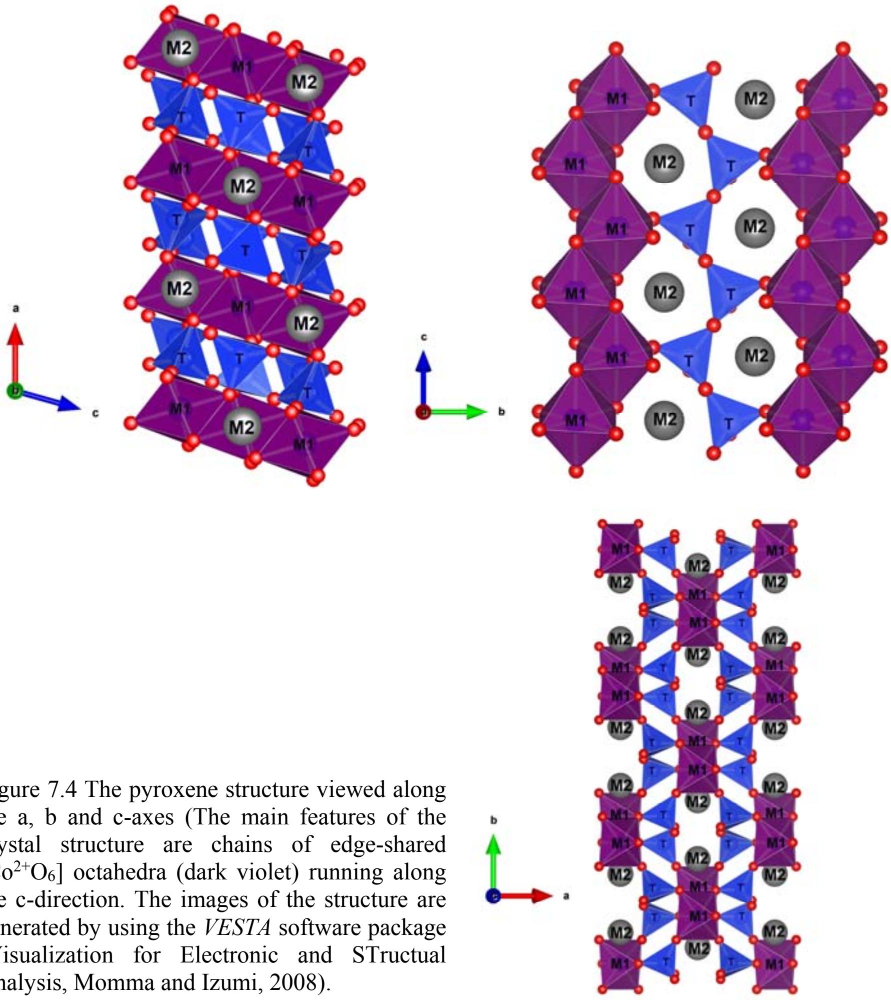

Figure 7.4 The pyroxene structure viewed along the a, b and c-axes (The main features of the crystal structure are chains of edge-shared $[Co^{2+}O_6]$ octahedra (dark violet) running along the c-direction. The images of the structure are generated by using the *VESTA* software package (Visualization for Electronic and STructual Analysis, Momma and Izumi, 2008).

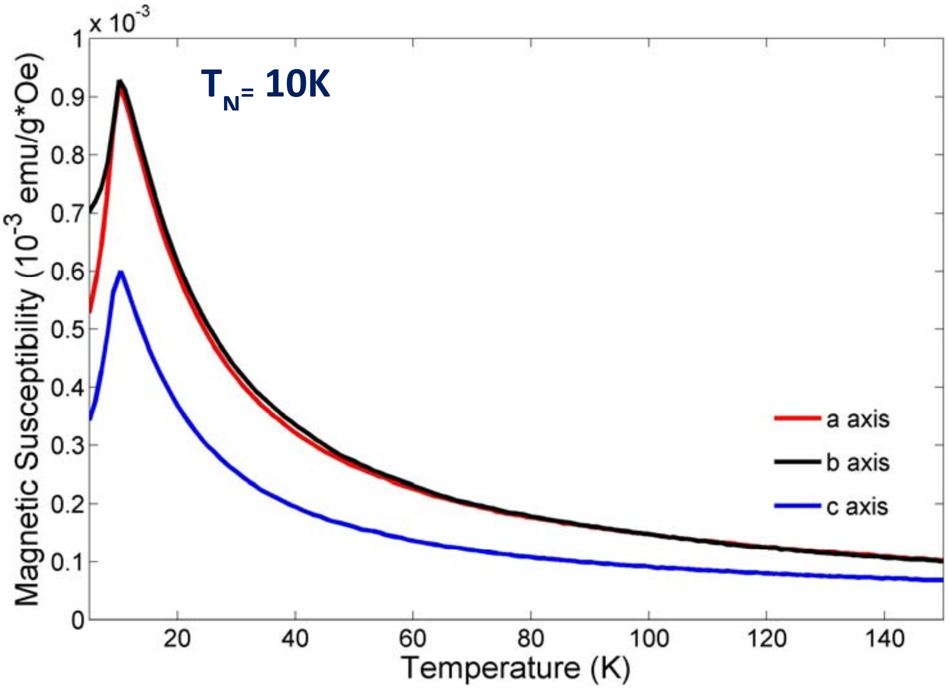

Figure 7.5. ZFC curves recorded with a magnetic field of 1000 Oe applied parallel to the a- (a-ZFC), b- (b-ZFC) and c- (c-ZFC) axes for Co100 flux(A)-grown sample.

Our analysis indicates that Co100 exhibits a magnetic anisotropy that reflects the structural anisotropy: in terms of magnetic exchange interactions the three crystallographic orientations are non-equivalent and mainly along c-direction there is a spin-coupling which provides an intra-chain antiferromagnetism.

Specifically, the magnetic anisotropy arises by the different Curie constant (C) values and the different superexchange integral (J) values between the Co^{2+} ions chains along the c-direction with respect to the other two directions (Table 7.1). Indeed, c-axis exhibits the highest J (1/C) values, while a- and b-axes are iso-J and they highlight a very weak strength of the spin coupling interaction.

TABLE 7.1. Magnetic Data Analysis for Co100 flux(A)-grown sample. Data were collected analyzing the curve of the Figure 7.5 that is the M(T) curve along the three different axes.

H parallel to	**T_N** K	**1/C** cm^3*Oe* K/emu	**J** meV	**H** Oe
a-axis	10	61,3	< 2	1000
b-axis	10	61,7	< 2	1000
c-axis	10	73,8	11	1000

In conclusion, our single crystal measurements show a considerably higher magnetic exchange energy along the c-axis*, i.e.* along the direction of the *M1* ribbon, which is indeed the sole cause of the magnetic ordering. Our results confirm the suggestions by Durand *et al*. (1996), that the magnetic behaviour in Co pyroxene is related to the infinite chains of edge-shared [$Co^{2+}O_6$] octahedra running parallel to the c-axis (Figure 7.6). Moreover our studies on the magnetic properties of Co pyroxene show that magnetic ordering occurs only when 75% of the *M1* polyhedra are filled by Co^{2+} ion. The further presence of a diamagnetic ion like Mg^{2+} breaks the magnetic symmetry and the structure behaves as a paramagnetic material at any temperature.

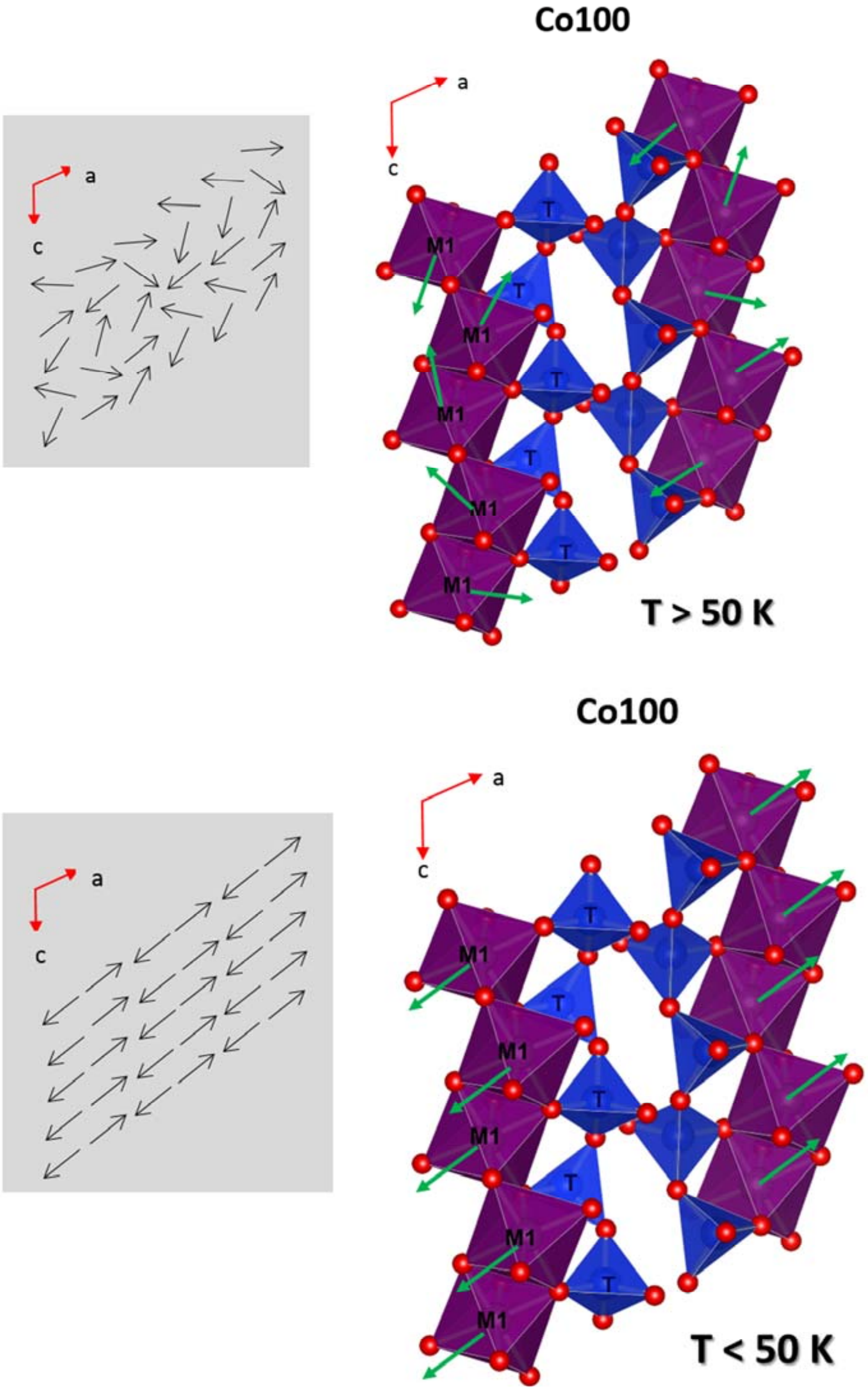

Figure 7.6. Schematic illustration of the magnetic moment arrangement in Co100 at (above) T > 50 K and (below) T < 50 K., *i.e.* in a paramagnetic and antiferromagnetic state, respectively. The images of the structure are generated by using the *VESTA* software package (Visualization for Electronic and STructual Analysis, Momma and Izumi, 2008).

Chapter 8

Ca-Zn SOLID SOLUTIONS IN CLINOPYROXENES

8. Ca-Zn SOLID SOLUTIONS IN CLINOPYROXENES

In this section it is reported a study written in the 2015 by Gori, C., Tribaudino, M., Mantovani, L., Delmonte, D., Mezzadri, F., Gilioli, E. and Calestani, G., in the published version in the *American Mineralogist*, 100, 2209-2218, but with few variations.

8.1. Introduction

As mentioned previously, experimental data on the Zn substitution mechanism, that is exchanged with Ca in the *M2* site of Ca-Zn pyroxenes, are present in the literature only regarding the two end-members (extreme terms of the solid solution), *i.e.* on $CaZnSi_2O_6$ (Huber *et al.*, 2012) and $Zn_2Si_2O_6$ (Syono *et al.*, 1971; Morimoto *et al.*, 1975); therefore we have synthesized the intermediate compositions along the $CaZnSi_2O_6$-$Zn_2Si_2O_6$ join. Zn has a ionic radius very similar to that of Co and Mg, *i.e.* 0.74 *vs*. 0.745 and 0.72 Å, respectively, but it enters differently in the *M2* site. Co, Mg and Fe in the *M2* site show a 4+2 sixfold coordination, whereas Zn exhibits a fourfold coordination (Morimoto *et al.,* 1975). Moreover, at room pressure and temperature, monoclinic $Zn_2Si_2O_6$ has a $C2/c$ structure, whereas monoclinic $Co_2Si_2O_6$, $Mg_2Si_2O_6$ and $Fe_2Si_2O_6$ show a $P2_1/c$ space group (Morimoto *et al.,* 1975; Ohashi *et al.,* 1975; Morimoto *et al.,* 1960; Sasaki and Takéuki 1981; Ohashi 1984). The fourfold coordination of Zn in the *M2* cavity was explained by the preference of Zn for covalent bonding and an sp^3 tetrahedral hybrid electronic configuration (Morimoto *et al.,* 1975).

Zn is a relatively common element, but due to its low affinity for silicates, it occurs in rock-forming silicates such as pyroxenes as a trace element; actually, in natural pyroxenes, it is found as a major constituent in only the rare mineral petedunnite (Essene and Peacor 1987). In petedunnite, the $CaZnSi_2O_6$ component is present in solid solution with johansennite ($CaMnSi_2O_6$). Pure $CaZnSi_2O_6$ pyroxene was synthesized at P> 0.8 GPa (Huber *et al.,* 2012); it has a $C2/c$ structure under room and high pressure conditions (Ohashi *et al.,* 1996; Nestola *et al.,* 2010). The Ca-free orthorhombic *Pbca* and monoclinic $C2/c$ polymorphs of the end member $Zn_2Si_2O_6$ were synthesized by Syono *et* *al.* (1971), and their crystal structure was refined by Morimoto *et al.* (1975). At high pressure, the monoclinic *C*2/*c* $Zn_2Si_2O_6$ polymorph shows two phase transitions with pressure, one to *P*2$_1$/*c* at P= 1.92 GPa and the other to a high pressure *C*2/*c* structure at P= 4.9 GPa (Arlt and Angel 2000). The high pressure *C*2/*c* structure has tetrahedral chain kinking and cell parameters quite different from the room pressure *C*2/*c* (Arlt and Angel 2000). Orthorhombic Zn pyroxenes with mixed Ni, Co, Mg and Zn occupancy were synthesized and refined by Syono *et al.* (1971) and Morimoto *et al.* (1975), showing that Zn partitions strongly in the *M2* site.

The relations between the *C*2/*c* structures of the end-members, one with Ca in eightfold and the other with Zn in fourfold coordination, are not clear, nor is the extent of mutual solid solution. A specific point of interest comes from the preference of Zn in the *M2* polyhedron for a tetrahedral coordination dictated by covalent bonding, whereas most cations substituting in the *M2* polyhedron of pyroxenes obey a simple ionic mechanism.

An investigation of Zn entrance in the *M2* site and its structural behaviour, provide a rationale for the geochemical and petrologic implications of Zn in pyroxenes. The partitioning of Zn between clinopyroxene and melt was recently proposed as a potential tracer for mantle source and an indicator for high temperature metamorphic conditions (Le Roux *et al.*, 2010; Huber *et al.*, 2012).

We have therefore synthesized at high pressure a series of pyroxenes between $CaZnSi_2O_6$ and $Zn_2Si_2O_6$, finding that complete solid solution may be attained. Single crystal and powder diffraction analysis detailed the structural mechanism for the Ca-Zn substitution; the implications for the partitioning of Zn between pyroxene and melt, in comparison with other trace elements, were eventually discussed. In Figure 8.1 is shown the crystal structure of one of the synthesized *C*2/*c* pyroxenes, *i.e.* $Ca_{0.5}Zn_{1.5}Si_2O_6$, viewed perpendicular to the *c*-axis.

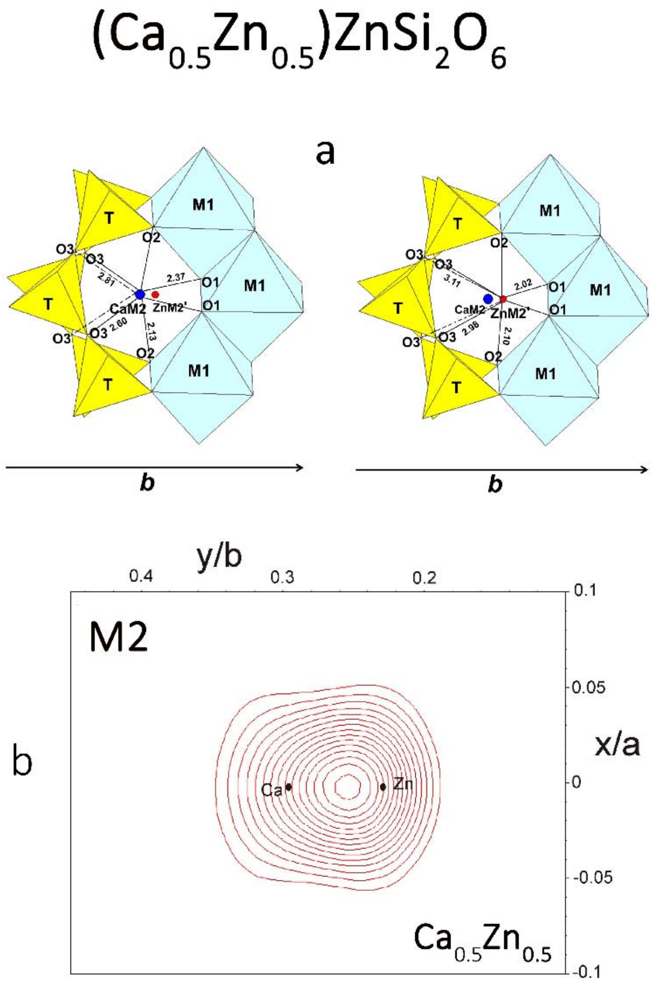

Figure 8.1. (**a**) Crystal structure of *C*2/*c* Ca$_{0.5}$Zn$_{1.5}$Si$_2$O$_6$ pyroxene, viewed perpendicular to the *c*-axis; (**b**) the electron density map at the *M2* site (*z* section); the cation occupancy of the site is reported. Ca*M2* and Zn*M2* site positions are always located, respectively, at the *M2* and *M2'*sites.

8.2. Experimental methods

8.2.1. Synthesis

A set of Ca-Zn pyroxenes with composition between CaZnSi$_2$O$_6$ and Zn$_2$Si$_2$O$_6$ (Table 8.1) was synthesized under high-pressure/high-temperature (HP/HT) conditions, using as a starting material a stoichiometric mixture of CaCO$_3$, ZnO and SiO$_2$ (Sigma-Aldrich> 99.99%). The mixtures were previously annealed in an electric furnace for 12 hours at T= 1000 ºC and room pressure, to obtain an assemblage of willemite (Zn$_2$SiO$_4$), hardystonite

($Ca_2ZnSi_2O_7$) and quartz. This assemblage, finely ground, was put in a multi-anvil Walker-type press (is described, in detail, in Appendix C), using Pt and Au capsules. The capsules (30 μm-thick Pt or Au foil) were loaded into an octahedral MgO pressure cell and then into the multi-anvil apparatus, in contact with a 10% Pt/Pt-Rh thermocouple for monitoring the temperature during the reaction.

The experiments were run at P= 5 GPa, and the capsules were heated up to T= 1200 ºC at a rate of 25 ºC/min for ($Ca_{0.8}Zn_{0.2}$)$ZnSi_2O_6$, ($Ca_{0.5}Zn_{0.5}$)$ZnSi_2O_6$, ($Ca_{0.3}Zn_{0.7}$)$ZnSi_2O_6$, and ($Ca_{0.2}Zn_{0.8}$)$ZnSi_2O_6$ (hereafter referred to as '$Ca_{0.8}Zn_{1.2}$', '$Ca_{0.5}Zn_{1.5}$', '$Ca_{0.3}Zn_{1.7}$', and '$Ca_{0.2}Zn_{1.8}$'). For $CaZnSi_2O_6$ and $Zn_2Si_2O_6$ (hereafter referred to as 'Ca_1Zn_1', 'Zn_2'), the runs were performed at P= 4 GPa and T= 1000 ºC. This condition was maintained for 3 hours of solid-state reaction, and then the capsules were quenched to room temperature by switching off the heater. Finally, the pressure was slowly released to prevent mechanical damage.

8.2.2. SEM-EDS and X-ray powder diffraction

A few grains of the run products were embedded in epoxy and polished for SEM-EDS analysis using a Jeol 6400 SEM equipped with an Oxford EDS, operated at 20 kV. Electron backscattered images were taken, showing that most of the sample was made by a phase with pyroxene stoichiometry, with a little excess of silica. The crystal size varies from 10 to 100 μm, depending on the samples. At least 10 analytical spots were collected on each run product. The chemical composition confirmed the expected stoichiometry.

Powder X-ray diffraction was performed using a Bruker D2 PHASER diffractometer and a Thermo ARL X'tra powder diffractometer equipped with a solid-state thermo electron detector, operating with $CuK_{\alpha 1}$ radiation (λ= 1.5406 Å). Rietveld analysis was performed to determine the unit cell parameters and the phase ratio, using the GSAS-EXPGUI software package (Larson and Von Dreele 1994; Toby 2001). Starting atomic parameters for the Ca-Zn pyroxenes were taken from Ohashi *et al.* (1996) for $CaZnSi_2O_6$ and from Morimoto *et al.* (1975) for $Zn_2Si_2O_6$. Rietveld analysis of powder patterns indicates that clinopyroxene is the major phase, together with a small amount of coesite, less than 10%. Rietveld refinement results are reported in Table 8.1.

TABLE 8.1. Synthesis conditions, cell parameters and phase abundance from Rietveld refinement of the X-ray diffraction powder pattern.

Sample	**Ca_1Zn_1**	**$Ca_{0.8}Zn_{1.2}$**	**$Ca_{0.5}Zn_{1.5}$**	**$Ca_{0.3}Zn_{1.7}$**	**$Ca_{0.2}Zn_{1.8}$**	**Zn_2**
P (GPa)	4	5	5	5	5	4
T (°C)	1000	1200	1200	1200	1200	1000
a (Å)	9.816(1)	9.801(1)	9.787(1)	9.783(1)	9.789(2)	9.807(2)
b (Å)	8.990(1)	9.004(1)	9.079(1)	9.125(1)	9.157(1)	9.197(1)
c (Å)	5.258(1)	5.251(1)	5.2652(1)	5.273(1)	5.288(2)	5.306(2)
β (°)	105.892(1)	106.494(8)	108.223(2)	109.777(5)	110.433(3)	111.454(4)
V (Å^3)	446.34(1)	444.27(3)	444.40(7)	443.01(9)	443.93(2)	445.48(2)
Diffractometer	Bruker D2	Thermo ARL X'tra	Thermo ARL X'tra	Bruker D2	Bruker D2	Bruker D2
Scan range (°)	7-80° 2θ	10-100° 2θ	10-100° 2θ	7-80° 2θ	7-80° 2θ	7-80° 2θ
pyroxene[a]	99.80%	97.10%	99.80%	96.20%	90.90%	97.70%
coesite[a]	0.20%	2.90%	0.20%	3.80%	9.10%	2.30%

[a] wt% as determined by Rietveld refinement.

8.2.3. X-ray single-crystal refinement

Single crystal X-ray diffraction data were collected on a Bruker AXS Smart diffractometer equipped with an APEX II CCD area-detector, on selected crystals chosen for sharp optical extinction, for the compositions $(Ca_{0.5}Zn_{0.5})ZnSi_2O_6$, $(Ca_{0.3}Zn_{0.7})ZnSi_2O_6$ and $(Ca_{0.2}Zn_{0.8})ZnSi_2O_6$. The data collection was also attempted for other compositions, but suitable single crystals were not found because of the highly twinned nature of the crystals.

Data collection conditions and refinement parameters are reported in Table 8.2. The MoK_α radiation was used, and the intensity data were corrected for absorption using the SADBS program (Sheldrick 1996). The $(Ca_{0.2}Zn_{0.8})ZnSi_2O_6$ crystals turned out to be systematically twinned on (100). The refinement was performed on the intensities of one of the individuals, after twin correction, during the data reduction. Preliminary analysis of the reflection extinctions and intensities, indicated a *C*2/*c* space group for all the samples.

Weighted structural anisotropic refinements were performed using the SHELX-97 program (Sheldrick 1997), within the WinGX suite (Farrugia 1999) and the coordinates of $CaZnSi_2O_6$ by Ohashi *et al.* (1996) and of $Zn_2Si_2O_6$ by Morimoto *et al.* (1975) as starting models. Full occupancy of Zn and Si in the *M1* and *T* sites was confirmed by site occupancy refinement. In the *M2* site, mixed occupancy of Zn and Ca were present and refined but without significant deviations from the expected stoichiometry. Similar to other pyroxenes where Ca (or Na) coexists with a smaller cation, we observed a significant improvement in the agreement factor by assuming that in the *M2* cavity, Ca and the smaller cation (here Zn) are split between two subsites (*M2* for Ca and *M2*' for Zn). In previous works, the *M2* and *M2'* subsites were located along the b-axis, at *y/b*~ 0.30 for Ca, and 0.25 for the smaller cation (Rossi *et al.,* 1987; Tribaudino *et al.,* 1989). In our case, the position for Zn was refined further away from Ca, at *y/b* ~0.23-0.24, at the same position found for Zn in *C*2/*c* $Zn_2Si_2O_6$ (Morimoto *et al.,* 1975). The electron density map along the diad axis at the *M2* site position clearly shows the two split atoms (Figure 8.1). Polyhedra volume and bond valence are calculated by IVTON (Balic Zunic and Vickovic 1996). Atomic coordinates, anisotropic displacement parameters and a selection of bond lengths and angles are reported in Tables 8.3 and 8.4.

TABLE 8.2. Structure refinement data and unit-cell parameters for Ca-Zn pyroxenes.

Sample	$\mathbf{Ca_{0.5}Zn_{1.5}}$	$\mathbf{Ca_{0.3}Zn_{1.7}}$	$\mathbf{Ca_{0.2}Zn_{1.8}}$
Space group	*C*2/*c*	*C*2/*c*	*C*2/*c*
Z	4	4	4
a (Å)	9.794(6)	9.773(6)	9.779(6)
b (Å)	9.071(5)	9.116(5)	9.146(5)
c (Å)	5.264(3)	5.272(2)	5.284(3)
β (°)	108.26(8)	109.74(8)	110.47(8)
V (Å^3)	444.1(5)	442.2(5)	442.8(4)
Diffractometer	Bruker AXS Smart	Bruker AXS Smart	Bruker AXS Smart
Radiation	Mo*K*α	Mo*K*α	Mo*K*α
Number of indep. refl. $I > 4\sigma$	712	736	724
$2\theta_{max}$ (°)	63.34	64.38	64.28
$R_{4\sigma}$ (F)%	3.3	3.6	4.4
w_{R2} (%)	8.4	8.6	10

TABLE 8.3. Fractional atomic coordinates and isotropic displacement parameters for Ca-Zn pyroxenes. Data for $CaZnSi_2O_6$ and $Zn_2Si_2O_6$ are taken from Ohashi *et al.* (1996) and Morimoto *et al.* (1975), respectively, here and in Table 8.4.

		Ca_1Zn_1*	**$Ca_{0.5}Zn_{1.5}$**	**$Ca_{0.3}Zn_{1.7}$**	**$Ca_{0.2}Zn_{1.8}$**	**Zn_2§**
M2 (Ca)	*y/b*	0.30015(5)	0.2955(3)	0.2883(7)	0.2838(10)	
	U_{eq}	0.0079(1)	0.0119(6)	0.0122(14)	0.0085(3)	
M2' (Zn)	*y/b*		0.2439(2)	0.2394(2)	0.2377(1)	0.2361(1)
	U_{eq}		0.0118(4)	0.0092(3)	0.0085(3)	0.0067(4)
M1 (Zn)	*y/b*	0.90583(3)	0.90033(6)	0.89680(7)	0.8949(9)	0.8919(1)
	U_{eq}	0.00625(6)	0.0141(2)	0.0130(2)	0.0122(2)	0.0073(2)
T (Si)	*x/a*	0.28631(5)	0.2936(10)	0.29784(13)	0.2996(2)	0.3016(1)
	y/b	0.09265(4)	0.08905(9)	0.08692(11)	0.0858(1)	0.0849(1)
	z/c	0.22916(9)	0.2455(2)	0.2562(2)	0.2609(3)	0.2668(2)
	U_{eq}	0.00424(9)	0.0114(2)	0.0098(3)	0.0083(3)	0.0042(2)
O1	*x/a*	0.1164(1)	0.1195(3)	0.1212(3)	0.1228(4)	0.1241(3)
	y/b	0.0889(1)	0.0880(2)	0.0872(3)	0.0866(3)	0.0868(3)
	z/c	0.1442(2)	0.1442(5)	0.1452(6)	0.1458(7)	0.1473(6)
	U_{eq}	0.0061(3)	0.0126(5)	0.0113(6)	0.0101(7)	0.0077(5)
O2	*x/a*	0.3602(1)	0.3695(3)	0.3747(4)	0.3761(4)	0.3787(3)
	y/b	0.2479(1)	0.2440(3)	0.2409(3)	0.2403(4)	0.2393(3)
	z/c	0.3212(2)	0.3478(6)	0.3625(7)	0.3668(8)	0.3719(6)
	U_{eq}	0.0082(3)	0.0235(6)	0.0193(7)	0.0139(7)	0.0090(5)
O3	*x/a*	0.3500(1)	0.3523(2)	0.3530(3)	0.3547(4)	0.3533(3)
	y/b	0.0190(1)	0.0219(3)	0.0239(3)	0.0241(4)	0.0238(3)
	z/c	0.9932(2)	1.0077(5)	1.0173(6)	1.0226(7)	1.0273(5)
	U_{eq}	0.0066(3)	0.0152(5)	0.0150(6)	0.0125(7)	0.0084(5)

Notes: *x/a* and *z/c* for the *M2* and *M1* special positions are 0 and 0.25.

*Data from Ohashi *et al*. (1996). §Data from Morimoto *et al*. (1975).

TABLE 8.4. Bond lengths (Å), polyhedral volumes (Å^3) and angles for Ca-Zn pyroxenes.

		Ca_1Zn_1*	**$Ca_{0.5}Zn_{1.5}$**	**$Ca_{0.3}Zn_{1.7}$**	**$Ca_{0.2}Zn_{1.8}$**	**Zn_2§**
M2	Ca-O1A1, B1× 2	2.356(1)	2.374(3)	2.347(6)	2.337(8)	
	Ca-O2C2, D2× 2	2.336(1)	2.133(4)	2.014(4)	1.975(4)	
	Ca-O3C1, D1× 2	2.601(1)	2.604(3)	2.644(6)	2.665(8)	
	Ca-O3C2, D2× 2	2.729(1)	2.812(3)	2.889(5)	2.934(7)	
	<Ca-O>	2.505	2.480	2.474	2.478	
M2'	Zn-O1A1, B1× 2		2.023(3)	2.018(3)	2.029(4)	2.031(3)
	Zn-O2C2, D2× 2		2.105(4)	2.004(4)	1.973(4)	1.933(2)
	Zn-O3C1, D1× 2		2.987(3)	3.018(4)	3.022(4)	3.027(2)
	Zn-O3C2, D2× 2		3.110(3)	3.174(3)	3.205(4)	3.255(3)
	<Zn-O>		2.556	2.554	2.557	2.561
	V_{M2} (Å^3) 8-coord.	25.91(11)	24.91(11)	24.39(13)	24.29(12)	24.27(12)
	M2 along b axis[a]	3.690	3.737	3.763	3.780	3.800
M1	Zn-O1A2, B2× 2	2.075(1)	2.041(3)	2.025(4)	2.022(4)	2.018(3)
	Zn-O1A1, B1× 2	2.158(1)	2.233(2)	2.272(3)	2.299(4)	2.333(3)
	Zn-O2C1, D1× 2	2.075(1)	2.079(3)	2.089(3)	2.090(4)	2.084(3)
	<Zn-O>	2.103	2.117	2.129	2.137	2.145
	V_{Zn}(Å^3)	12.26(5)	12.51(5)	12.62(5)	12.76(5)	12.83(7)
	OAV[b]	18.5	30.7	36.5	42.2	51.5
	M1 along b axis[a]	1.427	1.415	1.401	1.406	1.402
T	Si-O1	1.604(1)	1.619(3)	1.625(4)	1.620(4)	1.617(3)
	Si-O2	1.585(1)	1.603(3)	1.601(3)	1.605(4)	1.604(3)
	Si-O3A1	1.668(1)	1.649(3)	1.633(3)	1.634(4)	1.625(3)
	Si-O3A2	1.687(1)	1.659(3)	1.645(3)	1.640(4)	1.627(3)
	<Si-O>	1.636	1.632	1.626	1.625	1.618
	V_T(Å^3)	2.24(1)	2.22(2)	2.19(2)	2.19(2)	2.16(2)
	TAV[b]	27.9	16.2	13.1	12	11.6
	O3A1-Si-O3A2	104.2(1)	107.2(1)	109.2(1)	109.8 (1)	111.2(1)
	Si-O3-Si	135.7(1)	138.0(2)	139.6(2)	139.6(2)	141.6(2)
	O3-O3-O3	165.2(7)	162.8(2)	161.2(3)	161.0(3)	161.3(1)
	O3A1-O3A2	2.647(1)	2.662(2)	2.672(2)	2.679(2)	2.683(4)
	T along b axis[a]	2.263	2.322	2.362	2.375	2.397

Notes : [a]*M2* contribution: (0.5-*y/b*O1)*b*; *M1* contribution: (*y/b*O2-*y/b*O1)*b*; *T* contribution: (0.5-*y/b*O2)*b*.
[b]OAV and TAV are angle variance for tetrahedra and octahedra (Robinson *et al.*, 1971).
*Data from Ohashi *et al*. (1996). §Data from Morimoto *et al*. (1975).

8.3. Results and discussion

In Figure 8.2, the cell parameters of Ca-Zn pyroxenes are shown. For comparison, the trend observed in $CaCoSi_2O_6$-$Co_2Si_2O_6$ pyroxenes, with Co replacing Zn, is reported (Mantovani *et al.,* 2014); because the cation radius of Co is similar to that of Zn, the cell parameters are expected to vary similarly. However, this is observed in only the Ca-rich end-member, with no Zn in the *M2* site (Figure 8.2). As Zn enters the *M2* polyhedron, we find significant differences: the *a* parameter decreases little in Ca-Zn pyroxenes, much more than in Ca-Co ones; the *b* increases, but it is constant in Ca-Co pyroxenes; *c* decreases in Ca-Co pyroxenes and increases in Ca-Zn ones, and the β angle increases most in Ca-Zn pyroxenes. Volume changes are higher and non-linear in pyroxenes of the series $CaCoSi_2O_6$-$Co_2Si_2O_6$ and smaller and linear in Ca-Zn pyroxenes. Similar differences can also be observed between Ca-Zn (this work), Ca-Mg (Tribaudino *et al.,* 1989) and Ca-Fe (Ohashi *et al.,* 1975) pyroxenes. The lower volume change in Ca-Zn pyroxenes may be in part ascribed to the absence of a $C2/c$-$P2_1/c$ phase transition at intermediate compositions, but the Ca-Zn and Ca-Co trends are also different when both phases have $C2/c$ symmetry, *i.e.* when Ca is higher than 0.4 Ca atoms per formula unit (a.p.f.u.). The cell volume in Ca-Zn pyroxenes shows a linear change with composition, following an ideal behaviour (Figure 8.2). The same was observed in Ca-Mg, Ca-Fe and Ca-Co $C2/c$ pyroxenes (Arlt *et al.,* 2000; Mantovani *et al.,* 2014) where a deviation from the ideal behaviour occurs for only the $P2_1/c$-$C2/c$ phase transition. The phase transition occurs with a volume decrease of the $P2_1/c$ structure with respect to the volume that would be observed in a $C2/c$ pyroxene with the same composition; in the $P2_1/c$ field we observe linear changes in cell volume.

***M2* polyhedron:** in $CaZnSi_2O_6$ pyroxene, with only Ca in the *M2* site, the *M2*-O bond distances (Figure 8.3) are very close to those observed in $CaCoSi_2O_6$ (Mantovani *et al.,* 2013, 2014; Ghose *et al.,* 1987), which are, in turn, similar to those of diopside and

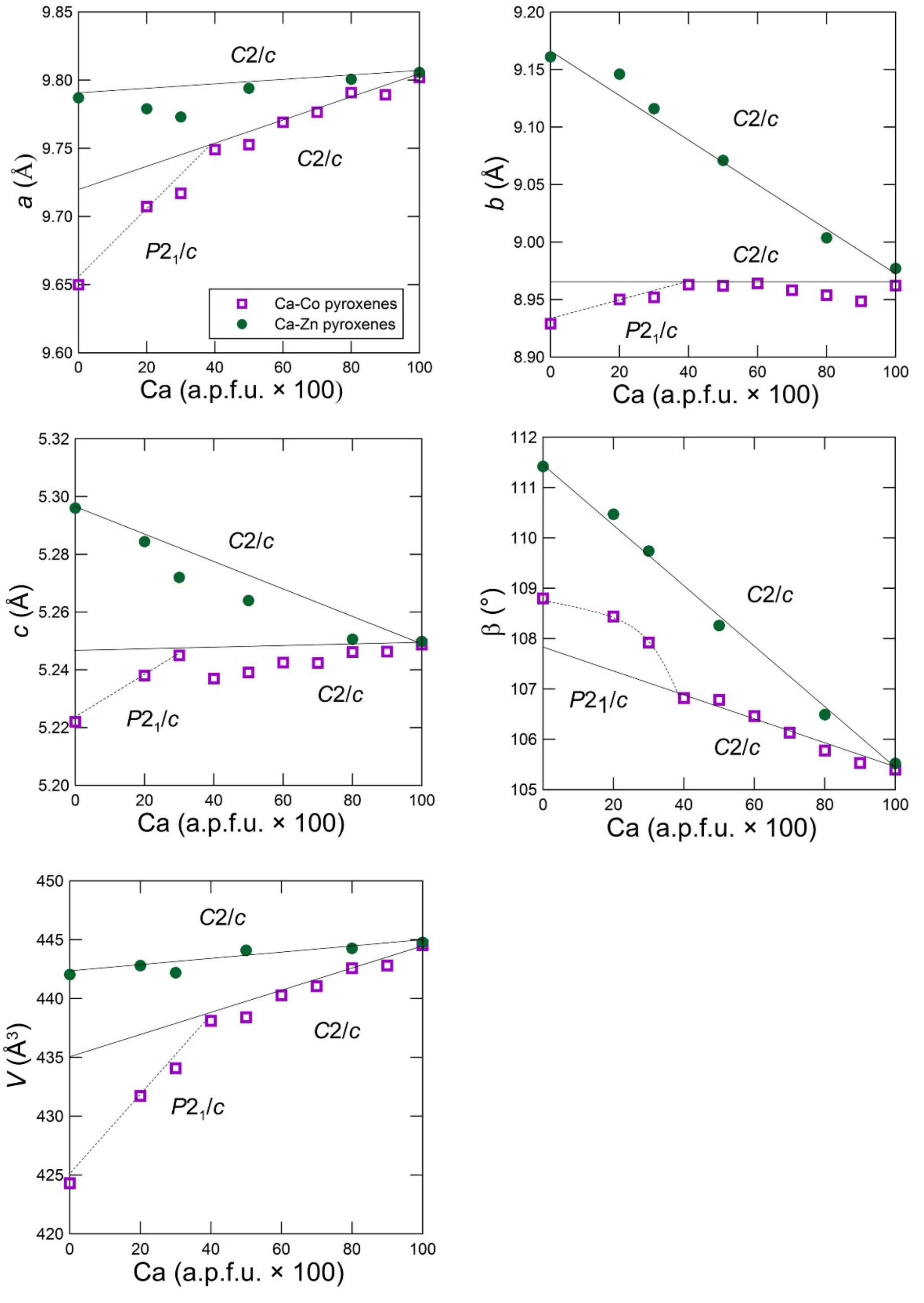

Figure 8.2. Unit-cell parameters *vs.* composition in Ca-Zn (green filled circles) and Ca-Co (purple open squares) pyroxenes. Solid and dashed lines show the trend for the *C2/c* and *P*2₁/*c* pyroxenes, respectively [Data for Ca-Co pyroxenes from Mantovani *et al.* (2014)].

hedenbergite (Bruno *et al.,* 1982; Nestola *et al.,* 2007) indicating that the different cations in *M1* have little effect on the Ca in the *M2* site.

However, when Zn exchanges for Ca into the irregular eightfold polyhedron surrounding Ca atoms, which we can call the *M2* cavity (Figure 8.1), the electron density map shows the coexistence of two distinct positions for Ca and Zn. The two atomic positions split so much that an average structure is hardly significant and, in our Zn-rich solid solution, we have to consider different distances for the Ca and the Zn environments. In agreement with previous investigations (Rossi *et al.,* 1987), we define *M2* as the polyhedron for Ca and *M2'* as that for the smaller cation (here Zn).

There are suggestions that oxygen also shows atom splitting as it was observed in synthetic pyroxenes along the Di-En series by the analysis of the size of the U_{eq} *vs*. composition (Figure 8.4) (Bruno *et al.,* 1982; Tribaudino *et al.,* 1989; Tribaudino *et al.,* 2003). In Ca-Zn pyroxenes, similar to other *C*2/*c* pyroxenes where Ca exchanges with a smaller cation, the U_{eq} for the O2 atoms are larger in the intermediate compositions than in the end members and are generally larger than for other atoms of oxygen. Positional disorder explains the increased size in intermediate compositions as the displacement parameters record an average of local positions, which are different if the O2 is bonded to Zn in *M2'* or Ca in *M2*. The *M2'*-O distances with the O2 and O1 atoms are close to 2.0 Å, whereas, as Ca is exchanged by Zn, the *M2'*-O3 interatomic distances are greater than 3.0 Å. This results in an irregular fourfold coordination of O1 and O2 atoms of oxygen around Zn (in the *M2*' site) (Figure 8.1). The same was found in $Zn_2Si_2O_6$ by Morimoto *et al.* (1975), and here, it is also observed in the intermediate compositions: it is likely that Zn enters into fourfold coordination in the *M2* polyhedron, even if present in a small amount. Zn-O1 and Zn-O2 distances do not change with composition, and Zn-O3 distances become even larger as zinc increases. However, from the geometrical point of view, we are far from a regular tetrahedron: for instance, in $Ca_{0.3}Zn_{1.7}$, the O2-*M2'*-O2 angle is 169.7° and the other angles of the O1 and O2 atoms of oxygen with *M2*' are between 90° and 100°, to compare with the ideal 109.4° predicted by tetrahedral coordination. The fourfold coordination of Zn in *M2'* is specific to *C*2/*c* clinopyroxenes: in the orthopyroxene and in the high pressure *P*2_1/*c* structure, Zn instead shows an asymmetric sixfold coordination, with two of the four O3 oxygens in coordination (Morimoto *et al.,* 1975; Arlt *et al.,* 2000). As Ca decreases, the bond distances with the furthermost O3 atoms of oxygen (*M2*-O3C2,D2) and those with the closer O3 (*M2*-O3C1,D1 distances) increase; the *M2*-O1 distance is constant, and the *M2*-O2 distance decreases. Within the eightfold *M2* cavity, Ca then shows a 4+2 sixfold coordination and Zn shows a fourfold one.

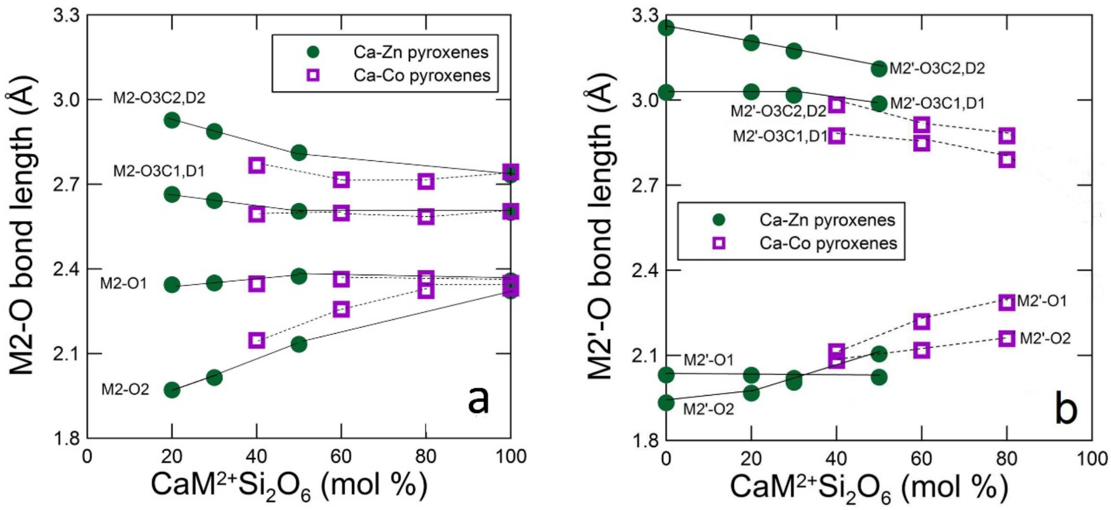

Figure 8.3. (**a**) *M2*-O bond lengths *vs*. composition in Ca-Zn and in Ca-Co pyroxenes; (**b**) *M2'*-O bond lengths with composition in Ca-Zn pyroxenes and in Ca-Co pyroxenes. [Data for Ca-Co pyroxenes from Mantovani et *al.*, 2013 and Ghose *et al.,* 1987; for Ca-Zn pyroxenes from Ohashi *et al.*, 1996, Morimoto *et al.*, 1975 and this work].

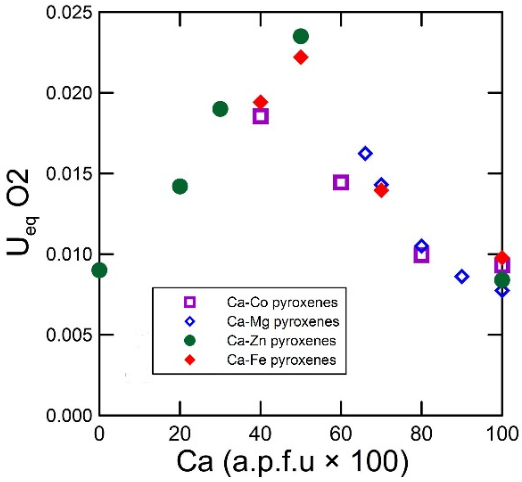

Figure 8.4. U_{eq}O2 *vs*. composition [Data for Ca-Co pyroxenes from Mantovani *et al.*, 2013 and Ghose *et al.*, 1987; for Ca-Zn pyroxenes from Ohashi *et al.*, 1996, Morimoto *et al.*, 1975 and this work; for Ca-Mg from Bruno *et al.*, 1982 and Tribaudino *et al.*, 1989; for Ca-Fe from Ohashi *et al.*, 1975 and Nestola *et al.*, 2007].

The contribution of the *M2* cavity to the cell volume can be obtained by the volume of the eightfold coordinated polyhedron, regardless of the actual coordination of the cation in the site. This volume is compared in Figure 8.5 with that of other pyroxenes where Ca exchanges with a smaller cation. The volume of the *M2* cavity changes in a way very similar to that of Ca-Co, Ca-Fe and Ca-Mg pyroxenes, with the only exception in the end-member $Zn_2Si_2O_6$, which has the same volume as $Ca_{0.2}Zn_{1.8}Si_2O_6$.

This result is quite surprising and indicates that the volume of the *M2* cavity changes almost completely for the different cation radii of Zn and Ca, despite the different bonding of Zn and Co in the *M2* cavity (Figure 8.5). This change is similar to what was found between Co and Ca. The suggestion is that the larger cation (Ca) accounts for the decrease in the size of the cavity, not considering the local coordination of Zn. The volume decrease in the *M2* cavity of Ca-Co pyroxenes explains the cell volume decrease almost completely; however, as it will discussed in the following paragraph, in Zn pyroxenes, a cell volume increase driven by the *M1* polyhedron opposes the decrease in the *M2* cavity and results in a lower volume change (Figure 8.5).

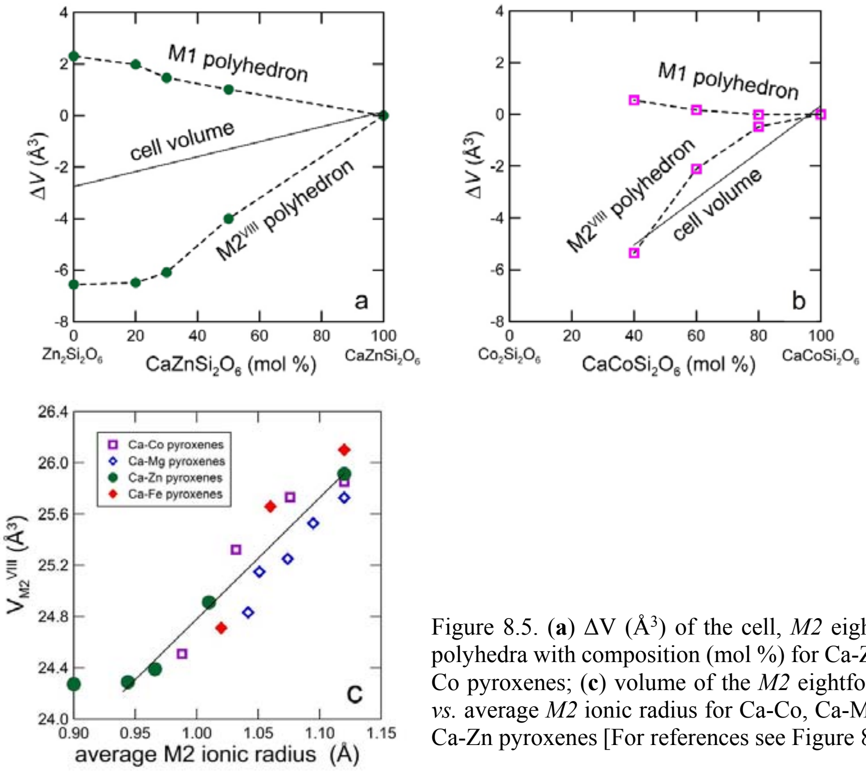

Figure 8.5. (**a**) ΔV (Å^3) of the cell, *M2* eightfold and *M1* polyhedra with composition (mol %) for Ca-Zn and (**b**) Ca-Co pyroxenes; (**c**) volume of the *M2* eightfold polyhedron *vs.* average *M2* ionic radius for Ca-Co, Ca-Mg, Ca-Fe, and Ca-Zn pyroxenes [For references see Figure 8.4].

***M1* polyhedron:** in the Ca-Zn series, Zn fully occupies the *M1* site. The *M1*-O bond lengths *vs*. Ca are shown in Figure 8.6 and compared with those of Ca-Co pyroxenes. The two longer and smaller *M1*-O1 distances (*M1*-O1 A1,B1 and *M1*-O1 A2,B2, respectively) show a strong and opposite change with Ca: the shorter distances decrease whereas the longer ones increase; the intermediate *M1*-O2 distances instead change slightly. The difference between shorter and longer distances also increases in Ca-Co pyroxenes, but at a lower rate (Mantovani *et al.,* 2013). For instance, the longer *M1*-O1 distance increases by 0.064 Å along the series $CaCoSi_2O_6$-$Co_2Si_2O_6$, but in Ca-Zn pyroxenes, it increases by 0.174 Å. As a result, in $Zn_2Si_2O_6$ a 4+2 coordination is observed, with the longer *M1*-O1B being less bonded. We also interpret this behaviour as an attempt of Zn in the *M1* site to approach the fourfold coordination, as in the *M2* cavity. However, a transition to a fourfold coordination in the *M1* site is hindered because the *M1* polyhedron is tighter and less flexible than the *M2* one; in the *M2* cavity, which is more flexible and enables higher deformation, Zn finds its own fourfold coordination.

Average bond distances and *M1* polyhedral volume are very similar in $CaZnSi_2O_6$ and $CaCoSi_2O_6$, although individual bond lengths are somewhat different. As shown in Figure 8.7, the polyhedral *M1* volume is related to the *M1* ionic radius in pyroxenes with only Ca in the *M2* site, suggesting that Zn in the *M1* site shows an ionic behaviour. In intermediate solid solutions, the average *M1*-O distances increase with substitution of Zn for Ca in the *M2* site, which is surprising as the *M1* site is always filled by Zn. In fact, the average bond distances (*M1*-O) are almost the same for the whole series in Ca-Fe, Ca-Co and Ca-Mg pyroxenes (Figure 8.8), where Fe, Co and Mg fill the *M1* polyhedron. The contribution of the increased size of the *M1* polyhedron to the cell volume explains why the *M2* cavity in the case of Zn-pyroxenes does not account for the change in volume as observed for the Co-pyroxenes: the Ca-Zn substitution in the *M2* polyhedron decreases the cell volume, but the increased *M1* polyhedral size opposes the decrease.

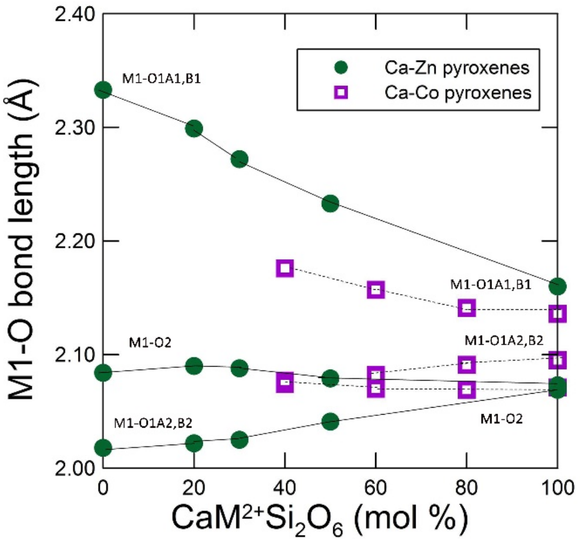

Figure 8.6. *M1*-O bond length variation with composition in Ca-Zn and Ca-Co pyroxenes [For references see Figure 8.3].

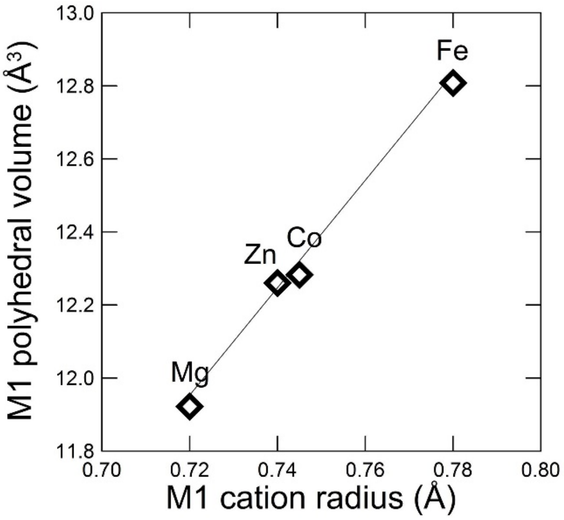

Figure 8.7. *M1* polyhedral volume *vs.* cation radius predicted by an 'ionic model' [Data for Ca-Co pyroxenes from Ghose *et al.*, 1987; for Ca-Zn pyroxenes from Ohashi *et al.,* 1996; for Ca-Mg from Tribaudino *et al.*, 1989; for Ca-Fe from Nestola *et al.*, 2007].

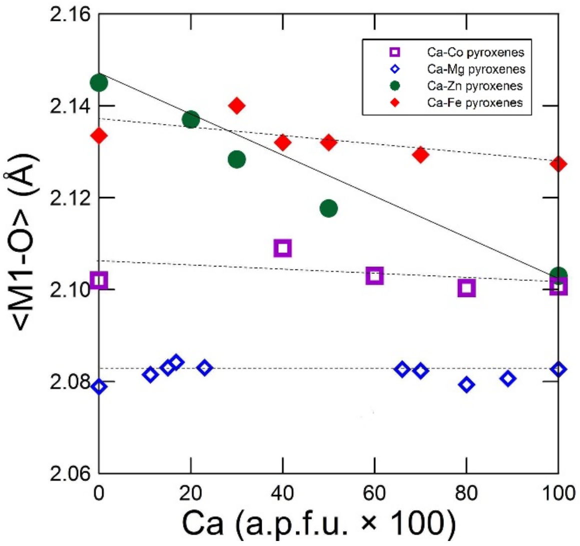

Figure 8.8. Average *M1*-O bond lengths *vs*. composition (Ca content in the *M2* site) for Ca-Zn, Ca-Co, Ca-Fe and Ca-Mg pyroxenes. It is assumed that polyhedral bond lengths are not different in the monoclinic and orthorhombic phases for $Co_2Si_2O_6$, $Mg_2Si_2O_6$ and $Fe_2Si_2O_6$ (Ohashi *et al.*, 1996; Sasaki and Takéuki, 1981; Hugh-Jones *et al.*, 1994, Morimoto *et al.,* 1960) [For the other references see Figure 8.4].

***T* tetrahedron and tetrahedral chain:** throughout the series, the volume and average bond distances in the Si-filled tetrahedron do not change significantly but the individual *T*-O bond distances and angles do show significant changes with Ca. The bond distances of Si with the O3 atoms, *i.e.* the *T*-O bridging (*T*-O_{br}), decrease with decreasing Ca, whereas the distances with O1 and O2 atoms (*T*-O non bridging, *T*-O_{nbr}), slightly increase (Figure 8.9). Moreover, the tetrahedral angle variation (TAV) decreases with decreasing Ca, showing that the tetrahedron becomes more regular. The *T*-O_{br} distances decrease for the lower electrostatic contribution from Ca and Zn as both the *M2*-O3 and *M2*'-O3 distances increase with Zn, making the tetrahedral chains further from the cations.

The O3-O3 distance, which is a shared edge with the *M2* polyhedron, increases as Ca decreases, accounting for the strong increase in the *c* parameter. As in the *M1* polyhedron, we have therefore an effect of the *M2*-O distances on the arrangement of the tetrahedral bond distances. The same rearrangement in Si-O bond lengths is also found in other pyroxenes when Ca is exchanged by a smaller cation (Figure 8.10a).

The geometry of the tetrahedral chain does not change much with Ca-Zn substitution: the kinking angle decreases, following the same trend in *C*2/*c* Ca-Co, Ca-Mg and Ca-Fe pyroxenes (Figure 8.10b). Rather than a high temperature fully extended configuration similar to that found in spodumene or high temperature pigeonite (Cameron *et al.,* 1973), in the *C*2/*c* end member $Zn_2Si_2O_6$, the tetrahedral chain shows intermediate kinking, close to that observed in diopside. The kinking of the end-member $Zn_2Si_2O_6$ is very close to that of $(Ca_{0.3}Zn_{0.7})ZnSi_2O_6$ and $(Ca_{0.2}Zn_{0.8})ZnSi_2O_6$.

The relationship between the kinking angle and the cell β angle (Thompson *et al.,* 2005) is not found here. The β angle increases much more in Ca-Zn than in Ca-Co pyroxenes (Figure 8.2), but the O3-O3-O3 kinking angle changes likewise (Figure 8.10b), with the exception of the end member $Zn_2Si_2O_6$. The strong increase in the β angle is described by the shift of the tetrahedral chains (Benna *et al.,* 1988; Tribaudino 1996; Mantovani *et al.,* 2013) that accounts for the offset between the two tetrahedral chains facing onto the *M2* polyhedron along the c direction (Tribaudino *et al.,* 1989). It was observed by Mantovani *et al.* (2013) that chain shift enables an increase in the bond distance between *M2* and the furthermost O3, maintaining the *C*2/*c* symmetry; in Ca-Fe, Ca-Mg and Ca-Co pyroxenes, it takes a maximum value of 0.9 Å, which was suggested to be a limiting value before the transition to the $P2_1/c$ symmetry. In Ca-Zn pyroxenes, higher shift can occur in the *C*2/*c* symmetry, accounting for the higher values in the β angle (Figure 8.10c).

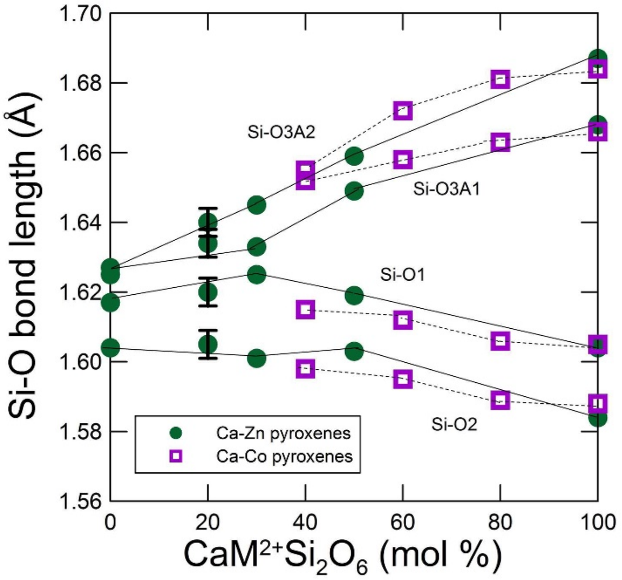

Figure 8.9. *T*-O bond lengths *vs*. composition in Ca-Zn and in Ca-Co pyroxenes. [For references see Fig. 8.3].

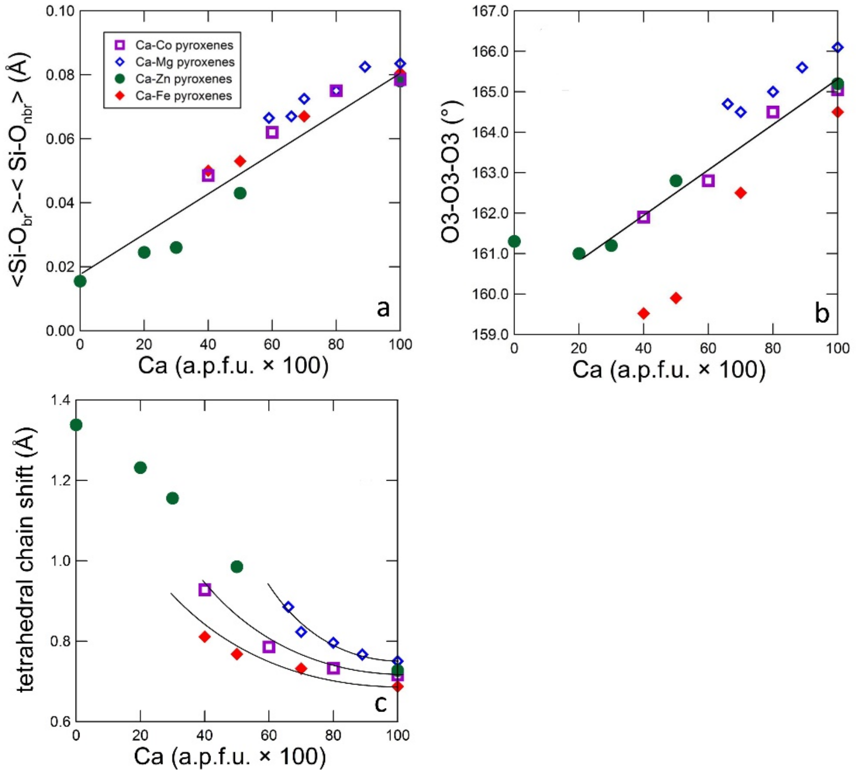

Figure 8.10. (**a**) Difference between average bridging and non-bridging *T*-O distances *vs*. Ca content in the *M2* site; (**b**) O3-O3-O3 kinking angle with composition; (**c**) tetrahedral chain shift *vs*. Ca content in the *M2* site: tetrahedral chain shift S= $2a\cos(\beta)(x_{O3}-0.5)+2cz_{O3}$. [For references see Figure 8.4].

8.3.1. Zn substitution and phase transition

The average ionic radius for six-coordinated *M2* decreases from 1.0 to 0.74 Å along the series. Following the prediction of a critical cation radius at approximately 0.86-0.88 Å, a $C2/c$-$P2_1/c$ phase transition should occur as Ca becomes less than 0.4-0.5 a.p.f.u., but the $C2/c$ symmetry is retained for any Zn substitution.

This effect reflects a different interaction of the cation in the *M2* site with the tetrahedral chain. In Ca-Mg, Ca-Fe, Ca-Co and Mn-Mg pyroxenes, the phase transition occurs as the size of the average *M2* cation decreases; then, in the $P2_1/c$ structure, the cation falls out from the special position along the diad axis and the tetrahedral chains are rearranged to alternatively decrease and increase the bond lengths with the *M2* cation. Therefore, there is an active interaction between the *M2* and O3 oxygen atom.

In the case of Ca-Zn pyroxenes, at least at room conditions, this interaction is not observed: the tetrahedral chain kinking does not change much along the series, and for Zn richer samples, it does not change at all. The tetrahedral chain kinking angle decreases only if the Ca content is large enough. For higher Zn content, the cation has no interaction with the tetrahedral chain and no significant kinking occurs. The reduced ionic radius for Ca-Zn exchange in *M2* is compensated by the tetrahedral chain shift. This effect does not occur simply because Zn lies in the *M2*' site at a position more displaced from the tetrahedral chain than Mg, Co or Fe (Tribaudino *et al.,* 1989; Rossi *et al.,* 1987; Mantovani *et al.,* 2013; Ohashi *et al.,* 1975; Nestola *et al.,* 2007) and the bond distances with the O3 oxygen atom are longer (Figure 8.3). A calculation on the charge on the O3 atom, which is, apart from Si, bonded by only the *M2-M2'* atoms (Figure 8.1), shows only little difference between Ca-Co and Ca-Zn pyroxenes (Figure 8.11). A likely explanation lies in the covalent character and the tetrahedral coordination of the Zn-O bonding, which does not involve the O3 atoms of the chains facing the *M2* polyhedron: the charge balance model, which assumes an ionic charge distribution, is not correct for Zn in *M2* in Zn pyroxenes. Bonding for Zn involves only the O1 and O2 atoms, and an interaction with the O3 atoms is not present. A switch from the above 'covalent' behaviour to a 'ionic' one occurs at high pressure, reducing the Zn-O3 distances and promoting an approach to the tetrahedral chains. At high pressure, an interaction of Zn with the O3 bridging atoms promotes the transition to the *P*2₁/*c* symmetry, at P= 1.9 GPa in $Zn_2Si_2O_6$ (Arlt and Angel 2000). In the high pressure *P*2₁/*c* structure, as well as in the *Pbca* structure of the orthopyroxene, which can be described as a twin at the unit cell scale of the *P*2₁/*c* structure, Zn is no longer fourfold coordinated (Morimoto *et al.,* 1975; Arlt and Angel 2000). Following the same rationale, we could also predict the transition to *P*2₁/*c* at low temperature, as a consequence of a supposed decrease in the volume of the *M2* polyhedron and approach of the tetrahedral chains to *M2*. This prediction is indeed supported by quantum mechanical calculations at 0 K on monoclinic $Zn_2Si_2O_6$ (Karazhanov *et al.,* 2009) but not by experiments. Powder XRD down to 100 K by Galkin *et al.* (2007) in $Zn_2Si_2O_6$ does not show any evidence of a transition to *P*2₁/*c*, and the transition, if any, should occur at even lower temperature.

8.3.2. Solid solution in *C*2/*c* pyroxenes

A complete solid solution is obtained in Ca-Zn clinopyroxenes at a temperature of 1200ºC; under the same conditions where the solid solution was very limited in the Ca-Co and Ca-Mg pyroxenes (Lindsley and Dixon 1976; Mantovani et *al.,* 2014). In Ca-Co, as in Ca-Mg and Ca-Fe pyroxenes, we have a miscibility gap separating a wider solid solution field of Ca-rich clinopyroxenes from a narrow Ca-poor orthopyroxene field. Here, the orthopyroxene is not stable and the two-pyroxene assemblage does not lead to a decrease in free energy with respect to the single phase pyroxene. Therefore, also in view of the ideal behaviour of cell volumes, as long as the symmetry is *C*2/*c*, complete solid solution can be expected. The different coordination of Zn in the *M2* cavity in *C*2/*c* and *Pbca* pyroxenes accounts for the above behaviour. In the *M2* site of the *Pbca* $Zn_2Si_2O_6$ orthopyroxene, two of the O3 atoms of oxygen are in coordination, although in an asymmetric position within the *M2* cavity, and the coordination in the *M2* site can be described as 4+2 sixfold (Domeneghetti *et al.,* 1995). The same was observed in high pressure *P*2₁/*c* $Zn_2Si_2O_6$ (Arlt and Angel 2000). In *C*2/*c* clinopyroxene, the shorter *M2*-O3 distances are out of bonding (~3.03 Å, Morimoto *et al.,* 1975) and the coordination of Zn in *M2* is fourfold. Given the preference of Zn for a fourfold coordination, the higher stability of the *C*2/*c* phase with respect to the *P*2₁/*c* and orthorhombic *Pbca* is not surprising (Syono *et al.,* 1971).

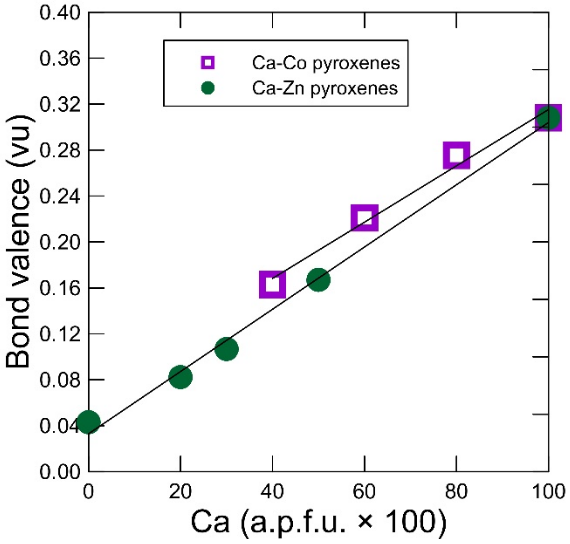

Figure 8.11. Bond valence of the O3 atoms coming from *M2-M2'* cations [For references see Figure 8.3].

8.4. Implications for Zn geochemistry

In this work on synthetic pyroxenes, we have filled the *M1* site with Zn and exchanged Zn for Ca in the *M2* site, which was possible because Ca does not enter the *M1* site and any Ca will buffer the *M2* site. In natural petedunnite, we also have the *M2* site completely filled by Ca and Zn enters only the *M1* site. However, Zn can enter both the *M2* and the *M1* sites if Ca does not buffer the *M2* site, as in clinopyroxenes from basalts and mantle peridotites.

Intracrystalline *M2-M1* site preference for trace elements can be tested by the analysis of the partition coefficients of the same elements between clinopyroxene and melt. Partitioning coefficients are modified by the different chemical environments, but in a given sample, for a given phase and in a given chemical site, they are related to the ionic radius of the partitioning element by Onuma diagrams (Onuma *et al.,* 1981). Onuma diagrams provide a curve showing the partitioning coefficient *vs.* cation radius for cations in each structural site. Different curves are provided for different structural sites. In general, cations with very similar ionic radii and charge, confined in a given structural site, have very similar mineral-melt partition coefficients. Cations in different structural sites may on the contrary have different crystal-melt partitioning even if they have similar ionic size. We could then expect that Zn will have a very similar partitioning coefficient to cations such as Co and Mg, with the same valence and similar size if they are concentrated in the same structural site. This similarity is not found. In Figure 8.12, the clinopyroxene-melt distribution coefficients for a series of divalent cations, as reported for a Ca-poor lherzolitic clinopyroxene by Adam and Green (2006), are plotted as a function of ionic radius. The six- and eight-coordinated radii were reported (Shannon 1976), respectively, for the *M1* and *M2* polyhedra. The Onuma diagram curves reported in Adam and Green (2006) for the specific case were calculated from the lattice strain model of Blundy and Wood (2003). In this model, the partition coefficients can be predicted by the polyhedral Young's modulus and the ideal radius that the cation should have in a given polyhedron. We observe that the clinopyroxene-melt partitioning coefficients for atoms such as Ca, Pb and Mn, which are completely (Ca, Pb) or almost completely (Mn) partitioned in the *M2* site, fall on the curve calculated for the *M2* site. Those for Co and Mg fall close to the curve calculated for the *M1* site, showing that their distribution is fully predicted, assuming that they enter the *M1* site. Zn instead shows a much lower clinopyroxene-melt distribution coefficient than expected if concentrated in the octahedral *M1* site, whereas, assuming that Zn enters the *M2* site, the observed partitioning agrees with predictions (Figure 8.12). The suggestion from crystal-melt partitioning is that Zn enters the *M2* site. Although this suggestion awaits experimental confirmation by an analysis of intracrystalline site partitioning between the *M2* and *M1* sites in natural clinopyroxene, a strong preference was shown by Zn for the *M2* site in a solid solution of Co, Ni, Zn orthopyroxenes and in $ZnMgSi_2O_6$ synthetic orthopyroxene (Morimoto *et al.,* 1975; Ghose *et al.,* 1975). A likely crystal chemical explanation of the preference of Zn in the *M2* site, in clinopyroxenes and in orthopyroxenes, is that the *M2* cavity is more flexible and better suited to host the Zn cation in a fourfold sub-site than is the *M1* polyhedron, which is a tighter cavity. Incidentally, Ghose *et al.* (1975) showed that there is a strong correlation between the intracrystalline partition coefficients and ionic radii in the *M1* site, and Zn is again an exception, being more concentrated in the

M2 site than expected by its ionic radius. The crystal chemical considerations put forward by the present work may also have a petrologic implication. The crystal chemical preference of Zn for the *M2* site results in a different (lower) partitioning of Zn in the clinopyroxene but also a higher partitioning in the melt. A melt formed by clinopyroxene-rich source rocks will be then enriched in Zn. The enrichment of Zn in basaltic melts resulting from partial melting of clinopyroxene-rich source rocks was used by Le Roux *et al.* (2010, 2011) to constrain the origin of the observed magmas, to track the source rock of the original magmas and to detect the mantle source heterogeneities. The above petrologic implications derive from the peculiar bonding requirements of Zn in pyroxenes that confine Zn to the *M2* cavity, and the clinopyroxene-melt partitioning coefficient is then lower than what we would have if Zn was present in the *M1* octahedral coordination. The empirical predictions by Onuma diagrams are respected, once it is assumed that the smaller Zn fits into the larger *M2* cavity.

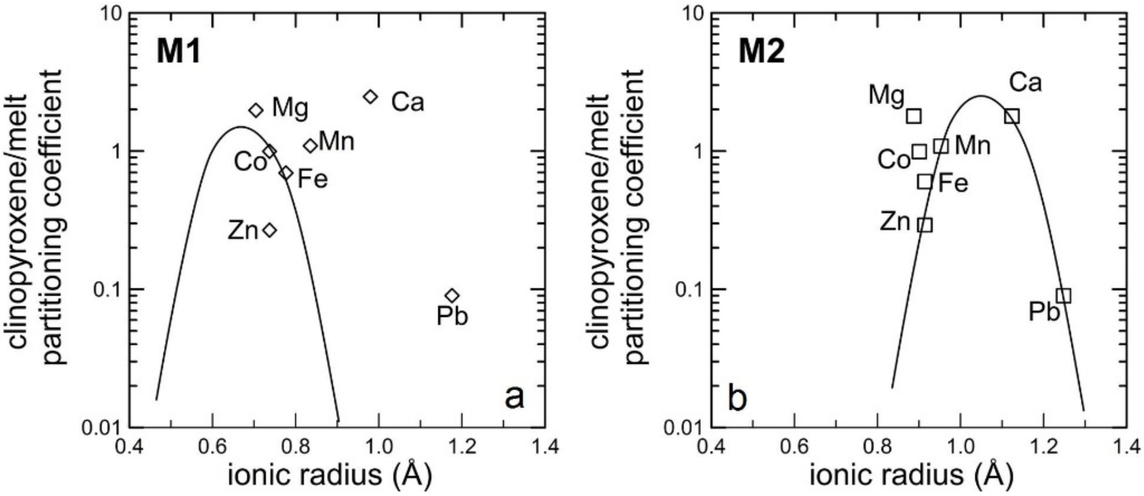

Figure 8.12. The ionic partitioning curves for *M1*(**a**) and *M2* sites (**b**) and divalent cations of different ionic radius calculated using the parameters reported for a Ca poor lherzolitic pyroxene by Adam and Green, 2006. The distribution coefficients for the cations are taken from the same paper.

8.5. Infrared characterization of Ca-Zn pyroxene solid solution

A suite of 6 synthetic Zn-clinopyroxene was analyzed by infrared spectroscopy at the Department of Geosciences, Swedish Museum of Natural History (Stockholm, Sweden), to investigate the vibrational bands related to the chain silicates and their trend across the solid solution.

The sample preparation consisted of polishing policrystalline sample (embedded in epoxy) to a typical thickness of 0.2-1.0 mm. Single crystals could not be oriented because of their tiny size, smaller than the thickness of section.

Unpolarized ATR (attenuated total reflection) spectra were recorded in the range 700-1200 cm^{-1} (14300-8300 nm) of the IR spectral region, using a Bruker Vertex 70 spectrometer equipped with a glow bar source, a KBr beam-splitter and a MCT detector using a Hyperion 2000 microscope with a ATR objective. The recorded spectra were fitted using the OriginLab software, assuming Gaussian peak shapes. The IR-powder spectra for the synthetic *C*2/*c* Zn-pyroxenes are shown in Figures 8.13 and 8.14.

For convenience, Zn-pyroxenes in Figures 8.13 and 8.14 are named Cpx_Zn10, Cpx_Zn13, Cpx_Zn15, Cpx_Zn17, Cpx_Zn18 and Cpx_Zn20, and are respectively related to the following compositions: $CaZnSi_2O_6$, $Ca_{0.7}Zn_{1.3}Si_2O_6$, $Ca_{0.5}Zn_{1.5}Si_2O_6$, $Ca_{0.3}Zn_{1.7}Si_2O_6$, $Ca_{0.2}Zn_{1.8}Si_2O_6$ and $Zn_2Si_2O_6$.

The frequency range examined corresponds to the series of strong peaks, related to tetrahedral bending and stretching, identified in the IR spectra for pyroxenes by Boffa Ballaran *et al.*, 2001. The characteristic infrared frequencies identified in the IR spectra, are reported in Table 8.5. From Table 8.5 and Figure 8.13, a comparison with the evolution of the peak positions with composition suggests that at least 7 modes are present in the series, each of them absent in some sample.

Moreover, for a Zn content higher than in $Ca_{0.5}Zn_{0.5}ZnSi_2O_6$, we need to split either the mode at 900 or that at 947 cm^{-1} in two modes, respectively at 892 and 918 cm^{-1} or at 918 and ca. 970 cm^{-1}. For the compositions $Zn_{1.7}$ and $Zn_{1.8}$, the band at ca. 1025 cm^{-1} is absent. We note that the region at ca. 900-950 cm^{-1} shifts towards the higher energy, while the 840 and 1040 cm^{-1} modes shift towards the lower energies (Figure 8.15). This can be related to the significant rearrangement in tetrahedral bond distances as Zn increases (see previous paragraph). As all the above peaks are related to tetrahedral stretching, there is an obvious link between the decrease in tetrahedral bond distances for the Si-O3bridging bond distances and an increase in peak frequency, whereas the opposite is expected in modes involving the stretching of Si-O1 and O2 non-bridging bonds. However, the definition of the split and an analysis of the above changes would require a modelling of the mode vibrations to ascribe each mode to a specific structural feature, which is beyond our scope.

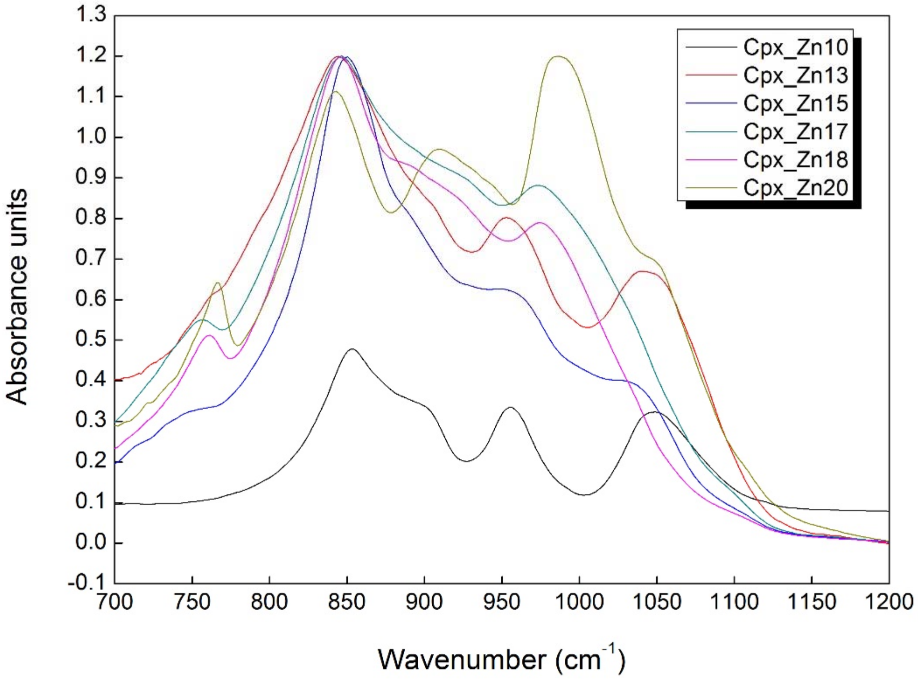

Figure 8.13. The IR-powder spectra for the synthetic *C*2/*c* Zn-pyroxenes, recorded in the 700-1200 cm^{-1} (14300-8300 nm) spectral range.

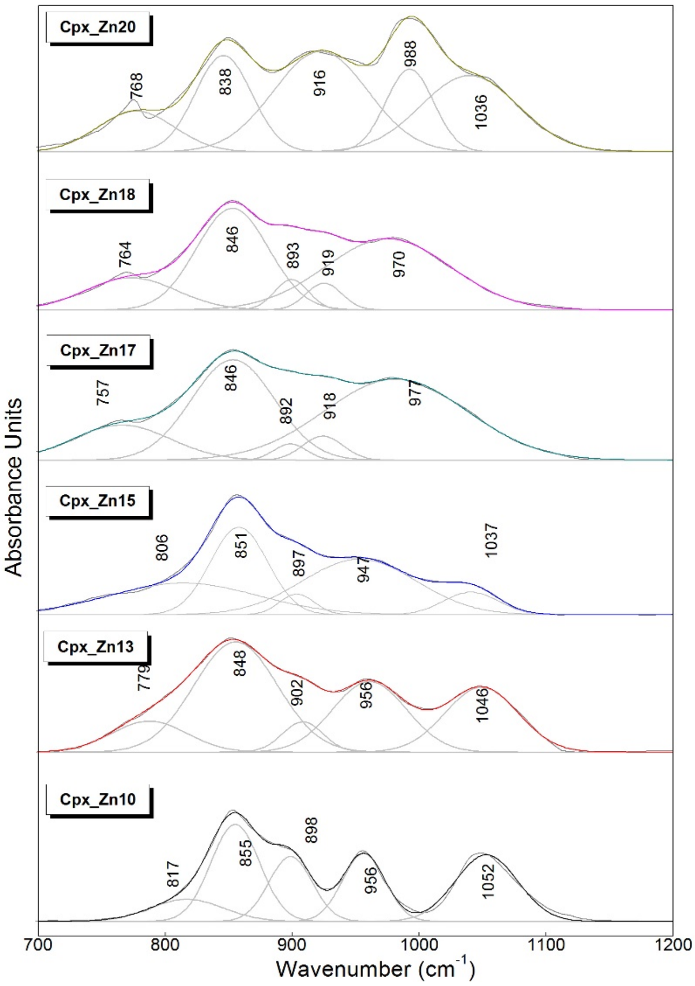

Figure 8.14. Fitted infrared powder spectra of *C*2/*c* synthetic clinopyroxenes recorded at room temperature.

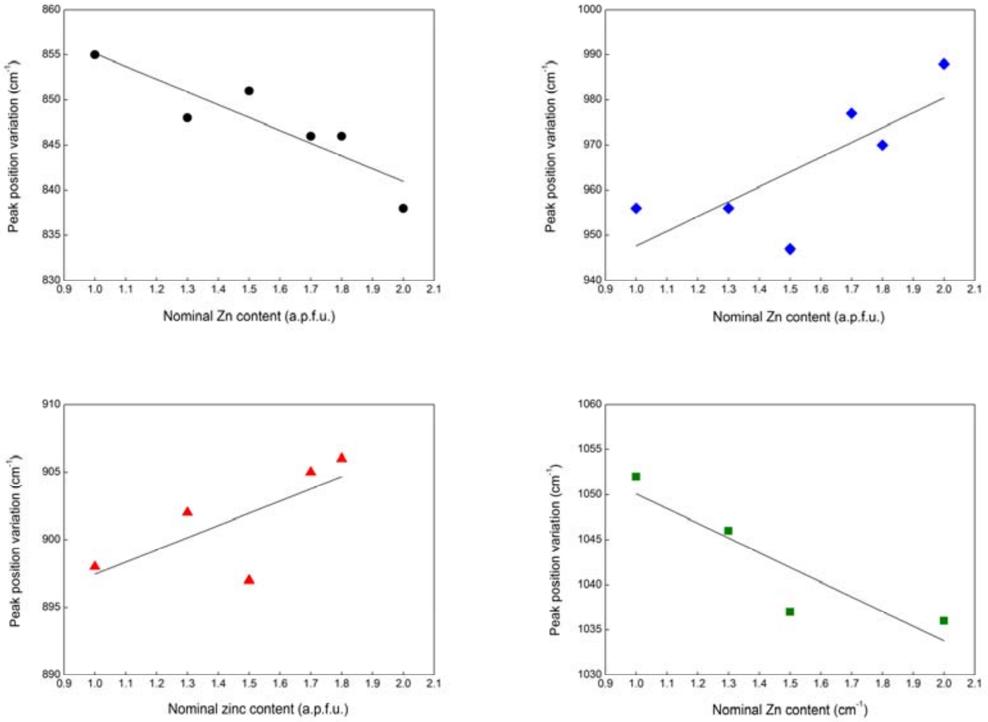

Figure 8.15. Peak position variation of the IR-bands.

TABLE 8.5. The peak wavelengths (in cm^{-1}) of the CaZn-ZnZn pyroxene series.

Ca-rich pyroxene	Solid solution				Zn-rich pyroxene
$CaZnSi_2O_6$	$Ca_{0.7}Zn_{1.3}Si_2O_6$	$Ca_{0.5}Zn_{1.5}Si_2O_6$	$Ca_{0.3}Zn_{1.7}Si_2O_6$	$Ca_{0.2}Zn_{1.8}Si_2O_6$	$Zn_2Si_2O_6$
	779		757	764	768
817		806			
855	848	851	846	846	838
898	902	897	892	893	
			918	919	916
956	956	947	977	970	988
1052	1046	1037			1036

Chapter 9

CONCLUDING REMARKS

9. CONCLUDING REMARKS

The present study gives a contribution to enlighten the crystal structures and the physical properties of pyroxenes with different chemical compositions. The effects of the cation substitutions of Co and Zn at the *M*1 and the *M2* sites on the crystal structure have been discussed.

The primary goal of this thesis has been the synthesis of the pyroxene phases with technological interest. $CaMgSi_2O_6$ (diopside)-$CaCoSi_2O_6$ (Co-pyroxene) solid solution has been synthesized and investigated by using different analysis techniques in order to give information about chemical, physical and crystallographic properties of the $CaCo_xMg_{1-x}Si_2O_6$ pyroxenes.

Structural changes induced by the cation substitution at the *M*1 site of a smaller cation ($^{VI}Mg^{2+}$ 0.72 Å) by a larger one ($^{VI}Co^{2+}$ 0.745 Å) in the calcium-magnesium pyroxene lattice ($CaCo_xMg_{1-x}Si_2O_6$), have shown the effect on the unit-cell volume and on the *M1* and *M2* polyhedral volumes.

Spectroscopic investigations (UV-VIS-NIR) have confirmed that the intense pink colour obtained in the synthesized pigments based on the $CaCo_xMg_{1-x}Si_2O_6$ pyroxene structure (*i.e.* 'Di-Co' pigments), is due to the absorption within the green-yellow region of the visible spectrum. The UV-VIS-NIR optical spectrum consists of three main optical absorption bands, which are the expected absorption bands for Co^{2+} ion in an octahedral site in the pyroxene structure, as reported in literature.

Magnetic measurements have explained how the antiferromagnetic interactions are related to the pyroxene crystal structure and depend on the intra-chain interactions involving the Co^{2+} ion. Magnetic characterization has shown also that the magnetic ordering in the $CaCo_xMg_{1-x}Si_2O_6$ pyroxene structure occurs only when 75% of the *M1* polyhedra are filled by Co^{2+} ions.

Technological tests have been performed by simulating the industrial processing of ceramic tiles and have shown that 'Di-Co' pigment applied into glazes, behaves like a dye, thus dissolving into the molten phase of the glaze and imparting a blue colour due to the diffusion of Co^{2+} ion into the glassy matrix, where it has a tetrahedral coordination.

Nevertheless, since the ‘Di-Co’ pigment synthesized with cobalt content (5 wt%, named ‘Di-Co20’) lower than conventional ceramic colorants (*i.e.* Co-spinel and Co-olivine pigments) maintains a blue colour under the ceramic treatments, it could be proposed as a blue pigment to minimize the Co content, thus improving manufacturing cost and sustainability. A possible drawback is the relatively high temperature of synthesis, at T ≥ 1200 °C. The ‘Di-Co20’ could be also used as a pink pigment, *e.g.* in painting, maintaining the pigment in a non-aggressive environment.

The second goal of this thesis has been to find the best synthesis conditions for the $CaZnSi_2O_6$ (petedunnite)-$Zn_2Si_2O_6$ (Zn-pyroxene) solid solution and to clarify the structure, preliminar to a study of the physical properties. A complete solid solution has been synthesized in Ca-Zn clinopyroxenes at a temperature of 1200 ºC and pressure of 4 GPa. The solid solution has been investigated by using powder and single crystal X-ray diffraction. Respect to Ca-Co, Ca-Mg and Ca-Fe pyroxenes showing the same Ca *vs.* metal substitution in the *M2* site, here we do not have a miscibility gap and no phase transition to a $P2_1/c$ structure. This is due to the peculiar properties of Zn in pyroxenes. Structural mechanism for the Ca-Zn substitution at the *M2* site in the pyroxene crystal lattice has shown that, in $C2/c$ clinopyroxenes, the coordination of Zn at the *M2* site is fourfold. Zn exhibits a preference for the *M2* site along the entire series because the *M2* cavity is more flexible and better suited to host the Zn cation in a four-fold coordination than the *M1* polyhedron, which is tighter and more regular. Incidentally, this crystal-chemical behaviour of zinc ion has a petrological implication, which results in a different partitioning of zinc between clinopyroxene and melt: a melt formed by clinopyroxene-rich source rocks is enriched in Zn.

Although Ca-Zn pyroxenes may be synthesized only in high pressure and high temperature conditions which are not easily reproducible in industrial applications, preliminary studies on their physical properties, in progress, have shown that the zinc pyroxene is an interesting material, which displays promising mechanical properties in terms of hardness, strength and electrical behaviour.

APPENDICES

APPENDIX A

Nomenclature of pyroxenes

The classification and nomenclature of the pyroxenes have been largely based on their crystal chemistry. Therefore it is necessary to subdivide the solid-solution series into ranges with specified compositions and names. Whenever there is a complete solid solution series between two end-members the mineral name is composed by the two end-member names A and B, resulting $A_{50}B_{50}$ (the 50% rule, Morimoto, 1988). The 50% rule has been applied to the Mg-Fe pyroxene series (En-Fs, ClinoEn-ClinoFs series), Ca pyroxene series (Di-Hd series) and Na pyroxene series (Jd-Ae series). However this rule cannot be applied rigorously to the Ca-Mg-Fe, Ca-Na and to the 'other' pyroxenes which show wide ranges of coupled substitutions. Taking this situation into account, 20 accepted names have been adopted as mineral species names of the pyroxenes (Table A.1). The 20 pyroxene species are grouped into six chemical subdivisions on the basis of the cation occupancy of the *M2* site and crystal chemical similarities (Morimoto, 1988). The pyroxenes which have been studied in my PhD project belong to the 'Ca-pyroxene mineral names' (see Table A.1).

The pyroxene formula $M2M1T_2O_6$, is obtained by the following procedure (Morimoto, 1988):

- sum *T* to 2.000 Si^{4+}, then Al^{3+} ,then Fe^{3+}.
- sum *M1* to 1.000 using all Al^{3+} and Fe^{3+} in excess of that used to fill the *T* sites. If there are insufficient Al^{3+} and Fe^{3+} to sum to 1.000, then add Ti^{4+}, Cr^{3+}, V^{3+}, Ti^{3+}, Zr^{4+}, Sc^{3+}, Zn^{2+}, Mg^{2+}, Fe^{2+} and Mn^{2+}, until the sum is 1.000.
- sum *M2* using all Mg^{2+}, Fe^{2+}, Mn^{2+} in excess that is used to fill the *M1* sites. Then add Li^{+}, Ca^{2+}, and Na^{2+}, until the sum close to 1.000.

An accurate site occupancy must be obtained and determined by structure determination because the distribution of cations among the sites is partially a function of temperature.

A method for classifying pyroxenes by their ideal site occupancies has been proposed by Bokij and Ginzburg (1985) where the *M1* and *M2* sites are considered together as a single *M* site (Table A.2).

TABLE A.1. Accepted pyroxene mineral names and their chemical subdivisions (Morimoto, 1988).

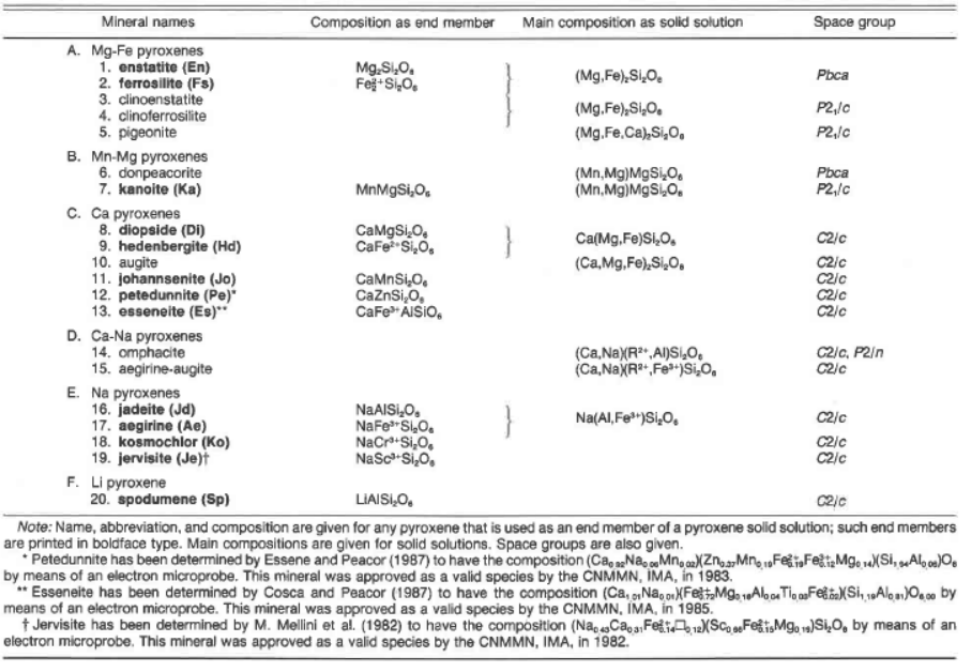

Mineral names	Composition as end member	Main composition as solid solution	Space group
A. Mg-Fe pyroxenes			
1. **enstatite (En)**	$Mg_2Si_2O_6$	$(Mg,Fe)_2Si_2O_6$	*Pbca*
2. **ferrosilite (Fs)**	$Fe_2^{2+}Si_2O_6$		
3. clinoenstatite		$(Mg,Fe)_2Si_2O_6$	$P2_1/c$
4. clinoferrosilite			
5. pigeonite		$(Mg,Fe,Ca)_2Si_2O_6$	$P2_1/c$
B. Mn-Mg pyroxenes			
6. donpeacorite		$(Mn,Mg)MgSi_2O_6$	*Pbca*
7. **kanoite (Ka)**	$MnMgSi_2O_6$	$(Mn,Mg)MgSi_2O_6$	$P2_1/c$
C. Ca pyroxenes			
8. **diopside (Di)**	$CaMgSi_2O_6$	$Ca(Mg,Fe)Si_2O_6$	*C2/c*
9. **hedenbergite (Hd)**	$CaFe^{2+}Si_2O_6$		
10. augite		$(Ca,Mg,Fe)_2Si_2O_6$	*C2/c*
11. **johannsenite (Jo)**	$CaMnSi_2O_6$		*C2/c*
12. **petedunnite (Pe)***	$CaZnSi_2O_6$		*C2/c*
13. **esseneite (Es)****	$CaFe^{3+}AlSiO_6$		*C2/c*
D. Ca-Na pyroxenes			
14. omphacite		$(Ca,Na)(R^{2+},Al)Si_2O_6$	*C2/c*, *P2/n*
15. aegirine-augite		$(Ca,Na)(R^{2+},Fe^{3+})Si_2O_6$	*C2/c*
E. Na pyroxenes			
16. **jadeite (Jd)**	$NaAlSi_2O_6$	$Na(Al,Fe^{3+})Si_2O_6$	*C2/c*
17. **aegirine (Ae)**	$NaFe^{3+}Si_2O_6$		
18. **kosmochlor (Ko)**	$NaCr^{3+}Si_2O_6$		*C2/c*
19. **jervisite (Je)†**	$NaSc^{3+}Si_2O_6$		*C2/c*
F. Li pyroxene			
20. **spodumene (Sp)**	$LiAlSi_2O_6$		*C2/c*

Note: Name, abbreviation, and composition are given for any pyroxene that is used as an end member of a pyroxene solid solution; such end members are printed in boldface type. Main compositions are given for solid solutions. Space groups are also given.

* Petedunnite has been determined by Essene and Peacor (1987) to have the composition $(Ca_{0.92}Na_{0.06}Mn_{0.02})(Zn_{0.37}Mn_{0.19}Fe^{2+}_{0.19}Fe^{3+}_{0.12}Mg_{0.14})(Si_{1.94}Al_{0.06})O_6$ by means of an electron microprobe. This mineral was approved as a valid species by the CNMMN, IMA, in 1983.

** Esseneite has been determined by Cosca and Peacor (1987) to have the composition $(Ca_{1.01}Na_{0.01})(Fe^{3+}_{0.72}Mg_{0.18}Al_{0.04}Ti_{0.03}Fe^{2+}_{0.02})(Si_{1.19}Al_{0.81})O_{6.00}$ by means of an electron microprobe. This mineral was approved as a valid species by the CNMMN, IMA, in 1985.

† Jervisite has been determined by M. Mellini et al. (1982) to have the composition $(Na_{0.43}Ca_{0.31}Fe^{2+}_{0.14}\square_{0.12})(Sc_{0.66}Fe^{2+}_{0.15}Mg_{0.19})Si_2O_6$ by means of an electron microprobe. This mineral was approved as a valid species by the CNMMN, IMA, in 1982.

TABLE A.2. Four coupled substitutions* of pyroxenes in the standard chemical formula $R^{2+}R^{2+}R_2^{4+}O_6$ (Morimoto, 1988). *shown by parentheses

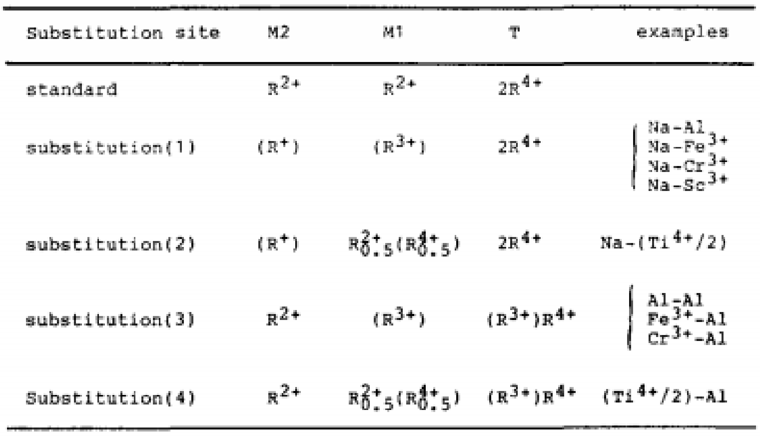

Substitution site	M2	M1	T	examples
standard	R^{2+}	R^{2+}	$2R^{4+}$	
substitution(1)	(R^{+})	(R^{3+})	$2R^{4+}$	Na-Al Na-Fe^{3+} Na-Cr^{3+} Na-Sc^{3+}
substitution(2)	(R^{+})	$R^{2+}_{0.5}(R^{4+}_{0.5})$	$2R^{4+}$	Na-(Ti^{4+}/2)
substitution(3)	R^{2+}	(R^{3+})	$(R^{3+})R^{4+}$	Al-Al Fe^{3+}-Al Cr^{3+}-Al
Substitution(4)	R^{2+}	$R^{2+}_{0.5}(R^{4+}_{0.5})$	$(R^{3+})R^{4+}$	(Ti^{4+}/2)-Al

APPENDIX A

Starting from the most common pyroxene formula $M2(R^{2+})$ $M1(\mathrm{R}^{2+})$ $T_2(2R^{4+})\mathrm{O}_6$, four coupled substitutions are possible if one assumes more than one R^{4+} in the T site. Substitution (1) encompasses the end-member jadeite ($NaAlSi_2O_6$), aegirine ($NaFe^{3+}Si_2O_6$), kosmochlor ($NaCr^{3+}Si_2O_6$) and jervisite ($NaScSi_2O_6$). Subsitution (2) results in components such as $NaFe^{2+}_{0.5}\ Ti^{4+}_{0.5}\ Si_2O_6$ and is less important than the other substitutions. Substitution (3) show that the Al-Al couple is often referred to as 'Tschermark's component'; $CaAlAlSiO_6$ is the calcium Tschermark's component. This type of substitution occurs in esseneite ($CaFe^{3+}AlSiO_6$), fassaite and in pyroxenes from the Allende meteorites (Dowty and Clark, 1973; Mason 1974). Substitution (4) show the component $CaMg_{0.5}\ Ti^{4+}_{0.5}\ AlSiO_6$ that is found in some pyroxenes. No particular names are given for the end-member components of substitutions (2) and (4).

Pyroxene name minerals

Clinopyroxenes (monoclinic)

Aegirine (Sodium Iron Silicate, $NaFe^{3+}Si_2O_6$)

Augite [Calcium Sodium Magnesium Iron Aluminium Silicate, $(Ca,Na)(Mg,Fe,Al,)(Si,Al)_2O_6$]

Clinoenstatite (Magnesium Silicate, $MgSiO_3$)

Diopside (Calcium Magnesium Silicate, $CaMgSi_2O_6$)

Esseneite (Calcium Iron Aluminium Silicate, $CaFe_{3+}AlSiO_6$)

Hedenbergite (Calcium Iron Silicate, $CaFeSi_2O_6$)

Hypersthene (Magnesium Iron Silicate, $(Mg,Fe)SiO_3$)

Jadeite (Sodium Aluminium Silicate, $NaAlSi_2O_6$)

Jervisite [Sodium Calcium Iron Scandium Magnesium Silicate, $(Na,Ca,Fe^{2+})(Sc,Mg,Fe^{2+})Si_2O_6$]

Johannsenite (Calcium Manganese Silicate, $CaMnSi_2O_6$)

Kanoite [Manganese Magnesium Silicate, $(Mn^{2+},Mg)_2Si_2O_6$]

Kosmochlor (Sodium Chromium Silicate, $NaCr^{3+}Si_2O_6$)

Namansilite (Sodium Manganese Silicate, $NaMn^{3+}Si_2O_6$)

Natalyite [Sodium Vanadium Chromium Silicate, $Na(V^{3+},Cr^{3+})Si_2O_6$]

Omphacite [Calcium Sodium Magnesium Iron Aluminium Silicate, (Ca,Na)(Mg,Fe,Al)Si_2O_6]

Petedunnite (Calcium Zinc Silicate, $CaZnSi_2O_6$)

Pigeonite [Calcium Magnesium Iron Silicate, $(Mg,Fe^{2+},Ca)(Mg,Fe^{2+})Si_2O_6$]

Spodumene (Lithium Aluminium Silicate, $LiAlSi_2O_6$)

Orthopyroxenes (orthorhombic)

Hypersthene [Magnesium Iron Silicate, $(Mg,Fe)SiO_3$]

Donpeacorite, $(MgMn)MgSi_2O_6$

Enstatite, $Mg_2Si_2O_6$

Ferrosilite, $Fe_2Si_2O_6$

Nchwaningite [Hydrated Manganese Silicate, $Mn_2^{2+}SiO_3(OH)_2 \bullet (H_2O)$]

Schefferite, $Ca(Mg,Fe,Mn)Si_2O_6$

Zinc schefferite, $Ca(Mg,Mn,Zn)Si_2O_6$

Jeffersonite, $Ca(Mg,Fe,Mn,Zn)Si_2O_6$

Leucaugite, $Ca(Mg,Fe,Al)(Al,Si)_2O_6$

Calcium-Tschermak's molecule, $CaAlAlSiO_6$

APPENDIX B

Ca-deficient flux-grown samples

The chemical, crystallographic and UV-VIS-NIR investigations were performed also on two samples with x= 0.5 and 1 Co atoms per formula unit (a.p.f.u.) which were grown using Ba-borate flux and with calcium content added in deficient quantities in the reagent precursors. These samples were named as 'Di-Co50_Cadef.' and 'Co100_Cadef.'

In order to avoid redundant part, we don't give a description of the experimental methodologies used because are the same adopted to investigate the flux(A)- and melt-grown samples (Chapter 5).

In the syntheses, the runs are the same to those performed for the flux(A)-grown samples and the products are pyroxene single crystals elongated along the c-axis with dimensions up to 1 mm and pink in colour. Electron backscattered images of Di-Co50_Cadef. and Co100_Cadef. in Figure B.1., show that crystals are less well shaped than the flux(A,B)-grown samples (Chapter 5, Figures 5.6 and 5.7).

Site occupancies and crystal chemical formulae of 'Ca-def.' samples were obtained taking into account the cation distribution between the *M1* and the *M2* sites, normalizing the number of cations to four, the results of single crystal X-ray diffraction and UV-VIS-NIR spectroscopy. Flux-grown 'Cadef.' crystals are free of impurities. The results of chemical WDS analyses performed on flux-grown 'Cadef.' samples are reported in Table B.1.

Like the flux(A)-grown samples, flux-'Cadef.' have tetrahedral sites completely filled by stoichiometric Si (Si= 2.00 a.p.f.u.) as revealed by both the refinement of site occupancies, and by the constant value of the <*T*-O> bond distances, to a value of 1.630 Å (Hugh Jones *et al.*, 1994). In all samples the measured Ca does not fill completely the *M2* site (see Table B.1); Co and Mg can be expected to be distributed over the *M1* and *M2* positions, with a preference of Co for the *M2* position due to its larger size and degree of distortion.

Di-Co50_Cadef.

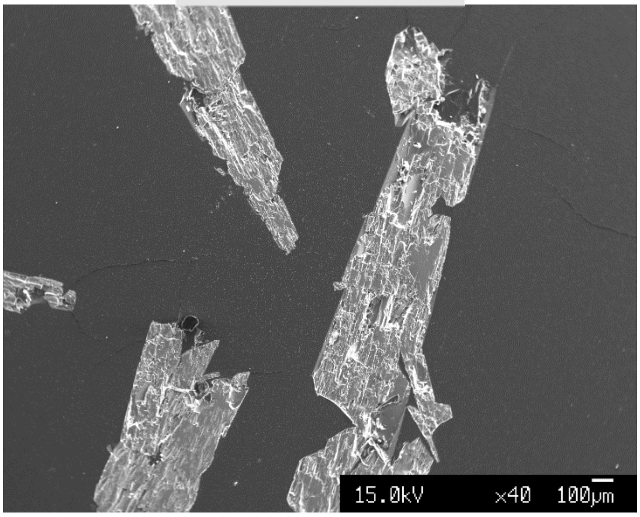

Co100_Cadef.

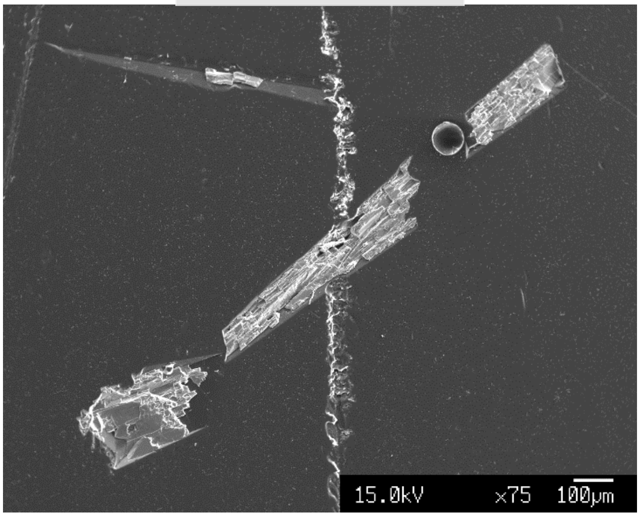

Figure B.1. Backscattered images of ‘Ca-deficient’ flux-grown samples: above Di-Co50_Cadef. sample, below Co100_Cadef. sample.

TABLE B.1. Chemical analyses

Flux-grown	Di-Co50_Cadef.	Co100_Cadef.
Oxide (wt.%)	*El. mass%*	*El. mass%*
Na^+	0.01	0.01
Ba^{2+}	0.03	0.02
Co^{2+}	12.73	32.80
Ca^{2+}	21.41	19.46
Mg^{2+}	13.53	0.11
Si^{4+}	52.58	47.97
Total:	**100.29**	**100.36**
Cation (a.p.f.u.)	Norm. El%	Norm. El%
Na^+	0	0
Ba^{2+}	0	0
Co^{2+}	0.39	1.10
Ca^{2+}	0.87	0.87
Mg^{2+}	0.76	0.01
Si^{4+}	1.99	2.01
Sum	**4.01**	**3.99**

The absorption spectra were measured along the three optical indicatrix directions (E//X, *i.e.* α ; E//Y, *i.e.* β; E// Z, *i.e.* γ) for Di-Co50_Cadef. (Figure B.2), while they were measured only along two (α, γ directions) for Co100_Cadef. crystal (Figure B.2) because it was not possible to find a crystal which could be suitably oriented on (100) or (001). Polarized, room-temperature optical absorption spectra were recorded in spectral range 30000-2000 cm^{-1} (333-5000 nm) and are dominated by the three set of absorption bands which originate from the electronic transitions of Co^{2+} in an octahedral ligand field (Llusar *et al.*, 2001, Taran and Rossmann, 2001), as discussed for melt and flux(A)-grown spectra (Chapter 6, paragraph 6.3.1). Like the flux(B)-grown samples (Chapter 6, paragraph 6.3.2) and unlike those melt and flux(A), the absorption band at ca. 14000 cm^{-1} (714 nm), that occurs only in γ polarized and is splitted in two strong absorption peaks, is probably due to Co^{2+} at the *M2* site. This confirms the results obtained from EMPA and single-crystal refinements.

Figure B.2 shows the absorption bands which fall within the 28000-4000 cm^{-1} (357-2500 nm) spectral range. The superposition of the electronic transitions in Co in the *M1* and *M2* sites, gives overlapping lines, that appears as a continuous absorption band.

The resultant curve fitting of the UV-VIS-NIR absorption spectra of representative polarized single crystals, are plotted in Figure B.3. The position of the most intense bands [$^4T_{1g}$ (P)**]** which is located within the green-yellow region of the visible spectrum [like the flux(A)- and melt-grown samples] explains the pink colour of the synthetic flux-'Cadef.' crystals.

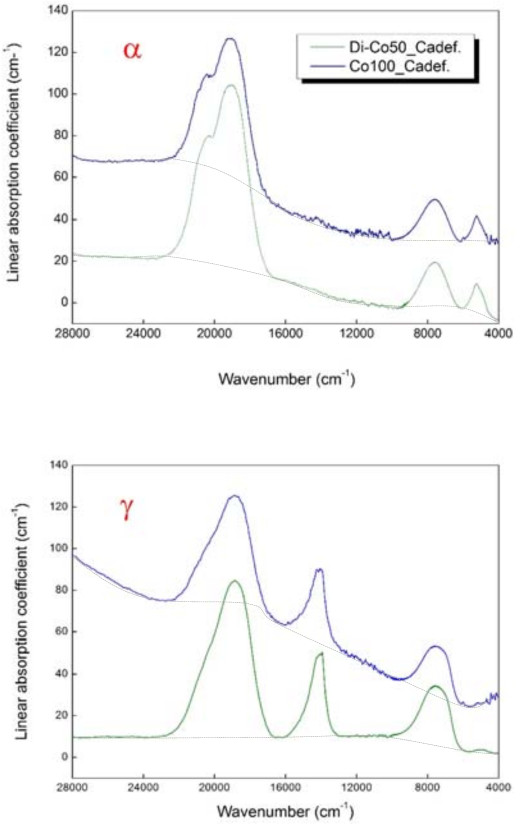

Figure B.2. Polarized optical absorption spectra of 'Ca-deficient' flux-grown samples, from Di-Co50_Cadef. (bottom) to Co100_Cadef. (top) in the 28000-4000 cm^{-1} (357-2500 nm) spectral range, along the α and γ optical indicatrix directions. These spectra are represented between 28000-4000 cm^{-1}, because of the lack of absorption bands at lower frequencies (4000-2000 cm^{-1}, 2500-5000 nm) and at frequencies higher than 28000 cm^{-1} (357 nm). The thin dotted lines represent the polynomial curve fitting used to obtain the baseline subtraction from each spectrum.

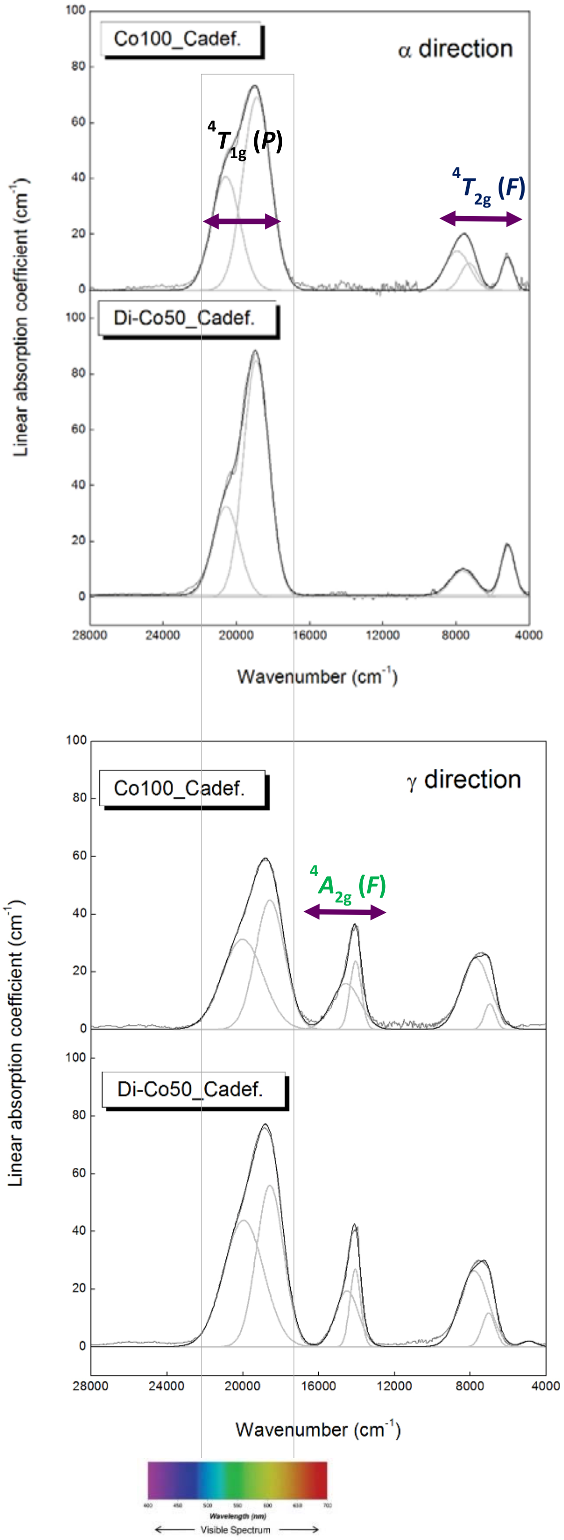

Figure B.3. Deconvolution of the α and γ polarized OAS and NIR spectra of Di-Co50_Cadef. and Co100_Cadef. flux-grown samples for the 28000-4000 cm^{-1} (375-2500 nm) spectral range, after baseline subtraction.

The peak positions of the absorption bands as determined from the peak-fitting procedure and their assignments are summarized in Table B.2.

TABLE B.2. Band frenquencies in cm^{-1} (average value along the optical indicatrix directions, *i.e.* α, β and γ for Di-Co50_Cadef.; α and γ for Co100_Cadef.) and assignments for 'Ca-deficient' flux-grown samples. The values for the 4800-5300 cm^{-1} spectral range are two in Di-Co50_Cadef. because along β direction the band is splitted while there is one value in the same spectral range for Co100_Cadef., since it was measured only along α and γ directions.

$CaCo_xMg_{1-x}Si_2O_6$		Assignment
$x = 0.50$	$x = 1$	
4890(3)	5079(1)	$T_{1g} \rightarrow T_{2g}$ (F)
5160(2)	-	
7200(13)	7240(4)	
8070(9)	8080(58)	
14050(3)	14060(4)	$T_{1g} \rightarrow A_{2g}$ (F)
14530(19)	14570(36)	
18800(10)	18740(12)	$T_{1g} \rightarrow T_{1g}$ (P)
20280(32)	20300(32)	

APPENDIX C

Multi Anvil Walker-type Press

A Multi-anvil apparatus (Figure C.1) is one of a class of devices used to generate high pressure in the laboratory. In particular, they are part of a class of high pressure devices called Large Volume Presses (LVP), because the pressurized volume is on the order of millimeters or larger as opposed to the Diamond Anvil Cell (DAC) for which the pressurized volume is on the order of tens of microns. The name multi-anvil refers to the fact that the pressure is achieved by compressing the sample volume with a number (typically 4 or 6) of hard anvils.

A multianvil apparatus allows us to perform:

- high-pressure experiments (at high temperature)
- high-pressure deformation experiments (at high temperature).

Multi anvil apparatus is used between 2.5 and 25 GPa and up to ~2500 K (Figure C.2). The high-pressure experiments with a multianvil apparatus enable us to study phase transitions, phase equilibria, physical properties and are useful for studies on the Earth's interior and high-pressure synthesis of materials.

‘Multi’ comes from the fact that there are actually two different sets of anvils: 6 outer anvils made of hardened steel which transmit the force onto 8 inner anvils made of tungsten carbide cubes. A corner of each tungsten carbide anvil is truncated, which creates an octahedral void at the center of the 8 inner anvils.

For achiving pressure from 2.5 GPa to 25 GPa it is possible to use different sizes of MgO octahedrons (smaller for higher pressures) and the cube truncations should also be variable to cover the whole pressure range (Figure C.3).

The multianvil geometry converts the applied uniaxial force of the press into a more isotropic force surrounding the sample, thereby minimizing differential stresses that may influence the results of the experiment. Samples are of the order of only milligrams to tens of milligrams in amount, but in sufficient quantity for a variety of analytical techniques.

Figure C.1. Multi Anvil Walker-type Press at *IMEM*-CNR, Parma, Italy.

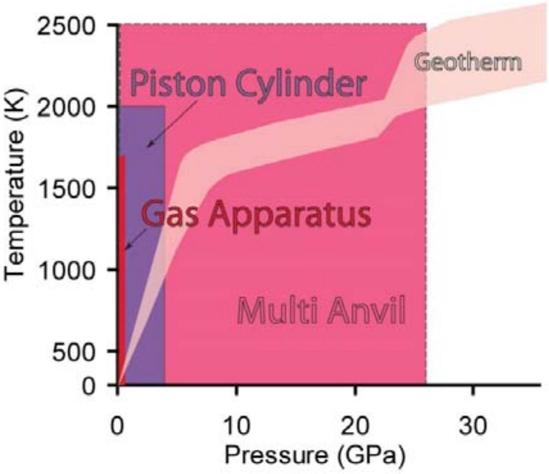

Figure C.2. Pressure and temperature conditions achievable in common large volume presses (image from http://serc.carleton.edu/NAGTWorkshops/mineralogy/mineral_physics/multi_anvil.html).

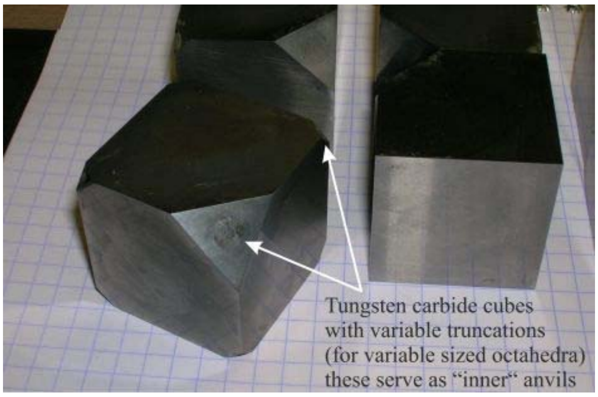

Figure C.3. Tungsten carbide cubes with different truncation lengths (image from enikobali.hupont.hu/6/high-pressure-and-temperature-experiments-pressure.

A multi-anvil apparatus is constituted of three main components: 1) a hydraulic press (Figure C.4) that provides the force and it is used to drive the anvils together, 2) a high pressure module (Walker-type module) that contains the anvils and 3) a sample assembly. All the high pressure devices utilize the principle that pressure (P) is equal to an applied force (F) divided by the area (A) over which it is applied (P= F/A). Therefore, pressure can be increased by reducing the area over which force is applied.

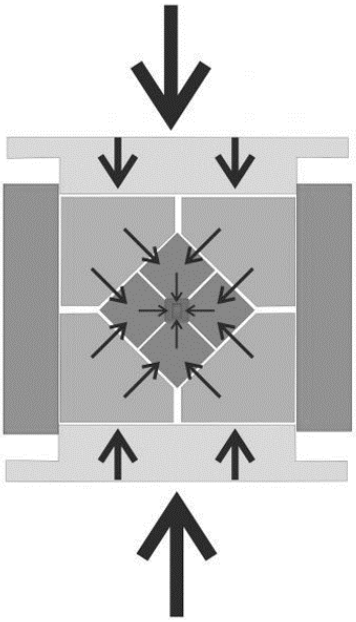

Figure C.4. Pressure generation by a hydraulic press. (image from enikobali.hupont.hu/6/high-pressure-and-temperature-experiments-pressure).

The pressure medium plays a very important role in the generation of high pressure. The pressure medium is larger than the space between the anvil when the anvils are touching (Figures C.5 and C.6). During pressurization, the pressure medium squeezes out into the spaces between the anvils until the friction between the pressure media and the anvils balances the pressure generated inside the sample assembly. Another function of the pressure media is to provide electrical insulation between the furnace, anvils, sample and any thermocouple or other sensor wires. The most commonly used materials are boron epoxy, mullite and pyrophyllite.

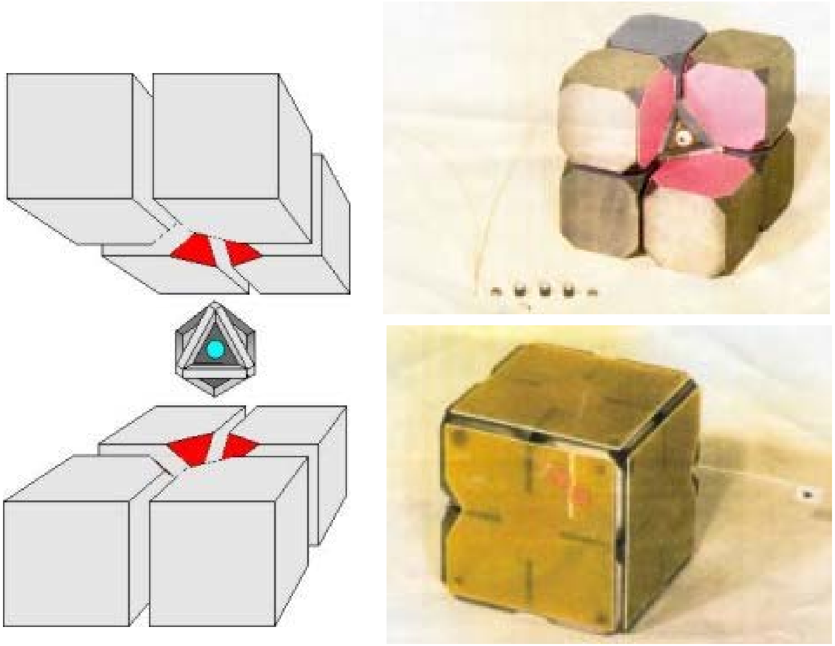

Figure C.5. Assembling of the 'inner' anvils. Anvils should be insulated from each other, otherwise it isn't possible to heat the experiment (image from ncemp.org/MultiAnvil.htm).

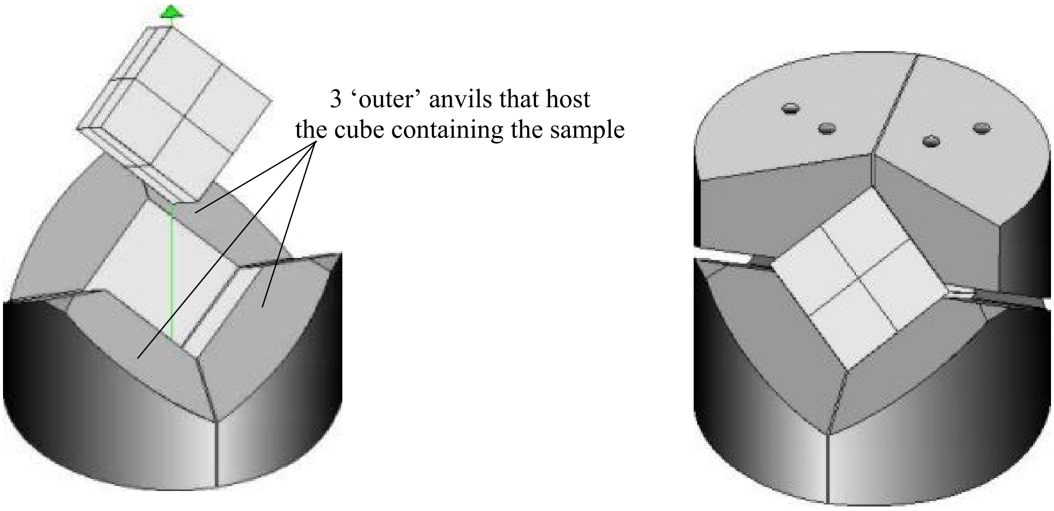

Figure C.6. The assembled cubes are put among the second set of 'outer' anvils which are formed to host the cube with the sample. These 'outer' anvils are than closed and pressurized by a hydraulic press (image from ncemp.org/MultiAnvil.htm).

Sample assemblies vary widely in design and size depending on the pressure (*P*) temperature (*T*) conditions desired and what type of experiment is conducted.

Noble metal capsules containing the starting material are placed in the hot spot of the furnace. An axial Pt-Pt13%Rh thermocouple (type S) is in direct contact with the capsule and control the temperature. MgO spacers and ceramic insulators are placed around the capsule and the thermocouple. Graphite discs on both the ends of the assembly provide electrical contact with the WC cubes (Figures C.7).

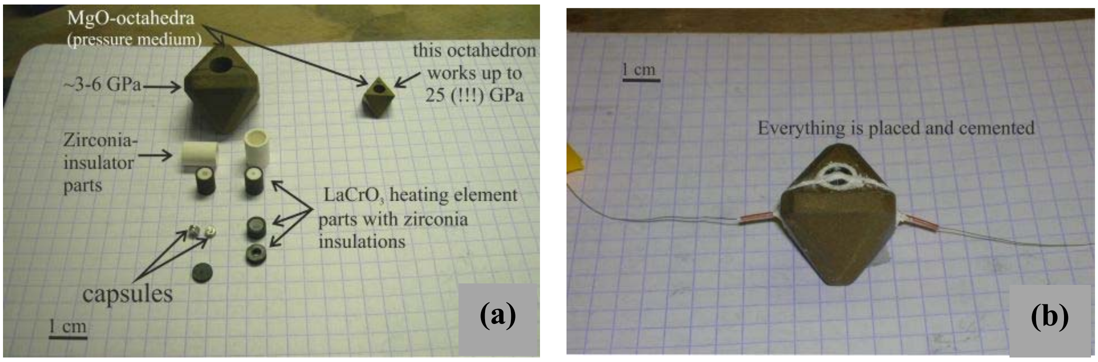

Figure C.7. (**a**) Different components of Pressure Media of Multi-Anvil apparatus. (**b**) Thermocouples at the sides of the octhedron (image from enikobali.hupont.hu/6/high-pressure-and-temperature-experiments-pressure).

The typical synthesis procedure is characterized by three operations which are mandatory stages to achieve reproducible results and to prevent mechanical and/or structural damages. Firstly the pressure is gradually increased from room pressure (100 KPa-1 bar) to the set-point pressure of the experiment whit a ramp rate of about 500-700 Pa/m. Secondly the system is Joule-heated from room temperature to the set-point temperature of the experiment, after reaching the set-point pressure. This temperature must be kept for few hours. Finally, at the end of the experiment, the system is quenched down to room temperature or the temperature of the system is slowly decreased with a controlled thermal ramp. When the measured external temperature of the outer surface of Walker-type module is equal to the internal temperature, the pressure is slowly released to the room pressure with a ramp of about 300 Pa/min.

The thermal quenching is applied to ‘freeze’ the obtained high-pressure phase and to stabilize its crystallographic structure.

BIBLIOGRAPHY

Adam, J. and Green, T. (2006). Trace element partitioning between mica-and amphibole-bearing garnet lherzolite and hydrous basanitic melt: 1. Experimental results and the investigation of controls on partitioning behavior. *Contributions to Mineralogy and Petrology*, **152**, 1-17.

Akimoto, S., Katsura, T., Syono, Y., Fujisawa, H. and Komada, E. (1965). Polymorphic transition of pyroxenes FeSiO, and CoSiO, at high pressures and temperatures. *Journal of Geophysical Research*, **70**, 5269- 5278.

Anderson, D.L. (1989). Theory of the Earth. Blackwell Scientific, Boston.

Angel, R.J. and Hugh-Jones, D.A. (1994). Equations of state and thermodynamic properties of enstatite pyroxenes. Journal of Geophysical Research, **99**, 19777–19783.

Angel, R.J., Chopelas, A. and Ross, N.L. (1992a). Stability of high-density clinoenstatite at upper-mantle pressures. Nature, **358**, 322-324.

Ardit, M., Cruciani, G. and Dondi, M. (2012). Local structural relaxation around Co^{2+} along the hardystonite–Co-åkermanite melilite solid solution. *Physics and Chemistry of Minerals*, **39**, 713-723.

Arlt, T. and Angel, R.J. (2000). Displacive phase transitions in *C*-centered clinopyroxenes: spodumene, $LiScSi_2O_6$ and $ZnSiO_3$. *Physics and Chemistry of Minerals*, **27**, 719-731.

Arlt, T., Kunz, M., Stolz, J., Armbruster, T. and Angel, R.J. (2000). PTX data on *P21/c*-clinopyroxenes and their displacive phase transitions. *Contributions to Mineralogy and Petrology*, **138**, 35-45.

Balic Zunic, T. and Vickovic, I. (1996). IVTON: a program for the calculation of geometrical aspects of crystal structures and some crystal chemical applications. *Journal of Applied Crystallography*, **29**, 305-306.

Ballhausen, C.J. and Weiner, M.A. (1963). Introduction to ligand field theory. *Journal of The Electrochemical Society*, **110**, 97C-97C.

Benna, P., Tribaudino, M. and Bruno, E. (1988). Crystal structure of $Di_{50}CaTs_{50}$ synthetic clinopyroxene ($CaMg_{0.5}AlSi_{1.5}O_6$). Crystal chemistry along the Di-CaTs join. *Mineralogy and Petrology*, **38**, 189-200.

Blundy, J. and Wood, B. (2003). Partitioning of trace elements between crystals and melts. *Earth and Planetary Science Letters*, **210**, 83-397.

Boffa Ballaran, T., Carpenter, M.A. and Ross, N.L. (2001). Infrared powder-absorption spectroscopy of Ca-free $P2_1/c$ clinopyroxenes. *Mineralogical Magazine*, **65**, 339-350.

Bokij, G. B. and Ginzburg, J. V. (1985). The systematics of mineral species in pyroxene family. *Trans. IGG Academy of Sciences*, Novosibirsk, **610**, 12-35.

Boyd, F.R. and Schairer, J.F. (1964). The System $MgSiO_3$-$CaMgSi_2O_6$. *Journal of Petrology*, **5**, 275-309.

Bruno, E., Carbonin, S. and Molin, G.M. (1982). Crystal structure of Ca-rich clinopyroxenes on the $CaMgSi_2O_6$-$Mg_2Si_2O_6$ join. *Tschermaks Mineralogische und Petrographische Mitteilungen*, **29**, 223-240.

Burnham, C.W., Clark, J.R., Papike, J.J. and Prewitt, C.T. (1967). A proposed crystallographic nomenclature for clinopyroxene structures. *Zeitschrift für Kristallographie-Crystalline Materials*, **125**, 109-119.

Burns, R.G. (1993). Mineralogical applications of crystal field theory, Vol. **5**, Cambridge University Press.

Cameron, M. and Papike, J.J. (1980). Crystal chemistry of silicate pyroxenes. *Reviews in Mineralogy and Geochemistry*, **7**, 5-92.

Cameron, M. and Papike, J.J. (1981). Structural and chemical variations in pyroxenes. *American Mineralogist*, **66**, 1-50.

Cameron, M., Sueno, S., Prewitt, C.T. and Papike, J.J. (1973). High-temperature crystal chemistry of acmite, diopside, hedenbergite, jadeite, spodumene and ureyte. *American Mineralogist*, **58**, 594-618.

Carpenter, M.A., Salje, E.K. and Graeme-Barber, A. (1998). Spontaneous strain as a determinant of thermodynamic properties for phase transitions in minerals. *European Journal of Mineralogy*, **10**, 621-691.

Colomban, P. (2013). Rocks as blue, green and black pigments/dyes of glazed pottery and enameled glass artefacts, a review. *European Journal of Mineralogy*, **25**, 863-879.

Deer, W.A., Howie, R.A. and Zussman, J. (1992). An introduction to the rock-forming minerals (Vol. **696**). London: Longman.

Delamare, F. (2013). Recherches sur l'érosion des grès des monuments d'Angkor. *Bulletin de l'École Française d'Extrême-Orient*, **52**, 453-534.

Domeneghetti, M.C., Molin, G.M., Stimpfl, M. and Tribaudino, M. (1995). Orthopyroxene from the Serra de Magé meteorite: structure refinement and estimation of *C2/c* pyroxene contributions to apparent *Pbca* diffraction violations. *American Mineralogist*, **80**, 923-929.

Dondi, M. and Eppler, R. A. (2014). Ceramic Colorants. Ullmann's Encyclopedia of Industrial Chemistry.

Dondi, M., Zanelli, C., Ardit, M., Cruciani, G., Mantovani, L., Tribaudino, M. and Andreozzi, G. B. (2013). Ni-free, black ceramic pigments based on Co-Cr-Fe-Mn spinels: A reappraisal of crystal structure, colour and technological behaviour. *Ceramics International*, **39**, 9533-9547.

Dondi, M., Ardit, M., Cruciani, G. and Zanelli, C. (2014). Tetrahedrally cooordinted Co^{2+} in oxides and silicates: Effect of local environment on optical properties. *American Mineralogist*, **99**, 1736-1745.

Doroshev, A.M., Olesch, M., Logvinov, V. M. and Malinovsky, I.J. (1983). High pressure stability of zinc clinopyroxene $ZnSiO_3$ and the occurrence of a new polytype of zinc orthosilicate Zn_2SiO_4 as a breakdown product. *Neues Jahrbuch für Mineralogie, Monatshefte*, **6**, 277-288.

Downs, R.T. (2003). Topology of the pyroxenes as a function of temperature, pressure, and composition as determined from the procrystal electron density. *American Mineralogist*, **88**, 556-566.

Dowty, E. and Clark, J.R. (1973). Crystal structure refinement and optical properties of a Ti^{3+} fassaite from the Allende meteorite. *American Mineralogist*, **58**, 230-242.

Durand, G., Vilminot, S., Rabu, P., Derory, A., Lambour, J.P. and Ressouche, E. (1996). Synthesis, Structure, and Magnetic Properties of $CaMSi_2O_6$ (M= Co, Ni) Compounds and Their Solid Solutions. *Journal of Solid State Chemistry*, **124**, 374-380.

Eeckhout, S.G., Grave, E.D., Lougear, A., Gerdan, M., McCammon, C.A., Trautwein, A.X. and Vochten, R. (2001). Magnetic properties of synthetic $P2_1/c$ (Mg-Fe)SiO_3 clinopyroxenes as observed from their low-temperature Mössbauer spectra and from SQUID magnetization measurements. *American Mineralogist*, **86**, 957-964.

Essene, E.J. and Peacor, D.R. (1987). Petedunnite ($CaZnSi_2O_6$), a new zinc clinopyroxene from Franklin, New Jersey, and phase equilibria for zincian pyroxenes. *American Mineralogist*, **72**, 157-166.

Farrugia, L.J. (1999). WinGX suite for small-molecule single-crystal crystallography. *Journal of Applied Crystallography*, **32**, 837-838.

Fehr, K.T. and Huber, A.L. (2001). Stability and phase relations of Ca $[ZnSi_3]$ O_8, a new phase with feldspar structure in the system CaO-ZnO-SiO_2. *American Mineralogist*, **86**, 21-28.

Forés, A., Llusar, M., Badenes, J.A., Calbo, J., Tena, M.A. and Monrós, G. (2000). Cobalt minimisation in willemite ($Co_xZn_{2-x}SiO_4$) ceramic pigments. *Green Chemistry*, **2**, 93-100.

Galkin, V., Kuznetsov, G. and Turkin, A. (2007). Thermal expansion of $ZnSiO_3$ high-pressure phases. *Physics and Chemistry of Minerals*, **34**, 377-381.

Gasparik, T. (1989). Transformation of enstatite-diopside-jadeite pyroxenes to garnet. *Contributions to Mineralogy and Petrology*, **102**, 389-405.

Gasparik, T. (1990). Phase relations in the transition zone. *Journal of Geophysical Research: Solid Earth*, **95**, 15751-15769.

Gasparik, T. and Lindsley, D.H. (1980). Phase equilibria at high pressure of pyroxenes containing monovalent and trivalent ions. *Reviews in Mineralogy and Geochemistry*, **7**, 309-339.

Ghomi, H., Fathi, M.H. and Edris, H. (2012). Fabrication and characterization of triple nanobioceramic composite foam. *Journal of Composite Materials*, **46**, 1809-1817.

Ghose, S., Wan, C., Okamura, P., Ohashi, H. and Weidner, J.R. (1975). Site preference and crystal-chemistry of transition-metal ions in pyroxenes and olivines. Acta Crystallographica, **A31**, S76 35.

Ghose, S., Wan, C. and Okamura, F.P. (1987). Crystal structures of $CaNiSi_2O_6$ and $CaCoSi_2O_6$ and some crystal-chemical relations in $C2/c$ clinopyroxenes. *American Mineralogist*, **72**, 375-381.

Gori, C., Tribaudino, M., Mantovani, L., Delmonte, D., Mezzadri, F., Gilioli, E. and Calestani, G. (2015). Ca-Zn solid solutions in $C2/c$ pyroxenes: Synthesis, crystal structure, and implications for Zn geochemistry. *American Mineralogist*, **100**, 2209-2218.

Gori, C., Tribaudino, M., Mantovani, L., Gatta, G.D., Delmonte, D., Mezzadri, F., Gilioli, E. and Calestani, G. (2016). Synthesis and crystal structure of $C2/c$ Ca(Co, Mg)Si_2O_6 pyroxenes: effect of the cationic substitution on the cell volume. *Mineralogical Magazine,* https://doi.org/10.1180/minmag.2016.080.160.

Hålenius, U., Andreozzi, G.B. and Skogby, H. (2010). Structural relaxation around Cr^{3+} and the red-green color change in the spinel (sensu stricto)-magnesiochromite ($MgAl_2O_4$-$MgCr_2O_4$) and gahnite-zincochromite ($ZnAl_2O_4$-$ZnCr_2O_4$) solid-solution series. *American Mineralogist*, **95**, 456-462.

Heuer, M., Huber, A. and Bromile, G. (2002a). Crystal structure of calcium iron zinc catena-disilicate, Ca ($Fe_{0.52}$ $Zn_{0.48}$) Si_2O_6. *Zeitschrift für Kristallographie-New Crystal Structures*, **217**, 465.

Heuer, M., Huber, A. and Redhammer, G.J. (2002b). Crystal structure of calcium iron zinc catena-disilicate, Ca ($Fe_{0.19}$ $Zn_{0.81}$) Si_2O_6. *Zeitschrift für Kristallographie-New Crystal Structures*, **217**, 467.

Heuer, M., Huber, A.L., Bromiley, G.D., Fehr, K.T. and Bente, K. (2005). Characterization of synthetic hedenbergite ($CaFeSi_2O_6$)-petedunnite ($CaZnSi_2O_6$) solid solution series by X-ray single crystal diffraction. *Physics and Chemistry of Minerals*, **32**, 552-563.

Huber, A.L. and Fehr, K.T. (2003). Thermodynamische Eigenschaften der Mischreihe Hedenbergit-Petedunnit Ca (Fe, Zn) Si_2O_6. *Mitteilungen der Österreichischen Mineralogischen Gesellschaft*, **48**, 172-173.

Huber, A.L., Heuer, M., Fehr, K.T., Bente, K., Schmidbauer, E. and Bromiley, G.D. (2004). Characterization of synthetic hedenbergite ($CaFeSi_2O_6$)–petedunnite ($CaZnSi_2O_6$) solid solution series by X-ray powder diffraction and ^{57}Fe Mössbauer spectroscopy. *Physics and chemistry of minerals*, **31**, 67-79.

Huber, A.L., Heuss-Aßbichler, S., Fehr, K.T. and Bromiley, G.D. (2012). Petedunnite ($CaZnSi_2O_6$): Stability and phase relations in the system CaO-ZnO-SiO_2. *American Mineralogist*, **97**, 739-749.

Hugh-Jones, D.A and Angel, R.J. (1994). A compressional study of $MgSiO_3$ orthoenstatite to 8.5 GPa. *American Mineralogist*, **79**, 405– 410.

Hugh-Jones, D.A., Woodland, A.B. and Angel, R.J. (1994). The structure of high-pressure *C2/c* ferrosilite and crystal chemistry of high-pressure *C2/c* pyroxenes. *American Mineralogist*, **79**, 1032-1041.

Hunault, M.O., Galoisy, L., Lelong, G., Newville, M. and Calas, G. (2016). Effect of cation field strength on Co^{2+} speciation in alkali-borate glasses. *Journal of Non-Crystalline Solids*, **451**, 101-110.

Jodlauk, S., Becker, P., Mydosh, J.A., Khomskii, D.I., Lorenz, T., Streltsov, S.V., Hezel, D.C. and Bohatý, L. (2007). Pyroxenes: a new class of multiferroics. *Journal of Physics: Condensed Matter*, **19**, 432201.

Jonynaitė, D., Senvaitienė, J., Kiuberis, J., Kareiva, A., Juškėnas, R. and Ramanauskas, R. (2009). XRD characterization of cobalt-based historical pigments and glazes. *Chemija*, **20**, 10-18.

Kanzaki, M. (1991). Ortho/clinoenstatite transition. *Physics and Chemistry of Minerals*, **17**, 726-730.

Karamiana, E., Khandan, A., Rafiee, N. and Eslami, M. (2014). Synthesis of Nano-Crystallite Diopside by Mechanical Activation to Use Medical Applications. *Abstract Book of the 5th International Conference on Nanostructures (ICNS5) 6-9 March 2014, Kish Island, Iran, Sharif University of Technology*, page 47, Abstract BIO-077.

Karazhanov, S.Z., Ravindran, P., Vajeeston, P., Ulyashin, A.G., Fjellvåg, H. and Svensson, B.G. (2009). Phase stability and pressure-induced structural transitions at zero temperature in $ZnSiO_3$ and Zn_2SiO_4. J*ournal of Physics: Condensed Matt*er, **21**, 485801.

Keppler, H. and Bagdassarov, N. (1999). The speciation of Ni and Co in silicate melts from optical absorption spectra to 1500 C. *Chemical Geology*, **158**, 105-115.

Kirk-Othmer (1998b). Encyclopedia of chemical technology fourth edition, Vol. **19**. Wiley, New York.

Langer, K. (2001). A note on mean distances, $R_{[MO_6]}$, in substituted polyhedra,$[(M_{1-x}M_x') O_6]$, in the crystal structures of oxygen based solid solutions: local versus crystal averaging methods. *Zeitschrift für Kristallographie-Crystalline Materials*, **216**, 87-91.

Langer, K., Platonov, A.N. and Matsyuk, S.S. (2004). Local mean chromium–oxygen distances in Cr^{3+}-centered octahedra of natural grossular-uvarovite garnet solid solutions from electronic absorption spectra. *Zeitschrift für Kristallographie-Crystalline Materials*, **219**, 272-277.

Larson, A.C. and Von Dreele, R.B. (1994). Gsas. General Structure Analysis System. LANSCE, MS-H805, Los Alamos, New Mexico.

Leon, K., Mery, D., Pedreschi, F. and Leon, J. (2006). Color measurement in L*a* b* units from RGB digital images. *Food research international*, **39**, 1084-1091.

Le Roux, V., Lee, C.T. and Turner, S.J. (2010). Zn/Fe systematics in mafic and ultramafic systems: Implications for detecting major element heterogeneities in the Earth's mantle. *Geochimica et Cosmochimica Acta*, **74**, 2779-2796.

Le Roux, V., Dasgupta, R. and Lee, C.T. (2011). Mineralogical heterogeneities in the Earth's mantle: Constraints from Mn, Co, Ni and Zn partitioning during partial melting. *Earth and Planetary Science Letters*, **307**, 395-408.

Lindsley, D.H. (1980). Phase equilibria of pyroxenes at pressures < 1 atmosphere. *Reviews in Mineralogy and Geochemistry*, **7**, 289-307.

Lindsley, D.H. and Munoz, J.L. (1969). Subsolidus relations along the join hedenbergite-ferrosilite. *American Journal of Science*, **267** (Schairer Volume), 295-324.

Lindsley, D.H. and Dixon, S.A. (1976). Diopside-enstatite equilibria at 850 to 1400°C, 5 to 35 kb. *American Journal of Science*, **276**, 1285-1301.

Llusar, M., Forés, A., Badenes, J.A., Calbo, J., Tena, M.A. and Monrós, G. (2001). Colour analysis of some cobalt-based blue pigments. *Journal of the European Ceramic Society*, **21**, 1121-1130.

Mantovani, L., Tribaudino, M., Mezzadri, F., Calestani, G. and Bromiley, G. (2013). The structure of $(Ca,Co)CoSi_2O_6$ pyroxenes and the Ca-M^{2+} substitution in $(Ca,M^{2+})M^{2+}Si_2O_6$ pyroxenes (M^{2+}= Co, Fe, Mg). *American Mineralogist*, **98**, 1241-1252.

Mantovani, L., Tribaudino, M., Bertoni, G., Salviati, G., and Bromiley, G. (2014). Solid solutions and phase transitions in $(Ca,M^{2+})M^{2+}Si_2O_6$ pyroxenes (M^{2+}= Co, Fe, Mg). *American Mineralogist*, **99**, 704-711.

Mantovani, L., Tribaudino, M., Dondi, M. and Zanelli, C. (2015). Synthesis and color performance of $CaCoSi_2O_6$ pyroxene, a new ceramic colorant. *Dyes and Pigments,* **120**, 118-125.

Mason, B. (1974). Aluminium-titanium-rich pyroxenes, with special reference to the Allende meteorite. *Ibid.*, **59**, 1198-1202.

Masse, S., Boch, P. and Vaissière, N. (1999). Trapping of nickel and cobalt in $CaNiSi_2O_6$ and $CaCoSi_2O_6$ diopside-like phases in heat-treated cement. *Journal of the European Ceramic Society*, **19**, 93-98.

McLaren, K. (1976). XIII-The development of the CIE 1976 (L* a* b*) uniform colour space and colour-difference formula. *Journal of the Society of Dyers and Colourists*, **92**, 338-341.

McLennan, S.M. and Taylor, S.R. (1999). Earth's continental crust. *Encyclopedia of Geochemistry*, 712.

Mestre, S., Gómez-Tena, M.P., Gazulla, M.F. and Gozalbo, A. (2013). Interaction of the chromium–iron black pigment with porcelanised stoneware. *Ceramics International*, **39**, 7453-7459.

Mirwald, P.W. and Massonne, H.J. (1980). The low-high quartz and quartz-coesite transition to 40 kbar between 600° and 1600° C and some reconnaissance data on the effect of $NaAlO_2$ component on the low quartz-coesite transition. *Journal of Geophysical Research: Solid Earth*, **85(B12)**, 6983-6990.

Momma, K. and Izumi, F. (2008). VESTA: a three-dimensional visualization system for electronic and structural analysis. *Journal of Applied Crystallography*, **41**, 653-658.

Morimoto, N., Appleman, D.E. and Evans, H.T. (1960). The crystal structures of clinoenstatite and pigeonite. *Zeitschrift für Kristallographie*, **114**, 120-147.

Morimoto, N., Nakajima, Y., Syono, Y., Akimoto, S. and Matsui, Y. (1975). Crystal structure of Pyroxene-Type $ZnSiO_3$ and $ZnMgSi_2O_6$. *Acta Crystallographica*, **B31**, 1041-1049.

Morimoto, N. (1988). Nomenclature of pyroxenes. *Mineralogy and Petrology*, **39**, 55-76.

Mukhopadhyay, S. and Jacob, K.T. (1996). Phase equilibria in the system $CaO-CoO-SiO_2$ and Gibbs energies of formation of the quaternary oxides $CaCoSi_2O_6$, $Ca_2CoSi_2O_7$, and $CaCoSiO_4$. *American Mineralogist*, **81**, 963-972.

Navrotsky, A. and Coons, W.E. (1976). Thermochemistry of some pyroxenes and related compounds. *Geochimica et Cosmochimica Acta*, **40**, 1281-1288.

Nelson, C. and White, W.B. (1986). Transition metal ions in silicate melts. IV. Cobalt in sodium silicate and related glasses. *Journal of Materials Research*, **1**, 130-138.

Nestola, F., Ballaran, T.B., Tribaudino, M. and Ohashi, H. (2005). Compressional behaviour of $CaNiSi_2O_6$ clinopyroxene: bulk modulus systematic and cation type in clinopyroxenes. *Physics and Chemistry of Minerals*, **32**, 222-227.

Nestola, F., Tribaudino, M., Boffa Ballaran, T., Liebske, C. and Bruno, M. (2007). The crystal structure of pyroxenes along the jadeite-hedenbergite and jadeite-aegirine joins. *American Mineralogist*, **92**, 1492-1501.

Nestola, F., Boffa Ballaran, T., Angel, R.J., Zhao, J. and Ohashi, H. (2010). High-pressure behavior of Ca/Na clinopyroxenes: The effect of divalent and trivalent 3d-transition elements. *American Mineralogist*, **95**, 832-838.

Newton, R. C., Charlu, T. V., Anderson, P. A. M. and Kleppa, O. J. (1979). Thermochemistry of synthetic clinopyroxenes on the join $CaMgSi_2O_6$-$Mg_2Si_2O_6$. *Geochimica et Cosmochimica Acta*, **43**, 55-60.

Ohashi, Y. (1972). A program to calculate the strain tensor. Program listing provided in Hazen and Finger (1982). *Comparative crystal chemistry*, 92-102.

Ohashi, Y. (1984). Polysynthetically-twinned structures of enstatite and wollastonite. *Physics and Chemistry of Minerals*, **10**, 217-229.

Ohashi, Y. and Burnham, C.W. (1973). Clinopyroxene lattice deformations: the roles of chemical substitution and temperature. *American Mineralogist*, **58**, 843-849.

Ohashi, Y. and Finger, L. (1974a). Symmetry reduction and twinning relationships in clino- and orthopyroxenes. *Carnegie Institution of Washington Year Book*, **73**, 531-535.

Ohashi, Y., Burnham, C.W. and Finger, L.W. (1975). The effect of Ca-Fe substitution on the clinopyroxene crystal structure. *American Mineralogist*, **60**, 423-434.

Ohashi, H., Osawa, T. and Sato, A. (1990). Structures of $Na(In,Sc)Si_2O_6$ clinopyroxenes formed at 6 GPa pressure. *Acta Crystallographica*, **B46**, 742-747.

Ohashi, H., Osawa, T., Sato, A. and Tsukimura, K. (1996). Crystal structures of (Na, Ca) $(Sc, Zn)Si_2O_6$ clinopyroxenes formed at 6 GPa pressure. *Journal of Mineralogy, Petrology and Economic Geology*, **91**, 22-27.

Olesch, M., Doroshev, A.M. and Nekhaev, P.Y. (1982). Low pressure stability of zinc clinopyroxene ($ZnSiO_3$). *Neues Jahrbuch für Mineralogie, Monatshefte*, 312-320.

Onuma, N., Ninomiya, S. and Nagasawa, H. (1981). Mineral/groundmass partition coefficients for nepheline, melilite, clinopyroxene and perovskite in melilite-nepheline basalt, Nyiragongo, Zaire. *Geochemical Journal*, **15**, 221-228.

Ozel, E. and Turan, S. (2003). Production and characterisation of iron-chromium pigments and their interactions with transparent glazes. *Journal of the European Ceramic Society*, **23**, 2097-2104.

Ozel, E., Yurdakul, H., Turan, S., Ardit, M., Cruciani, G. and Dondi, M. (2010). Co-doped willemite ceramic pigments: technological behaviour, crystal structure and optical properties. *Journal of the European Ceramic Society*, **30**, 3319-3329.

Pacalo, R.E.G. and Gasparik, T. (1990). Reversals of the orthoenstatiteclinoenstatite transition at high pressures and high temperatures. *Journal of Geophysical Research*, **95**, 15853–15858.

Papike, J.J., Prewitt, C.T., Sueno, S. and Cameron, M. (1973). Pyroxenes: comparisons of real and ideal structural topologies. *Zeitschrift für Kristallographie*, **138**, 254-273.

Partington, J. R. (1961). *A history of chemistry* (Vol. **2**). Macmillan.

Percival, M. J. L. and Salje, E. (1989). Optical absorption spectroscopy of the $P2_13$-$P2_12_12_1$ transformation in $K_2Co_2(SO_4)_3$ langbeinite. *Physics and Chemistry of Minerals*, **16**, 563-568.

Plum, L.M, Rink, L. and Haase, H. (2010). The essential toxin: impact of zinc on human health. *International journal of environmental research and public health*, **7**, 1342-1365.

Prewitt, C.T. (1980). Pyroxenes. Vol.**7**, Mineralogical Society of America.

Putnis, A. (1992). An introduction to mineral sciences. Cambridge University Press.

Qian, J., Xue, H.B., Sigg, L. and Albrecht, A. (1998). Complexation of cobalt by natural ligands in freshwater. *Environmental science & technology*, **32,** 2043-2050.

Raudsepp, M., Hawthorne, F.C. and Turnock, A.C. (1990). Evaluation of the Rietveld method for the characterization of fine-grained products of mineral synthesis: the diopside-hedenbergite join. *Canadian Mineralo*gist, **28**, 93-109.

Redhammer, G.J. and Roth, G. (2004). Structural changes upon the temperature dependent $C2/c \rightarrow P2_1/c$ phase transition in $LiMe^{3+}$ Si_2O_6clinopyroxenes, Me= Cr, Ga, Fe, V, Sc and In. *Zeitschrift für Kristallographie*, **219**, 585-605.

Redhammer, G.J. and Tippelt, G. (2014). Pyroxene-type compounds $NaM^{3+}Ge_2O_6$, with *M*= Ga, Mn, Sc and In. *Acta Crystallographica*, **70**, 852-857.

Redhammer, G.J., Nestola, F. and Miletich, R. (2012). Synthetic $LiAlGe_2O_6$: The first pyroxene with $P2_1/n$ symmetry. *American Mineralogist*, **97**, 1213-1218.

Redhammer, G.J., Roth, G., Senyshyn, A., Tippelt, G. and Pietzonka, C. (2013). Crystal and magnetic spin structure of Germanium-Hedenbergite, $CaFeGe_2O_6$, and a comparison with other magnetic/magnetoelectric/multiferroic pyroxenes *Zeitschrift für Kristallographie*, **228**, 140-150.

Redhammer, G.J., Roth, G., Treutmann, W., Paulus, W., Andre, G., Pietzonka, C. and Amthauer, G. (2008). Magnetic ordering and spin structure in Ca-bearing clinopyroxenes $CaM^{2+}(Si, Ge)_2O_6$, M = Fe, Ni, Co, Mn. *Journal of Solid State Chemistry*, **181**, 3163-3176.

Redhammer, G.J., Roth, G., Treutmann, W., Hoelzel, M., Paulus, W., Andre, G., Pietzonka, C. and Amthauer, G. (2009). The magnetic structure of clinopyroxene-type $LiFeGe_2O_6$ and revised data on multiferroic $LiFeSi_2O_6$. *Journal of Solid State Chemistry*, **182**, 2374-2384.

Ringwood, A.E. (1975). Composition and petrology of the Earth's mantle, 74-122. McGraw-Hill, New York.

Robinson, K., Gibbs, G.V. and Ribbe, P.H. (1971). Quadratic elongation: A quantitative measure of distortion in coordination polyhedra. *Science*, **17**2, 567-570.

Rossi, G., Oberti, R., Dal Negro, A., Molin, G.M. and Mellini, M. (1987). Residual electron density of the M2 site in *C*2/*c* clinopyroxenes relationship with bulk chemistry and sub-solidus evolution. *Physics and Chemistry of Minerals*, **14**, 514-520.

Rothon, R. (2012). Pigment and nanopigment dispersion technologies. Smithers Rapra Publishing.

Salem, S., Jazayeri, S.H., Bondioli, F., Allahverdi, A. and Shirvani, M. (2011). Characterizing thermal behavior of ceramic glaze containing nano-sized cobalt-aluminate pigment by hot stage microscopy. *Thermochimica acta*, **521**, 191-196.

Sasaki S. and Takéuchi Y. (1981). Electron-density distributions of three orthopyroxenes, $Mg_2Si_2O_6$, $Co_2Si_2O_6$, and $Fe_2Si_2O_6$. *Zeitschrift für Kristallographie*, **158**, 279-298.

Sawaoka, A., Miyahara, S. and Akimoto, S.I. (1968). Magnetic properties of several metasilicates and metagermanates with pyroxene structure. *Journal of the Physical Society of Japan*, **25**, 1253-1257.

Segal, D. (1991). *Chemical synthesis of advanced ceramic materials* (Vol. **1**). Cambridge University Press.

Segnit, E.R. (1954). The System CaO-ZnO-SiO_2. *Journal of the American Ceramic Society*, **37**, 273-277.

Shannon, R.T. (1976). Revised effective ionic radii and systematic studies of interatomic distances in halides and chalcogenides. *Acta Crystallographica Section A: Crystal Physics, Diffraction, Theoretical and General Crystallography*, **32**, 751-767.

Shannon, R.D. and Prewitt, C.T. (1970). Revised values of effective ionic radii.Acta Crystallographica Section B: *Structural Crystallography and Crystal Chemistry*, **26**, 1046-1048.

Sheldrick, G.M. (1996). SADABS, program for empirical absorption correction of area detector data. University of Göttingen, Göttingen, Germany.

Sheldrick, G.M. (1997). SHELXL-97, program for Crystal Structure Analysis. University of Göttingen, Göttingen, Germany.

Singh, H.B. and Bharati, K.A. (2014). Handbook of natural dyes and pigments. Woodhead publishing, New Dehli.

Smyth, J.R. and Burnham, C.W. (1972). The crystal structures of high and low clinohypersthene. *Earth and Planetary Science Letters*, **14**, 183-189.

Sueno, S., Kimata, M. and Prewitt, C.T. (1984). The crystal structure of high clinoferrosilite. *American Mineralogist*, **69**, 264-269.

Syono, Y., Akimoto, S.I. and Matsui, Y. (1971). High pressure transformations in zinc silicates. *Journal of Solid State Chemistry*, **3**, 369-380.

Tabira, Y., Ishizawa, N. and Marumo, F. (1993). Cobalt atoms at M (2) site in *C*2/*c* clinopyroxenes of the system $CaMgSi_2O_6$ (Di)-$CaCoSi_2O_6$ (CaCoPx). *Mineralogical Journal*, **16**, 225-245.

Taran, M. N. and Rossman, G. R. (2001). Optical spectra of Co^{2+} in three synthetic silicate minerals. *American Mineralogist*, **86**, 889-895.

Taran, M.N., Langer, K., Abs-Wurmbach, I., Frost, D.J. and Platonov, A.N. (2004). Local relaxation around $^{[6]}Cr^{3+}$ in synthetic pyrope–knorringite garnets,$^{[8]}Mg_3\,^{[6]}(Al_{1-X}\,Cr_X^{3+})_2\,^{[4]}Si_3O_{12}$, from electronic absorption spectra. *Physics and Chemistry of Minerals*, **31**, 650-657.

Tanabe, Y. and Sugano, S. (1954). On the absorption spectra of complex ions. I and II. *Journal of the Physical Society of Japan*, **9**, 753-779.

Thompson, Jr., J.B. (1970). Geometrical possibilities for amphibole structures: model biopyriboles. *American Mineralogist*, **55**, 292-293.

Thompson, R.M. and Downs, R.T. (2003). Model pyroxenes I: Ideal pyroxene topologies. *American Mineralogist*, **88**, 653-666.

Thompson, R.M. and Downs, R.T. (2004). Model pyroxenes II: Structural variation as a function of tetrahedral rotation. *American Mineralogist*, **89**, 614-628.

Thompson, R.M., Downs, R.T. and Redhammer, J.G. (2005). Model pyroxenes III: Volume of *C2/c* pyroxenes at mantle *P*, *T*, and *x*. *American Mineralogist*, **90**, 1840-1851.

Toby, B.H. (2001). EXPGUI, a graphical user interface for GSAS. *Journal of Applied Crystallography*, **34**, 210-213.

Tribaudino, M. (2000). A transmission electron microscope investigation of the $C2/c \rightarrow P2_1/c$ phase transition in clinopyroxenes along the diopside-enstatite ($CaMgSi_2O_6$-$Mg_2Si_2O_6$) join. *American Mineralogist*, **85**, 707-715.

Tribaudino, M. (1996). High-temperature crystal chemistry of *C2/c* clinopyroxenes along the join $CaMgSi_2O_6$-$CaAl_2SiO_6$. *European Journal of Mineralogy*, **8**, 273-279.

Tribaudino, M. and Mantovani, L. (2014). Thermal expansion in *C*2/*c* pyroxenes: a review and new high-temperature structural data for a pyroxene of composition $(Na_{0.53}Ca_{0.47})(Al_{0.53}Fe_{0.47})$ Si_2O_6 (Jd53Hd47). *Mineralogical Magazine*, **78**, 311-324.

Tribaudino, M., Benna, P. and Bruno, E. (1989). Average structure and M2 site configurations in *C*2/*c* clinopyroxenes along the Di-En join. *Contributions to Mineralogy and Petrology*, **103**, 452-456.

Tribaudino, M., Nestola, F., Cámara, F. and Domeneghetti, M. C. (2002). The high-temperature $P2_1/c$-$C2/c$ phase transition in Fe-free pyroxene ($Ca_{0.15}Mg_{1.85}Si_2O_6$): Structural and thermodynamic behavior. *American Mineralogist*, **87**, 648-657.

Tribaudino, M., Nestola, F., Meneghini, C. and Bromiley, G.D. (2003). The high-temperature $P2_1/c$-$C2/c$ phase transition in Fe-free Ca-rich $P2_1/c$ clinopyroxenes. *Physics and Chemistry of Minerals*, **30**, 527-535.

Tribaudino, M., Nestola, F. and Meneghini, C. (2005a). The structure behavior of intermediate pyroxenes along the diopside-enstatite join. *Canadian Mineralogist*, **43**, 1411-1421.

Tribaudino, M., Nestola, F. and Ohashi, H. (2005b). High temperature single crystal investigation in a clinopyroxene of composition $(Na_{0.5}Ca_{0.5})(Cr_{0.5}Mg_{0.5})Si_2O_6$. *European Journal of Mineralogy*, **17**, 297-304.

Tribaudino, M., Nestola, F. and Meneghini, C. (2005). Rietveld refinement of clinopyroxenes with intermediate Ca-content along the join diopside-enstatite. *Canadian Mineralogist*, **43**, 1411-1421.

Tribaudino, M., Bromiley, G., Ohashi, H. and Nestola, F. (2009). Synthesis, TEM characterization and thermal behavior of $LiNiSi_2O_6$ pyroxene. *Physics and Chemistry of Minerals*, **36**, 527-536.

Trussell, H.J., Saber, E. and Vrhel, M. (2005). Color image processing: Basics and special issue overview. *IEEE signal processing magazine*, **22,** 14-22.

Underhill, A.E. and Billing, D.E. (1966). Calculations of the racah parameter b for nickel (II) and cobalt (II) compounds. *Nature*, **210**, 834 – 835.

Ure, A.M. and Berrow, M.L. (1982). Environmental chemistry. *Spec. Period. Rep*, **2**, 94-204.

Wedepohl K.H. (1978). Handbook of Geochemistry 11, Sections 73, B-G. Springer-Verlag.

Wentzcovitch, R.M., Hugh-Jones, D.A., Angel, R.J. and Price, G.D. (1995). Ab initio study of $MgSiO_3$ *C*2/*c* enstatite. *Physics and Chemistry of Minerals*, **22**, 453-460.

White, B.W., McCarthy, G.J. and Scheetz, B.E. (1971). Optical spectra of chromium, nickel, and cobalt–containing pyroxenes. *American Mineralogist*, **56**, 72–89.

Wiedenmann, A., Regnard, J.R., Fillion, G. and Hafner, S. S. (1986). Magnetic properties and magnetic ordering of the orthopyroxenes $Fe_xMg_{1-x}SiO_3$. *Journal of Physics C: Solid State Physics*, **19**, 3683.

Wildner, M. and Langer, K. (1994). Co^{2+} in trigonal fields of oxygen based structures: Electronic absorption spectra of buetschliite-type $K_2Co\ (SeO_3)_2$, $K_2Co_2\ (SeO_3)_3$ and zemannite-type $K_2Co_2\ (SeO_3)_3 \cdot$ 2H2O. *Physics and Chemistry of Minerals*, **20**, 460-468.

Wildner, M. (1996). Polarized electronic absorption spectra of tetrahedrally coordinated Co^{2+} ions in the new compound $Ca_3Co\ (SeO_3)_4$ and its structural characterization. *Journal of Solid State Chemistry*, **124**, 143-150.

Wildner, M. (1996). Polarized electronic absorption spectra of Co^{2+} ions in the kieserite-type compounds $CoSO_4 \cdot H_2O$ and $CoSeO_4 \cdot H_2O$. *Physics and chemistry of minerals*, **23**, 489-496.

Zhang, Y., Huang, S., Schneider, D., Benoit, P.H., DeHart, J.M., Lofgren, G.E. and Sears, D. W. (1996). Pyroxene structures, cathodoluminescence and the thermal history of the enstatite chondrites. *Meteoritics & Planetary Science*, **31**, 87-96.

ACKNOWLEDGEMENTS

Giunta al termine di questo intenso e stimolante percorso, vorrei ringraziare tutti coloro che mi hanno seguita, sostenuta, e che hanno dispensato consigli utili alla mia crescita professionale e anche personale. In primo luogo rivolgo il più sincero ringraziamento al mio relatore, il prof. Mario Tribaudino senza il quale tutto ciò non sarebbe stato possibile e grazie al quale ho acquisito maggiore conoscenza e sicurezza in ambito scientifico.

Ringrazio anche i Professori Henrik Skogby e Ulf Hålenius del Dipartimento di Geoscienze presso il Museo di Storia Naturale di Stoccolma per avermi dato la possibilità di trascorrere un periodo di tre mesi come visiting student, seguendomi con meticolosità e dimostrandomi costantemente piena disponibilità. Colgo l'occasione per ringraziare anche i Prof. Ferdinando Bosi e G.B. Andreozzi dell'Università di Roma "La Sapienza", per avermi trasmesso le loro conoscenze e per aver contribuito a far nascere in me una profonda passione per la mineralogia.

Ringrazio di cuore tutte le persone che hanno collaborato alla mia attività di ricerca e senza le quali non sarebbe stato possibile ottenere tanti risultati: Michele Dondi, Chiara Zanelli e Guia Guarini dell'*ISTEC* di Faenza, Edmondo Gilioli e il suo gruppo di ricerca dell'*IMEM* di Parma, Gianluca Calestani e Francesco Mezzadri del Dipartimento di Chimica dell'Università di Parma, Claudio Oleari, Danilo Bersani e Pier Paolo Lottici del Dipartimento di Fisica e Scienze della Terra dell'Università di Parma.

Un ringraziamento particolare va ai miei colleghi/e Luciana, Antonella, Claudia e Angelo che si sono rivelati soprattutto degli amici con i quali ho condiviso gran parte del mio tempo e tanti bei momenti, lavorativi e non. Ringrazio Erica ed Irene per i pranzi, i consigli e i momenti di svago in questi tre anni.

Un ringraziamento particolare va ai miei genitori per la stima dimostratami e per avermi sostenuta sempre con tanto amore e ai miei nonni che non ci sono più, sono sicura che sarebbero fieri di me.

Un grazie, infine, alla persona più importante della mia vita, Andrea, mio complice e compagno che mi ha sempre rassicurata e ha sempre creduto in me, portandomi alla realizzazione di tanti obiettivi importanti.